Universitat Autònoma de Barcelona

Modeling the interaction of ferromagnetic skyrmionic structures with material defects and superconductors

Leonardo Gastón González Gómez

ADVERTIMENT. L'accés als continguts d'aquesta tesi queda condicionat a l'acceptació de les condicions d'ús establertes per la següent llicència Creative Commons: http://cat.creativecommons.org/?page_id=184

ADVERTENCIA. El acceso a los contenidos de esta tesis queda condicionado a la aceptación de las condiciones de uso establecidas por la siguiente licencia Creative Commons: http://es.creativecommons.org/blog/licencias/

WARNING. The access to the contents of this doctoral thesis it is limited to the acceptance of the use conditions set by the following Creative Commons license: https://creativecommons.org/licenses/?lang=en

Universitat Autònoma de Barcelona
Departament de Física

Modeling the interaction of ferromagnetic skyrmionic structures with material defects and superconductors

Leonardo Gastón González Gómez

Under the supervision and tutoring of:

Carles Navau Ros

Nuria Del Valle Benedí

Submitted in partial fulfillment of the requirements
for the degree of Doctor of Philosophy in Physics
of the Universitat Autònoma de Barcelona, December 2022

Abstract

This thesis is devoted to the theoretical modeling of skyrmionic structures and their interaction with other agents. First, we consider how defects in the material can affect the skyrmion trajectories. From an atomic defect, we propose a particle model to take into account extended (in space) defects, such as grain dislocations. This model allows us to obtain analytical expressions for the critical points of the skyrmion trajectories and for the threshold current velocity above which these critical points cease to exist. We found that a line defect (e.g. grain dislocation) can guide the skyrmions along the defect and speed them up. It is also found that a periodic arrangement of such defects creates a periodic pinning array for skyrmions. In this way we derive a scenario in which these types of potentials appear, giving some physical basis to previously used ad hoc potentials.

Then, we consider the interaction of a ferromagnetic disk with a coaxial superconducting disk. The interaction is mediated via the stray fields created by the magnetization structures and the currents, through a two-way coupling. For the ferromagnetic, we use the micromagnetic model and for the superconductor, we use the London model. This allows us to obtain the magnetization and current distributions simultaneously. To characterize the system as a function of the applied field, we first consider a hysteresis loop of applied field. We have characterized the transitions between different magnetic states. In particular, we find an additional skyrmion-to-2π transition caused by the presence of a superconductor. The results are complemented with geodesic nudged elastic band method calculations, which allow us to study the magnetic states' stability. We also study the system's behavior as a function of the separation distance between plates finding their interaction forces.

To sum up, in this thesis we propose different models that could enable novel skyrmionic devices to be developed. We discuss some possible applications such as skyrmionic racetracks, skyrmion-based atomic magnetic traps, ternary logic, and skyrmionic metamaterials.

Agradecimientos

El contenido de este documento representa muchas horas de trabajo y muchos errores. Mis ideas son en gran medida el resultado de años rodeado de físicos brillantes, de los cuales he podido empaparme de conocimientos.

Me gustaría empezar agradeciendo a Maria, que me ha acompañado a lo largo de este reto. Gracias por apoyarme moralmente en mis peores momentos y ayudarme a continuar motivado. Durante estos años han pasado muchas cosas a nuestro alrededor que eran imprevisibles y podrían habernos afectado, pero juntos hemos podido superar los momentos más críticos. También quiero agradecer el apoyo y comprensión estos últimos meses, sin ellos no creo que hubiese podido redactar la tesis como lo he hecho.

A continuación, quiero agradecer a la gente con la que he trabajado más de cerca. Sin la ayuda de Carles y Nuria, no hubiese podido acabar este documento manteniendo lo poco que me queda de cordura. Gracias por hacer que no me ahogara en un mar de ideas, vuestra dirección ha sido crucial para que finalmente terminase centrándome en un tema. Me siento muy afortunado de haber tenido unos directores tan atentos y pacientes como vosotros, que me han ayudado a crecer no sólo académicamente sinó también como persona.

También quiero agradecer a Josep por aguantarme tantas horas y perdonarme por hacer que Carles le diera trabajo extra. Sin tus cálculos micromagnéticos y tu código esta tesis no habría sido posible. Sé que en el fondo estás contento de que haya entregado antes, ¡al menos así no puedo seguir dándote la vara!

Quiero agradecer a mis compañeros de la UAB, tanto estudiantes de doctorado como profesores, por las discusiones que he tenido con ellos sobre otras áreas de la Física. Estas, han mantenido mi interés por la ciencia y han saciado un poco mis ganas de dispersarme. Desde mi punto de vista, la ciencia surge de compartir ideas y experiencias y creo que, a pesar de la pandemia, hemos sido capaces de adaptar nuestros valiosos debates a este nuevo paradigma. Espero que podamos seguir compartiendo ideas aunque nuestros caminos se separen. Especialmente quiero remarcar la amistad que tuve la suerte de forjar con Rosa y Sergi. Desgraciadamente nuestros caminos se bifurcaron demasiado pronto, pero espero que podamos encauzarlos de nuevo.

No podía olvidarme de dar las gracias a quienes han sido también muy importantes para mí, mis amigos fuera de la UAB. Vosotros que me habéis ayudado a continuar adelante y, en ocasiones, incluso a vislumbrar el camino. En concreto me gustaría agradecer a Marc por todas las veces que hemos hablado de física y de otras inquietudes fuera del trabajo. También quiero agradecer a David y Ainhoa, por haber hecho bastante más ameno este último año. David, gracias a ti me acabé sacando el máster (no nos engañemos, Alsedà hubiese podido conmigo). Supongo que en parte te debo el doctorado ya que sino, no hubiese podido siquiera inscribirme. Podríamos decir que has sido la *lus cuántica* que ha iluminado mi camino. Y por último, pero no menos importante, quiero agradecer a Martí. Creo que eres una de las personas más brillantes y apasionadas que conozco, una pena que estés chalado... Muchas gracias por proporcionarme la plantilla para la tesis y por ayudarme a pesar de estar en un país completamente distinto. Espero que esta nueva etapa te sea fructífera.

A mis padres, cuyo cariño y sacrificio ha sido primordial en el desarrollo de mi carrera científica. Seguramente no hubiese acabado la carrera de no haber sido por vuestro apoyo. Gracias por convencerme a continuar aunque no siempre fuese un camino de rosas.

Muchas gracias también a toda la gente que no nombro pero que han formado parte de esta experiencia.

Y, finalmente, muchas gracias a las personas que han dedicado su tiempo a leer esta tesis. Espero que la disfrutéis y, con un poco de suerte, os llevéis algo a cambio.

Acknowledgements

I would like to thank the financial support from Catalan project 2017-SGR-105, Spanish project MAT2016-79426-P of Agencia Estatal de Investigación/Fondo Europeo de Desarrollo Regional (UE), and Spanish project PID2019-104670GB-I00 of Agencia Estatal de Investigación / Fondo Europeo de Desarrollo Regional (UE).

‘Nothing in life is to be feared, it is only to be understood. Now is the time to understand more, so that we may fear less.’

Marie Curie

‘Progress is made by trial and failure; the failures are generally a hundred times more numerous than the successes, yet they are usually left unchronicled.’

William Ramsay

Acronyms

BC Boundary Condition.
BCS Barden-Cooper-Schrieffer.

DM Dzyaloshinskii-Moriya.
DW Domain Wall.

EHH Extendend Heisenberg Hamiltonian.

FC Field-Cooled.
FM Ferromagnet.
FSH Ferromagnet-Superconductor Hybrid.

GMR Giant Magneto-Resistance.
GNEB Geodesic Nudget Elastic Band.

HAMR Heat Assisted Magnetorecording.
HDD Hard Disk Drive.
HM Heavy Metal.
HTST Harmonic Transition State Theory.

iDM Interfacial Dzyaloshinskii-Moriya.
IT Information Technology.

LLG Landau-Lifshitz-Gilbert.

MEP Minimum Energy Path.
MRAM Magnetic Random Access Memory.

PV Pearl Vortex.

RAM Random Access Memory.

SC Superconductor.
SHE Spin Hall Effect.
STT Spin Transfer Torque.

TMR Tunnel Magneto-Resistance.

ZFC Zero-Field-Cooled.

Symbols

Symbol	**Description**	**Unit**
$\mathcal{H}$	Hamiltonian	J
$\mathbf{A}$	Magnetic vector potential	T m
$\mathbf{J}$	Volumic current density	A m^{-2}
$\mathbf{K}$	Sheet-current density	A m^{-1}
$\mathbf{f}$	Normalized force (Thiele), $\mathbf{f} = \mathbf{F}/(\gamma M_\mathrm{s}^2 t_f R_\mathrm{sk})$	
A_ex	Exchange interaction constant	J m^{-1}
D_DM	Dzyaloshinskii-Moriya constant	J m^{-2}
$F_{0,\mathrm{DM}}$	Force amplitude a local DM defect does over a skyrmion	m A s^{-1}
H_a	Applied magnetic field	A m^{-1}
J_ex	Exchange integral	Jm^2 A^{-2}
K_an	Anisotropy constant	J m^{-3}
M_s	Saturation magnetization	A m^{-1}
N_sk	Skyrmion number	
R_sk	Skyrmion radius	m
Λ	Superconducting screening length	m
Φ_0	Magnetic flux quantum	Wb
α	Gilbert damping constant	
$\mathbf{m}$	Normalized magnetization by M_s	
χ_an	Adimensional anisotropy constant, $\chi = 2K_\mathrm{an}/(\mu_0 M_s^2)$	
δ	Local variation factor of the DM constant	
γ	Gyromagnetic constant	m A^{-1} s^{-1}
λ_L	London penetration depth	m
$\mathbb{B}$	Adiabatic-SHE-torque tensor	A^2 m^{-1}

Symbol	Description	Unit
$\mathbb{D}$	Dissipative tensor	A^{2} m^{-1}
$\mathbb{G}$	Gyrotropic tensor	A^{3} m^{-2}
$\mathcal{B}$	Normalized dissipative tensor constant, $\mathcal{B} = B/M_s^2 R_{\mathrm{sk}}$	
$\mathcal{D}$	Normalized dissipative tensor constant, $\mathcal{D} = D/M_s^2 t_f$	
$\mathcal{E}$	Normalized energy, $\mathcal{E} = \frac{E}{\mu_0 M_s^2 l_{\mathrm{ex}}^3}$	
$\mathcal{G}$	Normalized gyrotropic tensor constant, $\mathcal{G} = G/Ms^3 t_f$	
μ_B	Bohr magneton	J T^{-1}
μ	Magnetic permeability	J T^{-1}
θ_{sk}	Skyrmion Hall angle	
$\varPhi_0$	Normalized magnetic flux quantum, $\varPhi_0 = \frac{\Phi_0}{\mu_0 M_s l_{\mathrm{ex}}^2}$	
ε	Energy density	J m^{-3}
φ_{HM}	Incident applied current angle in the HM	
ξ_{GL}	Superconducting coherence length	m
ξ	Adimensional DM constant, $\xi = D_{\mathrm{DM}} l_{\mathrm{ex}}/A_{\mathrm{ex}}$	
a	Atomic lattice constant	m
d_{DM}	Atomic Dzyaloshinskii-Moriya constant	Jm^{2} A^{-2}
e	Electron charge ($e > 0$)	C
h	Normalized magnetic field by M_s	
k_{B}	Boltzmann constant	J K^{-1}
k_{an}	Atomic anisotropy constant	Jm^{2} A^{-2}
l_{ex}	Exchange length, $l_{\mathrm{ex}} = \sqrt{2A_{\mathrm{ex}}/(\mu_0 M_s^2)}$	m
t_0	Characteristic precession time, $t_0 = (\gamma M_s)^{-1}$	s
t_f	Thickness of the ferromagnet, t_f	m
t_s	Thickness of the superconductor, t_s	m
$\mathcal{A}$	Normalized magnetic vector potential, $\mathcal{A} = \frac{\mathbf{A}}{\mu_0 M_s l_{\mathrm{ex}}}$	
$\mathcal{K}$	Normalized sheet-current density, $\mathcal{K} = \frac{\mathbf{K}}{M_s}$	

Contents

Abstract i

Agradecimientos iii

Acknowledgements v

Chapter 1: Introduction 1

1.1 Magnetism for data storage and handling 1

1.2 Magnetic skyrmions 3

Chapter 2: Basic concepts 7

2.1 Ferromagnetism 8

2.2 Micromagnetism 9

2.2.1 Brown equation 9

2.2.2 Landau-Lifshitz-Gilbert equation 10

2.2.3 Effective Fields and energy density 11

2.2.4 Boundary conditions 17

2.2.5 External Torques 17

2.2.6 Rigid model 21

2.2.7 Structure stability 26

2.3 Superconductivity 30

2.3.1 London model 31

Chapter 3: Skyrmion-Defect interaction **35**

3.1 A brief topical review . . . 36

3.2 Point Defect interaction . . . 38

3.2.1 Defects within the rigid model . . . 39

3.3 Extended defect interaction . . . 42

3.3.1 Segment and line defects . . . 43

3.3.2 More complex defects . . . 50

3.4 Chapter summary and conclusions . . . 57

Chapter 4: Skyrmion-Superconductor interaction **59**

4.1 A brief topical review . . . 59

4.2 FSH system modeling: Disk geometries . . . 63

4.2.1 Mutual interaction . . . 64

4.2.2 Discretization and algorithm . . . 70

4.3 Numerical results . . . 72

4.3.1 On the response to a uniform applied field . . . 72

4.3.2 On the response with plates' separation . . . 82

4.4 Generalizing the model: Ring geometries . . . 90

4.5 Chapter summary and conclusions . . . 92

Chapter 5: Conclusions and future perspectives **93**

Appendix A: Thiele equation **95**

A.1 From LLG to Thiele . . . 95

A.2 Complex Thiele equation . . . 98

Appendix B: Stability of magnetic structures **99**

B.1 GNEB table . . . 99

B.2 Beyond GNEB . . . 99

Appendix C: Interaction with a close SC 101

C.1 On the renormalization of the demagnetizing field 101

C.2 On the toy model with the 2π state 102

C.3 Summary of FM-SC hybrids response to plate separation 103

Bibliography 117

Chapter 1

Introduction

In this thesis, we deal with the use of skyrmions as bits of information and how they affect and are affected by other agents. We will study how defects can affect the transport of skyrmions and we will consider ferromagnetic-superconducting hybrid systems in confined geometries. This study is relevant in the field of skyrmionics as many applications demand precise control and knowledge of skyrmion creation, its dynamics, and its annihilation.

1.1 Magnetism for data storage and handling

During the 20th century, the understanding of magnetic phenomena in different materials spurred the technological development of magnetic recording media. It began in the 1950s with the creation of the first magnetic hard disk drives (HDDs). Since then, the need to store massive amounts of data in the smallest possible device has motivated the search for new mechanisms. The current paradigm consists of encoding information in the orientation of the magnetization of different magnetic grains, that can be read and switched individually.[1, 2] At present, the main limitation of this method is the reduction of the grain's size. We are reaching a scale at which grain magnetization fluctuates randomly, which makes them unstable and prevents reliable information storage. To address this problem, a series of alternative magnetic recording technologies have been proposed by the scientific community,[3, 4] but their real-life application remains difficult due to engineering challenges. Among these techniques, heat-assisted magnetorecording (HAMR) has been found to be promising. This technique takes advantage of the fact that the material's coercivity decreases with temperature, allowing materials with higher uniaxial anisotropies to be used. This gives rise to more stable grains that are heated when their magnetic state needs to be switched.[5]

But not only the information storage is relevant, but also the speed at which it can be accessed and processed. This is why random access memories (RAM) were developed, allowing faster data access at the expense of volatility[a]. On the one hand, there are the physical limitations of Moore's law, which states that the chip performance will be duplicated every two years, without increasing the production cost. To keep up with Moore's law, the number of transistors increased, and so did their density. We have reached the point where transistors are limited by heating and the Heisenberg uncertainty principle and it is unreliable to further scale transistors down.

---

[a] The information stored is lost if current is not applied.

On the other hand, the energy consumption of these technologies continues to skyrocket. With societies concerned about climate change, it is pertinent to consider the impact of even the most common applications. For example, it is estimated that each search performed on Google emits 0.2g of CO_2.[6] If the information technology (IT) sector were a country, it would be the third largest energy consumer in the world.

All the previous innovations and others have been the key factors for reaching the so-called information age. In the last decades, the storage and handling of information continuously demand faster, denser, non-volatile, and low-power-consuming technologies. In this context, spintronics, which uses both charge and spin degrees of freedom of the electrons, has provided some novel concepts to improve on previous technologies.[7,8] A breakthrough came with the discovery of the giant magnetoresistance (GMR) effect by Albert Fert[9] and Peter Grünberg.[10] This effect refers to a significant change in the resistance of two ferromagnetic layers separated by a metal spacer, depending on the relative magnetization orientation of the ferromagnets (FMs). This resulted in a remarkable increase in the storage capacity of HDDs. This discovery was awarded the Nobel Prize in 2007. Later, the tunneling magnetoresistance was discovered (TMR), which led to an order of magnitude higher resistance variation as compared to GMR. This led to magnetic tunnel junctions (in which the metal spacer is replaced with an insulator) and, with them, a new concept of memory devices, magnetic random access memories (MRAMs),[7] was born. MRAMs exploit the possibility of changing the magnetization direction of one of the ferromagnetic layers by means of an applied spin-polarized current. In Fig. 1.1, we show some examples of different device proposals, based on the TMR [Fig. 1.1(a)] and an implementation of the racetrack memory [Fig. 1.1(b)]. In parallel to MRAMs, an alternative idea to manipulate the information bits was proposed: using domain wall (DW) racetrack memories.[11] Here the information is not localized but is mobile along a nanowire, with the information encoded in the domains' magnetization direction (up or down) separated by DWs.

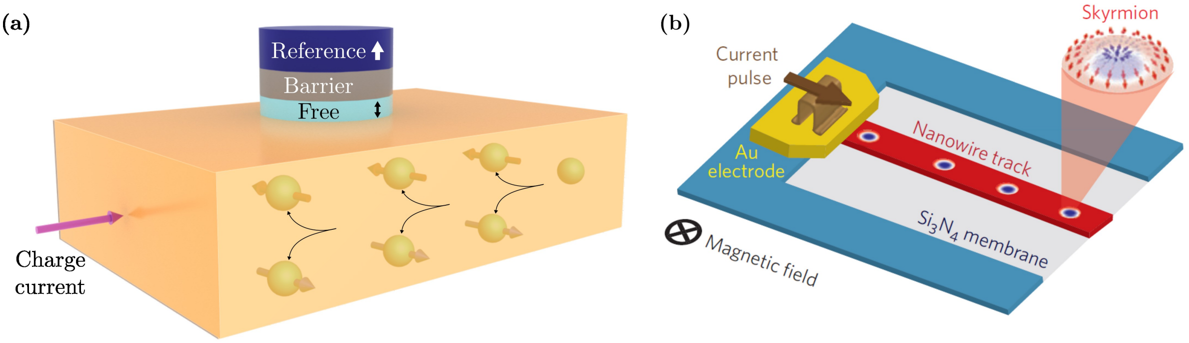

Figure 1.1: (a) Scheme of the simplest MRAM design. Its design is based on the dependence of the system's magnetoresistance as a function of the relative orientation of the magnetization of the free layer (light blue) with respect to the reference layer (dark blue). (b) Sketch of a magnetic racetrack memory, based on a magnetic skyrmion. The presence or not of a skyrmion would be a 1 or a 0. The skyrmion is moved with spin currents. Figure (b) is adapted from Woo et al.[12]

In recent years, attention has shifted to materials with broken inversion symmetry, in which the Dzyaloshinskii-Moriya (DM) interaction is present. This interaction allowed the stabilization of chiral structures in the magnetization of the material. The DM interaction has been shown to have an effect on the properties of the stabilized magnetic structures, such as their speed or stability, which are beneficial for future technologies.[13–15] Among these magnetic structures, great interest has been shown in magnetic skyrmions. The peculiar skyrmion topology makes them more robust against transitions to more topologically trivial magnetic structures (e.g. the uniform state), while their non-collinear spin texture makes them interact efficiently with spin currents. These features, together with the fact that they can be very small (a few nanometers in size), create great potential for their application as next-generation high-density information storage and handling devices.

Since skyrmions are going to be the central structures used in this thesis, it is worthwhile to make a brief introduction to them.

1.2 Magnetic skyrmions

Skyrmions were proposed by Tony Skyrme in the 1960s in the field of particle physics.[16] These particles are characterized by a quantized topological integer number that cannot be changed by a continuous deformation of the field configuration. In this sense, one refers to them as topologically protected particles. This theoretical model turned out to be useful in condensed matter systems such as Bose-Einstein condensates,[17] liquid crystals,[18] and quantum Hall systems.[19,20]

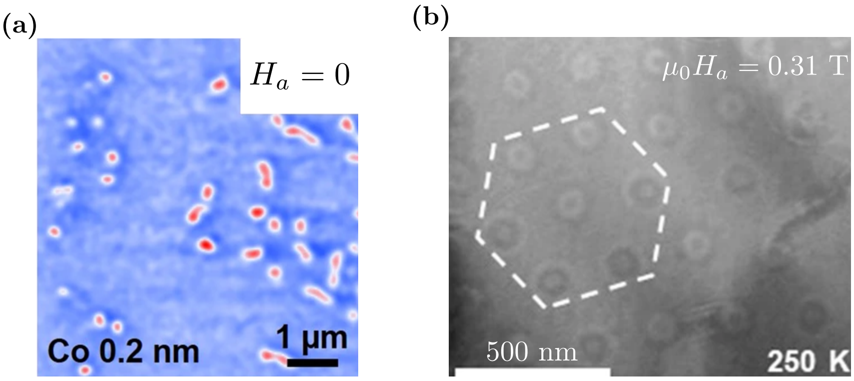

Figure 1.2: (a) Magnetic force microscopy images acquired with a Co thickness of 0.2 nm, finding isolated skyrmions at room temperature. Red and blue contrasts represent the out-of-plane magnetization. (b) Lorentz transmission electron microscopy images of magnetic skyrmions at 250 K. The hexagonal skyrmion lattices are marked with the dotted hexagon. Figure (a) adapted from Brandao et al.[21] Figure (b) is adapted from Chakrabartty et al.[22]

More recently, the field in which skyrmions reached their maximum impact would be in helimagnetic systems, where skyrmions are whirling spin textures with particle-like behavior.[15,23] Skyrmions were theoretically predicted in the 90s[24] and experimentally found in 2009,[25] with its real-space topology confirmed in 2010.[26] Nevertheless, their interest skyrocketed after they were proposed for a new kind of racetrack memory by Albert Fert in 2013.[27] Since then, skyrmions have been envisioned as the building blocks for a new generation of magnetic memories and spintronic devices thanks to their small sizes, efficiency in their movement, and stability.[14,15,28,29] This led to the field of skyrmionics, a subset of spintronics that makes use of skyrmions and other skyrmionic structures with similar topological properties to realize novel devices.[30,31] Among these devices one finds: skyrmionic racetracks,[27] logic gates,[32] transistors,[33] nano-oscillators,[34] and implementations of reservoir computing models[35] and probabilistic computing.[36,37]

Theoretically, skyrmions have been found in a diverse range of sizes depending on the hosting material, applied field, and temperature. From a few tens of nanometers at low temperatures[27, 38] to hundreds of nanometers at room temperature.[39] Experimentally, an important highlight was their finding at room temperature.[12, 21, 22, 40] In Fig. 1.2 we show some examples. Regarding their stability, it has been found that their lifetimes were long enough to be used as information carriers.[41] More recently, it was found that isolated skyrmions could potentially be stable, even for storage applications (lifetimes on the order of years), with small sizes on the order of 10 nm in ultrathin ferromagnetic films.[42]

Magnetic skyrmions are mainly found in materials with the asymmetric DM exchange interaction.[23, 40, 43–46] This interaction appears when there is a lack of inversion symmetry in the crystallographic structure of the material and can be present at the interfaces of ultrathin films or in bulk chiral ferromagnetic materials. The former is known as interfacial DM (iDM) interaction and favors the stabilization of Néel skyrmions [Fig. 1.3(a)]. In these magnetic structures, the magnetization rotates perpendicular to the DW plane, going from the core (pointing up) to the ferromagnetic background (pointing down). The latter favors the stabilization of Bloch skyrmions [Fig. 1.3(b)], whose magnetization rotates in the DW plane. In both cases, they are usually found isolated [Fig. 1.2(a)] or in hexagonal [Fig. 1.2(b)] lattices. Additionally, it has been shown that skyrmions can be stabilized without DM interaction in thin films with depressions or protrusions in the material.[47–54] Other skyrmionic structures have also been found such as antiskyrmions, bimerons, biskyrmions, ferrimagnetic skyrmions, antiferromagnetic skyrmions, chiral bobbers, and hopfions.[30] Among them, in ferromagnetic ultrathin films with DM interaction, one can also find the 2π and 3π states, which have a higher magnetization rotation as compared to the skyrmion (π rotation).[55]

Most applications in skyrmionics are focused on the storage and transport of information, as well as some logic devices. Typically, the information is encoded in bits, with the existence or not of a skyrmion being a 1 or a 0, respectively. The main processes that are necessary to achieve such devices are: controlled nucleation/annihilation (equivalent to writing/deleting data), efficient and fast transport of information, and the ability to "operate" with the skyrmions to fulfill a given task.[56]

From the theoretical point of view, these processes have been studied in depth at low temperatures with two theoretical models: the micromagnetic model[57, 58] and the rigid model.[59] The former studies the magnetization dynamics at the sub-micrometer length scale. The latter assumes that the magnetic structure is a rigid structure that behaves as a quasiparticle, and describes its center-of-mass trajectory. The rigid model is much simpler than the micromagnetic model, but it cannot simulate the deformation or creation/annihilation of the structures.

Specifically related to the subject of this work, the micromagnetic model has been used to simulate the nucleation/annihilation of skyrmions.[60–72] Both models have been used to study the transport of skyrmions in order to optimize the skyrmion racetrack memory[30, 73–83] or alternative devices.[84–86] The interaction between skyrmions with external agents such as defects in the material,[87–101] granularity,[102–112] voltage-controlled magnetic anisotropies,[113–118] other skyrmions,[109,119] notches,[120–124] oscillating magnetic fields,[125,126] magnetic field gradients,[68,127–129] temperature gradients,[130–132] spin-waves,[85, 98,133,134] or superconductors (SCs)[135–145] have been studied. Using these, some applications of skyrmions have been designed, such as logic devices[123,124,146] and transistors.[33]

However, most potential skyrmionic devices must work at room temperature to be viable alternatives to previous information storage and processing technologies. The number of works in this area is less abundant[147–153] but it is becoming a topic of interest. On the one hand, it is crucial to study the lifetimes of the structures, even more so for storage and memory applications. In 1963 Brown[154] developed a fully theoretical model to describe the transition rates of single magnetic grains. For more complex structures, such as skyrmions, a theoretical description of the transition rates is not possible and we must rely on numerical simulations. These simulations are mostly based on algorithms that allow finding the minimum energy path (MEP) between two stable magnetic configurations, and then using harmonic transition state theory (HTST) to predict the frequency rate of the transition.[155–159] On the other hand, it is essential to control the skyrmion dynamics. At non-zero temperatures, the skyrmion follows a Brownian-like motion, hugely increasing the complexity of the analytical models and the computational power required in numerical simulations. This phenomenon could potentially make racetrack devices unfeasible. Nevertheless, promising applications that take advantage of this stochasticity have been proposed to generate random numbers,[152] to nucleate skyrmions,[160] and for probabilistic[36,37,161] and neuromorphic computing.[162–164] See Refs. [165,166] for more details.

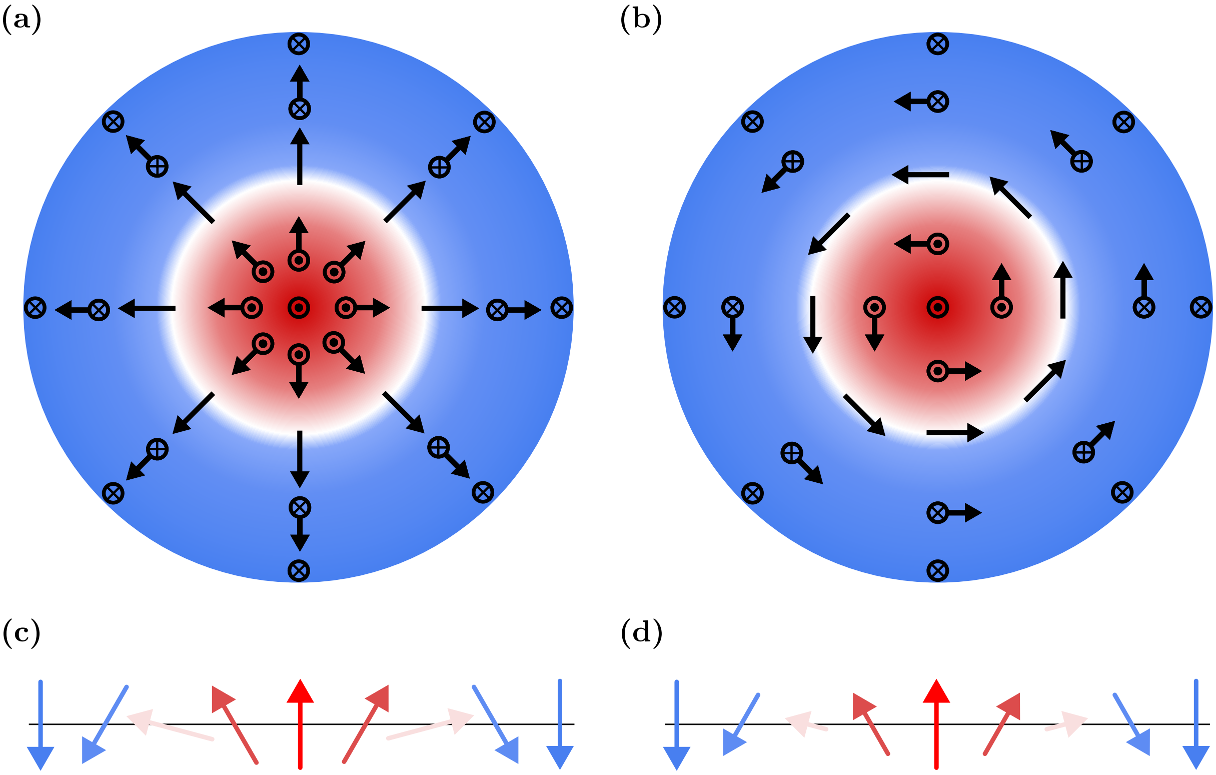

Figure 1.3: Top-view of (a) Néel-type and (b) Bloch-type skyrmions with the magnetization rotating from the up direction (red) at the skyrmion's center to the down direction (blue) of the external uniform magnetization at the skyrmion's edge. The radial magnetization distribution of (c) a Néel-type and (d) a Bloch-type skyrmion is sketched. The colors represent the z component of the magnetization. In (d) the magnetization arrows are smaller as they rotate out-of-plane.

This thesis is structured as follows. In Ch. 2 we provide the relevant theoretical tools used. We review magnetism in a FM and superconductivity in a SC. For the FM we introduce the micromagnetic model and the rigid model. Regarding the SC we present the London model to study the current distributions. We also introduce the geodesic nudged elastic band method (GNEB) to calculate the energy barriers between different magnetic states in the FM.

Once the theoretical tools have been presented we move forward to study the two main topics of this dissertation. These are related to two essential processes relevant to skyrmionic devices: transport and nucleation/annihilation of the magnetic structures. In Ch. 3 the transport of skyrmions in an infinite FM with iDM interaction is studied. We develop a model, within the rigid approximation, that enables us to compute the skyrmion trajectories under different types of defects in the materials, such as local and extended defects. Starting from a microscopically derived effective field produced by atomic impurities, we extend the model to take into account extended defects. We show that Thiele's equation can qualitatively predict the skyrmion behavior as well as the conditions for each possible regime to appear (for example pinning or not). The results found are compared with micromagnetic simulations and even though deformations on the skyrmion are present, we demonstrate that the predictions are valid. This model enables to study any skyrmion transport system without having to simulate the full micromagnetic dynamics, allowing for faster prototyping.

In Ch. 4, we focus our attention on the nucleation/annihilation processes, considering the interaction of a ferromagnetic disk with a coaxial superconducting disk. We present a model that allows obtaining, in the static limit, both the magnetization and current distributions at the same time. The mutual interaction between the ferromagnetic and superconducting elements is taken into account. We do so by solving the Brown equation (within the micromagnetic model) for the FM and the London equation for the SC.[167,168] To ease the discussions and phenomenology we have restricted the model to axisymmetric systems and consider a mathematically one-dimensional model. The interaction is analyzed as a function of the applied field and the distance between the FM and SC elements. Some transitions between magnetic states are found that are, in principle, not possible without a neighboring SC. To validate the results and transitions found, we use the GNEB method. This method allows us to find that in our systems all the transitions are mediated through the boundaries of the FM.

Finally, we present our conclusions in Ch. 5.

Chapter 2

Basic concepts

In this chapter, we review the basic concepts used in this thesis. We start by introducing ferromagnetism and its description from different points of view. First, the micromagnetic framework will be introduced. From it, the rigid model will be presented and an overview of the skyrmion trajectories driven by different spin-current torques will be discussed. Then, the GNEB method, which allows to evaluate the stability of magnetic structures, will be presented. We shall finish by briefly introducing superconductivity, with a special focus on the London model.

Magnetic materials are materials that can generate (and react to) a magnetic field around them. This field originates from magnetic moments associated with the atoms in the material. In Maxwell's equations, the source of magnetic fields can be linked to electric currents. In fact, classically, magnetic moments can be understood as bounded circular current loops, such as the electric current associated with the electron orbiting the nucleus (in a classical sense). Nevertheless, it is known that the classical picture is not enough to explain magnetism in materials. The origin of magnetic materials is mainly linked to the electron spin, an intrinsic angular momentum.

But, even though all atoms can have magnetic moments, if their interaction is negligible their direction is going to be random. Nevertheless, a net magnetization $\mathbf{M}$ can be induced either by external means (e.g. applied external field) or by intrinsic properties of the material. The latter gives rise to materials with spontaneous magnetization, the FMs. Some of these materials are Co, Fe, and Ni, among others. To predict the spontaneous magnetization, additional interactions from quantum origin between the magnetic moments are needed, which favor their alignment.

Another type of magnetic material that expels the magnetic field from their interior exists, the diamagnet. Among these materials, we highlight the superconductors, whose origin is quantum mechanical. Superconductivity is a thermodynamic state that, when cooled below a certain critical temperature, exhibits two simultaneous phenomena: zero electrical resistivity and a diamagnetic response. The reason for this transition is attributed to the formation of bosonic quasiparticles, Cooper pairs, from electron pairs.

2.1 Ferromagnetism

The magnetic moment is a fundamental magnitude in magnetism.[57] From a classical point of view, they can be associated with tiny electric current loops. For a circular planar loop of radius R with a circulating current I, the magnetic field generated far away from it (as compared to R) can be shown to be equivalent to a dipole field. Thus, the classical magnetic moment is defined as,

$$\mathbf{S} = I \oint_{\text{loop}} \mathbf{r} \times \, \mathrm{d}\mathbf{l} = I \pi R^2 \hat{\mathbf{n}}, \tag{2.1}$$

where $\hat{\mathbf{n}}$ points perpendicular to the current loop plane. In general, though, the dipolar magnetic moment created by a volume current density $\mathbf{J}$ is

$$\mathbf{S} = \frac{1}{2} \int_{V_c} \mathbf{r} \times \mathbf{J}(\mathbf{r}) \, \mathrm{d}V_c, \tag{2.2}$$

where V_c is the volume where the current density is present.

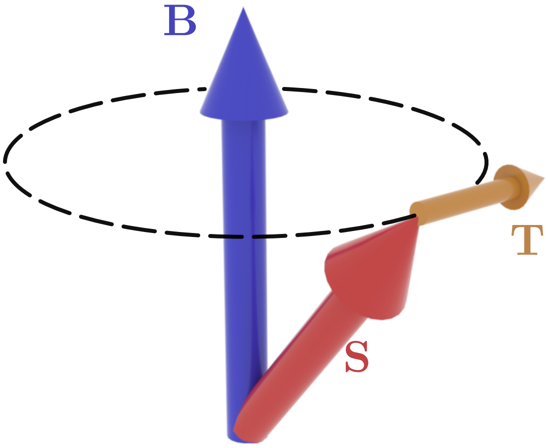

Figure 2.1: Magnetic moment **S** precessing around the magnetic induction field **B** due to a torque **T**.

If the magnetic moment is under an applied uniform magnetic induction field **B**, a torque appears given by

$$\mathbf{T} = \mathbf{S} \times \mathbf{B}. \tag{2.3}$$

Hence the magnetic moment precesses around the magnetic field **B** as sketched in Fig. 2.1.

Historically, Maxwell's equations have been used to describe classical electromagnetism. In materials in which the spins are locally aligned, one can define the macroscopic magnetization field as $\mathbf{M}(\mathbf{r}) = \sum \mathbf{S}(\mathbf{r})/V$, where V is a large volume from the microscopic point of view, yet small enough from the macroscopic point of view.[169] However, as the technology progressed to smaller scales, the quantum interactions could no longer be neglected. In addition to the classical magnetic dipole, there is an intrinsic magnetic moment of quantum origin associated with the electron spin.[57] As such, Maxwell's equations break down when approaching the atomistic scale. Unfortunately, solving a system of coupled Schrödinger equations for each atom of the material is not practical in many cases, as many interesting phenomena can be found at the nanometric to micrometric scale.

To bridge the gap between classical electromagnetism and spin quantum mechanics, a semiclassical theory was developed: *Micromagnetism*.

2.2 Micromagnetism

Micromagnetism[57, 58] is the framework that studies magnetic systems at submicrometer length scales. This length scale is large enough so that one can ignore the fine atomistic structure of the material and use mean field theory approaches to derive effective fields that act over the magnetic moments, yet small enough to resolve magnetic structures such as DWs, magnetic vortices, or (more recently) skyrmions.[170] This leads to an effective mesoscopic theory that makes compatible the exchange energy (from quantum mechanical origin) with Maxwell's equations. These effective fields will be responsible for the magnetization distribution evolution inside the FM and, in most cases, their origin is quantum-mechanical.

In this semiclassical model, one assumes that each atom has a single localized classic magnetic moment $\mathbf{S}$, which represents the average of the spins of all the nucleons and electrons that constitute the atom. In a FM, the atoms tend to align due to the exchange interaction (from quantum origin). If we have a large number of atoms, one may assume the spatial variation of $\mathbf{S}$ to be smooth. Therefore, a continuum description of the magnetic moment can be done using a continuous magnetization field distribution $\mathbf{M}(\mathbf{r})$. Another assumption is that the magnetization modulus $|\mathbf{M}(\mathbf{r})| = M_s$ is constant throughout the sample, where M_s is the saturation magnetization. This saturation magnetization, in general, depends on the temperature.[57, 58] In fact, ferromagnetism is suppressed near the Curie temperature. Therefore, micromagnetism assumes that we work under isothermal conditions (constant M_s), far from the Curie temperature.

The consideration of a constant modulus allows to define the magnetization distribution as $\mathbf{M}(\mathbf{r}) = M_s\mathbf{m}(\mathbf{r})$, where $\mathbf{m}$ is a dimensionless unit vector determining the magnetization direction.

2.2.1 Brown equation

Within micromagnetism, given an effective field, $\mathbf{H}_{\text{eff}}$, one can find the stable magnetization distributions of the FM by minimizing its Gibbs free energy.[57] The particular Gibbs free energy will depend on the geometry of the system and the considered interactions affecting the FM.

It is possible to find an equation that $\mathbf{m}(\mathbf{r})$ must satisfy so that the energy of the sample is an extremal (maximum or minimum). This equation can be obtained by doing first-order variations on $\mathbf{m}$ of the Gibbs free energy and is commonly referred to as the Brown equation. This vectorial equation reads,[57, 58]

$$\mathbf{m}(\mathbf{r}) \times \mathbf{H}_{\text{eff}}(\mathbf{r}) = 0, \tag{2.4}$$

inside the FM. This vectorial equation has to be solved coupled with the boundary conditions (BCs) of the system, ensuring they are fulfilled. These BCs are also found using variational calculus.[57, 58]

The Brown equation can be interpreted as that a stable solution (static in time) is the one with zero torque [see Eq. (2.3)]. The magnetization at each point of the magnetic sample is aligned to the effective field $\mathbf{H}_{\text{eff}}$ for any stable magnetization distribution.

Solving the Brown equation allows to describe quasi-adiabatic hysteresis loops, in which the system is allowed to completely relax before changing the applied field by a tiny amount. This is because the relative energy minimum in a given applied field can be found by taking into account the magnetization distribution in the previous applied field, and hence the history of the magnetic sample.

2.2.2 Landau-Lifshitz-Gilbert equation

Even though the Brown equation [Eq. (2.4)] is helpful to study many systems, it is not able to resolve the time evolution of the magnetic moments. For these cases, the time evolution of the system is given by the empirical Landau-Lifshitz-Gilbert (LLG) equation. The LLG equation is a partial differential equation describing the precessional motion of the magnetization **m** around an effective field $\mathbf{H}_{\mathrm{eff}}$.[171–173] The LLG equation (at each point of the FM) reads,

$$(1+\alpha^2)\frac{d\mathbf{m}}{dt} = -\gamma\mathbf{m}\times\mathbf{H}_{\mathrm{eff}} - \frac{\gamma\alpha}{M_s}\mathbf{m}\times(\mathbf{m}\times\mathbf{H}_{\mathrm{eff}}) + \mathbf{T}, \tag{2.5}$$

where α is the dimensionless Gilbert damping constant, γ the gyromagnetic constant ($\gamma = 2.21\times10^5$ m A^{-1} s^{-1}), and **T** are the external torques that apply to the magnetization, such as the torques exerted by spin-polarized currents. In the following sections, we will expand on the effective fields and torques used in this thesis.

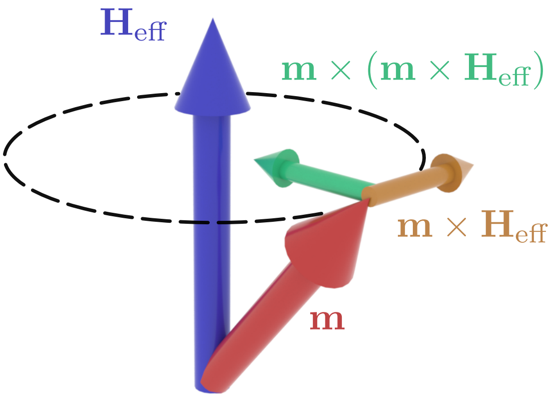
$\mathbf{H}_{\mathrm{eff}}$
$\mathbf{m}\times(\mathbf{m}\times\mathbf{H}_{\mathrm{eff}})$
$\mathbf{m}\times\mathbf{H}_{\mathrm{eff}}$
$\mathbf{m}$

Figure 2.2: Magnetization **m** precessing around the magnetic field $\mathbf{H}_{\mathrm{eff}}$ and dampened due to the material. At a later time, the magnetization will have precessed (golden arrow) and aligned a bit (green arrow) with the effective field.

From this empirical equation, one can describe the magnetization distribution's time evolution. Since we have assumed that $\mathbf{m}(\mathbf{r},t)$ has a constant modulus, its evolution is restricted to rotations. This can be seen from the terms on the right-hand side of Eq. (2.5), which are torques acting on the magnetization. The first term is the precession torque and represents the Larmor precession but on the micromagnetic scale [similar to Eq. (2.3)]. Taking into account only the first term, the magnetic moment will infinitely precess around $\mathbf{H}_{\mathrm{eff}}$ (similarly as in Fig. 2.1). This is illustrated in Fig. 2.2 with the golden arrow, which is tangential to the circular "orbit". However, inside real materials, there are energy losses when the magnetic moment precesses, damping the precessional motion. This is the role of the second term in the right-hand side of Eq. (2.5), where one finds the Gilbert damping constant α. As the precession is damped, **m** tends to align, at each point, with $\mathbf{H}_{\mathrm{eff}}$, decreasing the energy in the process. This is illustrated in Fig. 2.2 with the green arrow. Therefore the evolution of **m** at a later time would be to precess and align with $\mathbf{H}_{\mathrm{eff}}$ by some amount. Apart from internal interaction, $\mathbf{H}_{\mathrm{eff}}$ also includes the external applied field. Other external torques will be included in **T**. In this thesis, we will consider torques coming from spin-polarized currents.

Therefore, to obtain the dynamics of the magnetization distribution one needs to compute $\mathbf{H}_{\mathrm{eff}}$ and **T** at each point of the magnetization distribution and solve the LLG equation. Furthermore, as was the case with the Brown equation, the BCs of the system are needed. The effective fields, torques, and BCs depend on the system under consideration.

The focus of this work is on ultrathin skyrmion-hosting ferromagnetic systems. These systems will consist of a FM with a heavy metal (HM) substrate or multilayers of the aforementioned structure (see Fig. 2.3). We consider that the FM is in the XY plane.

Note that the damping term in Eq. (2.5), tends to align $\mathbf{m}$ to $\mathbf{H}_{\text{eff}}$, reducing the energy. As such the LLG equation can be used to minimize the energy of the system to obtain the static magnetization distributions of the FM. We can solve Brown's equation by using a high numerical damping constant α, so that we minimize the energy of the system faster.[174] The additional rotational precession helps to avoid some numerical instabilities and helps converge to physical solutions, in many cases, quicker and more reliably than by directly using Eq. (2.4).

2.2.3 Effective Fields and energy density

In the micromagnetic model, the quantum-mechanical effects (interactions responsible for ferromagnetism, among others) can be incorporated by transforming each interaction Hamiltonian into effective fields using the micromagnetic approximation.[57,58,175] To do so, we will start from the discrete atomistic Hamiltonian of the interaction, $\mathcal{H}(\mathbf{S})$, where $\mathbf{S}$ are the atomistic magnetic moments, or spin[a]. Then, by doing the continuous limit[b], the discrete Hamiltonian will be transformed into a continuous volumic energy density $\varepsilon(\mathbf{m})$. From the expression for the magnetic energy density $\varepsilon(\mathbf{m})$, the corresponding effective field of the interaction, $\mathbf{H}_{\text{eff}}(\mathbf{m})$, can be obtained (by taking the variational derivative) as follows,

$$\varepsilon = -\frac{1}{2}\mu_0 M_s \mathbf{m}\cdot\mathbf{H}_{\text{eff}}(\mathbf{m}) \qquad \rightarrow \qquad \mathbf{H}_{\text{eff}} = -\frac{1}{\mu_0 M_s}\frac{\delta\varepsilon(\mathbf{m})}{\delta\mathbf{m}}, \tag{2.6}$$

In this thesis, the basic interactions that will be considered are the exchange, the uniaxial magnetocrystalline anisotropy, and the (DM). Therefore, the Hamiltonian ($\mathcal{H}$) reads,

$$\mathcal{H} = \mathcal{H}_{\text{ex}} + \mathcal{H}_{\text{an}} + \mathcal{H}_{\text{DM}}, \tag{2.7}$$

where $\mathcal{H}_{\text{ex}}$ is the Hamiltonian of the exchange interaction, $\mathcal{H}_{\text{an}}$ is the Hamiltonian of the uniaxial anisotropy interaction, $\mathcal{H}_{\text{DM}}$ is the Hamiltonian of the DM interaction.[55,175] The exchange interaction favors neighboring spins to be parallel to each other. The uniaxial anisotropy favors the alignment of the atomic spins with an axis. The DM interaction favors neighboring spins to be perpendicular to each other.

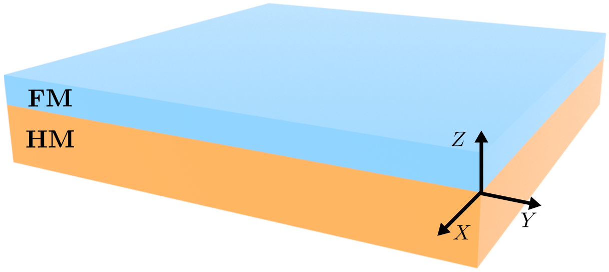

Figure 2.3: Sketch of the geometry of the considered FM in this thesis. An ultrathin FM (light blue) is placed on top of a HM (orange) substrate. The ultrathin film is in the XY plane.

---

[a] For the sake of readability, we will indistinguishably use "atomistic magnetic moment" and "spin".

[b] For a detailed derivation of each interaction we suggest reading Refs. [57] and [175].

It has been shown that for infinite ultrathin ferromagnetic systems (as in the sketch of Fig. 2.3) the classical demagnetizing field, created by the atomic magnetic moments in the FM, can be considered by just renormalizing the uniaxial anisotropy term.[99,176–178] The main reason is that despite the long-range nature of the interaction, in ultrathin systems, the demagnetizing field function shape is almost the same as the anisotropy field one, but opposing it. It has recently been shown that, in some cases, this may still be valid for finite geometries.[179] We have checked that for the cases presented here, considering the demagnetizing field yields the same results as considering it normalized in the anisotropy term[c].

Exchange interaction

The exchange interaction originates from a quantum mechanical effect, discovered independently by Werner Heisenberg[180] and Paul Dirac[181] in 1926. This interaction favors the alignment of neighboring magnetic moments in the same direction.[57,182,183] As a simplified picture, when two fermions are identical, due to the Pauli exclusion principle, they cannot have the same wave function: the fermions cannot be in the same place if they have the same spin state (↑↑ or ↓↓). Consequently, the atomic magnetic moments that point in the same direction are further apart. Since these fermions have the same charge (they repel each other), being spaced apart decreases the electrostatic energy and the overall energy of the system is reduced.

The atomistic Hamiltonian of this interaction can be written as,[57]

$$\mathcal{H}_{\mathrm{ex}} = -\sum_{\langle i,j \rangle} J_{\mathrm{ex},ij} \mathbf{S}_i \cdot \mathbf{S}_j, \tag{2.8}$$

where $J_{\mathrm{ex},ij}$ are the so-called exchange integrals and the sum is taken over all (i,j) pairs of neighboring atomic magnetic moments $\mathbf{S}$. In an homogeneous and isotropic FM, $J_{\mathrm{ex},ij}$ are considered constant across the sample ($J_{\mathrm{ex},ij} = J_{\mathrm{ex}}$). After doing the micromagnetic approximation, the exchange volumic energy density is found to be,

$$\varepsilon_{\mathrm{ex}} = -A_{\mathrm{ex}} \mathbf{m} \cdot \nabla^{\mathbf{2}} \mathbf{m}, \tag{2.9}$$

where A_{ex} is the mesoscopic exchange interaction constant, related to J_{ex}, $|\mathbf{S}|$, and the crystal structure of the FM.[174] Usually, A_{ex} is determined experimentally, although it can be computed from first principle calculations.[184] From the energy density, the effective field of the exchange interaction, $\mathbf{H}_{\mathrm{eff}}^{\mathrm{ex}}$, can be obtained as[57]

$$\mathbf{H}_{\mathrm{eff}}^{\mathrm{ex}} = \frac{2A_{\mathrm{ex}}}{\mu_0 M_s} \boldsymbol{\nabla}^2 \mathbf{m}. \tag{2.10}$$

---

[c] See Appendix C.1 for additional details.

Uniaxial anisotropy

Depending on the crystal structure of a ferromagnetic material, it is energetically favorable to align the magnetization along certain directions.[57,185] This energy contribution results from the interaction between the crystal's magnetic moments with the crystal's electric field, so it depends on the particular crystal structure. The favorable directions are usually referred to as easy axes. These axes are undirected so that a local energy minimum is degenerated as long as the moments are along the same axis, so that $\mathcal{H}_{\text{an}}(\mathbf{S}_{\text{min}}) = \mathcal{H}_{\text{an}}(-\mathbf{S}_{\text{min}})$. Depending on the lattice structure, one or more easy axes may appear. In this thesis, we will only consider systems with uniaxial anisotropy with the easy axis perpendicular to the ultrathin film ($\hat{\mathbf{z}}$ direction, see Fig. 2.3). The atomistic Hamiltonian of this interaction can be written as,

$$\mathcal{H}_{\text{an}} = -\sum_i k_{\text{an},i}(\mathbf{S}_i \cdot \hat{\mathbf{z}})^2, \tag{2.11}$$

where $k_{\text{an},i}$ is the local anisotropy parameter of the ith atomic spin. This parameter depends on the crystal structure of the material. For the considered Hamiltonian, the atomic magnetic moments tend to align along the Z-axis. In an homogeneous and isotropic FM, $k_{\text{an},i}$ are considered constant across the sample ($k_{\text{an},i} = k_{\text{an}}$). Following the micromagnetic approach, the uniaxial anisotropy volumic energy density is found to be,

$$\varepsilon_{\text{an}} = -K_{\text{an}} m_z^2, \tag{2.12}$$

where K_{an} is the anisotropy constant, which depends on k_{an}, $|\mathbf{S}|$, and the crystal structure of the FM.[174] The effective field associated with the uniaxial anisotropy, $\mathbf{H}_{\text{eff}}^{\text{an}}$, reads

$$\mathbf{H}_{\text{eff}}^{\text{an}} = \frac{2K_{\text{an}}}{\mu_0 M_s} m_z \hat{\mathbf{z}}. \tag{2.13}$$

At this point, we can use the fact that thin ferromagnetic films are considered in this thesis. As said previously, the classical demagnetizing field can be renormalized inside the uniaxial anisotropy.[99,176–178] In this way, one obtains an effective anisotropy $K_{\text{eff,an}} = K_{\text{an}} - \frac{1}{2}\mu_0 M_s^2$. For simplicity in this thesis, we will refer to the effective anisotropy as K_{an}. That is, for all the presented results, the demagnetizing field is taken into account as an effective anisotropy.

Dzyaloshinskii-Moriya interaction

The DM interaction energetically favors neighboring spins to be oriented perpendicularly. This can stabilize Néel or Bloch skyrmions (see Fig. 1.3). It is a type of indirect exchange interaction responsible for the stabilization of most of the skyrmionic states studied in the literature.[40,43–46,186] Two ingredients are necessary: spin-orbit coupling and broken inversion symmetry. Due to spin-orbit coupling, two magnetic moments interact indirectly through a third one.[187,188] Such interactions can be induced by two different mechanisms that restrict the systems in which it is relevant: the interaction between magnetic moments in a bulk lattice with lack of inversion symmetry[189] or between the magnetic moments of a thin film and its HM substrate,[190] where the inversion symmetry is broken at the interface. The latter is known as interfacial DM (iDM) interaction, and it is the one used in this thesis. An illustration of the iDM interaction is shown in Fig. 2.4, where two atoms from the FM (light blue) interact through spin-orbit coupling with a third atom in the HM (orange), breaking inversion symmetry at the interface between the FM and the HM.

To better understand this interaction it is helpful to take a look at the DM Hamiltonian between two interacting spins,

$$\mathcal{H}_{\mathrm{DM}} = -\sum_{\langle i,j\rangle} \mathbf{d}_{\mathrm{DM},ij} \cdot (\mathbf{S}_i \times \mathbf{S}_j), \tag{2.14}$$

where $\mathbf{d}_{\mathrm{DM},ij}$ depends on the position of the three atoms, being always perpendicular to the plane defined by them. The summation is taken over all neighboring spin pairs. For the case of iDM see Fig. 2.4. Using Eq. (2.14) it becomes clear that the interaction energy is minimized when $(\mathbf{S}_i \times \mathbf{S}_j)$ is parallel to $\mathbf{d}_{\mathrm{DM},ij}$, when the directions of the two magnetic moments form an angle of $\pi/2$. This can stabilize Néel or Bloch skyrmions (sketched in Fig. 1.3). In an homogeneous and isotropic FM, $\mathbf{d}_{\mathrm{DM},ij}$ is considered constant across the sample ($\mathbf{d}_{\mathrm{DM},ij} = \mathbf{d}_{\mathrm{DM}}$).

In the micromagnetic approximation, the volumic energy density of the iDM interaction with an interface pointing to $+\hat{\mathbf{z}}$ (see Fig. 2.4) reads

$$\varepsilon_{\mathrm{DM}} = -D_{\mathrm{DM}}\mathbf{m} \cdot [(\nabla \cdot \mathbf{m})\hat{\mathbf{z}} - \nabla m_z], \tag{2.15}$$

where D_{DM} is the iDM interaction parameter which depends on $\mathbf{d}_{ij}$, $|\mathbf{S}|$, and the crystal structure of the material.[89] The effective field in this case reads,

$$H_{\mathrm{eff}}^{\mathrm{DM}} = \frac{2D_{\mathrm{DM}}}{\mu_0 M_s} \left[(\nabla \cdot \mathbf{m})\, \hat{\mathbf{z}} - \nabla m_z \right]. \tag{2.16}$$

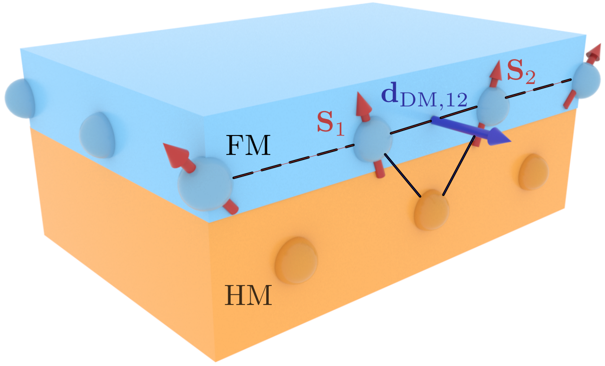

Figure 2.4: Sketch of the iDM interaction in a crystal. The interaction is produced at the interface between a ferromagnetic metal (light blue) and a HM substrate (orange) with a strong spin-orbit coupling, as described by the 3-site mechanism proposed by Fert and Levy.[27]

To get a more complete picture of the interplay between all these interactions (exchange, uniaxial anisotropy, and iDM), consider the following discussion. The anisotropy favors the alignment of the spins in the z-axis (easy axis), whilst the exchange favors neighboring magnetic moments to point in the same direction (have the most uniform distribution possible). Therefore, if we only had these two interactions, the most stable configuration would be to have all the magnetic moments pointing in the z-axis direction. If the magnetic moments have to flip along the sample, then a DWs appears: a smooth (exchange) transition between magnetic moments pointing at both directions along the easy axis (anisotropy). But if now one considers the iDM interaction (see Fig. 2.4), which favors orienting neighboring magnetic moments perpendicularly, then the trade-off between these three interactions could favor a smooth (exchange) magnetization canting (iDM) which can yield Néel skyrmions metastable.

Zeeman interaction

To all the previous *internal* energetic interactions of the FM, we can consider also external interactions. Among them, we consider an externally applied magnetic field, $\mathbf{H}_{\mathrm{a}}$. This interaction is commonly referred to as the Zeeman interaction. This is the interaction energy between the magnetic moments of the system with an applied external field. It favors the alignment between $\mathbf{H}_{\mathrm{a}}$ and $\mathbf{m}$.

The atomistic Hamiltonian of this interaction reads,

$$\mathcal{H}_{\mathrm{Z}} = -\mu_0 \sum_i \mathbf{S}_i \cdot \mathbf{H}_{\mathrm{a},i}, \tag{2.17}$$

where $\mathbf{H}_{\mathrm{a},i}$ is the applied magnetic field at the ith atom position. In this case, the definition of the volumic energy density reflects that the interaction is external. Now it reads,

$$\varepsilon_{\mathrm{Z}} = -\mu_0 M_s \mathbf{m} \cdot \mathbf{H}_{\mathrm{a}}, \tag{2.18}$$

where the 1/2 factor is dropped. The effective field resulting from the Zeeman interaction, $\mathbf{H}_{\mathrm{eff}}^{Z}$, can be directly obtained as

$$\mathbf{H}_{\mathrm{eff}}^{\mathrm{Z}} = \mathbf{H}_{\mathrm{a}}. \tag{2.19}$$

As a summary of this subsection, the total energy density is

$$\varepsilon = -A_{\mathrm{ex}} \mathbf{m} \cdot \nabla^{\mathbf{2}} \mathbf{m} - K_{\mathrm{an}} m_z^2 - \mu_0 M_s \mathbf{H}_{\mathrm{a}} \cdot \mathbf{m} + D_{\mathrm{DM}} \mathbf{m} \cdot \left[(\nabla \mathbf{m})\, \hat{z} - \nabla m_z \right], \tag{2.20}$$

where we have dropped the “effective” subscript for simplicity. Note that ε is a functional of $\mathbf{m}$.

The complete effective field that should be used in the Brown equation [Eq. (2.4)] or LLG equation [Eq. (2.5)] is given by

$$\mathbf{H}_{\mathrm{eff}} = \frac{2A_{\mathrm{ex}}}{\mu_0 M_s} \nabla^2 \mathbf{m} + \frac{2K}{\mu_0 M_s} m_z \hat{\mathbf{z}} + \mathbf{H}_{\mathrm{a}} + \frac{2D}{\mu_0 M_s} \left[(\nabla \mathbf{m})\, \hat{z} - \nabla m_z \right]. \tag{2.21}$$

Limitations of the micromagnetic model

In the micromagnetic model the magnetization distribution $[\mathbf{M}(\mathbf{r})]$ is described by a continuous vector field with a constant magnitude M_s. This approximation is valid only if we are working under isothermal conditions (and far from the Curie temperature) and the magnetization direction changes on a length scale that is large compared to the distance of two atomic magnetic moments (the distance between two atoms). By considering the Hamiltonian of the system, one can compute that the minimum width of a DW in a system with uniaxial anisotropy is given by,[58,174,191]

$$l_{\mathrm{min}} = \sqrt{\frac{A_{\mathrm{ex}}}{K_{\mathrm{an}} + \mu_0 M_s^2/2}}, \tag{2.22}$$

where $\mu_0 M_s^2/2$ is the maximum anisotropy due to the shape of the sample and K_{an} is the intrinsic uniaxial anisotropy. In the case of materials with negligible anisotropy, such as Permalloy, the magnetization change scale is given by the exchange length

$$l_{\mathrm{ex}} = \sqrt{\frac{2A_{\mathrm{ex}}}{\mu_0 M_s^2}}. \tag{2.23}$$

Thus, the micromagnetic model cannot predict variations in the magnetization distribution smaller than the corresponding minimum length (l_{min} or l_{ex}). This is specially relevant in magnetization reversal processes, in which the magnetization direction of the film is reversed by applying an external magnetic field or current.[192] These processes end up with a point with opposite magnetization directions, known as magnetization reversal points, at which Bloch points occur.[193,194]

In Fig. 2.5 we illustrate a Bloch point in a ferromagnetic thin disk where there is some resemblance to a Néel skyrmion [Fig. 2.5(a)] or an antiskyrmion,[195] where the iDM is antisymmetric, [Fig. 2.5(b)]. It can be seen that near Bloch points, the neighboring magnetic moments point in opposite directions. This has two implications: (i) A continuous rotation of the magnetization is not possible at the length scale resolution of micromagnetism, l_{min}; (ii) the magnetization at a Bloch point vanishes. The former is not compatible with the continuum approximation, whilst the latter is not compatible with the assumption that the magnetization modulus is constant across the sample. These types of points are a singularity in the exchange energy as two neighboring magnetic moments with opposite magnetization can be infinitely close to each other.

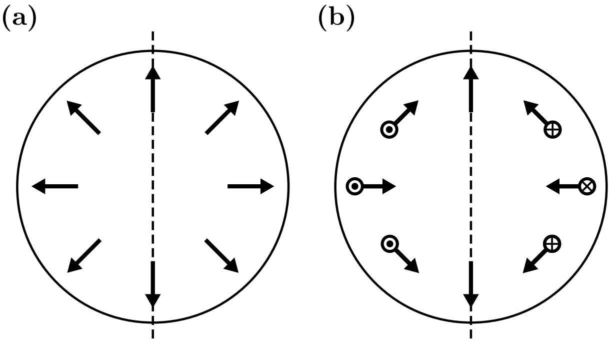

Figure 2.5: Illustrations of some possible Bloch point configurations with revolution axis vertical to the FM: (a) hedgehog and (b) spiraling Bloch points. (a) is reminiscent of a Néel skyrmion and (b) to a Néel antiskyrmion.[195] This Figure is adapted from Thiavile et al.[193]

Despite the theoretical incompatibility, it has been shown that the numerical discretization of the equations makes it possible to take into account Bloch points, even though the energy associated with it is highly dependent on the discretization.[193] As the distance between magnetic moments is not infinitely close to zero, one avoids the singularity in the exchange energy. As an example, in Ref. [194], they take advantage of this fact to describe a hysteresis loop with magnetization reversal (with some reasonable physical validity).

2.2.4 Boundary conditions

As we discussed in sections 2.2.1 and 2.2.2, in addition to the effective fields [Eq. (2.21)] the BCs are needed to solve the Brown [Eq. (2.4)] or LLG [Eq. (2.5)] equations. These BCs will depend on the system that is being solved. In this thesis two different BCs will be considered: periodic and Von Neumann.

Periodic BC

When a system is periodic we can simulate only a unit cell by using periodic BCs. These BCs are also used to simulate an infinite material by using a large enough unit cell. For example, this BC has proven useful when simulating magnetic structures in infinite materials or infinitely long racetracks. Its mathematical expression is,

$$\mathbf{m}(\mathbf{r}) = \mathbf{m}(\mathbf{r} + \mathbf{r}_L), \tag{2.24}$$

where $\mathbf{r}_L$ is the vector of the Bravais lattice of the periodic arrangement. In this work, these BCs are used to solve the LLG equation for an infinite ultrathin film in Ch. 3. More details on the micromagnetic simulations can be found in Ref. [196].

Von Neumann BC

If the system is finite, then a BC at the edges of the material is needed. This BC depends, in general, on the interactions of the system and can be obtained by applying variational calculus to minimize the energy density. In this thesis, where the exchange, iDM, anisotropy, and Zeeman interactions are considered, the energy density is given by Eq. (2.20). In these systems, one can find that the magnetization $\mathbf{m}$ at the edge must satisfy,^{55}

$$\left.\frac{d\mathbf{m}}{d\hat{\mathbf{n}}}\right|_{\text{edge}} = \left.\frac{\xi}{2}(\hat{\mathbf{z}} \times \hat{\mathbf{n}}) \times \mathbf{m}\right|_{\text{edge}} \tag{2.25}$$

where $\hat{\mathbf{n}}$ is the vector normal to the edge, $\xi = D_{\text{DM}} l_{\text{ex}}/A_{\text{ex}}$, and $\hat{\mathbf{z}}$ is perpendicular to the ultrathin FM film (see Fig. 2.3). This results in a tilting in the magnetization at the edges of the FM.

2.2.5 External Torques

Two kinds of torques appear in the LLG equation, Eq.(2.5). The first two terms on the right-hand side depend on $\mathbf{h}_{\text{eff}}$ which, in turn, depends on $\mathbf{m}$. They are torques produced on the magnetization by the magnetization itself (and the applied magnetic field). These torques were discussed in Sec. 2.2.2. However, the last term in Eq. (2.5) allows influencing the magnetization with external torques. There are several ways in which one can generate a torque acting over the magnetization by using spin-polarized currents.

We discuss two main types of torques in ultrathin films: the spin-transfer torque and the torque produced by the spin currents induced due to the spin Hall effect in the HM substrate.

Spin-transfer torque

Similar to electric currents produced by moving charges, spin currents are produced by moving spins. The spin current carries angular momentum, which can be transferred to the magnetization, a phenomenon known as spin-transfer torque (STT). When a spin current flows through a FM it can interact with the magnetization. This interaction is local and can be very strong. Thus, by controlling the regions where spin currents flow, precise control over the interaction can be achieved, which is useful for spintronic devices. This torque was first derived from quantum mechanics by J.C. Slonckzewski.[197] That is why sometimes the LLG equation with these torques is known as the Landau-Lifshitz-Gilbert-Slonckzewski equation.

STTs have been found to be present in all known magnetic materials, including transition metal FMs, magnetic semiconductors, and oxide FMs.[198] In fact, STTs are not limited to them. They can also occur in ferrimagnets,[199] in antiferromagnets,[200, 201] and even at the interfaces of insulating magnetic materials.[198]

The importance of having a spin-polarized current resides in the following. If the current is not spin-polarized (ordinary electric currents), then the average spin polarization is $< \mathbf{S}_p >= 0$. If the angular momentum of these spins is transferred to the magnetization the net interaction over the magnetic moments of the material cancels out. However, if the current is spin-polarized ($< \mathbf{S}_p >\neq 0$), then a net angular momentum can be transferred to the magnetization and the torque becomes relevant.

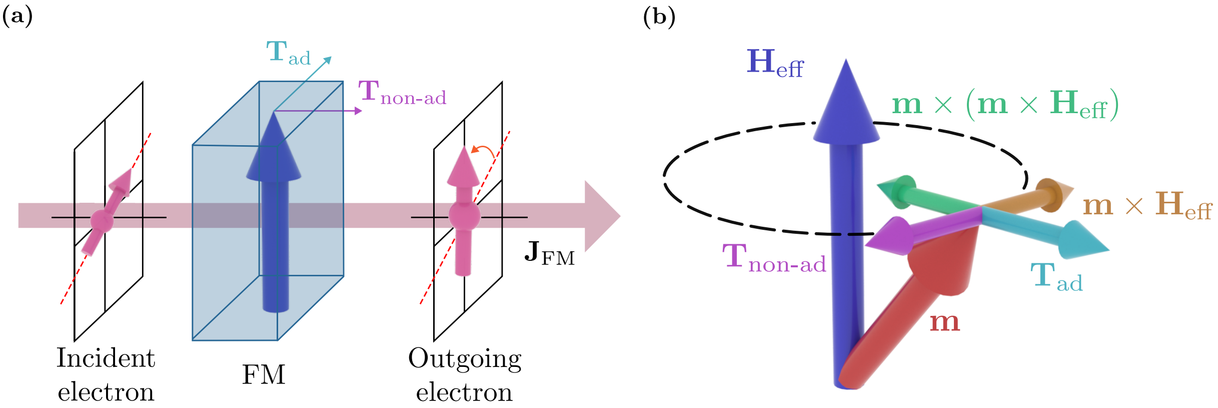
(a)
(b)
$\mathbf{T}_{\text{ad}}$
$\mathbf{T}_{\text{non-ad}}$
$\mathbf{J}_{\text{FM}}$
Incident electron
FM
Outgoing electron
$\mathbf{H}_{\text{eff}}$
$\mathbf{m} \times (\mathbf{m} \times \mathbf{H}_{\text{eff}})$
$\mathbf{m} \times \mathbf{H}_{\text{eff}}$
$\mathbf{T}_{\text{non-ad}}$
$\mathbf{T}_{\text{ad}}$
$\mathbf{m}$

Figure 2.6: (a) A spin-polarized current enters a FM (blue region). The interaction between the spin-polarized current, $\mathbf{J}_{\text{FM}}$, and the magnetization, $\mathbf{m}$, causes a change in the spin direction of the outgoing electron compared with the incident electron (orange arrow). The difference in spin polarization causes adiabatic and non-adiabatic torques on the FM. The blue vertical arrow is the magnetization of the ferromagnetic layer. (b) Magnetization $\mathbf{m}$ precessing around the magnetic field $\mathbf{h}_{\text{eff}}$, dampened due to the material and influenced by the adiabatic and non-adiabatic torques. Figure (a) is adapted from Braatas et al.[198]

If these spin-polarized currents are applied perpendicular to the ferromagnetic plane, the torques can be used to trigger the nucleation of skyrmions[60, 202] or drive skyrmions in nano-oscillators.[202, 203] If the current is fed in-plane, then skyrmions can be driven alongside it (e.g. in skyrmion racetrack memories[77]). This will be the most relevant one for the discussions in this dissertation.

If an in-plane current density $\mathbf{J}_{\rm FM} = J_{\rm FM}\hat{\boldsymbol{\varphi}}$ (where $\hat{\boldsymbol{\varphi}}$ is in the XY plane) is fed directly to the FM, two types of torques can be found. On the one hand, in the adiabatic approximation the spins of the current align with the magnetization [see Fig. 2.6(a)], resulting in a reaction torque over the magnetization given by[204]

$$\mathbf{T}_{\text{STT, ad}} = -\frac{\mu_B P J_{\rm FM}}{e}\mathbf{m}\times[\mathbf{m}\times(\hat{\boldsymbol{\varphi}}\cdot\nabla)\mathbf{m}] = \frac{\mu_B P J_{\rm FM}}{e}\mathbf{m}\times(\hat{\boldsymbol{\varphi}}\cdot\nabla)\mathbf{m}, \tag{2.26}$$

where e (> 0) is the electron charge, μ_B is the Bohr magneton, and P the spin-polarization factor of the current. This torque is usually referred to as adiabatic or damping-like torque, due to its resemblance to the damping torque in Fig. 2.6(b) (green arrow). On the other hand, when there is some spatial mistracking of the spins of the conduction electrons and the local magnetization (non-adiabatic approximation), an extra torque appears, given by[205, 206]

$$\mathbf{T}_{\text{STT, non-ad}} = -\beta\frac{\mu_B P J_{\rm FM}}{e}\mathbf{m}\times(\hat{\boldsymbol{\varphi}}\cdot\nabla)\mathbf{m} = -\beta\mathbf{m}\times\mathbf{T}_{\text{STT, ad}}, \tag{2.27}$$

where β is a dimensionless constant that takes into account the non-adiabaticity of the spin transfer. Note that the latter torque is perpendicular to its adiabatic counterpart. This torque is usually referred to as non-adiabatic or field-like torque, since the torque resembles the one that generates the precession on the magnetic moment [golden arrow in Fig. 2.6(b)].

Spin Hall effect Torque

Even though feeding a spin-polarized current through the FM was predicted to be able to drive magnetic textures in the FM and many early skyrmionic devices designs were based on skyrmion driving by STT,[27, 72, 81] it was found that it had its drawbacks. For skyrmions to be stable a large iDM interaction is desired. Due to its interfacial nature, the thicker the FM, the weaker the interaction will be. Thus, ultrathin ferromagnetic films (thickness $\sim$ 1 nm) were experimentally desired. This led to the main drawback: such thin films are hardly conductors. As such, the heating produced by the flowing currents could be detrimental to the driven structures.

If it is difficult to feed an electric current through the thin FM but a spin current is necessary, what can be done? Fortunately, there is another possibility. The spin currents can be generated at the HM substrates (see Fig. 2.3) through the spin Hall effect (SHE).[39, 207, 208] The SHE originates from the coupling of the charge and spin currents due to spin-orbit interaction.[209, 210] In practice, it consists in a spin accumulation at the lateral boundaries of a current-carrying conductor, with each spin direction going to an opposite boundary [see Fig. 2.7]. The induced spin current can transfer its carried angular momenta, producing a torque over the magnetization, the SHE torque. Another relevant advantage over the traditional STT is the efficiency of the induced torques.

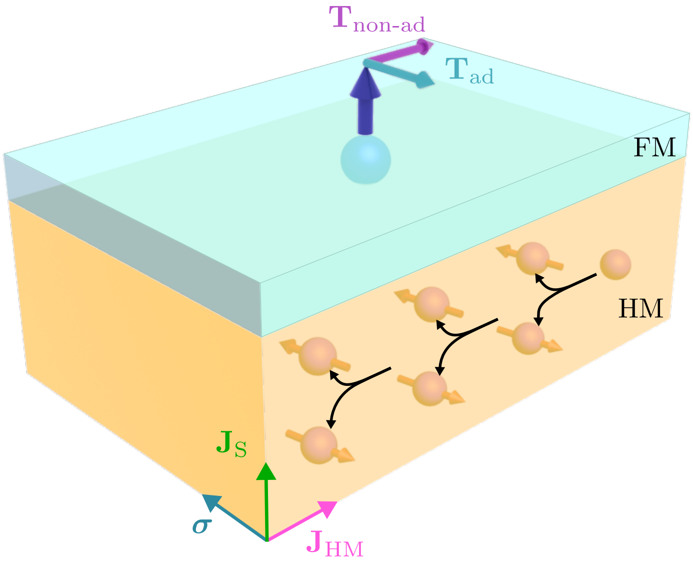

Figure 2.7: Schematics of the SHE and the torques it produces. An electron current, $\mathbf{J}_{\text{HM}}$, is fed into the HM and is converted into a transverse spin current by spin-orbit scattering. The spin current $\mathbf{J}_{\text{S}}$ leads to a spin accumulation at the HM/FM interface that diffuses across the interface into the FM and exerts torques. The spin current then interacts with the magnetic moment in the FM, producing two torques over it. These torques are analogous to the ones in the STT case shown in Fig. 2.6(b).

In ultrathin films, the HM substrate has ideally no restrictions on the thickness, as the iDM interaction is not weakened. In multilayered systems, the HMs are still thick enough so that major heating problems can be avoided. Hence an electric current $\mathbf{J}_{\text{HM}} = J_{\text{HM}}\hat{\boldsymbol{\eta}}$ (where $\hat{\boldsymbol{\eta}}$ is in the XY plane) can flow through the much thicker HM substrate. Due to the SHE in the HM, an accumulation of spin-polarized electrons appears on the interface, being polarized in the $\hat{\boldsymbol{\sigma}} = \hat{\mathbf{z}} \times \hat{\boldsymbol{\eta}}$ direction. These spin-polarized electrons can then diffuse into the FM generating two torques. The damping-like (adiabatic) torque is given by

$$\mathbf{T}_{\text{SHE, ad}} = -\frac{\mu_B \theta_{\text{H}} J_{\text{HM}}}{e t_f} \mathbf{m} \times (\mathbf{m} \times \hat{\boldsymbol{\sigma}}), \tag{2.28}$$

where t_f is the thickness of the FM and θ_{H} is the spin Hall angle factor. θ_{H} represents the ratio between the electronic current density through the HM and the spin-polarized current density diffusing through the FM. An additional field-like (non-adiabatic) torque can be found

$$\mathbf{T}_{\text{SHE, non-ad}} = -\nu \frac{\mu_B \theta_{\text{H}} J_{\text{HM}}}{e t_f} \mathbf{m} \times \hat{\boldsymbol{\sigma}} = -\nu \mathbf{m} \times \mathbf{T}_{\text{SHE, ad}}, \tag{2.29}$$

where ν is a dimensionless parameter indicating the strength of $\mathbf{T}_{\text{SHE, non-ad}}$ with respect to $\mathbf{T}_{\text{SHE, ad}}$. These torques can be used to locally modify the magnetic moments, as depicted in Fig. 2.7(b). In practice, the SHE torques have allowed skyrmions to reach velocities on the order of 100 m/s experimentally,[211] as was theoretically predicted.

For the sake of completeness, and although we will not use them here, it is worth mentioning that there are other torques that are relevant in the field of spintronics.[198] Among them, we highlight an additional interfacial torque, found in multilayered systems, that was recently proposed to drive magnetic structures.[212–214] It is found that at a skyrmion or other magnetic texture, spin accumulation may be generated.[212] This spin accumulation may diffuse in-between layers producing a vertical spin current that affects the magnetization dynamics.

2.2.6 Rigid model

Magnetic skyrmions have been found to be very stable from both a theoretical and experimental point of view. Theoretically, it has been shown that in an ideal case (infinite ferromagnetic sample) the energy barrier for a skyrmion to be destroyed diverges in the micromagnetic formalism. In reality, though, the barrier is large enough so that skyrmions are very stable, even at room temperature.[40,64,164,215–222] It has been shown experimentally and theoretically by micromagnetic simulations that, although deformable, skyrmions conserve their global shape except in some extreme cases, where it could lead to skyrmion annihilation.[42,211,223] In most cases, to consider the skyrmion as a rigid magnetization distribution is reasonable.

This stability against annihilation and large deformations enables to study the skyrmion dynamics as a point-like quasiparticle. This is the rigid approximation, in which we consider the magnetic structure as a rigid structure (without internal degrees of freedom): we assume that during its motion it will not be deformed. Within this approximation, the skyrmion dynamics are characterized by the generalized coordinates $\mathbf{r}_{\rm sk}$ and $\mathbf{V}_{\rm sk}$ ($\mathbf{V}_{\rm sk} = \dot{\mathbf{r}}_{\rm sk}$), the skyrmion geometric center and its velocity, respectively [see Fig. 2.8(a)]. In the case of an ultrathin film, the motion of the skyrmion is restricted to the XY plane.

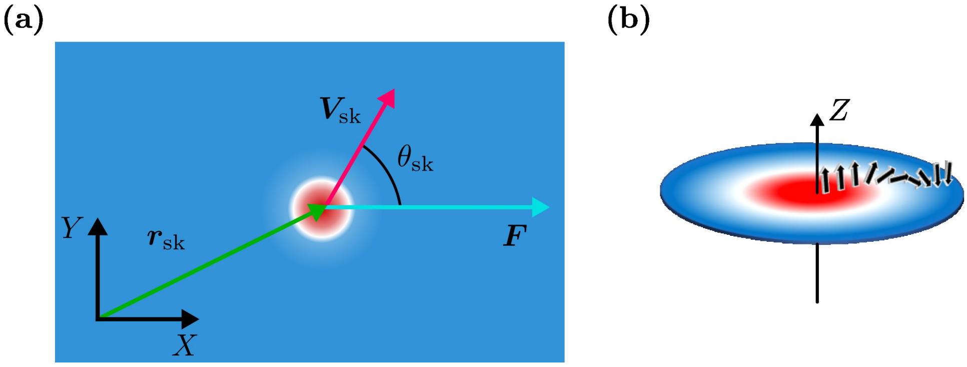

Figure 2.8: (a) Illustration of the vectors $\mathbf{r}_{\rm sk}$, $\mathbf{V}_{\rm sk}$, and $\mathbf{F}$. The skyrmion is propelled at an angle $\theta_{\rm sk}$ with respect to the incident force $\mathbf{F}$. The colors represent the z-component of the magnetization which in the skyrmion goes from pointing in $\hat{\mathbf{z}}$ (red), to the ferromagnetic background pointing in $-\hat{\mathbf{z}}$ (blue), going through zero out-of-plane magnetization (white). The skyrmion experiments a force $\mathbf{F}$ that drives it at a velocity $\mathbf{V}_{\rm sk}$ with an angle $\theta_{\rm sk}$ with respect to it. (b) Illustration of an axisymmetric Néel skyrmion as could be found in (a). The arrows represent the local magnetization along the radius.

The equation that describes the skyrmion dynamics, within this approximation, is the Thiele equation. To derive this equation one assumes that $\mathbf{m}(\mathbf{r}) = \mathbf{m}_0[\mathbf{r} - \mathbf{r}_{\text{sk}}(t)]$, where $\mathbf{m}_0$ represents the magnetization distribution centered at $\mathbf{r}_{\text{sk}} = 0$. Hence we are assuming that the whole magnetization moves rigidly with $\mathbf{r}_{\text{sk}}(t)$. Starting from the LLG equation [Eq. (2.5)] one can derive the Thiele equation by following Ref. [59], which reads[d],

$$(\mathbb{G} - M_s\alpha\mathbb{D})\mathbf{V}_{\text{sk}} + \mathbf{F} = 0, \tag{2.30}$$

where $\mathbb{G}$ and $\mathbb{D}$ are the gyrotropic and dissipative tensors, respectively. The components of these tensors are given by,

$$\mathbb{G}_{uv} = M_s^3 \int_V \mathbf{m}_0 \cdot \left(\frac{\partial \mathbf{m}_0}{\partial u} \times \frac{\partial \mathbf{m}_0}{\partial v}\right) \mathrm{d}V, \tag{2.31}$$

$$\mathbb{D}_{uv} = M_s^2 \int_V \frac{\partial \mathbf{m}_0}{\partial u} \cdot \frac{\partial \mathbf{m}_0}{\partial v} \mathrm{d}V. \tag{2.32}$$

where u, v are either x or y. $\mathbb{G}$ and $\mathbb{D}$ depend on the magnetization distribution of the skyrmion. If one considers ideal, radially symmetric Néel skyrmions [see Fig. 2.8(b)] of radius R_{sk} whose magnetization is given by

$$m_\rho(\rho) = \frac{2\rho R_{\text{sk}}}{R_{\text{sk}}^2 + \rho^2}, \tag{2.33}$$

$$m_z(\rho) = \frac{R_{\text{sk}}^2 - \rho^2}{R_{\text{sk}}^2 + \rho^2}, \tag{2.34}$$

where the core points to $+\hat{\mathbf{z}}$ while the ferromagnetic background points to $-\hat{\mathbf{z}}$ when the radial coordinate $\rho \gg R_{\text{sk}}$, the tensors read $\mathbb{G} = \begin{pmatrix} 0 & G \\ -G & 0 \end{pmatrix}$ and $\mathbb{D} = \begin{pmatrix} D & 0 \\ 0 & D \end{pmatrix}$, where $G, D > 0$.

F is the "force" term. It is called force in the literature without really being a force to do an analogy with Newtonian dynamics. **F** contains the effects on the skyrmion dynamics caused by the external torques in the LLG equation and all the external agents that the skyrmion may encounter, such as defects in the materials,[87–90, 90–101] applied magnetic field gradients,[68,127–129] temperature gradients,[130–132] the material edges,[120–124] or other magnetic structures,[109,119] among others.[75,77, 224–227] Therefore, **F** depends on the external agents considered.

Before presenting the external torques that we will consider (STTs and SHE torques), the Thiele equation can already give some interesting general properties of the rigid skyrmion dynamics. Eq. (2.30) is a first-order ordinary differential equation, whose solution gives the trajectory of the skyrmion $\mathbf{r}_{\text{sk}}(t)$. In Thiele's equation, the accelerations are instantaneous and only velocities are relevant, as rigid skyrmions are assumed to have no inertia. For example, if one considers a spin current flowing in the FM, the torque generated would drive the skyrmion through the **F** term in Eq. (2.30). When the current is switched off, due to the lack of inertia, the skyrmion instantly stops. Some generalizations have been done to the Thiele equation that lead to inertia in skyrmion dynamics, either from skyrmion deformation or others.[228–232]

---

[d] See Appendix A.1 for an example of the derivation.

In addition to the lack of inertia, there is another interesting property of rigid skyrmion dynamics: the "forces" it receives are Magnus-like torques. The skyrmion motion is not completely parallel to the "force" that is driving it. The angle between the skyrmion motion and the driving torque is known as the skyrmion Hall angle, θ_{sk}.[30,75,77,94,233,234] For example, in the case of an applied spin current, it would be the angle between the incident current and $\mathbf{V}_{\mathrm{sk}}$. This can be seen in general for an arbitrary $\mathbf{F}$. From Eq. (2.30) one finds that

$$\mathbf{V}_{\mathrm{sk}} = -(\mathbb{G} - M_s\alpha\mathbb{D})^{-1}\mathbf{F}, \tag{2.35}$$

where the skyrmion velocity is the force-term $\mathbf{F}$ rescaled and rotated by the matrix $(\mathbb{G} - M_s\alpha\mathbb{D})^{-1}$. Since the skyrmion is considered to be rigid (it is not deformed in time), the matrices are constant in time and so is the rotation. The angle of rotation is θ_{sk}. This is illustrated in Fig. 2.8(a), where a skyrmion receiving a force in the X-axis is propelled at an angle θ_{sk}, thus having velocity components in both axes.

It is convenient to normalize the Thiele equation [Eq. (2.30)] and use non-dimensional variables to describe the system. To do so we normalize the length to the exchange length l_{ex} and the times to $t_0 = (\gamma M_s)^{-1}$. Regarding the tensors [Eqs. (2.31) and (2.32)] we use the dimensionless variables $\mathcal{G} = G/(M_s^3 t_f)$ and $\mathcal{D} = D/(M_s^2 t_f)$. For an ideal radially symmetric Néel skyrmion [Eqs. (2.33) and (2.34)], these variables are found to be $\mathcal{G} = \mathcal{D} = 4\pi$. Another important magnitude that is usually used to characterize the skyrmionic structure in thin films is the skyrmion number, N_{sk}. For a axisymmetric magnetic skyrmion $N_{\mathrm{sk}} = \mathcal{G}/4\pi$. One can readily see that for an ideal skyrmion [Eqs. (2.33) and (2.34)], $N_{\mathrm{sk}} = 1$ (-1 if the skyrmion polarity is reversed). The importance of this number is that it can be viewed as the number of times the magnetization distribution winds around the unit sphere. Hence in the case of an ideal skyrmion, the whole magnetization distribution completely wraps the sphere once. In this sense, the skyrmions are said to be topologically protected if N_{sk} is an integer.[13,234–236] This means that the energy barrier to destroy them should be expected to be rather large[e]. In fact, a Bloch point must be formed to destroy it, which in micromagnetism leads to an infinite energy barrier. In contrast, when the ferromagnetic sample is finite the skyrmion may see the edges of the material producing two effects: the magnetization would be tilted [Von-Neumann BCs given by Eq. (2.25)] and the skyrmion number will, in general, not be an integer. The latter, if following the topological stability arguments, can be attributed to the fact that an additional transition path for the skyrmion annihilation appears: it can unwind through the boundaries of the sample. This tilting mechanism has been found to be prevalent under strong confinement (i.e. skyrmion size on the order of the FM size).[41,148]

As with the LLG equation [Eq. (2.5)], to solve the Thiele equation [Eq. (2.30)] we need to know the torques that act over the skyrmion. To characterize these torques we decided to separate them into driving torques, produced by a spin-polarized current (STT and SHE torque), and torques produced by external agents, such as defects in the material.[87]

---

[e] Note that, strictly speaking, this mathematical topological protection does not imply an infinite energy barrier in physical systems.

Driving torques

Following the methodology used to derive the Thiele equation[59] [Eq. (2.30)] from the LLG equation [Eq. (2.5)], one can derive[f] the terms corresponding to the STTs [Eqs. (2.26) and (2.27)] or SHE torques [Eqs. (2.28) and (2.29)]. An example of a system with both fed currents is shown in Fig. 2.9. The corresponding force term for each torque is given by,[77]

$$\mathbf{F}_{\mathrm{STT}} = -(\mathbb{G} - M_s\beta\mathbb{D})\mathbf{V}_{\mathrm{FM}}, \tag{2.36}$$

$$\mathbf{F}_{\mathrm{SHE}} = M_s(\mathbb{B} - M_s\nu\mathbb{Y})\boldsymbol{\sigma}_{\mathrm{HM}}, \tag{2.37}$$

where the elements of the $\mathbb{B}$ and $\mathbb{Y}$ tensors are

$$\mathbb{B}_{uv} = \frac{M_s^2}{t_f}\int_V \left(\frac{\partial \mathbf{m}_0}{\partial u} \times \mathbf{m}_0\right)_v \mathrm{d}V, \tag{2.38}$$

$$\mathbb{U}_{uv} = \frac{M_s}{t_f}\int_V \frac{\partial \mathbf{m}_{0,v}}{\partial u}\mathrm{d}V, \tag{2.39}$$

with $\mathbf{m}_0$ representing the centered magnetization distribution, and u and v being either x or y (for our case). V is the ferromagnetic sample volume (where there is magnetization distribution). These matrices can be further simplified in the case of a radially symmetric Néel skyrmion (as done previously). In fact one obtains that $\mathbb{B} = \begin{pmatrix} 0 & -B \\ B & 0 \end{pmatrix}$ and $\mathbb{U} = \begin{pmatrix} U & 0 \\ 0 & U \end{pmatrix}$.

The velocity, $\mathbf{V}_{\mathrm{FM}}$, is

$$\mathbf{V}_{\mathrm{FM}} = -\frac{\mu_B P}{eM_s}\mathbf{J}_{\mathrm{FM}}, \tag{2.40}$$

and $\boldsymbol{\sigma}_{\mathrm{HM}}$ is

$$\boldsymbol{\sigma}_{\mathrm{HM}} = -\frac{\mu_{\mathrm{B}}\theta_{\mathrm{H}}}{eM_{\mathrm{s}}}\left(\hat{\mathbf{z}} \times \mathbf{J}_{\mathrm{HM}}\right) = \left(\hat{\mathbf{z}} \times \mathbf{V}_{\mathrm{HM}}\right), \tag{2.41}$$

where we have defined the driving velocity, $\mathbf{V}_{\mathrm{HM}} = -\frac{\mu_{\mathrm{B}}\theta_{\mathrm{H}}}{eM_{\mathrm{s}}}\mathbf{J}_{\mathrm{HM}}$, for comparison with the STT case [Eq. (2.40)]. One can see that the SHE torque is perpendicular to the fed current [Eq. (2.37)]. Note that the $V_{\mathrm{FM,HM}}$ variables have units of velocity. As such, given the normalization of lengths by l_{ex} and time by $(\gamma M_s)^{-1}$ they can be normalized as $v_{\mathrm{FM,HM}} = V_{\mathrm{FM,HM}}/(\gamma M_s l_{\mathrm{ex}})$.

---

[f] See Appendix A.1 for an example of the derivation.

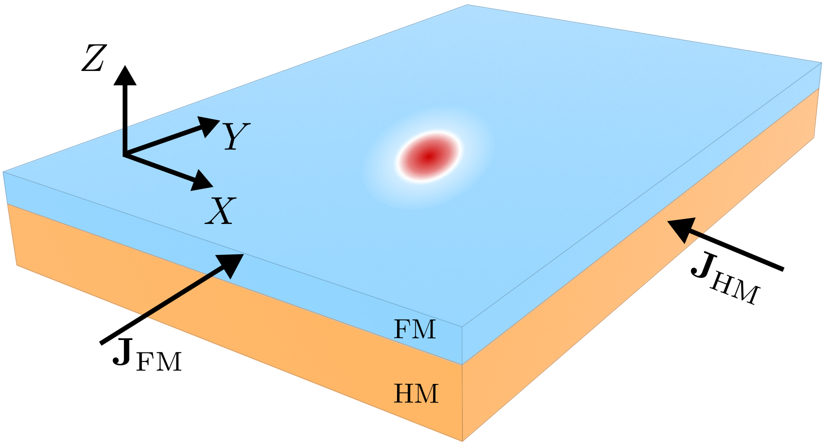

Figure 2.9: Sketch of a possible configuration for the currents. $\mathbf{J}_{\rm FM}$ and $\mathbf{J}_{\rm HM}$ are the current densities flowing through the FM (light blue region) and the HM (orange region), respectively. These current densities are associated with a spin current that interacts with the skyrmion (red-white-blue circular structure) stabilized in the FM.

As a final remark, when using the rigid approximation it can be shown that an adequate rescaling and rotation of the driving torques effectively produces the same dynamics on the skyrmion (see Appendix A.2 for a discussion).

External torques

Taking into account the effects of external agents such as defects in the material is not straightforward. The external force terms can be computed as (see Appendix A.1),

$$(\mathbf{F}_{\rm ext})_u = -\gamma M_s^3 \int_V \mathbf{H}_{\rm ext} \cdot \frac{\partial \mathbf{m}_0}{\partial u} {\rm d}V, \tag{2.42}$$

where u is x or y, V is the FM sample volume, and $\mathbf{h}_{\rm ext}$ is the normalized field generated by the external element. However, a key question arises: what is the $\mathbf{h}_{\rm ext}$ generated by an external element such as a material edge, a defect in the material, or another skyrmion? As the number of possible external agents is gargantuan, we restrict ourselves to studying the case of material defects generated from a local variation of iDM. In Ch. 3 we shall develop a model to study these types of point defects and generalize it to take into account extended defects in space (e.g. dislocations in the material).

2.2.7 Structure stability

A key problem of fundamental and applied interest is the stability of magnetic textures. For example, skyrmions (being a metastable state) have a finite energy barrier over which thermal fluctuations can lead to their creation/annihilation. In fact, understanding the possible paths to annihilation and the rate at which they occur is crucial to design feasible skyrmionic devices.

In material systems, most approaches combine elastic band methods[237–239] with statistics to determine the transition rates. Elastic band methods, determine the likely paths and saddle points along which a transition occurs, also obtaining the energy barrier for the transition. They are referred to as elastic band methods because the main idea is to use a “band” between two local minimum states and minimize the energy perpendicular to it, allowing it to “stretch” along the phase space. These elastic band methods are combined with a linearization near the minimum and saddle points, to determine the excitation spectrum of the initial state (minimum energy) and the saddle point. The theory that allows to combine both approaches to obtain the transition rates (and hence the lifetime) of the structure is called transition state theory.[240]

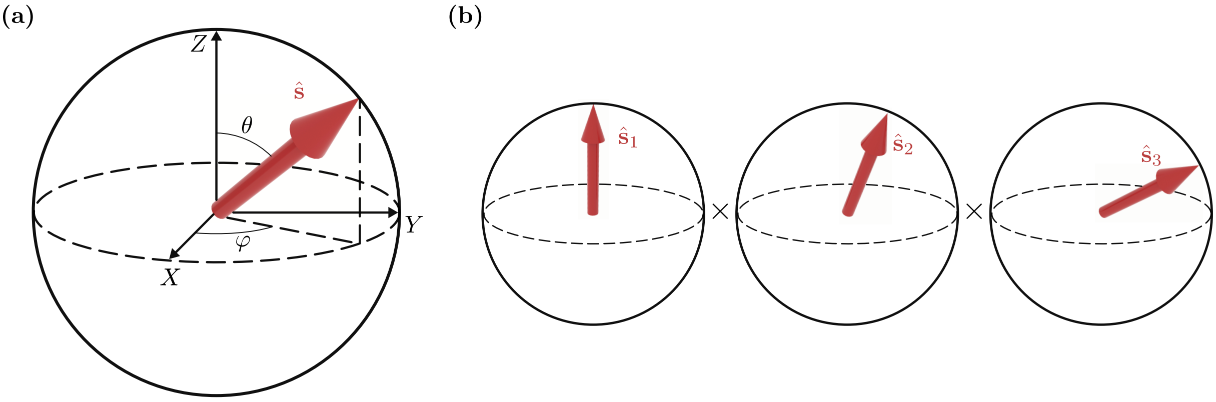

Figure 2.10: (a) Sketch of an atomic magnetic moment embedded in a unit sphere. $\mathbf{s}$ can be described by the polar and azimuthal angles, θ and φ respectively. (b) Three neighboring atomic moments can be taken into account as the direct product of the unit spheres.

One drawback of elastic band methods is that the constraints on the system (for example $|\mathbf{S}|$ constant across the sample) are difficult to take into account, slowing convergence to a solution or even preventing it altogether.[156] In magnetic systems, though, one can consider the unitary magnetic moment direction $\hat{\mathbf{s}} = \mathbf{S}/|\mathbf{S}|$. This constraint can be taken into account by projecting the magnetic moment to the unit sphere. This is sketched in Fig. 2.10(a), where $\hat{\mathbf{s}}$ can be described by the polar (θ) and azimuthal (φ) angles. When N moments are taken into account, this allows taking the direct product of the moments instead of considering the $3N$ dimensional Euclidean space with N constraints, as depicted in Fig. 2.10(b) for $N = 3$. In magnetic systems, it was shown that the GNEB method could be used to obtain the MEPs and energy barriers faster and more robustly than using conventional elastic band methods.[156] A MEP is found when the saddle point is a maximum along the transition path and minimum with respect to the other directions in the phase space. See Fig. 2.11 for an example of the energy landscape in the θ-φ phase-space of a single atomic magnetic moment.

In the literature, combining the GNEB method with HTST has allowed studying the thermal stability of skyrmions.[148,158,241,242] The MEPs and energy barriers (ΔE) obtained with the GNEB method for a transition between states can be used to compute the transition rate k_{HTST}. The HTST predicts an Arrhenius law for the lifetime,[155]

$$k_{\mathrm{HTST}}^{-1} = \tau_{\mathrm{HTST}} = \tau_0 \exp\left(\frac{\Delta E}{k_{\mathrm{B}} T}\right), \tag{2.43}$$

where τ_{HTST} is the mean lifetime, k_{B} is the Boltzmann constant, and T the temperature. The pre-exponential factor τ_0 is the attempt frequency which takes into account the reaction velocity and the entropic effects. To accurately assess small skyrmion (< 10 nm) lifetimes it has been shown that the pre-exponential factor may dominate over the exponential, changing by up to two orders of magnitude with the applied field, due to entropic effects in the skyrmion collapse mechanism.[148] Hence, both ΔE and τ_0 have to be numerically determined to accurately assess the magnetic structure's lifetime.

GNEB

To perform GNEB or HTST calculations, the energy of the system must be known. In the atomistic spin model, the magnetic moments are localized at atom positions and their magnitude ($|\mathbf{S}|$) is assumed to be constant. The commonly used Hamiltonian is the Extended Heisenberg Hamiltonian (EHH),

$$\begin{aligned}\mathcal{H} = & - \sum_i \sum_{\langle i,j \rangle} J_{\mathrm{ex},ij} \mathbf{S}_i \cdot \mathbf{S}_j - \sum_i \sum_{\langle i,j \rangle} \mathbf{d}_{\mathrm{DM},ij} \cdot (\mathbf{S}_i \times \mathbf{S}_j) \\ & - \sum_i k_{\mathrm{an},i} (\hat{\mathbf{u}}_k \cdot \mathbf{S}_j)^2 - \mu_0 \sum_i \mathbf{S}_i \cdot \mathbf{H}_{\mathrm{a}} - \mu_0 \sum_i \sum_{j \neq i} \mathbf{S}_i \cdot \mathbf{H}_{\mathrm{d},j}^{(i)},\end{aligned} \tag{2.44}$$

where $\mathbf{S}_i$ is the spin at site i, $\hat{\mathbf{u}}_k$ defines the uniaxial anisotropy easy-axis, and $\langle i, j \rangle$ means that the summation is done over the first neighbors of site i. The last term on the right-hand side is the magnetostatic energy. The other terms were previously discussed in Sec. 2.2.2.

Given the Hamiltonian, we want to see how to transition from an initial state A to a final state B (e.g. from the uniform state to the skyrmion state). The GNEB method can be used to find such transitions, giving an energetically favorable path, the MEP of the transition. This method can be thought of as having an initial rough estimate of the transition path and then, using the Hamiltonian, one can move through the phase space until a first-order saddle point is reached. These kinds of saddle points are minimum in all degrees of freedom except along the transition path, defining thus an MEP of the system. Unfortunately, it may be possible that there is more than one MEP for a given transition. As such, the selection of an initial rough estimate can determine the MEP found as it usually gives the closest (in the phase-space) first-order saddle point. This means that the transition found may not be the most favorable one. But, all in all, it is still helpful to give good estimates of the transition paths and the magnetic structure's lifetime in most cases. Note that a displacement along the transition path is a discrete analog of a reparametrization of the continuous path itself, so only transverse displacements of the path should be included.[243] Other approaches have been proposed to avoid some of the GNEB method shortcomings. See Appendix B.2 for more information on them.

In practice, the GNEB method can be described by the following algorithm:[156]

1. The initial (A) and final (B) stable states (energy minima) are connected by a discrete chain of states, called images. This path is an initial guess (e.g. a uniform rotation of the spins) of the transition path and, hopefully, is close to the real one. The initial path is depicted by the black line in Fig. 2.11. Each image (dots in the figure) is one realization of a possible spin configuration along the connecting path. The configuration space is embedded into a unit sphere to ensure the magnetic moment magnitude is conserved [see Fig. 2.10(a)].
2. The configuration space is written as a direct product of all the magnetic moments projected onto spheres (θ, φ) [see Fig. 2.10(b)].
3. From the energy model [Eq. (2.44)], the energy gradient is evaluated and a force over each image k (dots in Fig. 2.11) can be obtained, $\mathbf{F}_k^{\text{mag}} = -\nabla\mathcal{H}_k$, where the energy gradient is taken over each atomic spin. For clarity, this can be rewritten as $-\partial_{\hat{\mathbf{s}}_i}\mathcal{H}_k = \mathbf{H}_{\text{eff},ki}$, where $\mathbf{H}_{\text{eff},ki}$ is the effective field acting over the i-th spin in image k. Only the component *perpendicular* to the current approximation to the transition path will be considered.
4. To ensure a somewhat uniform distribution of images along the path and not lose "resolution" in highly curved regions (i.e near the saddle point), an additional force is considered over each (k) image: a spring-like force between adjacent images, $\mathbf{F}_k^{\text{spring}}$.[156] This force is considered *along* the transition path.
5. A quasi-Newtonian relaxation method can be used,[156] solving the dynamics of each spin for each image given the total force obtained $\mathbf{F}_k^{\text{GNEB}} = -(\nabla\mathcal{H}_k)\hat{\mathbf{n}} + \mathbf{F}_k^{\text{spring}}$, where $\hat{\mathbf{n}}$ is a unit vector perpendicular to the current approximation of the transition path. This allows obtaining a new set of images with lower energy and (hopefully) closer to an MEP of the system.
6. With the new set of images, we repeat steps 3 to 5 until convergence[g].

---

[g] On convergence, the hessian of the system can be evaluated to ensure it indeed is an MEP.[156] To obtain a first-order saddle point, only one eigenvalue must be positive. Then, an additional interpolation method along the path can be used to obtain a better estimation of the saddle point. See Appendix of Ref. [156] for additional details.

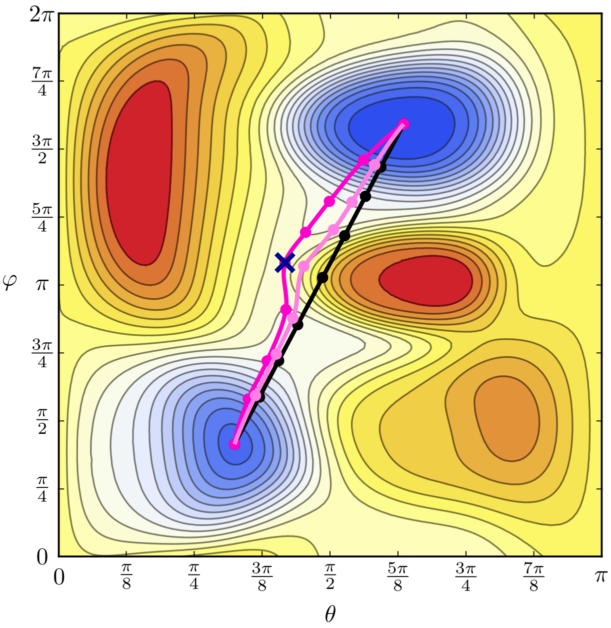

Figure 2.11: An illustration of a GNEB calculation of an MEP for a single spin system. The positions of the images are shown with filled circles. The initial path was chosen to lie along the short geodesic path (linear path in the θ-φ phase-space) between the energy minima (indicated in blue). It turned out to lie near a maximum (indicated in red). The converged path is shown in pink. One intermediate configuration of the path is also shown in light pink. The saddle point is marked with a dark blue cross. Eight images were used in the illustration (dots along the path). The Hamiltonian of the spin system is given in Appendix B.1.

To illustrate the results that can be obtained with the GNEB algorithm a simple example will be studied, where two minima and several maxima are considered. Consider a single atomistic spin that has two configurations that are local energy minima (blue regions in Fig. 2.11). We want to compute the transition path between those states, given a complex energy landscape with several maxima (red regions in Fig. 2.11). The energy surface used in this example can be found in Appendix B.1. Following the GNEB algorithm, we start by initializing a rough estimate of the transition path along the shortest geodesic path connecting both minima: a linear interpolation in the θ-φ phase-space. The initial geodesic path is depicted in black, with the dots being the 8 images considered, for this example, along the path. This path is obviously not an optimal one since it lies close to an energy maximum (red and orange regions). The images are then iteratively brought closer to the MEP (pink dots) with the GNEB method, by minimizing the energy perpendicular to the current transition path (step 5).

In this thesis, the GNEB method, within micromagnetism, is used in Ch. 4. The same approach is used, but the effective field $\mathbf{H}_{\text{eff}}$ comes from the micromagnetic Hamiltonian [Eq. (2.20)] instead of the EHH [Eq (2.44)]. Thus we use Eq. (2.21) for the effective fields when minimizing the energy, in step 5 of the algorithm.

HTST

Once the saddle point of the MEP is found using the GNEB method, one can use HTST to find the transition rates k_{HTST} between two local energy minima. From the saddle point, given a system with N spins ($2N$ configuration space), one can define a $2N-1$ dividing surface that divides the phase space into two parts, one for each minimum. The transition rate k_{HTST} is given by the flux of states through that dividing surface. By using the Boltzmann distribution function for occupied states and doing harmonic expansions near the minimum and saddle point, one obtains that the transition rate follows an Arrhenius law [Eq. (2.43)] and the pre-exponential factor, τ_0^{-1}, can be obtained.[155]

Note that the transition rates will not be computed as the micromagnetic approach's ability to predict some of the creation/annihilation mechanisms, such as Bloch point formation, is a bit controversial. Therefore, we will only use the GNEB predictions to check whether our results are coherent and assume that the transitions follow an Arrhenius law [Eq. (2.43)], dominated by the exponential factor as is the case when the annihilation is mediated through the material edges.[148]

2.3 Superconductivity

In diamagnets, the magnetization and the magnetic field have opposite directions. These materials expel magnetic field lines. In the case of a perfect diamagnet, the magnetic induction field $\mathbf{B} = 0$ inside it. One material usually considered as a perfect diamagnet is an ideal SC. Strictly speaking, in a SC $\mathbf{B}$ can enter the material over a superficial region of thickness λ_{L}, the London penetration depth. This state is known as the Meissner state.[244]

Superconductivity is a thermodynamic state found in some materials that, when cooled below a certain critical temperature T_c, exhibit two properties simultaneously: zero electrical resistivity and they present diamagnetic behavior, excluding and expelling (Meissner effect) the magnetic induction field from their interior.

SCs can be classified in many ways. A common classification, motivated by the historical progression, is depending on their critical temperature. The first discovered superconducting materials were metals such as mercury, lead or niobium, whose critical temperature is below 10 K. Other subsequent alloys reached higher temperatures, but not higher than 30 K. Due to the low critical temperatures, these materials are known as low-temperature SCs. A huge breakthrough was made in 1986 when J.G. Bednorz and K.A. Müller[245] found superconductivity in cuprate oxides. The main relevance was that the critical temperatures in these compounds were much higher. For example, YBaCuO-123 has a $T_c = 93$ K[246] and BiSrCaCuO-1112 a $T_c = 105$ K.[247] These temperatures are above the boiling temperature of liquid nitrogen (77 K), allowing them to be cooled easier than previous SCs. These are known as high-temperature SCs.

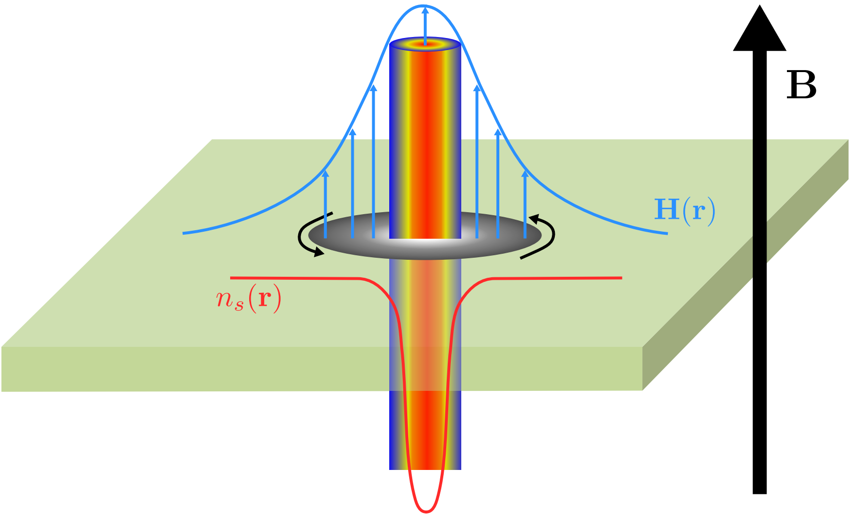

Figure 2.12: Sketch of a superconducting vortex that has penetrated a SC sample (green region) under an applied magnetic induction field, $\mathbf{B}$. The Cooper pair density, n_s, decays over distances on the order of ξ_{GL}, defining the vortex core (red cylinder). The vortex core allows magnetic flux ($\mathbf{H}$) to penetrate the sample over a distance λ_L. Around the vortex one finds circulating currents denoted by the gray region.

Several theories have attempted to explain superconductivity. Microscopically, the superconducting state can be explained by the Bardeen, Cooper, and Schrieffer (BCS) theory,[248] through the appearance of Cooper pairs. These bosonic quasiparticles consist of electron pairs coupled via phonon interactions. The presence of Cooper pairs becomes energetically favorable below T_c. Another important advance was the Ginzburg-Landau theory.[249] This theory uses a complex phase parameter ψ, related to the Cooper pair density ($n_s = \psi\psi^*$), that explains the phenomena taking place near the thermodynamic second order phase transitions (near T_c). It was found that ψ varies over distances on the order of ξ_{GL}, the coherence length. In 1957, Abrikosov found a particular solution of the Ginzburg-Landau equations[250] which showed that a SC with $\kappa_{\mathrm{GL}} \equiv \lambda_{\mathrm{L}}/\xi_{\mathrm{GL}} > 1/\sqrt{2}$, allowed magnetic flux to penetrate the SC in the form of vortices. These vortices, composed of a current circulating around a non-superconducting core, are distributed in a triangular lattice inside the SC. In Fig. 2.12 we show an illustration of a vortex in a SC. The order parameter decays over distances on the order of ξ_{GL} whilst the magnetic field decays over distances on the order of λ_{L}. These findings by Abrikosov provide another type of classification of SCs by their magnetic properties in type-I ($\kappa_{\mathrm{GL}} < 1/\sqrt{2}$) and type-II ($\kappa_{\mathrm{GL}} > 1/\sqrt{2}$) SCs. In type-I SCs, when a magnetic field is applied below a certain critical temperature T_c and below a critical field H_c, shielding currents appear in the surface of the SC. Usually, these currents extend over a region of thickness λ_{L}, to make $\mathbf{B} = 0$ inside the SC. In this shell of flowing currents, $\mathbf{B}$ decreases towards the interior of the SC, partially penetrating the sample. The Meissner state is explained by the London theory.[251] According to this theory, the fields and currents decay, from the SC surface towards its interior, over distances of the order of λ_{L}. A perfect diamagnet (complete field expulsion) is found when $\lambda_{\mathrm{L}} = 0$, with the currents diverging in the SC surface. For fields above H_c, the superconducting Cooper pairs start to break down and superconductivity is lost.

In contrast, type-II SCs exhibit richer phenomenology. For an applied field smaller than a critical field $H_{c,1}$ one finds the Meissner state. For fields above $H_{c,1}$ but below the second critical field $H_{c,2}$, partial flux penetration occurs inside the SC, forming the mixed state. In the mixed state, usually, each vortex carries a single flux quantum ($\Phi_0 = 2\pi\hbar/2e$). For higher fields, superconductivity is suppressed. In the mixed state, the vortices can be moved by Lorentz forces produced by transport currents ($\mathbf{J}_t$) flowing in the SC, for example. This movement dissipates energy and thus resistive losses appear. This can be explained as the motion of the vortex implies a local magnetic flux variation, which in turn produces an induced electrical field $\mathbf{E}$. As there are transport currents flowing in the SC, ohmic losses ($\mathbf{J}_t \cdot \mathbf{E}$) appear. However, the vortex motion can be prevented with material impurities and defects which may pin them. Actually, defects are artificially introduced at will to produce this pinning effect, reducing the ohmic losses[252] or even allowing higher transport currents before superconductivity is suppressed.

In Ch. 4, the London model will be used to describe a SC. As such, a special focus on this model is given below.

2.3.1 London model

The London model is based on the assumptions of free moving particles with charge e^*, mass m^*, volume density n_s, and zero trapped flux far from the SC surface (flux penetrates in a shell of the order of λ_{L}). The London equation relates the magnetic induction field $\mathbf{B}$ and the volume current density $\mathbf{J}_s$ inside the SC as,

$$\mathbf{B} = -\mu_0 \nabla \times (\lambda_{\mathrm{L}}^2 \mathbf{J}_s), \tag{2.45}$$

with

$$\mu_0 \lambda_{\mathrm{L}}^2 = \frac{m^*}{n_s (e^*)^2}. \tag{2.46}$$

Note that in an anisotropic and inhomogeneous superconducting material, λ_L is a position-dependent tensor. For the case considered in this thesis, the material will be considered isotropic and homogeneous so that λ_L is a constant. Since the discovery of the Cooper pairs, it is known that $e^* = 2e$ and $m^* = 2m_e$, with e (>0) being the electron charge and m_e its mass. This theory predicts that the fields decay within the SC.

It should be noted that assuming a uniform n_s is equivalent to considering $\xi_{GL} \ll \lambda_L$, and therefore not taking into account the spatial variations of the order parameter.

Superconducting slab

To illustrate some of the general trends derived from the London equation, we first consider the simple case of a homogeneous and isotropic SC of width W in the X direction and infinite in the YZ plane (see Fig. 2.13 for a sketch). Due to the symmetry, this problem is mathematically one-dimensional.

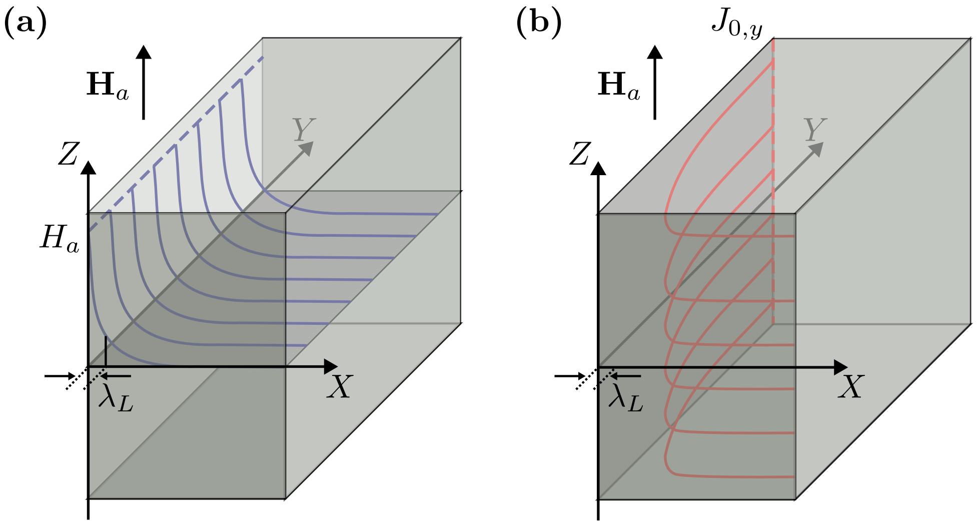

Figure 2.13: Sketch of a semi-infinite slab in the Meissner state under an applied field $\mathbf{H}_a$. (a) The magnetic induction field (blue lines) exponentially decays, penetrating the SC a depth on the order of λ_L. (b) The superconducting currents (red lines) shield the applied field.

Consider an applied uniform magnetic field $\mathbf{H}_a = H_a\hat{\mathbf{z}}$. The London equation can be solved and the field distribution inside the SC can be found to be

$$H_z(x) = \frac{H_a \cosh(x/\lambda_L)}{\cosh(W/2\lambda_L)}, \tag{2.47}$$

and H_a outside it. From Ampere's law, the volume current density is found to be

$$J_{s,y}(x) = -\frac{H_a \sinh(x/\lambda_L)}{\lambda_L \cosh(W/2\lambda_L)}. \tag{2.48}$$

When $W \gg \lambda_{\mathrm{L}}$, the magnetic field and current density approximately decay exponentially inside the SC, sketched in Figs. 2.13(a) and 2.13(b) respectively. The maximum value of the current is found to be,

$$J_{0,y} = \frac{H_{\mathrm{a}}}{\lambda_{\mathrm{L}} \cosh\left(W/2\lambda_{\mathrm{L}}\right)}, \tag{2.49}$$

located at the surface of the SC. The induced volume current density flows in the opposite direction at each end of the SC [Eq. (2.48)].

Fluxoid inclusion

The slab geometry considered above is a simply connected one. When the superconducting sample presents non-superconducting regions (i.e. holes or the vortex core), for any surface S whose contour δS runs along the interior of the SC, the flux threading it is

$$\Phi = \int_S \mathbf{B} \cdot \hat{\mathbf{n}} \mathrm{d}S + \mu_0 \lambda_{\mathrm{L}} \oint_{\delta S} \mathbf{J}_s \cdot \mathrm{d}\mathbf{l} = N_f \Phi_0, \tag{2.50}$$

This flux is *always* an integer multiple, N_f, of the fluxoid quantum Φ_0. In particular, when a sample that presents a non-superconducting region is cooled below T_c at zero applied field, $N_f = 0$. This is known as a Zero-Field-Cooled (ZFC) SC. In contrast, when the superconducting transition is done under some external applied field, a multiple of fluxoids can thread the non-superconducting region, leading to $N_f \neq 0$. This is known as a Field-Cooled (FC) SC.

In this way, the London model can be expanded to take into account superconducting vortices.[253] They are approximated as the loss of superconductivity (normal metal) at a region inside the SC, where flux penetrates. In that case, a vortex in position $\mathbf{r}_v$ can be added into the London equation [Eq. (2.45)] as follows,

$$\mathbf{B} + \mu_0 \lambda_{\mathrm{L}}^2 \nabla \times \mathbf{J_s} = N_f \Phi_0 \delta_2(\mathbf{r} - \mathbf{r}_v). \tag{2.51}$$

This directly handles the flux quantization as the vortex can have a multiple of the flux quanta Φ_0. Usually, if there are no holes in the SC, each vortex carries a single flux quantum. This equation portrays each vortex as a filament of flux at a point $\mathbf{r}_v$, thus the field and supercurrents diverge at the vortex center.

Ultrathin

In this dissertation, ultrathin geometry is considered. This geometry is found when the thickness (t_s) is much smaller than the size of the SC. In this case, the currents can be considered to flow homogeneously across its thickness, so that one can define the sheet-current density $\mathbf{K}_s = \mathbf{J}_s t_s$. Furthermore, in this geometry, the vortices appear in the form of Pearl vortices[254] (PV). Hence Eq. (2.45) reads,

$$\mathbf{B} + \frac{\mu_0 \Lambda}{2} \nabla \times \mathbf{K}_s = N_f \Phi_0 \delta_2(\mathbf{r} - \mathbf{r}_v), \tag{2.52}$$

with $\Lambda = 2\lambda_{\mathrm{L}}^2/t_s$ being the screening length. This equation can be rewritten as a function of the magnetic vector potential $\mathbf{A}$,[255]

$$\mathbf{K}_s + \frac{2}{\mu_0 \Lambda} \nabla \times \mathbf{A} = \mathbf{A}_\Phi, \tag{2.53}$$

where $\mathbf{A}_\Phi$ is the magnetic vector potential associated with the flux that penetrated the sample. This term is due to the gradient of the phase of the complex superconducting order parameter Ψ. It must be noted that this term acts as the corresponding boundary conditions necessary in Eq. (2.45).

To exemplify the current profiles obtained in thin films, we show in Fig. 2.14(a) some of the obtained sheet-current profiles for a thin superconducting infinitely long strip of width $2W$. The z component of the total magnetic field is shown in Fig. 2.14(b). As $\Lambda \to 0$, the currents are more abrupt near the edge whilst the field penetrates less inside the sample.

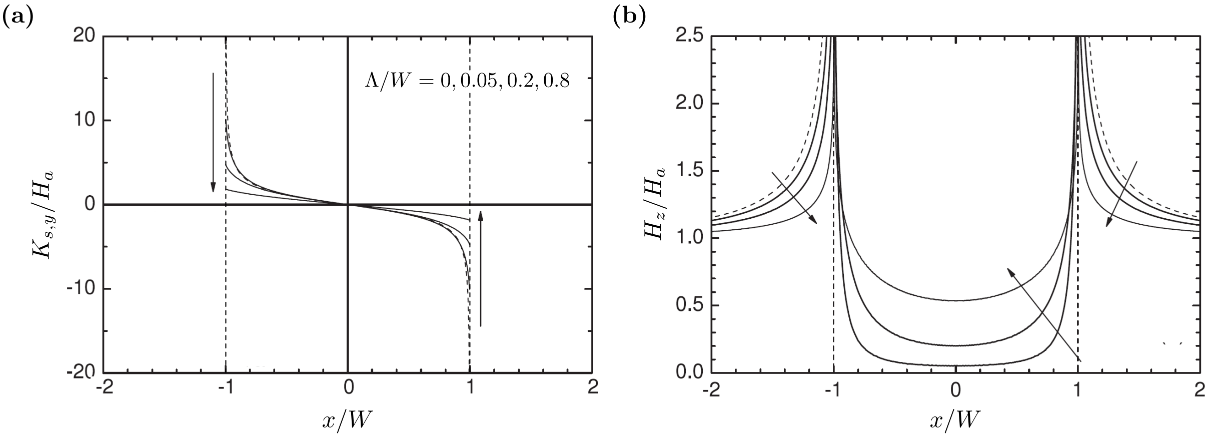

Figure 2.14: The current (a) and field (b) profiles of a thin superconducting strip of width $2W$, with $\Lambda/W = 0, 0.05, 0.2$ and 0.8 under a perpendicular applied field H_{a}. As $\Lambda \to 0$, the currents are more abrupt near the edge whilst the field penetrates less inside the sample. The vertical dashed lines indicate the edges of the material. Figure adapted from Chen et al.[256]

Chapter 3

Skyrmion-Defect interaction

The object of this thesis is the study of skyrmions. All the concepts introduced in Ch. 2 are going to be used henceforward. In particular, in this chapter, we will study the skyrmion-defect interaction when driven under spin-polarized currents. In skyrmion-hosting magnetic materials, defects or impurities may influence both stability (statics) and motion (dynamics) of skyrmions. As such, the study of the skyrmion-defect interaction and its effects is paramount to bringing to reality feasible skyrmionic devices.

One of the most prominent potential applications of skyrmions is the use of skyrmionic racetrack memories[257] to store and transport information based on the basic one-skyrmion one-bit principle[15, 27, 28, 60, 118] or in multi-lane racetracks to code information on the lane the skyrmion is on.[86] Racetracks are designed to drive skyrmions along them via different mechanisms.[85,128,129,131,133,134] One of the most promising is the use of the spin-orbit torque produced by a spin-polarized current fed into the system.[77] In racetrack systems, the edges of the ferromagnetic material create a confining potential that helps suppress the skyrmion Hall angle, below a threshold current density. Above that threshold, the skyrmion would escape through the boundaries. In skyrmionic racetrack memories, it is very important to characterize the dynamics of the skyrmions to ensure proper functionality. Among the different agents that influence skyrmion motion, one is the presence of defects (or granularity), which are hardly avoidable in real materials. It is known that defects in the material (e.g. local variations of some magnetic parameters) have a drastic effect on the behavior of skyrmions:[87] modifying their trajectories or, in the most extreme cases, pinning or even destroying them. As such, it is key to understand the influence of defects on a skyrmion.

We start this chapter by giving a brief summary of the state-of-the-art related to the skyrmion-defect interaction.Then, a theoretical model within Thiele's rigid approximation (see Sec. 2.2.6) will be presented. Starting from the force exerted by a local defect, it will allow us to consider the interaction of the skyrmion with defects extended in space. The model provides an ordinary differential equation for evaluating the skyrmion trajectories. From it, the threshold driving current under which the skyrmion may undergo pinning and its pinning position can be computed as a function of the system parameters.

Different arrangements of these extended defects will be studied, making a special focus on the case when the defects are extended along a line (line defects). First, we will start by studying the interaction of a skyrmion with a single (finite and infinite) line defect and characterize its dynamics. Then, different arrangements of these line defects will be considered, such as a cross or a periodic grid. The validity of the presented approach will be contrasted by solving the dynamics using the LLG equation, where the skyrmion is allowed to deform. Some possible applications for the presented arrangements of defects will be discussed.

3.1 A brief topical review

Several studies have focused on characterizing the skyrmion-defect interaction, both theoretically and experimentally (see Refs. [87] and [258] for a review). To better explain some of the theoretical works made on this topic, a distinction depending on the scale is made. At the most fundamental level, one works at the atomistic scale, where magnetic interactions are studied by means of first principles. At the opposite end of the scale, one works at the mesoscopic scale where the relevant parameters are the averages of the fundamental interactions, using the micromagnetic model (the LLG equation [Eq. (2.5)] or the Thiele equation [Eq. (2.30)]).

At the atomistic scale

From a classical point of view, magnetic materials can be considered as a collection of atoms on a regular lattice. Each atom is represented by a localized magnetic moment whose modulus corresponds to the effective spin of the atom. This translates into the EHH, given by Eq. (2.44).

Within the atomistic scale, one finds two ways of considering atomic defects. At the most fundamental level, defects can be simulated by directly modifying the atomic structure of the material by, for example, replacing[90] or adding[92, 96] a few atoms. In these works, density functional theory is used to evaluate the energy landscape in the presence of a defect. It is found that depending on the atomic modification the defect can attract or repel skyrmions. Another option, not requiring first-principles calculations, is to consider a local modification of the magnetic interaction constants $(J, d_{\mathrm{DM}}, k_{\mathrm{an}})$[89, 97] or directly modifying some of the magnetic moments of the lattice.[97, 259] In Ref. [97] it is found that the pinning position depends on both the origin of the defect (exchange, DM, or anisotropy modification) and the skyrmion size, with the skyrmion shape changing near the defect. Ref. [89] also studied the effective field acting over a skyrmion that a local or an elongated defect produced by variations in the exchange, DM, and anisotropy constants. This study and their results for the effective field are used in this chapter as a starting point for the local defect force acting over a skyrmion.

Lastly, when considering a modification in the magnetic moments themselves it was found that a defect produced by a non-magnetic impurity can increase the activation energies of the creation and annihilation of skyrmions and pin them.[259] These effects grow with the defect size. But, when the defect is due to some missing atoms in the material, such as a hole, the skyrmion stability can be compromised.[97]

At the "micromagnetic" scale

The previous approaches are useful when considering small sample sizes. When the sizes studied are larger (tens of nanometers to microns), they become computationally prohibitive. In these cases, the micromagnetic model is employed (see Sec. 2.2). The works at these scales are usually based on the use of the LLG equation [Eq. (2.5)]. Here we separate the works into two main branches: geometrically induced defects (e.g. holes, depressions, or protrusions of the material) and modifications of the interaction constants.

In the case of geometrically induced defects produced by holes in the material, several works come to attention. It was found that holes in the material[226] or semicircular,[121] rectangular,[123] or triangular[124] notches were able to pin skyrmions. The notches are specially relevant in racetrack applications, such as skyrmionic logic devices, where constraining the skyrmion motion is beneficial to synchronize the operations done on them.[114, 146, 161, 260, 261]

Another interesting approach is to change the shape of the material itself using depressions or protrusions in the material. For example, it has been shown that it is possible to induce effective exchange, DM, anisotropy and magnetostatic interactions in curvilinear geometries.[47–54] These induced effective magnetic constants allow to nucleate skyrmions[47] or pin them at curved regions of a racetrack.[48]

As for the second approach, the modification of the interaction constants has been done in several ways. One way is to consider that, in a certain region, some constant is changed following a mathematical function that varies with the distance to the defects, such as Gaussian functions[91, 262] or exponential decays.[263] Another approach is to simulate the system by solving the LLG equation, considering that a magnetic constant is modified in a region.[60, 93, 99, 196, 264]

The latter is commonly used when considering the granularity of the material, usually varying the uniaxial anisotropy constant.[78, 104, 105, 216, 219, 265, 266] We separate the works into two categories depending on the region size. On the one hand, if the region is small (as compared to the skyrmion), the defects are considered local (point-like) anisotropy defects. In this limit, it was found that the granularity could be the origin for the threshold current density for skyrmion movement activation.[78] On the other hand, for larger regions, one finds the disorder is considered to be due to granular anisotropy. That is, each grain has a local uniaxial anisotropy that is given by a Gaussian distribution centered on the anisotropy value of the pristine sample.[104, 105, 216, 219, 265, 266] In non-confined scenarios, it was found that disorder strongly affects the direction of skyrmion propagation, modifying the skyrmion Hall angle (θ_{sk}), and thus explaining its current-dependence.[104, 105]

At the "Thiele" scale

A coarser level of approximation is considering the skyrmionic structures as rigid particles within the rigid model (see Sec. 2.2.6). At this level, the most common approach is to use analytical expressions for the external force and/or potential that the defect creates on the skyrmion. These can be fitted from studying the skyrmion energy as a function of the distance to the defect[226, 263] or from empirical observations.

Granularity in materials has also been modeled within the rigid model (see Ref. [87] for a review). Each grain is considered as an effective potential acting over the skyrmion. These effective potentials are usually phenomenological (from empirical observations). In these works, the general trend found is that, in non-confined materials, the disorder strongly affects the skyrmion Hall angle, θ_{sk}.[109–112, 224, 226] This has been found for defects due to vacancies in the material[226] harmonic traps,[109, 110, 224] and Gaussian-like traps.[267–271] In materials with periodic disorder,[224, 268] the underlying symmetry of the substrate makes θ_{sk} to not change continuously as a function of the driving force but rather forming a series of discrete steps, saturating to the defect-free value for large driving spin currents. For non-periodic disorder,[109–112, 226] θ_{sk} also depends on the applied current density, but continuously.[109, 110, 226] In these systems, it has also been found that when skyrmions are pinned in randomly placed pinning traps, an incoming skyrmion can unpin them and avalanches can be found.[112] The skyrmion dynamics have also been studied when driven with AC-drives.[267, 269, 270] Furthermore, temperature has also been added to these models, by adding an effective force following a white-noise distribution, converting the Thiele equation into a Langevin equation.[111]

The work presented in this chapter belongs to this scale. Starting from an atomistic point defect,[89] the Thiele equation [Eq. (2.30)] will be used to develop a model that gives analytical insight into the skyrmion dynamics for point-like and extended defects. This model allows us to find the critical points of the skyrmion trajectories (i.e. pinning positions and saddle points) and the threshold current densities above which these critical points disappear. Thus, theoretically predicting the different driving regimes possible in the system for other scenarios than point defects, such as a material dislocation, we are motivating the artificial engineering of such defects.

3.2 Point Defect interaction

To study the effect of defects in the material over a skyrmion we will study a simple scenario. Consider an infinite ultrathin FM (without borders) with a current density, $\mathbf{J}_{\mathrm{HM}}$, flowing into the HM substrate (see Fig. 3.1). The skyrmion is driven by the SHE torque at a velocity $\mathbf{V}_{\mathrm{sk}}$ (see Sec. 2.2.6).

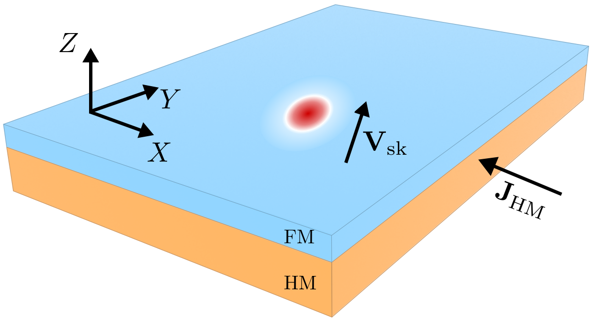

Figure 3.1: Sketch of the studied system. $\mathbf{J}_{\mathrm{HM}}$ represents the current density flowing into the HM (light orange region). The skyrmion (red-white-blue structure) moves with a velocity $\mathbf{V}_{\mathrm{sk}}$ in a FM background (light blue region).

The simplest defect is a variation in some of the magnetic parameters at the atomistic scale. In this section, we will consider defects produced by a single-atom variation of some magnetic parameter. In the work by Navau et al. [89] a closed expression for the forces arising from different kinds of magnetic parameter variation was obtained. Modification of the exchange, anisotropy, and DM constants were taken into account. They concluded that the force a skyrmion receives depends on the nature of the atomistic defect. The forces were computed considering a non-deformed Néel skyrmion with magnetization profile given by Eqs. (2.33) and (2.34).

Assuming a squared atomic lattice, they obtained that the forces of different magnetic parameter variations were given by,

$$\mathbf{F}_{\mathrm{ex}} = 0, \tag{3.1}$$

$$\mathbf{F}_{\mathrm{DM}} = -\frac{8D_{\mathrm{DM}}(\delta-1)a^2\gamma t_f}{\mu_0 R_{sk}^2}\frac{\rho/R_{sk}}{[1+(\rho/R_{sk})^2]^3}\hat{\boldsymbol{\rho}} = -F_{0,\mathrm{DM}}\frac{\rho/R_{sk}}{[1+(\rho/R_{sk})^2]^3}\hat{\boldsymbol{\rho}}, \tag{3.2}$$

$$\mathbf{F}_{\mathrm{an}} = \frac{4K_{\mathrm{an}}(\kappa-1)a^2\gamma t_f}{\mu_0 R_{sk}}\frac{\rho/R_{sk}[1-(\rho/R_{sk})^2]}{[1+(\rho/R_{sk})^2]^3}\hat{\boldsymbol{\rho}} = F_{0,\mathrm{an}}\frac{\rho/R_{sk}[1-(\rho/R_{sk})^2]}{[1+(\rho/R_{sk})^2]^3}\hat{\boldsymbol{\rho}}, \tag{3.3}$$

where t_f is the thickness of the FM, $R_{\rm sk}$ is the skyrmion radius, a the lattice constant, δ (κ) the factor that the DM (anisotropy) value has been modified at the defect position with respect to its non-modified sample value $D_{\rm DM}$ ($K_{\rm an}$). The defect has been considered at the origin of coordinates and ρ is the radial distance to the skyrmion. A negative force over the skyrmion means that it points towards the defect. A local variation of the exchange parameter results in no net force over the rigid skyrmion [Eq. (3.1)].

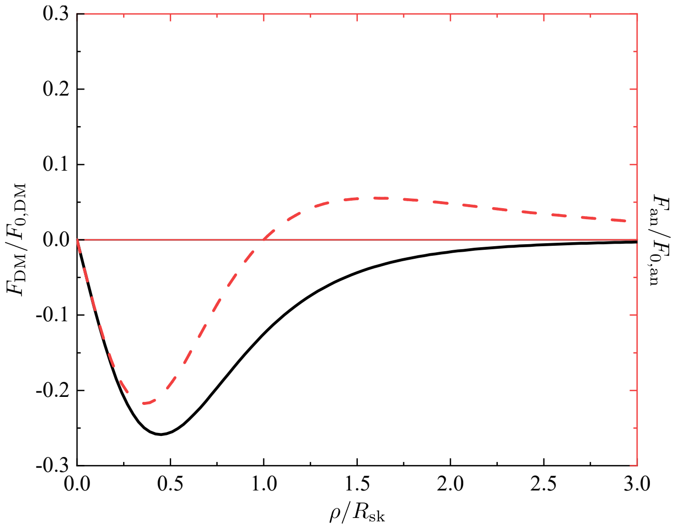

Figure 3.2: Forces over a skyrmion as derived in Ref. [89], considering $\delta = 2$ and $\kappa = 2$. A negative force points towards the defect. A local modification of the exchange interaction results in zero net force.

In Fig. 3.2, the forces [Eqs. (3.2) and (3.3)] are plotted for comparison. The main takeaway is that the behavior of the skyrmion near the (point) defect depends strongly on the atomistic origin of the defect itself. If the defect is due to a local variation of the DM interaction, the force is always attractive (negative) and has a single maximum. In contrast, a defect produced by a local variation of the anisotropy may be attractive (negative) or repulsive (positive) depending on the distance to the defect. Both forces decay to zero for large distances to the defect. Notice that in both cases, the force grows linearly at small distances ($\rho/R_{sk} \lesssim 0.5$). For the sake of simplicity, a thorough study will only be done with DM defects.

3.2.1 Defects within the rigid model

The rigid model allows to characterize the dynamics of the skyrmions under the presence of a driving spin current and defects on the material. In some cases, even analytical expressions can be obtained for the threshold current density above which the skyrmion escapes through the borders and the critical points below that current.

From the LLG equation [Eq. (2.5)], after considering the skyrmion as a rigid structure that translates over space, one may write Thiele's equation in the present context as,

$$(\mathbb{G} - M_s\alpha\mathbb{D})\mathbf{V}_{\rm sk} + \boldsymbol{F}_{\rm drv} + \boldsymbol{F}_{\rm ext} = 0. \tag{3.4}$$

Without loss of generality, we will only consider the adiabatic torque $T_{\rm SHE,\ ad}$ [Eq. (2.28)], as discussed in Sec. 2.2.6.

This torque, under the rigid approximation, will drive the skyrmion with $\boldsymbol{F}_{\rm drv}$ given by,

$$\mathbf{F}_{\rm drv} = \mathbf{F}_{\rm SHE} = M_s\mathbb{B}\ \boldsymbol{\sigma}_{\rm H}, \tag{3.5}$$

where the elements of the $\mathbb{B}$ tensor are given by Eq. (2.38).

For radially symmetric ideal Néel skyrmions on a ferromagnetic background pointing to $-\hat{\boldsymbol{z}}$ [Eqs. (2.33) and (2.34)] the matrices can be further simplified. In fact one obtains that $\mathbb{G}_{\mathrm{xy}} = -\mathbb{G}_{\mathrm{yx}} = G$, $\mathbb{D}_{\mathrm{xx}} = \mathbb{D}_{\mathrm{yy}} = D$, and $\mathbb{B}_{\mathrm{xy}} = -\mathbb{B}_{\mathrm{yx}} = -B$. All the other elements are zero. In the present definition G, D, and B are positive.

Once a local defect is considered, a $\mathbf{F}_{\mathrm{ext}}$ term will appear in the Thiele equation. If the defect is due to a local variation of the DM parameter, one obtains that the force it produces is

$$\mathbf{F}_{\mathrm{ext}} = -F_{0,\mathrm{DM}} \frac{\rho/R_{sk}}{[1+(\rho/R_{sk})^2]^3} \hat{\boldsymbol{\rho}}, \tag{3.6}$$

where $\hat{\boldsymbol{\rho}}$ is a vector that points radially outwards from defect. Hence the force will be attractive (repulsive) if $F_{0,\mathrm{DM}} > 0$ (< 0). Thiele's equation for the studied system then reads

$$(\mathbb{G} - M_s\alpha\mathbb{D})\mathbf{V}_{\mathrm{sk}} + M_s(\mathbb{B} + \nu M_{\mathrm{s}}\mathbb{Y})\boldsymbol{\sigma}_{\mathrm{H}} - F_{0,\mathrm{DM}} \frac{\rho/R_{sk}}{[1+(\rho/R_{sk})^2]^3} \hat{\boldsymbol{\rho}} = 0, \tag{3.7}$$

with the previous definitions.

Before proceeding to solve Eq. (3.7), it is convenient to normalize the equation, using the skyrmion radius R_{sk} for the length and $\tau = (\gamma M_{\mathrm{s}})^{-1}$ for the time. We also use the following definitions $\mathcal{G} = G/(M_s^3 t_f)$, $\mathcal{D} = D/(M_s^2 t_f)$, $\mathcal{B} = B/(M_s^2 R_{\mathrm{sk}})$, $\mathbf{v}_{\mathrm{HM}} = \mathbf{V}_{\mathrm{HM}}\ \tau/R_{\mathrm{sk}}$, and $\mathbf{f} = \mathbf{F}/(\gamma M_{\mathrm{s}}^2 t_f R_{\mathrm{sk}})$. From now on all the magnitudes in this chapter will be normalized unless stated, including x,y, and ρ. An illustration of the system is shown in Fig. 3.3.

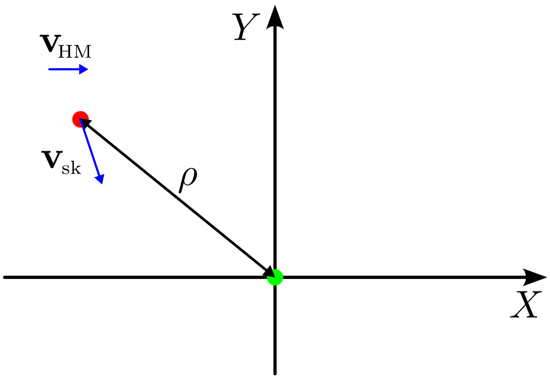

Figure 3.3: Illustration of the local defect system. The red dot represents the center-of-mass of the incoming skyrmion and ρ is the distance to the defect (green dot). The blue arrows are the driving velocity ($\mathbf{v}_{\mathrm{HM}}$) and the drift velocity of the skyrmion ($\mathbf{v}_{\mathrm{sk}}$).

Note that within the rigid approximation, the values of $\mathcal{G}$, $\mathcal{D}$, and $\mathcal{B}$ are critical to determine the skyrmion motion. The most common values used are the ones found for an ideal infinite skyrmion [Eqs. (2.33) and (2.34)] $\mathcal{G} = \mathcal{D} = \mathcal{B} = 4\pi$. Instead of using directly these ideal values, we do a previous step to take into account the initial shape of the driven skyrmion (without defects). A skyrmion is simulated using the LLG equation with a moderate spin current and the skyrmion Hall angle is used to fit the matrix parameters. The magnetic parameters used in the simulation are: saturation magnetization $M_{\mathrm{s}} = 580$ kA m^{-1}, exchange constant $A_{\mathrm{ex}} = 15$ pJ m^{-1}, DM constant $D_{\mathrm{DM}} = 3$ mJ m^{-2}, uniaxial effective anisotropy constant $K_{\mathrm{an}} = 0.425$ MJ m^{-3}, and Gilbert damping constant $\alpha = 0.1$. We obtain that $\mathcal{G} = 3\pi$, $\mathcal{D} = 5\pi$, and $\mathcal{B} = 2\pi$ fit much better the skyrmion motion. with a normalized driving current, v_{HM} in the range of 0.001 to 0.1. The magnetic parameters and the values for these constants will be used throughout this chapter.

Simulation results

Consider a local defect at the origin of coordinates as illustrated in Fig. 3.3. It is expected that if the defect is attractive, a pinning position appears below a threshold driving current velocity v_{th}. To simplify the discussion of this academic example, we will consider that $\mathbf{v}_{\text{HM}} = (v_{\text{HM}}, 0)$ as any other current angle would be just a rotation of the whole system. In order to characterize the skyrmion dynamics it is convenient to study the critical points present in the system of equations obtained from the normalized Thiele equation,

$$\begin{cases} \left(\alpha^2\mathcal{D}^2 + \mathcal{G}^2\right)\dot{x} = \alpha\mathcal{D}\mathcal{B}v_{\text{HM}} - \left(\alpha\mathcal{D}x + \mathcal{G}y\right) f_{0,\text{DM}}\dfrac{1}{(1+x^2+y^2)^3}, \\ \left(\alpha^2\mathcal{D}^2 + \mathcal{G}^2\right)\dot{y} = -\mathcal{G}\mathcal{B}v_{\text{HM}} - \left(\alpha\mathcal{D}y - \mathcal{G}x\right) f_{0,\text{DM}}\dfrac{1}{(1+x^2+y^2)^3}, \end{cases} \tag{3.8}$$

where $f_{0,\text{DM}} = 8D_{\text{DM}}(\delta - 1)a^2/(\mu_0 M_s^2 R_{\text{sk}}^3)$ and we have used that $\mathbf{v}_{\text{sk}} = (\dot{x}, \dot{y})$, $\rho = \sqrt{x^2+y^2}$ is the distance to the defect, and x, y are the skyrmion center-of-mass coordinates (see Fig. 3.3). Now, with some algebra, one can obtain the critical points ($\dot{x} = \dot{y} = 0$) of the system by solving the system of equations,

$$\begin{cases} 0 = \alpha\mathcal{D}\mathcal{B}v_{\text{HM}} - \left(\alpha\mathcal{D}x + \mathcal{G}y\right) f_{0,\text{DM}}\dfrac{1}{(1+x^2+y^2)^3}, \\ 0 = -\mathcal{G}\mathcal{B}v_{\text{HM}} - \left(\alpha\mathcal{D}y - \mathcal{G}x\right) f_{0,\text{DM}}\dfrac{1}{(1+x^2+y^2)^3}. \end{cases} \tag{3.9}$$

The points (x, y) which are solutions to this system of equations, are critical points of the trajectories. Depending on the derivatives at those points, one might find a minimum, a maximum, or a saddle point. When the local defect is attractive and the solution exists, these critical points can be classified into a spiral attractor point (minimum) and a saddle point. For the skyrmion pinning points to exist it is necessary that two conditions must be met: the defect must be attractive (if not pinning is impossible) and the driving current must be below a certain threshold. For the case under study, one can find the driving velocity threshold to be,

$$v_{\text{th, pt}} = \frac{25\sqrt{5}f_{0,\text{DM}}}{216\mathcal{B}} \simeq 0.041 f_{0,\text{DM}}, \tag{3.10}$$

where $\mathcal{B} = 2\pi$ was used. Note that it only depends on the driving torque and the defect strength, not on α.

The vector field corresponding to the defect force [Eq. (3.6)] is presented in Fig. 3.4(a). Due to the skyrmion Hall angle, the skyrmion drifts at an angle with respect to that force (see Sec. 2.2.6). To illustrate this, when *only* a defect is present, the force-term [$v_{\text{HM}} = 0$ in Eq. (3.8)] is shown in Fig. 3.4(b). If the driving velocity is also taken into account ($v_{\text{HM}} \neq 0$), critical points may appear such as depicted in Fig. 3.4(c). Another way of representing the same information is to do a phase portrait (Figs. 3.4(d) and (e)). In a phase portrait, each set of initial skyrmion positions is represented by a different curve, with the arrows indicating the skyrmion flow direction and the background color the modulus of the velocity. To do these phase portraits we numerically solve the system of Eqs. (3.8), with $f_{0,\text{DM}} = 0.0015$ and an applied current velocity $\mathbf{v}_{\text{HM}}$. When $v_{\text{HM}} \leq v_{\text{th, pt}}$ and $f_{0,\text{DM}} < 0$, a spiral sink (red dot) and a saddle point (red cross) appear [see Fig. 3.4(d)]. Depending on the initial position of the incoming skyrmion it may be pinned at the spiral sink or not. As the driving velocity increases the skyrmion trapping region becomes narrower until it disappears for $v_{\mathrm{HM}} > v_{\mathrm{th,pt}}$ [see Fig. 3.4(e)]. This behavior agrees with the results found in Ref. [272] where a parabolic pinning potential was assumed. The critical points depicted in Fig. 3.4 are obtained by numerically solving the system of Eqs. (3.9).

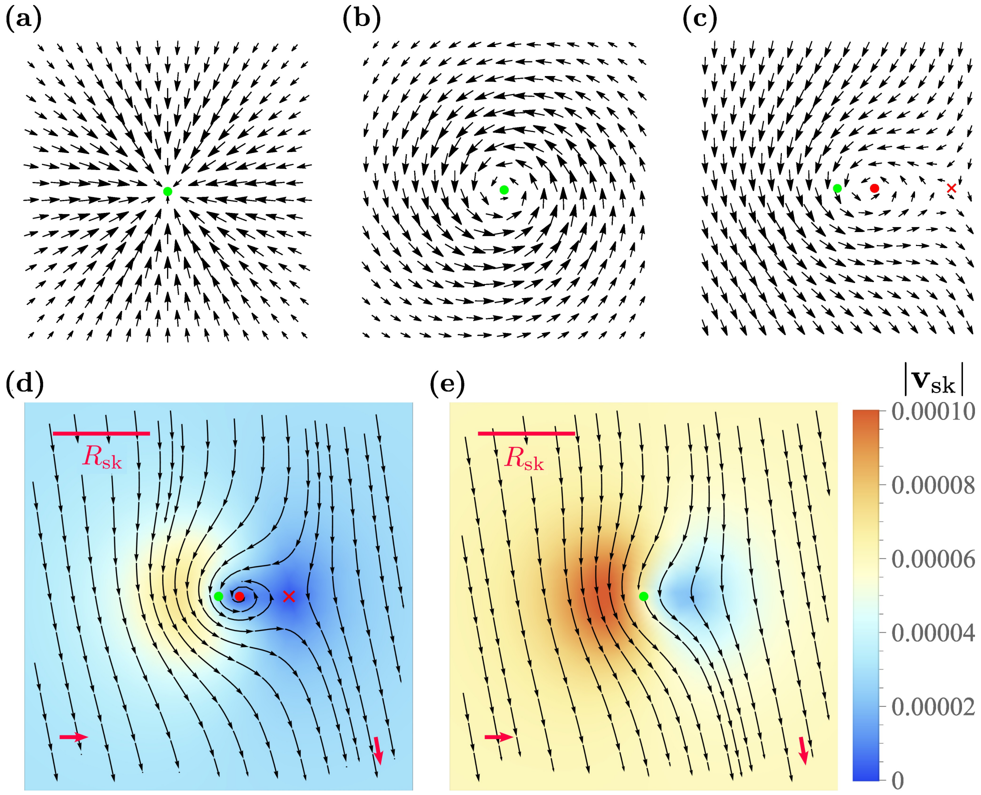

Figure 3.4: Vector field corresponding to (a) the attractive local defect force [Eq. (3.6)], (b) the velocity it produces over the skyrmion, and (c) the addition of driving current. The skyrmion tends to circle around the defect in a counter-clockwise motion or spirals into the defect. Phase portrait of Thiele's equation considering $f_{0,\mathrm{DM}} = 0.0015$ and driving velocities v_{HM} (d) below and (e) above the threshold value [Eq. (3.10)]. The background color indicates the speed of the skyrmion. The green dot corresponds to the defect position. The red dot (cross) indicates the attractor (saddle) point. The red arrows indicate the direction of (left) the driving current density $\mathbf{v}_{\mathrm{HM}}$ and (right) the direction of the skyrmion velocity in the absence of defects. In this particular example the driving velocity angle is $\varphi_{\mathrm{HM}} = 0$ and its modulus is (c,d) $v_{\mathrm{HM}} = 0.75 v_{\mathrm{th,\ pt}}$ and (e) $v_{\mathrm{HM}} = 1.5 v_{\mathrm{th,\ pt}}$, for (c,d) and (e) respectively.

When the defect size is comparable to or larger than the skyrmion size, the previous formalism needs to be further developed to consider extended defects. This problem will be tackled in the following section.

3.3 Extended defect interaction

A frequent type of defect in FM thin films are elongated defects such as dislocations or grain boundaries, among others. The elongated nature of such defects cannot be taken into consideration with the previous model for local defects. In the literature, little work has been devoted to the description of line defects, specially finite ones (segments). In this section, the point-defect model will be expanded to consider different types of extended defects. First, we will consider elongated defects, both finite (segment) and infinite (line). Then different arrangements of these defects will be studied and some possible applications will be discussed. These results will be compared to their micromagnetic simulation counterparts to check for the validity of the rigid approximation.

When considering extended defects, the key idea is to consider the force density created by the defects. Indeed, one can consider each local defect as a surface with an atomic defect density $\sigma = 1/a^2$. Each surface differential $\mathrm{d}S$ generates a differential force that can be integrated over the defect surface S_d to obtain the total force exerted over the skyrmion

$$\mathbf{f}_\mathrm{ext} = \int_{S_\mathrm{d}} \sigma \mathbf{f}_\mathrm{DM}(\mathbf{r}_\mathrm{sk} - \mathbf{r}_0)\mathrm{d}S, \tag{3.11}$$

where $\mathbf{r}_\mathrm{sk}$ is the skyrmion center-of-mass position, $\mathbf{r}_0$ is the defect position, and

$$\mathbf{f}_\mathrm{DM} = -f_{0,\mathrm{DM}} \frac{\rho}{(1+\rho^2)^3}\hat{\rho}. \tag{3.12}$$

3.3.1 Segment and line defects

A particular case of such defects would be to consider an arrangement of local defects aligned forming a defect segment of width Δ and length l_d (see Fig. 3.5). The consideration of width for the elongated defects is for generality. This will allow us to be able to compare the rigid model results to micromagnetic simulations, where the defect has an inherent width given by the numerical space discretization. If the defect segment width is small ($\Delta \ll R_\mathrm{sk}$), one obtains that the force can be expressed as

$$\mathbf{f}_\mathrm{sgm} = \Delta \int_{l_\mathrm{d}} \sigma \mathbf{f}_\mathrm{DM}(\mathbf{r}_\mathrm{sk} - \mathbf{r}_0)\mathrm{d}l, \tag{3.13}$$

where l_d indicates the segment over which the defects are located.

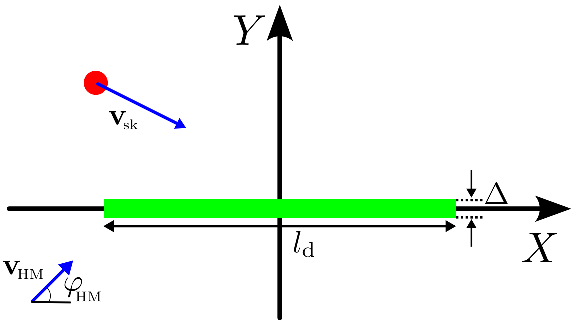

Figure 3.5: Sketch of the system with a segment defect of width Δ and length l_d. The red dot represents the center-of-mass of the incoming skyrmion and the green segment the defect. The blue arrows are the driving velocity ($\mathbf{v}_\mathrm{HM}$) and the drift velocity of the skyrmion ($\mathbf{v}_\mathrm{sk}$).

Consider a defect segment located at $x \in [-l_\mathrm{d}/2, l_\mathrm{d}/2]$ with a current applied at an angle φ_HM with respect to the x-axis (see Fig. 3.5). In this case, the rotational symmetry of the local defect is lost. As such, the behavior of the system depends not only on the intensity of the applied current but also on the angle. When the defect is repulsive the trajectory of the skyrmion is modified but as in the case with single defects, no pinning can occur for a single-segment defect.

In order to proceed, it can be done similarly as was done with the local defect. First, we derive the force exerted over the skyrmion and then use the Thiele equation to obtain relevant information on the skyrmion dynamics.

The force exerted by a finite segment defect can be obtained from Eqs. (3.13) and Eq. (3.12),

$$\begin{aligned}\mathbf{f}_{\rm sgm} =& -f_{0,\rm DM}\Delta\int_{-l_{\rm d}/2}^{l_{\rm d}/2}\frac{(x-x_{\rm d})\hat{\boldsymbol{x}}+y\hat{\boldsymbol{y}}}{[1+(x-x_{\rm d})^2+y^2]^3}\mathrm{d}x_{\rm d}\\ =& -\frac{f_{0,\rm DM}\Delta}{8}\left[\left(\frac{2}{[1+(x-x_{\rm d})^2+y^2)]^2}\right)\hat{\boldsymbol{x}}\right.\\ &\left.-\frac{y}{(1+y^2)^2}\left(\frac{(x-x_{\rm d})[3(x-x_{\rm d})^2+5(1+y^2)]}{[1+(x-x_{\rm d})^2+y^2]^2}+\frac{3\arctan\left(\frac{x-x_{\rm d}}{\sqrt{1+y^2}}\right)}{(1+y^2)^{1/2}}\right)\hat{\boldsymbol{y}}\right]_{x_-}^{x_+},\end{aligned}\tag{3.14}$$

where $x_{\rm d}$ should be evaluated at $x_\pm = \pm l_{\rm d}/2$. Thus, Thiele's equation reads (recall that all the magnitudes, including tensors, are dimensionless),

$$(\mathbb{G}-\alpha\mathbb{D})\mathbf{v}_{\rm d}+\mathbb{B}\mathbf{v}_{\rm HM}+\mathbf{f}_{\rm sgm}=0.\tag{3.15}$$

Unfortunately, the expression of the force in the case of a segment defect is too complicated to obtain closed-form formulas for the critical points and the upper threshold of current velocity, above which these points do not exist. However, some information may be obtained from Eq. (3.15) regardless. In Fig. 3.6(a) we show the force field that the segment defect produces on an incoming skyrmion. That force produces a drift velocity on the skyrmion shown in Fig. 3.6(b). As it can be seen, for an attractive ($f_{0,\rm DM} > 0$) defect segment, the skyrmion is attracted towards it in a counter-clockwise spiraling motion. In Figs. 3.6(c-e) we show the phase portraits obtained by solving the skyrmion dynamics [Eq. (3.15)]. It is observed that if the defect is attractive and the skyrmion is driven with a velocity $v_{\rm HM} = 0.0049$, a spiral sink and a saddle point appear, as indicated with the red dots and crosses in Fig. 3.6.

Given that the skyrmion is bound to be somewhat deformed by the defect, the rigid approximation may no longer hold. In order to confirm the results obtained using the rigid model, micromagnetic simulations by solving the LLG equation were performed[a]. These simulations were done ad hoc to check the found results from the Thiele equation. The normalized driving velocity used for these simulations is $v_{\rm HM} = 0.0049$. The defect has been simulated considering a local increase of the DM constant by a factor of $\delta = 1.5$, which results in a force given by Eq. (3.14) where

$$f_{0,\rm DM}\Delta = \frac{8D_{\rm DM}(\delta-1)}{\mu_0 M_s^2 R_{sk}^2}\Delta \simeq 0.264,\tag{3.16}$$

with $\Delta = 4.2$ nm, and $R_{\rm sk} \simeq 22$ nm (according to micromagnetic simulations far from the defect). The calculated micromagnetic trajectories for the skyrmion center and different driving current angles $\varphi_{\rm HM}$, are shown in Figs. 3.6(c-e) with purple lines.

---

[a] The development and details on the calculations of the LLG equation with defects are presented in another thesis done in parallel to this one. Thus, they are not included here.

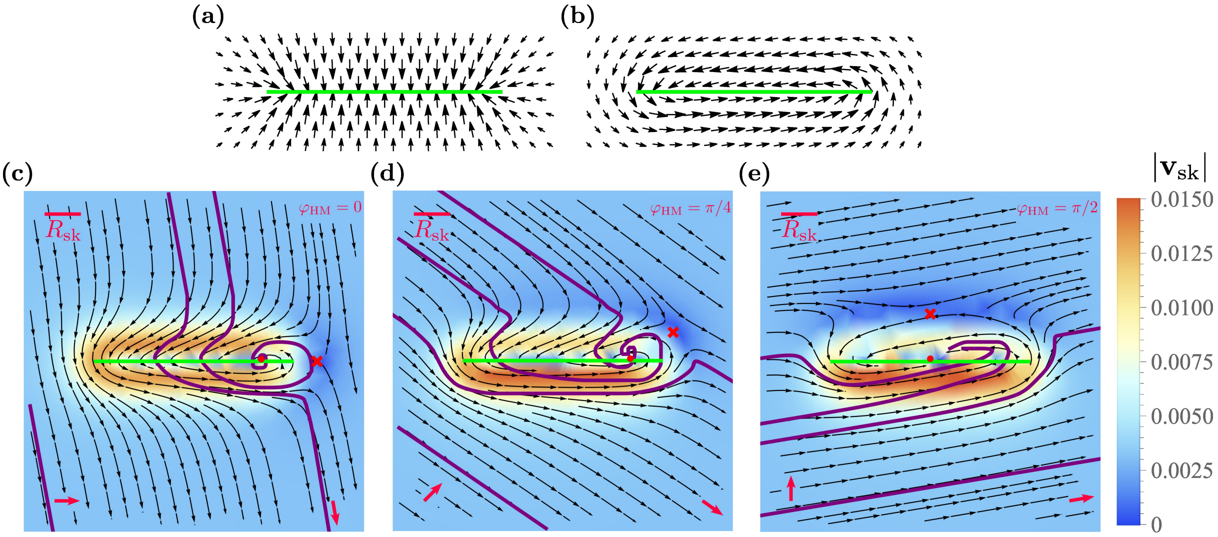

Figure 3.6: Vector field corresponding to (a) the force made by an attractive finite defect segment and (b) the velocity it produces over the skyrmion. The defect length is $l_{\rm d}=6$. The skyrmion can be pinned by a defect with a counter-clockwise spiraling motion. Phase portrait of Thiele's equation for the finite defect segment considering $v_{\rm HM}=0.0049$ for different values of the driving current angle (c) $\varphi_{\rm HM}=0$, (d) $\varphi_{\rm HM}=\pi/4$, and (e) $\varphi_{\rm HM}=\pi/2$. For these plots $f_{0,{\rm DM}}\Delta=0.38$ and $v_{\rm HM}=0.0049$. The rest of the parameters are the same as in Fig. 3.4. The solid purple lines correspond to trajectories of a skyrmion's center obtained by solving the LLG equation with $v_{\rm HM}=0.0049$ and $\delta=1.5$, for several initial positions. The rest of the parameters in the LLG equation are indicated in the text. The meaning of symbols, bars, colors, and arrows is the same as in Fig. 3.4.

To obtain the results plotted in Figs. 3.6(c-e), the force $f_{0,{\rm DM}}\Delta=0.38$ was fitted so as to match the pinning points. It can be seen that the force predicted by the atomistic model is slightly smaller. Nevertheless, we observe good agreement with the predictions of the rigid model. The discrepancies are attributed to the skyrmion deformations when interacting with the defect, which are not taken into account in the rigid model nor in the atomistic force. Nonetheless, the deformations are not drastic and the rigid model seems valid for the predictions in this parameter range as demonstrated by Figs. 3.6(c-e). Since the discrepancy in $f_{0,{\rm DM}}\Delta$ can be explained, we will use the value that better fits the micromagnetic simulations, $f_{0,{\rm DM}}\Delta=0.38$, for the rest of the chapter.

In fact, as long as the driving velocity $v_{\rm HM}$ is below the threshold and the defect is attractive, a spiral sink and a saddle point will appear as found in Figs. 3.6(c-e). The threshold velocity for the critical points to exist is found to be proportional to the minimum value between the maximum force along each axis (X or Y). It reads

$$v_{\rm th,sgm}=-\frac{1}{\mathcal{B}}\min\left\{\max\left[\frac{\mathbf{f}_{\rm sgm}\cdot\hat{\boldsymbol{x}}}{\cos\varphi_{\rm HM}}\right],\max\left[\frac{\mathbf{f}_{\rm sgm}\cdot\hat{\boldsymbol{y}}}{\sin\varphi_{\rm HM}}\right]\right\}, \tag{3.17}$$

where $\varphi_{\rm HM}$ is the angle of the applied current (see Fig. 3.5). Note that the threshold velocity and critical points now depend on both the defect length $l_{\rm d}$ (through $\mathbf{f}_{\rm sgm}$) and the angle of the applied current $\varphi_{\rm HM}$ [see Figs. 3.6(c-e)].

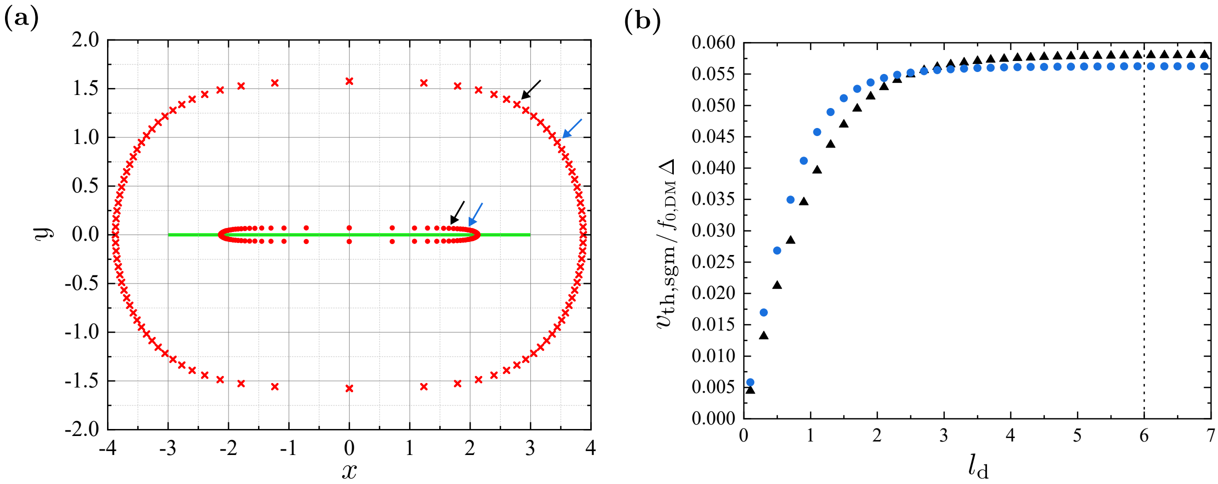

Figure 3.7: (a) Position of the spiral sink (red dots) and the saddle points (red crosses) for different driving current angles φ_{HM}. The defect segment is indicated by the horizontal green line. (b) Threshold velocity as a function of the defect size l_{d} [Eq. (3.17)] for $\varphi_{\mathrm{HM}} = \pi/4$ (blue squares) and $\varphi_{\mathrm{HM}} = 3\pi/8$ (black triangles). The vertical line indicates the defect length shown in (a). The colored arrows in (a) correspond to the angles shown in (b). The parameters used are the same as in Fig. 3.6.

For a more comprehensive study on the threshold velocity ($v_{\mathrm{th,sgm}}$), we have numerically solved Eq. (3.15) when $\dot{x} = \dot{y} = 0$. In Fig. 3.7(a) the positions of the critical points are shown as a function of the driving current angle, φ_{HM}, for an attractive ($f_{0,\mathrm{DM}} > 0$) defect segment of length $l_{\mathrm{d}} = 6$ and a velocity, $v_{\mathrm{HM}} = 0.0049$, below the threshold driving current. It can be seen that both the spiral sink (inner red dots) and saddle points (outer red crosses) circle around the defect with the angle of the applied driving current. As the threshold driving current velocity depends on both the incident angle and defect length [see Eq. (3.17)], we computed it as a function of the defect length for two different driving angles: $\varphi_{\mathrm{HM}} = \pi/4, 3\pi/8$. The results are shown in Fig. 3.7(b). It can be seen that for long defects ($l_{\mathrm{d}} \gtrsim 6$) the threshold driving current saturates on a value depending on the driving current angle. As the defect gets shorter the threshold driving current density becomes smaller. In the limit where $(l_{\mathrm{d}}, \Delta) = a$ we recover the local defect case [see Fig. 3.7(b)]. This can also be obtained by taking Eq. (3.14) in the limit $(l_{\mathrm{d}}, \Delta) \to a$, recovering the point defect [Eq. (3.6)]. If one ought to obtain the driving current threshold for another driving current angle, it can be obtained by numerically solving Eq. (3.17).

In general, the critical points and threshold velocity were found to depend on the length of the defect l_{d} and the angle of the driving velocity φ_{HM} and its velocity $|\mathbf{v}_{\mathrm{HM}}|$. An interesting limit, where analytical treatment of the equations is possible, is when $l_{\mathrm{d}} \gg R_{\mathrm{sk}}$. This corresponds to a defect line that is much longer than the skyrmion radius. Recall that in Eq. (3.13) we already considered the defect width Δ to be small ($\Delta \ll R_{\mathrm{sk}}$). In this limit, the defect segment becomes a line that spans across one dimension. This kind of defect was numerically studied by solving the LLG equation in our group.[196] It was found that skyrmions can be guided along the defect line if the driving velocity is below a threshold. This behavior is found when the defect line is attractive (guided at the right of the defect) or repulsive (guided at the left of the defect).[196]

The guiding regime found with line defect can be predicted and studied analytically with the presented model. The force exerted by a line defect can be obtained by taking Eq. (3.14) in the limit $l_\mathrm{d} \to \infty$,

$$\mathbf{f}_\mathrm{line} = -\frac{3\pi f_{0,\mathrm{DM}}\Delta}{8}\frac{x}{[1+x^2]^{5/2}}\hat{\boldsymbol{x}}, \tag{3.18}$$

where we have set the line defect along the y axis, as was done in Ref. [196]. Note that there is no net force along the defect line. Thiele's system of equations is found to be,

$$\begin{cases} \left(\alpha^2\mathcal{D}^2+\mathcal{G}^2\right)\,\dot{x} = \alpha\mathcal{D}\mathcal{B}v_\mathrm{h,x} + \mathcal{G}\mathcal{B}v_\mathrm{h,y} - \dfrac{3\pi\alpha\mathcal{D}f_{0,\mathrm{DM}}\Delta}{8}\dfrac{x}{(1+x^2)^{5/2}}, & (3.19)\\ \left(\alpha^2\mathcal{D}^2+\mathcal{G}^2\right)\,\dot{y} = -\mathcal{G}\mathcal{B}v_\mathrm{h,x} + \alpha\mathcal{D}\mathcal{B}v_\mathrm{h,y} + \dfrac{3\pi\mathcal{G}f_{0,\mathrm{DM}}\Delta}{8}\dfrac{x}{(1+x^2)^{5/2}}. & (3.20)\end{cases}$$

In this case, no critical point can be found except when the driving current angle $\varphi_\mathrm{HM} = 0$ or π, because it is not possible to cancel both components of the skyrmion drift velocity otherwise. This can be seen more clearly is we set $\dot{x} = \dot{y} = 0$,

$$\begin{cases} \alpha\mathcal{D}\mathcal{B}v_\mathrm{h,x} + \mathcal{G}\mathcal{B}v_\mathrm{h,y} = -\alpha\mathcal{D}f_\mathrm{line},\\ -\mathcal{G}\mathcal{B}v_\mathrm{h,x} + \alpha\mathcal{D}\mathcal{B}v_\mathrm{h,y} = \mathcal{G}f_\mathrm{line},\end{cases} \tag{3.21}$$

since if $v_\mathrm{h,y} \neq 0$, one of the equations can not be satisfied. This becomes apparent if we set $v_\mathrm{h,x} = 0$,

$$\begin{cases} v_\mathrm{h,y} = -\dfrac{\alpha\mathcal{D}}{\mathcal{G}\mathcal{B}}f_\mathrm{line},\\[2ex] v_\mathrm{h,y} = \dfrac{\mathcal{G}}{\alpha\mathcal{D}\mathcal{B}}f_\mathrm{line},\end{cases} \tag{3.22}$$

where there is a sign change that cannot be fulfilled simultaneously. Therefore, the velocity cannot be canceled in both axis and no critical points exist. However, an interesting result arising from this fact is that the skyrmion drift velocity perpendicular to the line defect can cancel out with the force [Eq. (3.18)], whilst the parallel component can not. This results in the guiding regime ($\dot{x} = 0$) which was already predicted numerically with micromagnetic simulations by our group in Ref. [196]. Note that, when $\varphi_\mathrm{HM} = 0, \pi$, any small perturbation would prevent the pinning found. As such, we will not consider this case, since it will not be found experimentally or in LLG simulations, as even the numerical error would break such feeble pinning.

From the system of Eqs. (3.22), the threshold velocity for such behavior can be found. To do so, the easiest way is to use the complex Thiele formulation, as presented in Appendix A.2. The threshold velocity is found to be,

$$v_{\text{th,line}} = \frac{6\pi}{25\sqrt{5}\mathcal{B}} \frac{\alpha\mathcal{D}}{\alpha\mathcal{D}\cos\varphi_{\text{HM}} + \mathcal{G}\sin\varphi_{\text{HM}}} f_{0,\text{DM}}\Delta, \tag{3.23}$$

which corresponds to the saturation value found for the longer defect lines in Fig. 3.7(b).

When the skyrmion is being guided ($\dot{x} = 0$), one can find that the skyrmion velocity along the defect line is

$$\dot{y} = \frac{\mathcal{B}}{\alpha\mathcal{D}} v_{\text{HM}} \sin\varphi_{\text{HM}}. \tag{3.24}$$

This indicates that in the guiding regime, the skyrmion velocity: (i) does not depend on the force of the defect (as long as the driving velocity is below the threshold, $v_{\text{th,line}}$); (ii) is maximum when $\varphi_{\text{HM}} = \pi/2$; and (iii) is inversely proportional to α, indicating a larger speed-up for smaller α. The latter was also found[273] when the guiding occurs near the edge of the material. Note that, even though the skyrmion velocity does not depend on the defect force, the threshold velocity does.

To illustrate our findings and have information on the transient skyrmion dynamics before being guided, we have solved Eqs. (3.19) and (3.20). The phase portraits are shown in Fig. 3.8. When the skyrmion is driven below the threshold velocity with an attractive defect [Figs. 3.8(a) and (b)], the guiding regime is found for different values of the driving current (a) $\varphi_{\text{HM}} = \pi/4$, (b) $\varphi_{\text{HM}} = \pi/2$. As can be seen, the guiding is found at the right of the defect line, as found in Ref. [196], and the velocity in the driving regime is maximum when $\varphi_{\text{HM}} = \pi/2$ as we previously found in Eq. (3.24). When the defect is repulsive ($f_{\text{line}} < 0$), the guiding is found to be along the left side of the defect [see Figs. 3.8(d) and (e)]. If the driving current is above the threshold [Eq. (3.23)], the skyrmion crosses the defect line for both attractive [Fig. 3.8(c)] and repulsive [Fig. 3.8(f)] defects. In general, the phase portraits in the attractive and repulsive cases are somewhat similar considering that: (i) the velocity component perpendicular to the defect is mirrored with respect to the defect line; (ii) the velocity component parallel to the defect remains unchanged; and (iii) the guiding line is the furthest from the defect (not the closest as for an attractive defect).

To validate these results we have solved the LLG equation [Eq. (2.5)] as in Fig. 3.6. In general, the Thiele trajectories are similar to the ones obtained by simulating the LLG equation. It can be seen that our model's predictions are more accurate for a repulsive defect in the guiding regime. We attribute this effect to the fact that since the skyrmion does not reach the defect, the skyrmion is less modified by it (recall that a change in the skyrmion size is not captured by the Thiele model). In the case of an attractive defect, it is known that the skyrmion grows larger and is more deformed, in some cases being elliptical.[196] Thus the Thiele approximation is at its best for repulsive defects. The guiding regime is also found when solving the LLG equation, as can be seen in Fig. 3.8 and we reported in Ref. [196]. It must be noted that the α^{-1} dependence has also been found with micromagnetic simulations,[196] even though the magnitude of the speedup factor is slightly smaller. We attribute the small discrepancies to the skyrmion deformations close to the defect lines. When the driving current is above the threshold ($v_{\text{HM}} > v_{\text{th,line}}$) in both cases the skyrmion overcomes the defect as predicted.

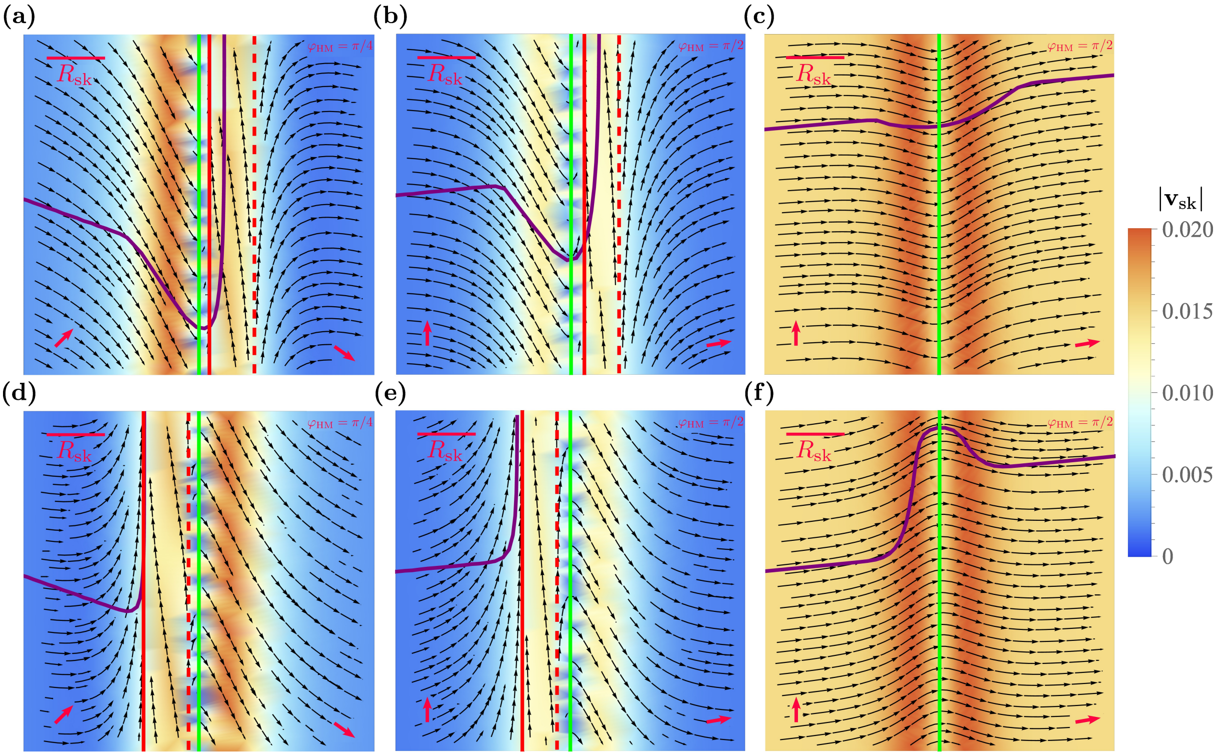

Figure 3.8: Phase portrait of Thiele's equation for an infinite attractive (a-c) or repulsive (d-f) defect line considering $v_{\rm HM} = 0.0025$ for different driving current angles (a, d) $\varphi_{\rm HM} = \pi/4$, (b,e) $\varphi_{\rm HM} = \pi/2$. For currents $v_{\rm HM} = 0.0225 \simeq 6.6 v_{\rm th,line}$ and $\varphi_{\rm HM} = \pi/2$, the skyrmion goes through the defect line for both attractive (c) and repulsive (f) line defects. The red solid (dashed) line is the guiding (saddle) nullcline. The meaning of symbols, bars, lines, colors, and arrows is the same as in Fig. 3.4. For these plots, the parameters are the same as in Fig. 3.6.

The prospect of using artificial defect lines to guide the skyrmions whilst accelerating them is interesting on its own. The lack of control over the skyrmion Hall angle has been a potential bottleneck for many racetrack implementations, e.g. by pushing skyrmions towards the racetrack's edges and annihilating them. As was found, the skyrmion velocity along the defect can be enhanced by orders of magnitude due to its α^{-1} dependence [Eq. (3.24)]. This behavior is also obtained with the micromagnetic simulations (see Fig. 3.8). But the skyrmion deformation due to the defects can further enhance the skyrmion transport part of skyrmionic devices. For example in Ref. [196], it was found that using skyrmionic rails made of an attractive defect line (skyrmion guided on its right) followed by a close repulsive defect line (skyrmion guided on its left) can both increase the speed-up factor of the guided skyrmion whilst compressing it. This compression is possible as the rail width can be as small as the skyrmion radius far from the defect. This could potentially result in an enhancement in both the velocity as well as the information density while avoiding the undesirable skyrmion Hall angle. Other approaches have been based on guiding the skyrmion along regions with some modified material magnetic parameters both theoretically[86,118,274,275] and, more recently, experimentally.[276]

An interesting consideration is that it is not realistic to consider an infinite defect line in real materials. As such, the skyrmion is bound to reach an end at some point. The behavior found can be readily explained by what has been seen in this section: far from the end, the skyrmion is guided along the defect line and speedup, but as we approach the end we recover the results found for the finite segment defect, where pinning may occur if the defect is attractive [see Fig. 3.6(c-e)].

3.3.2 More complex defects

A natural extension of the line defect is to consider their superposition in different arrangements. An interesting consideration would be what happens at the crossing between two defects. To study that behavior and build upon the previously known phenomena we will consider a semi-infinite defect line $y \in (-\infty, 0]$ that merges at the end of it with a defect segment along the x axis (see green lines in Fig. 3.9). We will refer to this kind of defect as an L-shaped defect.

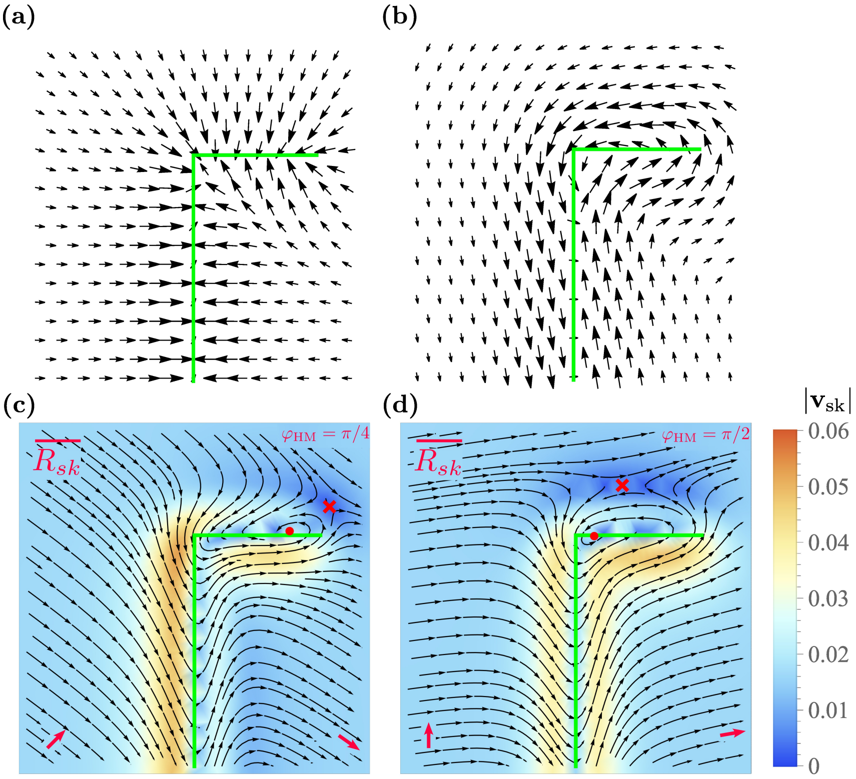

Figure 3.9: Vector field corresponding to (a) the force made by an attractive L-shaped defect and (b) the velocity it produces over the skyrmion. The horizontal segment length is $l_{\mathrm{d}} = 3$. (c,d) Phase portrait of Thiele's equation for an attractive L-shaped defect considering $v_{\mathrm{HM}} = 0.025$ for different driving current angles (c) $\varphi_{\mathrm{HM}} = \pi/4$ and (d) $\varphi_{\mathrm{HM}} = \pi/2$. The meaning of the symbols, bars, colors, and arrows is the same as in Fig. 3.4. For these plots, the parameters are the same as in Fig. 3.6.

Unfortunately, due to the complex dynamics, obtaining the critical points and threshold driving currents has to be done numerically. Nevertheless, the critical points can be found as done previously, considering the external force coming from all the segments that compose the defect.

The vector fields of the defect force and the skyrmion drift velocity associated with an attractive L-shaped defect are shown in Figs. 3.9 (a) and (b), respectively. It can be seen that the skyrmion tends to circle around the defect counterclockwise [Fig. 3.9(b)]. When considering a driving current, depending on its value, this could result in the presence of spiral sinks. The phase portraits of the skyrmion drift velocity obtained for attractive defects with different incident driving current angles ($\varphi_{\mathrm{HM}} \neq 0$) are shown in Figs. 3.9(c-d). Near the horizontal segment defect we see that saddle points and spiral sinks (sources) appear for attractive (repulsive) defects [see Figs. 3.9(c-d)]. The position of these critical points depends on the driving current angle, the horizontal defect length, and their strength.

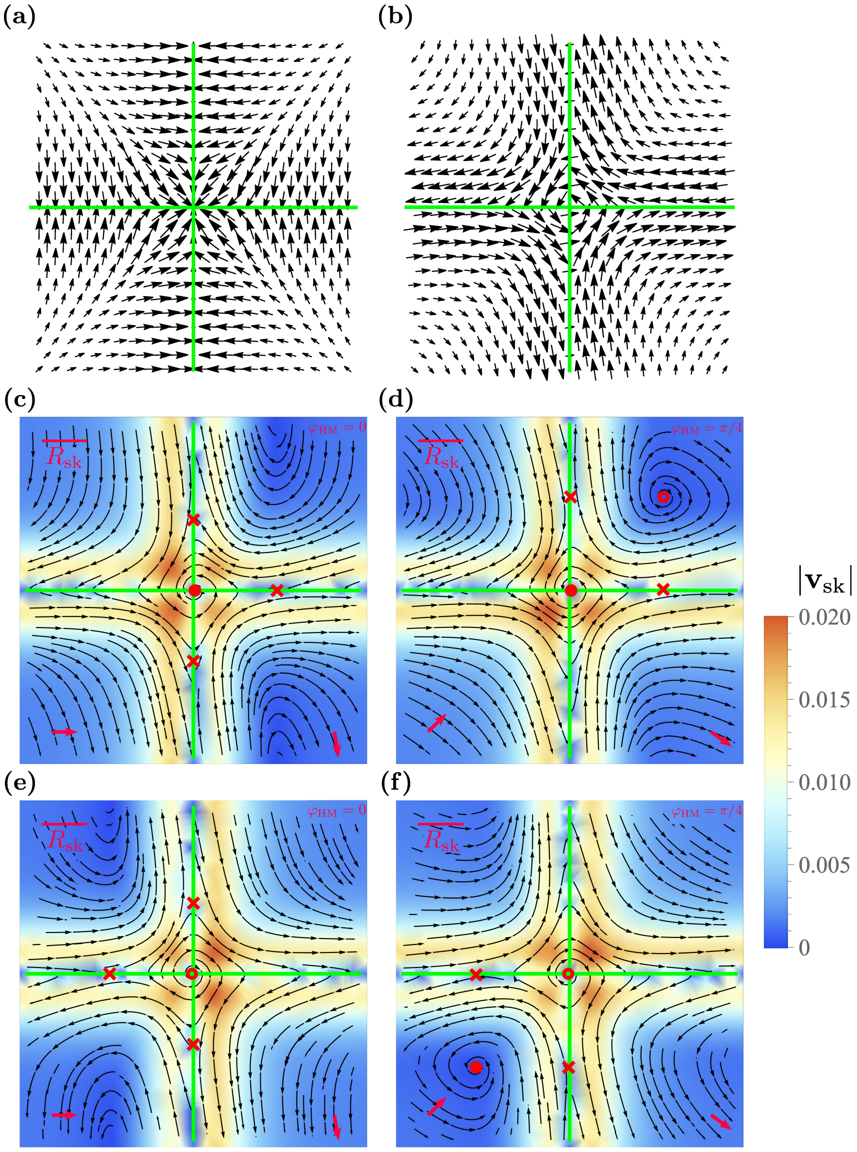

Figure 3.10: Vector field corresponding to (a) the force made by an attractive cross defect and (b) the drift velocity it produces to the skyrmion. Phase portrait of Thiele's equation for an attractive (c,d) or repulsive (e,f) defect cross, considering $v_{\rm HM} = 0.0025$ with different driving current angles (c,e) $\varphi_{\rm HM} = 0$ and (d,f) $\varphi_{\rm HM} = \pi/4$. The meaning of symbols, bars, colors, and arrows is the same as in Fig. 3.9. For these plots, the parameters are the same as in Fig. 3.6.

These arrangements could potentially guide skyrmions along the defect line and pin them near their end. Furthermore, it seems that the skyrmion tends to follow the horizontal defect. So a question arises: Is it possible to steer skyrmions in a controlled and reproducible manner?

To that end, we consider a crossing of two perpendicular line defects. Far from the crossing, both defects are expected to guide the skyrmion along them as was found in Fig. 3.8. Due to the findings with the L-shaped defects, it is expected that some critical points appear near the crossing of both line defects.

To quantitatively study them in detail, we consider a cross-shaped defect. As with the L-shaped defect, the Thiele equation does not shed any relevant information unless numerically solved.

The vector fields of the defect force and the skyrmion drift velocity associated with an attractive defect are shown in Figs. 3.10 (a) and (b), respectively. Since the system has $\pi/2$ rotational symmetry we will only consider driving current angles $\varphi_{\mathrm{HM}} \in [0, \pi/2)$. When the defect is attractive a spiral sink is found near the crossing. If the driving current goes along one of the defects, three saddle points are found: one along the driving current direction and two in the perpendicular one [Fig. 3.10(c)]. For other driving current angles, a spiral source is found [Fig. 3.10(d)]. In contrast, a cross made of repulsive defects has a spiral sink near the crossing, and if $\varphi_{\mathrm{HM}} \neq 0$ a spiral sink is found [see Figs. 3.10(e-f)]. Note that only two saddle points are found near the crossing if $\varphi_{\mathrm{HM}} \neq 0$.

With the present results in mind, one can envisage the periodic arrangement of such pinning positions by using a periodic arrangement of such cross defects, forming a grid. It should be expected that the skyrmion would be trapped in a controlled manner. The periodicity would allow having a periodic arrangement of skyrmions in a rectangular lattice.

Periodic infinite lines (Grid)

Consider a set of line defects arranged as a periodic rectangular grid [see Fig. 3.11], each line separated a distance δ_x and δ_y in the x and y axis, respectively. For simplicity, we will consider that all line defects have the same $f_{0,\mathrm{DM}}$. Using the expression for the force obtained for a line defect [Eq. (3.18)] we obtain that the total force of the grid at a position $\mathbf{r} = (x, y)$ is given by,

$$\mathbf{f}^{g}_{\mathrm{grid}} = -\frac{3\pi f_{0,\mathrm{DM}}\Delta}{8}\left[\sum_{m=-\infty}^{\infty}\frac{x - m\delta_x}{[1 + (x - m\delta_x)^2]^{5/2}}\hat{\boldsymbol{x}} + \sum_{n=-\infty}^{\infty}\frac{y - n\delta_y}{[1 + (y - n\delta_y)^2]^{5/2}}\hat{\boldsymbol{y}}\right]. \tag{3.25}$$

These series converge, but no analytical closed-form expression was found. As such it proves difficult to obtain any insight directly from Thiele's equation and only its numerical solution is possible. To avoid this shortcoming, we propose an alternative model that has proven helpful for these types of periodicity. The trade-off for obtaining a closed expression for the force will be the need of using two fitting parameters.

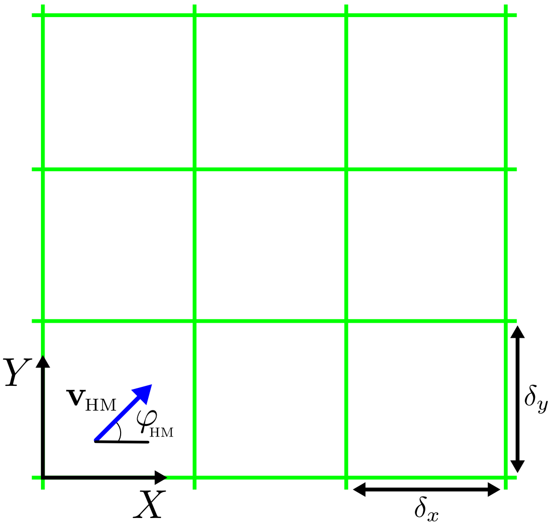

Figure 3.11: Illustration of the grid defect system. The defect lines that form the periodic grid are shown in green. The defect lines are separated a distance δ_x (δ_y) in the X (Y) axis. The blue arrow is the driving velocity ($\mathbf{v}_{\mathrm{HM}}$) applied at an angle φ_{HM}.

Let's consider that a local defect produces a Gaussian potential over the skyrmion of the form $U(\rho) = -U_0 \exp\left(-\rho^2/2\lambda_{\mathrm{g}}^2\right)$, where U_0 is a parameter that controls the intensity of the defect and λ_{g} is the radial scope of the defect. We consider that a $U_0 > 0$ results in an attractive defect (same convention as in Ref. [89]).

In a previous work, we used these types of Gaussian potentials to study all the previous defect arrangements. The results we obtained in Ref. [277] are similar to the ones obtained using Eq. (3.2). Thus, the model is robust to the election of the defect force expression, as long as it grows linearly at close range and decays smoothly to zero as the distance with the defect grows.

The force created by a Gaussian potential [$\mathbf{F}_{\rm ext} = -\nabla U(\rho)$], after normalization, reads

$$f^g_{\rm loc} = -\frac{U_0 R_{\rm sk}}{\lambda_0^2}\rho e^{-\frac{\rho^2}{2\lambda_0^2}} = -f^g_0 \rho e^{-\frac{\rho^2}{2\lambda_0^2}}\hat{\boldsymbol{\rho}}, \tag{3.26}$$

where $\lambda_0 = \lambda_{\rm g}/R_{\rm sk}$ is the normalized scope of the defect, and the g-superscript indicates the Gaussian shape while the loc subscript its point-like nature. A $f^g_0 > 0$ (< 0) results in an attractive (repulsive) force. This is the same convention that was used previously in this chapter.

This force has a similar behavior as Eq. (3.2): close to the defect, we have a linear increase of the force, followed by a decay to zero for larger distances. A comparison of both functions is shown in Fig. 3.12(a). The force coming from a local variation of the DM interaction is obtained from Eq. (3.2) using $\delta = 2$ and normalized to $f_{0,\rm DM}$. The force maximum is found at $x_{\rm m} = 1/\sqrt{5}$. To compare with the Gaussian-like force we set $\lambda_0 = 1/\sqrt{5}$ so that both force maximum positions match. Both forces are normalized so that the forces peak at 1. From Fig. 3.12(a) it is clear that for smaller distances the approximation is at its best whilst the exponential decay is stronger than the polynomial one found in Eq. (3.2). Nonetheless, the general trend is captured.

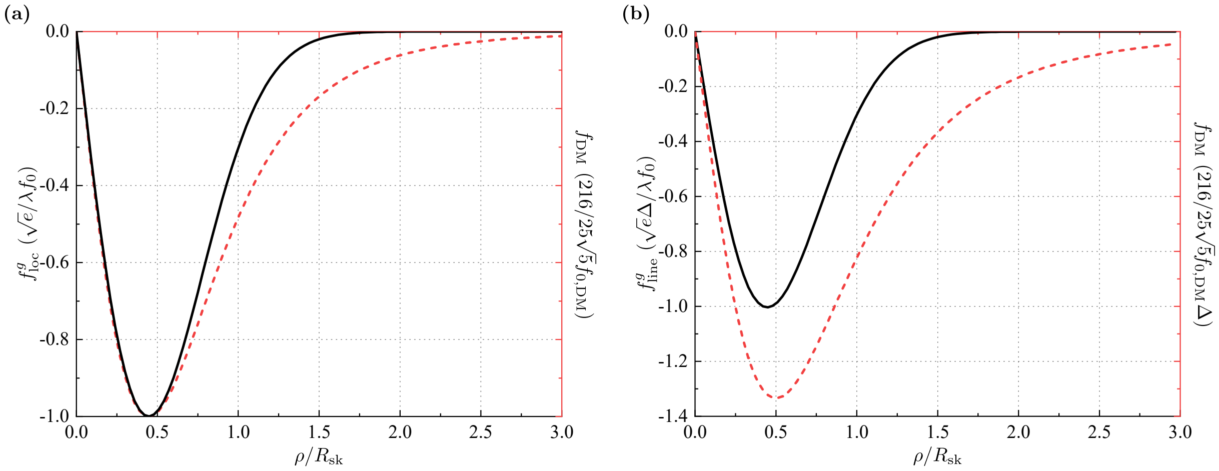

Figure 3.12: Comparison of the proposed Gaussian defect (solid black line) with the force arising from an atomistic variation of the DM parameter[89] (dashed red line) for (a) a local defect and (b) a line defect. The parameters used are $\lambda_0 = 1/\sqrt{5}$ and $\delta = 2$. A negative force points towards the defect. In (a) the forces are scaled so their maximum is 1. The same scaling is kept in (b).

Consider the atomic defect density given by $\sigma = 1/\Delta^2$. For a vertical defect line [Fig. 3.8], we can use Eq. (3.13) to obtain the force coming from Gaussian defects,

$$\mathbf{f}^g_{\rm line} = -\frac{f^g_0}{\Delta}\lambda_0\sqrt{\pi}x e^{-\left(\frac{x^2}{\lambda_0^2}\right)}\hat{\boldsymbol{x}}. \tag{3.27}$$

In Fig. 3.12(b) we show the comparison between the Gaussian line defect force [Eq. (3.27)] and the derived expression from an atomistic variation of the DM parameter [Eq. (3.18)]. Even though the Gaussian force parameters λ_0 and f_0^g could be fitted to better match the atomistic line defect force, we present the comparison with the chosen values from the local defect [Fig. 3.12(b)]. The Gaussian defect force maximum is 1.33 times smaller and it decays faster than the atomistic defect. Nonetheless, the behavior found using the rigid model with this force has been found to match micromagnetic simulations with some minor deviations due to skyrmion deformation.[277]

As such, three relevant facts arise: (i) the rigid model is able to predict the skyrmion dynamics quite well; (ii) the results obtained are not very sensible to the exact force one decides to use; (iii) this force can be used as an approximation to the atomistic defect force [Eq. (3.18)]. The results obtained for point-like, segments, and line defects can be found in Ref. [277] to see that the results obtained for the local and line defects are qualitatively the same.

Revising the grid defect and rewriting Eq. (3.25) using the Gaussian defect force [Eq. (3.27)], one obtains

$$\mathbf{f}^g_{\text{grid}} = -\frac{\sqrt{2\pi}\lambda_0 f_0}{\Delta}\left[\sum_{m=-\infty}^{\infty}(x-m\delta_x)\exp\left(-\frac{(x-m\delta_x)^2}{2\lambda_0^2}\right)\hat{\boldsymbol{x}} + \sum_{n=-\infty}^{\infty}(y-n\delta_y)\exp\left(-\frac{(y-n\delta_y)^2}{2\lambda_0^2}\right)\hat{\boldsymbol{y}}\right]. \tag{3.28}$$

This expression can be expressed in terms of the elliptic theta functions. Note that

$$\frac{\partial}{\partial x}\left(\exp\left(-\frac{(x-m\delta_x)^2}{2\lambda_0^2}\right)\right) = \frac{1}{\lambda_0^2}(x-m\delta_x)\exp\left(-\frac{(x-m\delta_x)^2}{2\lambda_0^2}\right).$$

The infinite sum of that function converges to

$$\sum_{m=-\infty}^{\infty}\exp\left(-\frac{(x-m\delta_x)^2}{2\lambda_0^2}\right) = \frac{\sqrt{\pi}\lambda_0}{\delta_x}\vartheta_3\left(\frac{-\pi x}{\delta_x}, e^{-2\left(\frac{\pi\lambda_0}{\delta_x}\right)^2}\right), \tag{3.29}$$

where ϑ_3 is the Jacobi theta function.[278] Hence Eq. (3.28) can be expressed as,

$$\mathbf{f}^g_{\text{grid}} = -\frac{2\pi^2\lambda_0^4 f_0}{\Delta}\left[\frac{1}{\delta_x^2}\vartheta_3'\left(\frac{-\pi x}{\delta_x}, e^{-2\left(\frac{\pi\lambda_0}{\delta_x}\right)^2}\right)\hat{\boldsymbol{x}} + \frac{1}{\delta_y^2}\vartheta_3'\left(\frac{-\pi y}{\delta_y}, e^{-2\left(\frac{\pi\lambda_0}{\delta_y}\right)^2}\right)\hat{\boldsymbol{y}}\right]. \tag{3.30}$$

As an specially interesting limit, if $\pi\lambda_0 \gtrsim \delta_x, \delta_y$, the force can be approximated by

$$\mathbf{f}^g_{\text{grid}} \simeq -\frac{8\pi^2\lambda_0^4 f_0}{\Delta}\left[\frac{1}{\delta_x^2}e^{-\left(\frac{2\pi^2\lambda_0^2}{\delta_x^2}\right)}\sin\left(2\pi x/\delta_x\right)\hat{\boldsymbol{x}} + \frac{1}{\delta_y^2}e^{-\left(\frac{2\pi^2\lambda_0^2}{\delta_y^2}\right)}\sin\left(2\pi y/\delta_y\right)\hat{\boldsymbol{y}}\right]. \tag{3.31}$$

This limit corresponds to the case when the skyrmion size is of the order of the grid-lines separations (δ_x, δ_y). Note that, in this limit, the dependencies on the position (x and y) are only through the sin() functions. The force and the skyrmion drift velocity produced by the grid defect are shown in Fig. 3.13(a) and (b), respectively. In the literature, this kind of periodic functions have been used to describe periodic or ratchet substrate-induced potentials.[109, 110, 224, 267–270, 279–281] In those works, the force is taken ad hoc. Our derivation from the point-like defect allows us to give some physical meaning to the mechanism behind a way for such forces to emerge. The advantage of this approximation is that it can be used with the Thiele equation and obtain close-form expressions for the critical points and the upper threshold current for them to exist.

We use this derived grid force, $\mathbf{f}^g_{\text{grid}}$, in Thiele's equation [Eq. (3.7)] to characterize the system analytically. The threshold velocity can be found to be proportional to the minimum of the force along the X and Y axis. The threshold reads,

$$v_{\text{th,grid}} = 8 f_0^g \frac{\pi^2 \lambda_0^4}{\mathcal{B}\Delta} \min\left[\frac{1}{\delta_x^2 \cos\varphi_{\text{HM}}} \exp\left(-2\frac{\pi^2\lambda_0^2}{\delta_x^2}\right), \frac{1}{\delta_y^2 \sin\varphi_{\text{HM}}} \exp\left(-2\frac{\pi^2\lambda_0^2}{\delta_y^2}\right)\right], \tag{3.32}$$

where the threshold velocity depends on the driving current angle, φ_{HM}.

As long as the driving current is below the threshold [Eq. (3.32)] the skyrmion will be pinned at an attractor of the system, wherever it is initially nucleated [see Fig. 3.13]. This phenomenon holds true for both attractive and repulsive defect lines. For attractive defects ($f_0^g > 0$) the attractors are close to the intersections with a repulsor near the center of each cell, as can be seen in Figs. 3.13(c) and (d). In contrast, for repulsive defects ($f_0^g < 0$) their location is somewhat reversed as can be seen in Figs. 3.13(f) and (g): the attractors are near the center of the unit cells whilst a repulsor can be found at the crossings. The position of the critical points depends on the driving current v_{HM} and its incident angle φ_{HM}.

Such periodic pinning array can create skyrmion lattices of arbitrary quadrilateral arrangements that can be used for several applications. For example, it is known that a magnetic field can trap diamagnetic atoms, potentially allowing to cool them below the optical limit.[282] Recently it has been shown that the stray field of a skyrmion lattice[283] or of two magnetic skyrmions[284] can be used to trap ultracold atoms. In this way, the presented grid could give additional control on the trapping potential for the atoms, as the skyrmion arrangement and position can be artificially controlled. Another possibility is to *pixelate* the skyrmion motion in the two axes where there are defects.[285]

But this system is not only interesting when pinning occurs. Even when the driving current is above the threshold and pinning is no longer possible for neither attractive nor repulsive line defects [see Figs. 3.13(e) and (f), respectively] it still might be useful. Even though the skyrmions will not be pinned, the skyrmion trajectories are modified by the underlying grid defect. The behavior found has been widely studied in the literature in which the periodicity of the grid sets an effective skyrmion Hall angle and commensurability can be studied.[224, 268, 280, 281] In this way, the geometric arrangement of the defects can be used to have the particular movement control needed for a specific application.

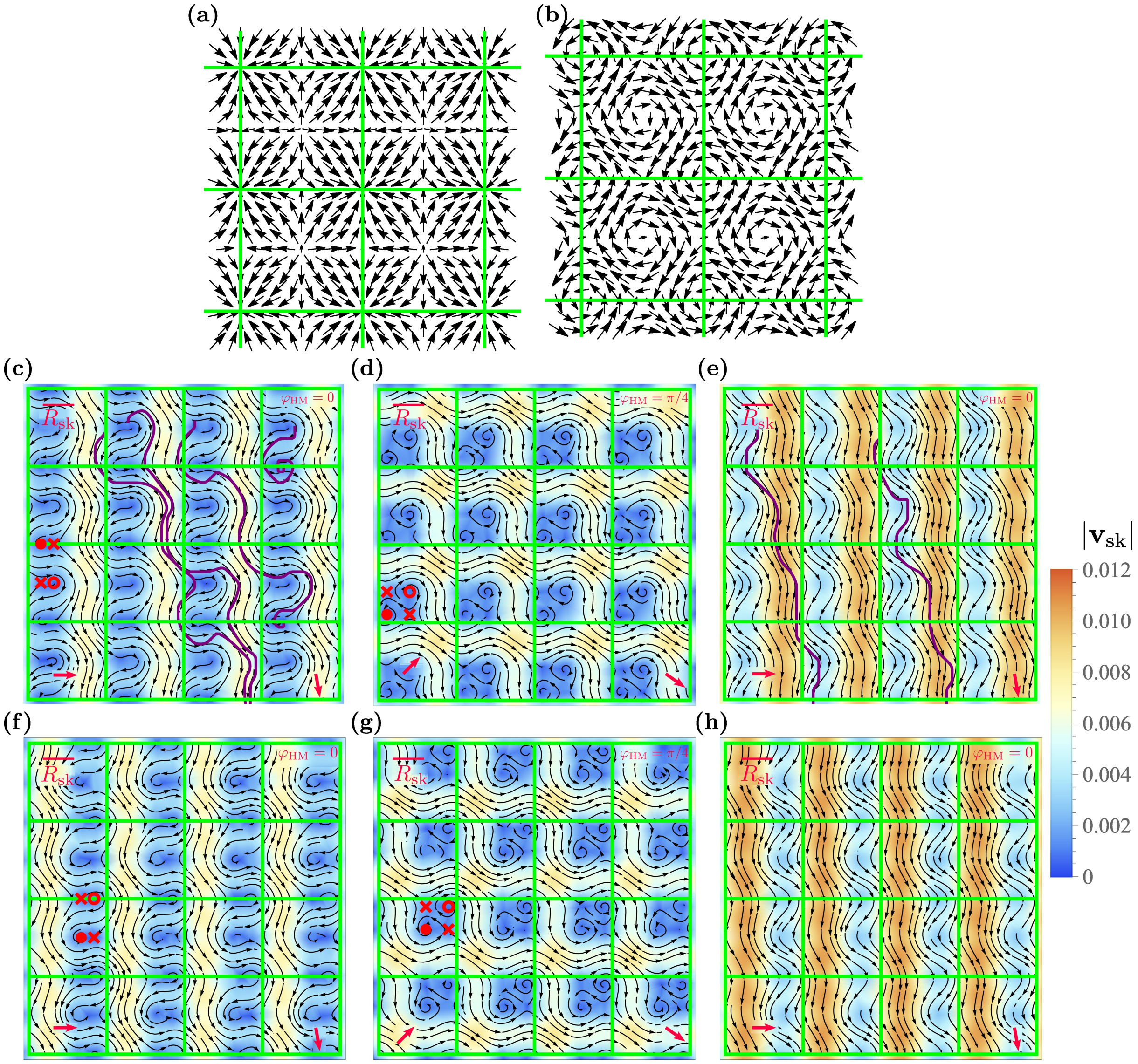

Figure 3.13: Vector fields of (a) the force $\mathbf{f}^{g}_{\rm grid}$ [Eq. (3.31)] produced by a grid defect and (b) the drift velocity it produces. Phase portrait of Thiele's equation for an attractive (c-e) or repulsive (f-h) defect lines considering a driving current $v_{\rm HM} = 0.0049 < v_{\rm th,grid}$ with different incident angles: (c, f) $\varphi_{\rm HM} = 0$ and (d,g) $\varphi_{\rm HM} = \pi/4$. For currents $v_{\rm HM} = 0.0098 > v_{\rm th,grid}$, the skyrmion goes through the defect line for both attractive (e) and repulsive (h) defects. The solid purple lines in (c) and (e) correspond to trajectories of a skyrmion center obtained by solving the LLG equation for several initial positions. For simplicity, these are shown in two cases, (c) and (e), as a similar agreement is also found for the rest. The meaning of symbols, bars, colors, and arrows is the same as in Fig. 3.4 (for simplicity we have only plotted the critical points in one cell as the system is periodic). For these particular examples $f^{g}_{0}/\Delta = 0.05$, $\lambda_0 = 1$, $\delta_x = \delta_y = 2.8$, and the micromagnetic simulated defects correspond to $\delta = 1.2$ (purple lines). The rest of the parameters are the same as in Fig. 3.6.

To validate that the rigid model combined with the Gaussian defect force [Eq. (3.31)] is able to predict the general behavior of the skyrmion under a periodic arrangement of defect lines, its predictions are compared to micromagnetic simulations. For these simulations, the defect is a local increase of the DM parameter with $\delta = 1.2$, which results in attractive line defects that form the periodic grid. The results are shown with purple lines in Figs. 3.13 (c) and (e). A good agreement is found between the predictions with the presented Gaussian force and the micromagnetic simulations, validating our approximation. The fitted force parameters are $f_0^g/\Delta = 0.05$ with $\lambda_0 = 1$.

3.4 Chapter summary and conclusions

In this chapter, we have modeled the skyrmion-defect interaction with extended defects, composed of an arrangement of local defects, using the rigid model. We have developed analytic expressions to calculate the critical points of the skyrmion trajectories, as well as the threshold current velocities above which skyrmions overcome the defect (i.e. no pinning is found).

We have shown that for a defect line (e.g. material dislocations), the skyrmion can be guided along the defect. We found that such guiding has two main advantages: (i) the skyrmion Hall angle is compensated as it is guided along the line defect; (ii) the skyrmion velocity along the defect is sped-up by a factor α^{-1}, achieving up to an order of magnitude (for realistic α values) higher velocities than in the defect-free case. This has enabled us to envisage novel platforms for skyrmion transport such as the skyrmion rails.[196] These rails consist of a pair of line defects, that if arranged adequately, can guide and speed up the skyrmion whilst compressing it. In this way, the amount of skyrmionic information that can be transported could be boosted.

We have also presented an approximation for the atomistic defect potential that allows having analytic closed-form expressions for the skyrmion trajectories in more complicated periodic arrangements. These defects are regarded as Gaussian potentials. We focus on a periodic defect grid composed of line defects. It is found that a periodic arrangement of skyrmions is possible, even under small applied current densities. We give expressions for the critical points as well as the threshold current velocity at which the skyrmion overcomes the defects. This could enable a periodic arrangement of skyrmions in a rectangular lattice (not the regular or hexagonal skyrmion lattice) that could be envisaged to devise a periodic pinning potential to trap diamagnetic atoms. We believe that the small scale of the skyrmions as well as their “strong” and localized magnetic field, could make for atomic traps with higher quality factors.

We also want to stress that, in the literature, periodic arrangements of pinning potentials have been studied ad hoc. In those studies, the skyrmion Hall angle is found to change in a step-wise manner and commensurability can be studied. Here we are able to derive a way in which such defects could occur in a more realistic scenario.

Another advantage is that it is easily extendable to consider other types of defects, such as local variations of the uniaxial anisotropy parameter, or other types of two-dimensional extended defects (e.g squared and circular regions).

We conclude that the presented model is a powerful analytic tool for studying the skyrmion dynamics in the presence of extended defects. We believe that avoiding costly micromagnetic simulations can speed up the development of new skyrmionic devices. The analytic insights it brings may help and guide further theoretical modeling of skyrmion-defect interaction, as well as enable faster device prototyping.

Chapter 4

Skyrmion-Superconductor interaction

Up to this point, in this dissertation, Néel skyrmions stabilized in ultrathin infinite ferromagnetic films have been considered from different approximations (rigid model or the LLG equation) and their motion was studied. The study of these topological structures in the FM has already proven fruitful for many possible applications in real devices.[286] But topological structures are not only present in FMs, they can also be found in SCs. The combination of two states of matter with opposite responses to the magnetic field, superconductivity and ferromagnetism, leads to the so-called FM-SC hybrid (FSH) systems. In these hybrid systems, a strong mutual interaction between subsystems has been found to be able to dramatically change the properties of the constituent materials. The different physical phenomena that may arise from FSH systems offer vast opportunities for science and technology.

In this chapter, some examples of possible applications of FSH will be introduced. Afterward, we will present a new model to take into account the mutual interaction between the FSH subelements via stray field. This model will allow us to characterize the interaction between a skyrmion-hosting FM and a SC. The interplay between the stray fields generated by the topological defect in the FM (skyrmion, 2π, etc.) and/or in the SC (superconducting vortices), allows for new potentially interesting behavior and applications. First, quasistatic hysteresis loops of applied field, considering a SC in the Meissner state, will be simulated and it will be shown that, when the SC is ZFC, the FM can transition to a new skyrmionic-like state (the 2π state). Secondly, we will characterize their mutual interaction as a function of the distance between the sub-elements, using the force between them as a figure of merit. For this part, we will consider a SC where a superconducting vortex may be present.

The system discussed in this section is formed by a ferromagnetic and a superconducting coaxial disks. Lastly, the model will be expanded to consider ring geometries.

4.1 A brief topical review

The study of FSHs has been a focus of interest for the past decades.[287–289] There are several branches of research in which FSHs are a fundamental part of them. The interactions may be separated into the two fundamental mechanisms that may drive them: the proximity effect and/or the stray field. When the FM and SC are in contact, the proximity effect (also called exchange interaction) is present. This effect may cause that either the superconducting wave function extends to the FM and the Cooper pairs diffuse into it (partially suppressing the magnetic order in the FM) or that the magnetization penetrates the SC, suppressing superconductivity locally.[287] But even if the FSH elements are not in direct contact with each other, the stray field, generated by the magnetization in the FM or by the currents in the SC, is also able to enable new nontrivial physical phenomena.

The study of these heterostructures has not only been interesting from a purely theoretical point of view but also many practical applications have been found. Some of these applications are: magnetic levitation, manipulation of superconducting properties (vortex dynamics, critical currents, etc.), spin injection and spin valves, Josephson devices, spintronics, and achieving topological superconductivity for topological quantum computing, among others.[135–137, 290–297]

One interesting remark is that these applications and physical phenomenology have a wide range of scales, from the microscopic scale to the macroscopic scales. Depending on the scale of the application and the constituent elements, one may use different approximations to ease the study. In general, the larger the system the less relevant the microscopic details are and some approximations can be done. For example, at large scales, one might use the critical-state model for the currents in a hard (strong vortex pinning) type-II SC with many vortices[298] or use magnetic permeabilities or susceptibilities to characterize the FM or SC elements.[299] As the scale gets smaller, closer to the sizes of superconducting vortices or the magnetization structures in the FM, these approximations no longer hold and the microscopic details need to be taken into account.

Since there is a wide range of potential applications for such devices we think that a brief explanation of some of them might prove useful for the reader. For the sake of simplicity, we will classify them according to the most relevant interaction that gives rise to the studied phenomenology: the proximity effect and the stray field. In general, the proximity effect will only be relevant at microscopic scales whilst the stray field may be relevant across all sizes.

Interaction via proximity effect

In homogeneous systems with coexisting superconductivity and ferromagnetism, the superconducting order oscillates in space due to the presence of the exchange field coming from the FM.[300, 301] This oscillation leads to a series of interesting phenomena:

- The critical-current density in the SC oscillates as a function of the thickness of the FM (t_f) and temperature.
- The critical temperature in the SC oscillates as a function of t_f.
- In SC/FM/SC Josephson junctions when varying t_f one can change the phase of the superconducting currents across the Josephson junction with a phase from 0 to π. Normal Josephson junctions have null phase. If t_f is tuned properly, the sign of the Josephson current can be changed.[291] Recently, it was shown that in the presence of two skyrmions in the FM, the Josephson effect depends strongly on their relative helicity, allowing for a helicity-transition effect for the supercurrent.[292]

Another interesting property of SC is the possibility to host Majorana bound states. Majorana fermions are their own antiparticle.[293] These particles have been proposed for more robust quantum computing technologies in which the information is ‘topologically’ protected, making it more resilient to noise. In solid-state physics, they can be found in p-wave SCs.[302] In order to obtain p-wave SCs it was shown that one can use a combination of SC and semiconductor in nanowires.[303] In the last decade, these Majorana bound states were found in SCs in contact with a FM with a topological texture such as skyrmions.[136, 294, 295]

Another extensive area of research in which such heterostructures have proven useful is spintronics. The emerging field of superconducting spintronics leverages the use of FSH to transport spin currents more efficiently. One way to do so is to use the spin-polarized triplet Cooper pairs to transport spin. Compared with spin-polarized quasiparticle currents, equilibrium spin-polarized triplet supercurrents are dissipationless and phase coherent.[296] For a recent state-of-the-art review see Ref. [304].

The FM-SC interaction through proximity effect may also imprint vortices in the SC. It has been found that if one considers a skyrmion-hosting FM, vortices can be spontaneously created in the SC due to the proximity effect.[135,136] Furthermore, the skyrmions in the FM and vortices in the SC can form bound pairs[137] whose dynamics and stability may be different from their independent constituent parts, making it potentially interesting for spintronics.

Interaction via stray field

The stray field generated by the magnetization distribution in the FM or the superconducting currents in the SC affect each other at all scales. Many approaches have been used to try and harness the effects generated by the stray field when a FM and SC are present. Among them, here we highlight the use of FSH to: engineer new magnetic metamaterials, levitate diamagnetic elements, manipulate some superconducting property, or use emergent physical states for new applications.

Historically since the discovery of superconducting materials, they have been envisioned as the epitome material for power applications (e.g. avoiding energy losses when transporting currents). In real systems though, superconductivity may break due to many factors. For example, above a certain critical value of temperature (T_c) or current density (J_c) superconductivity starts to break down. The superconductivity community has always tried to lessen these challenges by increasing T_c (giving birth to high-temperature SCs) or increasing J_c. It has been found that the stray field from a neighboring FM material can change J_c and its response with the applied field.[305] One effect that appears in FSH systems with ferromagnetic parts in the form of ordered structures such as periodic arrays of magnetic dots, antidots, or even inclusions, is that some peaks or plateaus appear in the applied-field dependence of the critical current and the magnetization curve.[306] Recently it was also found that when inclusions of ferromagnetic nano-rods are present in a SC, the competition between their non-homogeneous stray fields can enable new functionalities such as the pinning of vortices in the SC or 3D magnetic domains in the nano-rods.[305]

Metamaterials are artificial media made from ensembles of multiple unit constituents, usually arranged in repeating (or quasi-repeating) patterns, at scales smaller than the wavelength of the field they address. They differ from conventional materials in that their properties are obtained from the structure of their constituent units rather than from the constituent atoms.[307,308] Because of this property, metamaterials can be engineered to interact and shape fields beyond what is possible with conventional materials.

Magnetic metamaterials have been used to shape magnetic fields.[309–311] In the case of static magnetic fields, the combination of ferromagnetic and diamagnetic materials (such as SCs) is particularly appealing. Their opposite magnetic response makes it possible to obtain effective magnetic permeabilities not found in nature.[312,313] Typically, in those works, neither the FM nor the SC has any internal structure. These elements are considered to a linear, isotropic, and homogeneous permeability, and are not usually simulated by solving the magnetization distribution in the FM or the consideration of vortices in the SC.

Another application that has proven fruitful is magnetic levitation. Levitation is the process by which an object or body is suspended by a force against gravity remaining in a stable position without contact. In magnetic levitation systems, it is difficult to have stability without a feedback loop. In 1842 Earnshaw mathematically proved that stable and *static* levitation is impossible for a body placed in a repulsive or attractive static force which decays with the inverse square of the distance, which unfortunately is the case for the magnetostatic force.[314] Nevertheless, there are some systems in which the Earnshaw theorem can be circumvented using diamagnetic materials.[315] This is because diamagnets *repel* the magnetic field.

Although the levitation of any diamagnetic body is possible (a frog was shown to levitate in Ref. [316]), it is the use of SCs that have proven to be much more useful as their magnetic response is much larger than other diamagnetic materials. Their applications range from large scale, in transportation systems leading to the Maglev train,[290, 317, 318] to the atomistic scale, where a diamagnetic atom can be cooled, below what is possible with optical techniques, for quantum magnetomechanics.[282, 319, 320]

Most of the previously mentioned applications have a considerable distance between elements so that the internal structure of the FM and SC elements can be neglected, simplifying the theoretical treatment. When the distance between elements is smaller, this simplification is no longer valid and new phenomenology appears.

In those cases, the ferromagnetic and superconducting elements are usually separated by an insulating barrier so that the wave function of one material can no longer diffuse into the other. Nonetheless, it has been found that superconducting vortices may also be created due to the stray field generated by magnetization structures in the FM[321–323] and, more recently, topological structures such as skyrmions,[138–140,143] the latter being experimentally demonstrated.[145] The opposite is also possible. It has been shown that, under certain conditions, the magnetic field produced by a Pearl Vortex (PV) in the SC can stabilize skyrmions in a FM with iDM interaction[69] and without it.[141] In Ref. [142] it was experimentally shown that the field from a SC can indeed stabilize skyrmions in FM multilayers with DM interaction.

The presence of structures in the FM (e.g. skyrmions) and the SC (superconducting vortices) has been shown to interact strongly. In some cases, the structures can form bound pairs whose dynamics may be different from those of the isolated elements. Among some of the potential applications one may:

- Use the skyrmion stray field to trap or repel superconducting vortices.[138] If pinning occurs, this in turn may increase the critical-current density that can be passed through the SC and decrease losses due to dissipation during vortex motion.
- The skyrmion Hall angle may be compensated with the Lorentz force of the superconducting vortex.[139] In skyrmion racetrack devices the precise control of skyrmion motion is desirable.

In the works with an insulating barrier presented before, the mutual interaction between FM and SC elements via stray field is usually modeled via a one-way coupling. If the focus of the study is the FM, then the SC is treated as a set of frozen currents that produce a stray field that does not change due to the magnetization distribution.[137,139,141,143] If the focus is on the SC, the same treatment is done on the FM element and the magnetization is not affected by the currents in the SC.[135,144]

Here we develop a model that successfully captures the mutual interaction between the elements with a two-way coupling. For the first time (to the best of our knowledge), we find the static magnetization and superconducting current distributions simultaneously in confined geometries. This enables us to more accurately characterize the skyrmion-superconductor interaction as a function of the applied field or the distance between the elements. In this chapter, the FM will be considered within the micromagnetic model (LLG) and the SC within the London model.

4.2 FSH system modeling: Disk geometries

Consider a superconducting planar and axially symmetric ultrathin disk, with radius R_s and thickness $t_s \ll R_s$, centered at the origin of coordinates on the $z = 0$ plane. Coaxially on top of it, a ferromagnetic planar and axially symmetric ultrathin disk, with radius R_f and thickness $t_f \ll R_f$, is located with its center at $d\hat{\mathbf{z}}$. Consider that this FM is coupled with heavy metal samples that provide iDM interaction, allowing the stabilization of Néel skyrmionic structures such as: skyrmions, 2π states (target skyrmions), or other skyrmionic structures.[55] We show a sketch of the considered system in Fig. 4.1(a) and some examples of the different possible magnetization states are sketched in Fig. 4.1(b).

We model the ultrathin SC with the London model (see Sec. 2.3.1), which is characterized by the screening length Λ[324, 325] and the sheet-current density, $\mathbf{K}(\rho)$ (ρ is the radial coordinate). Because of the system's symmetry, the sheet-current density has only angular component $\mathbf{K}(\rho) = K_\phi(\rho)\hat{\boldsymbol{\phi}}$.

The London model assumes that the generated superconducting current does not modify the modulus of the superconducting order parameter. Therefore, the criterion for applicability of the London approach is that the generated current density should be smaller than a critical sheet-current density K_c. The value for the critical current is known to be $K_\mathrm{c} \propto 2\Phi_0/\mu_0\Lambda\xi_\mathrm{GL}$,[135, 253] where Φ_0 is the quantum fluxoid and ξ_GL is the superconducting coherence length (see Sec. 2.3).

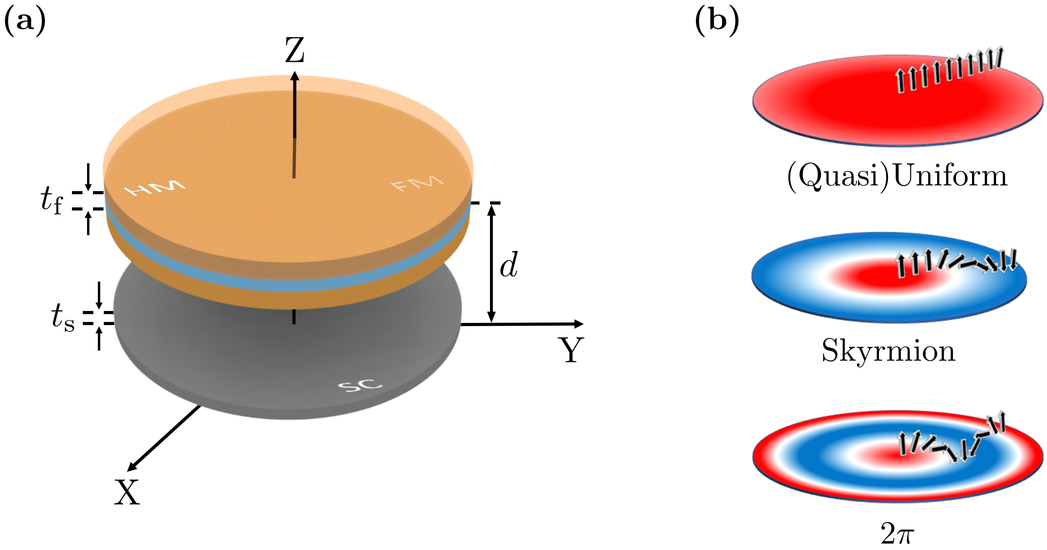

Figure 4.1: (a) Sketch of the studied hybrid systems: A superconducting element (gray) coaxial to a ferromagnetic element (light blue) with iDM interaction due to two different attached heavy metal layers (light orange). Ferromagnetic and superconducting elements are separated by a distance d. Both plates are considered ultrathin. (b) Sketch of some possible stable skyrmionic structures in a ferromagnetic disk.[55] The colors represent the z-component of the magnetization and the arrows the local magnetization along the radius.

Regarding the FM, it is modeled within the micromagnetic model (Sec. 2.2). The magnetization is considered to be uniform in magnitude all over the sample and not varying across its thickness. Due to symmetry considerations $\mathbf{m}$ is cylindrically symmetric ($\mathbf{m} = \mathbf{m}(\rho)$), where $\mathbf{m} = (\sin\theta\cos\varphi, \sin\theta\sin\varphi, \cos\theta)$ is a dimensionless unit vector that determines the local magnetization direction via the polar (θ) and azimuthal (φ) angles. In the systems under study we will consider that the magnetization distribution of the FM is determined by: the local exchange field ($\mathbf{H}_{\mathrm{ex}}$), the iDM field ($\mathbf{H}_{\mathrm{DM}}$), the uniaxial out-of-plane anisotropy field ($\mathbf{H}_{\mathrm{an}}$), the stray field coming from the currents in the SC ($\mathbf{H}_k$), and an applied field ($\mathbf{H}_{\mathrm{a}}$). For the sake of simplicity, we will consider a uniform applied field, $\mathbf{H}_{\mathrm{a}} = H_{\mathrm{a}}\hat{\mathbf{z}}$, that complies with our symmetry considerations.

The demagnetizing field is considered to be renormalized in the uniaxial anisotropy[99,176,196] (see Sec. 2.2.3). To ensure the validity of this approximation for our finite samples, the demagnetizing field of the structures was computed in some cases. We find that its z-component is approximately proportional to m_{z}, justifying the renormalization[a]. This has been studied in more detail in Ref. [179].

4.2.1 Mutual interaction

The mutual interaction between FM and SC elements via stray field is usually modeled with a one-way coupling as was previously pointed out.

In contrast, our model allows us to find the equilibrium magnetization distribution $\mathbf{m}(\rho)$ in the FM and the current distribution $\mathbf{K}(\rho)$ in the SC, *simultaneously* without ‘freezing’ any of them. The hybrid system is simulated considering a two-way coupling between the plates. The magnetization distribution $\mathbf{m}(\rho)$ and superconducting currents $\mathbf{K}(\rho)$ are found by solving the London equation with a superconducting vortex (see Sec. 2.3.1) and the static Brown equation inside the FM (see Sec. 2.2.1),

$$\begin{cases} \dfrac{\Lambda}{2}\mathbf{K} + \mathbf{A} = \mathbf{A}_{\Phi}, & \text{for } z = 0 \text{ and } \rho < R_s, \quad (4.1a) \\ \mathbf{m} \times \mathbf{H}_{\mathrm{eff}} = 0, & \text{for } z = d \text{ and } \rho < R_f\ , \quad (4.1b) \end{cases}$$

where $\mathbf{A}$ is the total magnetic vector potential in the SC, $\mathbf{A}_{\Phi}$ is the magnetic vector potential due to trapped flux in the SC (see Sec. 2.3.1), and $\mathbf{H}_{\mathrm{eff}}$ the total effective field inside the FM. The total magnetic vector potential $\mathbf{A}$ and the total effective field $\mathbf{H}_{\mathrm{eff}}$ have different terms depending on the different interactions that may be present.

Before proceeding, it is convenient to normalize the equations. To do so, we define the normalized effective field, $\mathbf{h}_{\mathrm{eff}} = \mathbf{H}_{\mathrm{eff}}/M_s$, the normalized sheet-current density, $\boldsymbol{\mathcal{K}} = \mathbf{K}/M_s$, and the normalized magnetic vector potential, $\boldsymbol{\mathcal{A}} = \mathbf{A}/\mu_0 M_s l_{\mathrm{ex}}$. The lengths (including Λ, d, R_f, and R_s) are normalized to l_{ex}, without introducing new symbols for better readability.

The normalized London and Brown system of equations that we solve read

$$\begin{cases} \dfrac{\Lambda}{2}\boldsymbol{\mathcal{K}} + \boldsymbol{\mathcal{A}} = \boldsymbol{\mathcal{A}}_{\Phi}, & \text{for } z = 0 \text{ and } \rho < R_s, \quad (4.2a) \\ \mathbf{m} \times \mathbf{h}_{\mathrm{eff}} = 0, & \text{for } z = d \text{ and } \rho < R_f. \quad (4.2b) \end{cases}$$

---

[a] See Appendix C.1 for some examples and details.

In this dissertation we consider that,

$$\begin{aligned} \boldsymbol{\mathcal{A}} &= \boldsymbol{\mathcal{A}}_k + \boldsymbol{\mathcal{A}}_m + \boldsymbol{\mathcal{A}}_\mathrm{a}, && (4.3)\\ \mathbf{h}_\mathrm{eff} &= \mathbf{h}_\mathrm{ex} + \mathbf{h}_\mathrm{DM} + \mathbf{h}_\mathrm{an} + \mathbf{h}_k + \mathbf{h}_\mathrm{a}, && (4.4) \end{aligned}$$

where $\boldsymbol{\mathcal{A}}_k$ is the magnetic vector potential due to the sheet-current density ($\boldsymbol{\mathcal{K}}$), $\boldsymbol{\mathcal{A}}_m$ due to the magnetization in the FM ($\mathbf{m}$), and $\boldsymbol{\mathcal{A}}_\mathrm{a}$ the magnetic vector potential of the applied external field ($\mathbf{h}_\mathrm{a}$). Except for the stray field generated by the currents ($\mathbf{h}_k$), the other effective fields have already been discussed during the previous chapters of this thesis (see Sec. 2.2.3).

Notice that inside $\boldsymbol{\mathcal{A}}$ [Eq. (4.3)] and $\mathbf{h}_\mathrm{eff}$ [Eq. (4.4)] a term coming from the other plate, $\boldsymbol{\mathcal{A}}_m$ and $\mathbf{h}_k$ respectively, coupling the Brown and London models. Starting from the Brown-London Eqs. (4.2) and considering cylindrically symmetric geometries [Fig. 4.1(a)], one can simplify the system to a 1D problem in cylindrical coordinates. In this way, the different terms in Eqs. (4.2) are rewritten in a more convenient way below.

The magnetic vector potential created by the currents produced by a trapped flux in the SC is given by (see Sec. 2.3.1),

$$\boldsymbol{\mathcal{A}}_\Phi(\rho) = \frac{N_f \mathit{\Phi}_0}{2\pi\rho}\hat{\boldsymbol{\phi}}, \tag{4.5}$$

where N_f is the integer number of fluxoids trapped in the SC and $\mathit{\Phi}_0 = \frac{\Phi_0}{\mu_0 M_s l_\mathrm{ex}^2}$. The magnetic vector potential created by the currents at any point can be computed from the Biot-Savart Law, resulting in

$$\boldsymbol{\mathcal{A}}_k(\rho, z) = \hat{\boldsymbol{\phi}}\frac{1}{4\pi}\int_0^{R_s} \mathcal{K}_\phi(\rho')Q(\rho,\rho',z)\rho'\mathrm{d}\rho', \tag{4.6}$$

where

$$Q(\rho,\rho',z) = \int_0^{2\pi} \frac{\cos\phi'}{\sqrt{\rho^2 + z^2 + \rho'^2 - 2\rho\rho'\cos\phi'}}\mathrm{d}\phi'. \tag{4.7}$$

This kernel function can be rewritten in terms of elliptic functions. Either way it has to be numerically evaluated. The magnetic field generated by these currents inside the FM is,

$$\mathbf{h}_k(\rho, d) = (\nabla \times \boldsymbol{\mathcal{A}}_k)\Big|_{(\rho,d)}. \tag{4.8}$$

The magnetic vector potential created by a radially symmetric magnetization distribution, in the ferromagnetic disk, can be evaluated from the Biot-Savart Law. In the SC it reads

$$\begin{aligned}\boldsymbol{\mathcal{A}}_m(\rho,0) &= \frac{t_f}{4\pi}\Bigg[R_f\ m_z(R_f)Q(\rho,R_f,-d)\\ &+ \int_0^{R_f} m_\rho(\rho')\ \frac{\partial Q(\rho,\rho',z)}{\partial z}\bigg|_{z=-d}\rho'\,\mathrm{d}\rho'\\ &- \int_0^{R_f}\frac{\partial m_z(\rho')}{\partial\rho'}Q(\rho,\rho',-d)\,\rho'\,\mathrm{d}\rho'\Bigg]\hat{\boldsymbol{\phi}},\end{aligned} \tag{4.9}$$

whilst the applied magnetic vector potential of a uniform applied field ($\mathbf{h}_\mathrm{a} = h_\mathrm{a}\hat{\mathbf{z}}$) is

$$\boldsymbol{\mathcal{A}}_\mathrm{a} = (1/2)\mathbf{h}_\mathrm{a}\times\mathbf{r} = (1/2)\rho h_\mathrm{a}\hat{\boldsymbol{\phi}}. \tag{4.10}$$

The other fields are (see Sec. 2.2.3):

$$\mathbf{h}_\mathrm{ex} = \nabla^2\mathbf{m} \tag{4.11}$$

$$\mathbf{h}_\mathrm{DM} = \xi\left[(\nabla\cdot\mathbf{m})\hat{\mathbf{z}} - \nabla m_z\right] \tag{4.12}$$

$$\mathbf{h}_\mathrm{an} = \chi m_z\hat{\mathbf{z}}, \tag{4.13}$$

where $\xi = D_\mathrm{DM}l_\mathrm{ex}/A_\mathrm{ex}$ and $\chi = 2K_\mathrm{an}/(\mu_0 M_s^2)$ are the normalized iDM and anisotropy constants, respectively.

Boundary conditions

In order to solve the system of Eqs.(4.2) one must impose the correct boundary conditions (see Sec. 2.2.4). The magnetic vector potential formulation of the London equation does not need boundary conditions to be correctly solved and obtain a unique solution.[255] Therefore the only relevant boundary conditions are those of the FM (Sec. 2.2.4). At the edge of the sample the boundary condition is $\frac{\mathrm{d}\theta}{\mathrm{d}\rho}\big|_{\rho=\mathrm{edge}} = \xi/2$.[55]

In the case of a ferromagnetic ultrathin disk of radius R_f, the boundary conditions used are:

$$\begin{cases}\mathbf{m} = \pm\hat{\mathbf{z}}, & \text{for } \rho\to 0,\\ \dfrac{\mathrm{d}\theta}{\mathrm{d}\rho}\bigg|_{\rho=R_f} = \dfrac{\xi}{2}, & \text{for } \rho = R_f,\end{cases} \tag{4.14}$$

where the innermost magnetic moment is fixed due to symmetry considerations. Since the structure is axisymmetric the central magnetic moment can only have out-of-plane magnetization, as any other component would result in a non-axisymmetric structure that would violate the symmetry of the system. This cannot happen if every interaction in the system conserves the symmetry, as we have shown in Ref. [326][b].

---

[b] Note that solving these equations in a quadrilateral mesh could result in spurious stable solutions that break the symmetry of the system. Such unphysical solutions can be avoided with both meshes we proposed in Ref. [326]

For the numerical simulations that follow we will consider the central magnetic moment to point in $+\hat{\mathbf{z}}$. This limits our solution space to magnetic states with positive polarity. The model, as is, cannot simulate the switching to magnetic states with opposite polarity. In some extreme conditions a Bloch point could numerically be generated [see Fig. 2.5], as the energy barrier to flip the central magnetic moment is infinite due to the model considerations. This would occur, for example, when the FM is in the skyrmion state and a large negative field is applied. One would expect the sample to saturate to the uniform state pointing in the-$\hat{\mathbf{z}}$ direction,[327] something our model does not contemplate.

To avoid this, we propose another way to find the magnetization distribution. Instead of fixing the innermost magnetization moment and thus the magnetic structures' polarity artificially, we use a compatibility condition on the derivative of the central magnetic moment. Note that due to the axisymmetry of the magnetic structure, as one gets closer to the center the magnetization has to smooth out. This is the same reason why usually the central magnetic moment is fixed to be out-of-plane. It is necessary that at the center of the sample $\frac{d\theta}{d\rho}\Big|_{\rho\to 0} = 0$. This allows to model the switching of the core magnetic moment when the derivative at the center becomes abrupt, as one would expect to happen in reality. Furthermore it naturally would be compatible with the inclusion of thermal effects along the line. The proposed boundary conditions are:

$$\begin{cases} \left.\dfrac{d\theta}{d\rho}\right|_{\rho\to 0} = 0, & \text{for } \rho \to 0, \\[2em] \left.\dfrac{\mathrm{d}\theta}{\mathrm{d}\rho}\right|_{\rho=R_f} = \dfrac{\xi}{2}, & \text{for } \rho = R_f. \end{cases} \tag{4.15}$$

Characterization of the magnetization structures

Our model simulates the coupled FSH system and finds the static solutions for the magnetization distribution $[\mathbf{m}(\rho)]$ in the FM and current distribution $(\mathcal{K}_\phi)$ in the SC for a set of internal (Λ, ξ, and χ) and external (distance between plates d and uniform applied field $\mathbf{h}_\mathrm{a}$) parameters.

To characterize the currents in the SC, due to their reversible (linear) nature within the London model, their distribution will be used. In the case of the FM, even though the magnetization distribution $[\mathbf{m}(\rho)]$ may change, the overall topology of the solution itself might not change. As such, we will differentiate between the magnetization distribution, which will change as a function of the applied and/or the stray fields, and the magnetization state, which refers to the topology of the magnetization distribution. Some possible stable states that are found are the (quasi)uniform state, the skyrmion state, and the 2π state[55] [Fig. 4.1(b)]. The (quasi)uniform state is the uniform state with tilted magnetization at the edges due to the iDM interaction [see Eq. 4.14]. For simplicity, we will refer to this state as the uniform state.

To characterize the magnetization states in the FM, two magnitudes will be used: the averaged z-component of the magnetization, $\langle m_z\rangle$ ($\langle m_z\rangle = \frac{1}{\pi R_f^2}\int m_z \rho d\rho d\varphi$), and the skyrmion number, N_sk). Recall (Sec. 2.2.6) that the skyrmion number gives information on the topology of the structure, representing the number of times the magnetic moments wind around a unit sphere.[234, 328] In the ideal case (infinite sample) the skyrmion number will be an integer and it will be a conserved quantity. As such the structure is said to be topologically protected. Ideally one has that the skyrmion number for the uniform state is $N_\mathrm{sk} = 0$, for the skyrmion state is $N_\mathrm{sk} = 1$, and for the 2π state is again $N_\mathrm{sk} = 0$. Therefore, the combination of N_sk and $\langle m_z\rangle$

allows to distinguish between the different magnetization structures. For finite samples though, the skyrmion number is neither an integer nor must be conserved and special care should be taken into account. Consequently, the topological stability of the structures is reduced, the energy to flip the central magnetic moment is finite, contrasting with the infinite ideal magnetic structure [e.g Eqs. (2.33) and (2.34) for an ideal infinite skyrmion]. This will be further discussed in the results below.

From the energy density of each interaction, ε, one can compute the total energy contribution it has as,

$$E = \int_V \varepsilon \mathrm{d}V, \tag{4.16}$$

where the integration is taken over the volume, V, where the interaction is present. For convenience, we define the normalized energy of the interaction as,

$$\mathcal{E} = \frac{E}{\mu_0 M_s^2 l_{\mathrm{ex}}^3}. \tag{4.17}$$

For the system considered in this chapter [sketched in Fig. 4.1(a)], the normalized total energy of the system will be computed. Note that, since we study FM and SC ultrathin films, ε is constant across their thickness (t_f or t_s, respectively). The total energy can be expressed as,[135,138]

$$\mathcal{E}_{\mathrm{tot}} = \mathcal{E}_m + \mathcal{E}_k + \mathcal{E}_{\mathrm{int}}, \tag{4.18}$$

where the first term is the magnetic energy in the FM,

$$\mathcal{E}_m = -2\pi t_f \int_0^{R_f} \left(\mathbf{m} \cdot \nabla^{\mathbf{2}} \mathbf{m} + \chi m_z^2 + \xi \mathbf{m} \cdot \left[(\nabla \mathbf{m})\, \hat{z} - \nabla m_z \right] + \mathbf{m} \cdot \mathbf{h}_{\mathrm{a}} \right) \rho\, \mathrm{d}\rho. \tag{4.19}$$

The second term is the energy of the SC due to the superconducting currents,

$$\mathcal{E}_k = \frac{1}{2} \mu_0 \Lambda \int_0^{R_s} \mathcal{K}_\phi^2 \mathrm{d}S_s + \frac{1}{2} \int_0^{R_s} \mathcal{K}_\phi \mathcal{A}_\phi \mathrm{d}S_s. \tag{4.20}$$

The last term is the interaction energy of the superconducting currents and the magnetization distribution,

$$\mathcal{E}_{\mathrm{int}} = -2\pi t_f \int_0^{R_f} \mathbf{m} \cdot \mathbf{h}_k \, \rho \, d\rho. \tag{4.21}$$

One important remark is that the presence of the SC does not only change the last term in Eq. (4.18), but also changes the magnetization itself. As such it contributes to changing all the terms of the magnetostatic energy of the FM (if compared to the case without a SC present). Therefore, even though the terms have been separated for convenience, they cannot be decoupled completely and the total energy should be taken into consideration.

However, when quasiadiabatic hysteresis loops are considered, $\mathcal{E}_k$ is more sensitive to the applied field than $\mathcal{E}_m$. This is due to the linear response of the SC, which will keep feeding the necessary currents needed to shield the applied field. As a result, $\mathcal{E}_k$ will scale quadratically with the applied field. In contrast, the magnetization at most can saturate the sample leading to a linear $\mathcal{E}_m$ scaling with the applied field (for the saturation fields we may neglect the other energy terms). As the focus of this dissertation is on the magnetization distributions (i.e. skyrmions), only $\mathcal{E}_m$ will be shown. This eases the discussions and readability of the results.

Stability study of the magnetization structures

In order to study the feasibility and applicability of any phenomena found, the stability of the simulation results must be assessed. Since within the London approximation[167, 251, 329] any change in the current distribution ($\mathcal{K}_\phi$) is reversible, there is no energy barrier associated to that change. As such, the stability study will focus on the magnetization states. Nonetheless, the calculated superconducting currents will briefly be presented for completeness.

To assess the stability it is critical to evaluate in some way the transition mechanism between different stable states and the energy barrier associated to it. Our model finds the stable states in a static scenario and therefore we cannot obtain the magnetization distribution along the transitions. However, close to the transition, we may estimate the energy barriers by finding the minimum energy path (MEP) between two stable magnetic structures. To follow a MEP in our system means to rotate magnetic moments in a way as to minimize the energy with respect to all degrees of freedom perpendicular to the transition path. In order to estimate the different MEPs we use the Geodesic Nudged Elastic Band (GNEB) method[156] and compare the two possible transitions mediated by the magnetization boundaries (see Sec. 2.2.7).

As a brief reminder, the GNEB method is a quasi-static method by which we set an initial transition path (discrete set of magnetic moment configurations interpolating between two stable states) that is iteratively optimized by zeroing the transverse component of the gradient force at each point along the path. This ensures the convergence to a first-order saddle point in the phase space, giving the MEP of the transition.

4.2.2 Discretization and algorithm

To numerically solve the system of Eqs. (4.2), for the the axisymmetric 1D case are discretized following the *radial mesh* presented in Ref. [326]. A disk sample with outer radius R, will be divided into $N + 1$ cells of size $\Delta\rho = R/N$. In that way, the radial position of the i-th cell is given by their central position $\rho_i = (i + 1/2)\Delta\rho$ with $i = 0, 1, 2, \ldots, N$. We will use the same $\Delta\rho$ for the FM and the SC.

One important remark is that when discretizing, the kernel function Q [Eq. (4.7)] will become a matrix, whose diagonal terms strictly diverge when $z = 0$. To avoid this discretization problem, these diagonal terms are evaluated from the condition that an infinite disk ideally shields two coils separated by the superconducting disk.[255] A different study, yielding the same limit, can be done by studying the logarithmic divergence when $\rho \simeq \rho'$ and doing a numerical cut-off such that instead of evaluating the fields at the center of the cells, we evaluate one of them at the division between them. In this way we consider that, when $\rho \simeq \rho'$, $\rho - \rho' \simeq \Delta\rho/2$. Using this in the logarithmic divergence, one obtains that the matrix terms are:

$$\begin{cases} Q_{ij} = Q(\rho, \rho', z), & i \neq j \text{ or } z \neq 0, \\ Q_{ii} = \frac{1}{2\pi}\left(\log\frac{16\pi\rho}{\Delta\rho} - 2\right), & z = 0\ . \end{cases} \tag{4.22}$$

After discretizing the system of Eqs. (4.2), the London and Brown equations become a system of linear equations that will be solved with different methods for numerical purposes. The London's system of linear equations

$$\frac{\Lambda}{2}\mathcal{K}_{i,\phi} + \mathcal{A}_{i,\phi} = \mathcal{A}_{i,\Phi}\ , \text{ for } i = 0, 1, 2, \ldots, N \tag{4.23}$$

is solved by using an iterative Gauss-Seidel scheme.[330] For the Brown Eq. (4.2b), a relaxation method based on the LLG equation [Eq. (2.5)] is used. This method consists in solving the pseudo-dynamics of an initially set magnetization distribution (ideally, close to the stable solution) with a numerically high damping constant α such that the system loses energy and relaxes to the static solution.

The advantages of this method are two-fold: it can speed up convergence to the solution while avoiding possible numerical instabilities due to certain symmetries in the effective fields of the system (i.e. ending up stuck near saddle points, obtaining non-physical solutions).[326]

Both systems of equations need to be solved simultaneously since they are coupled. For a given set of external parameters (i.e. distance between plates and applied field h_a), we iteratively solve them until convergence. More precisely, the algorithm can be found in Algorithm 1.

Algorithm 1 Hybrid system relaxation

```
Choose internal parameters ($\Lambda$, $\mathit{\Phi}$, $\xi$, and $\chi$)
Choose numerical damping parameter $\alpha \gtrsim 0.1$ and tolerance $\epsilon$
Choose external parameters (distance between plates $d$ and applied field $h_\mathrm{a}$)
Set to zero stray field from current distribution $\mathbf{h}_k = 0$
Initialize FM with ansatz solution $\mathbf{m}(\rho)$ (ideally close to the desired one)
Solve Brown equation [Eq. (4.2b)] with LLG-based relaxation method (see Sec. 2.2.2)
while Energy variation $\geq \epsilon$ do
    Compute $\boldsymbol{\mathcal{A}}_m$ [Eq. (4.9)]
    Solve London equation [Eq. (4.2a)] with Gauss-Seidel
    Compute $\mathbf{h}_k$ [Eq. (4.8)]
    Solve Brown equation [Eq. (4.2b)] with LLG-based relaxation method.
    Compute energy variation of the current iteration
end while
```

This approach allows to characterize their mutual interaction for a given distance between elements and uniform applied field ($\mathbf{h}_\mathrm{a}$). If one wants to obtain the mutual interaction as a function of any external parameter it can be done simply by looping over the external parameter values in Algorithm 1. If one wants the presence of trapped flux in the SC it can be done with the Φ parameter, which is an integer multiple of Φ_0 [Eq. (4.5)], for the cases considered.

Once the stable magnetization and current distributions are found, the GNEB method can be used to study the stability of the structures. As discussed before, the phase space needed to be explored to find the transition mechanism is too large to feasibly obtain any solution in reasonable computation times. Therefore even though the field from the superconducting currents may affect the magnetization transitions, we will consider them as an external source of field that does not change along the magnetization state transition. In other words, for the stability study, the superconducting currents are assumed to produce a similar stray field in the FM for every possible stable magnetization distribution. This approximation will *only* be used for the stability study of the found structures. The GNEB algorithm is introduced in Sec. 2.2.7. The algorithm to compute the transition is introduced in Algorithm 2.

Algorithm 2 Magnetization state stability with GNEB method

```
Set internal parameters ($\Lambda$, $\mathit{\Phi}$, $\xi$, and $\chi$)
Set force tolerance $\epsilon$ over spins or magnetic moments of each iteration[156]
Set external parameters (distance between plates $d$ and applied field $h_\mathrm{a}$)
Obtain initial magnetization distribution before the transition [$\mathbf{m}_A(\rho)$] with Algorithm 1
Obtain final magnetization state after the transition [$\mathbf{m}_B(\rho)$] with Algorithm 1
Obtain currents by solving London's equation [Eq. (4.2a)]. Assume constant $\boldsymbol{\mathcal{A}}_m$ given by
  initial magnetization state and applied field. Currents will remain constant
Compute stray field from current distribution $\mathbf{h}_k$
GNEB algorithm [see Sec. 2.2.7] to obtain the initial to final state transition.
```

4.3 Numerical results

A huge plethora of Néel skyrmion-hosting materials can be found in the literature.[23, 40, 46, 118, 145, 331–334] In general, different phenomenology might occur depending on the magnetic constants, the ratio between radii R_s/R_f, and the screening length Λ. As the interaction is mediated by the stray fields, the shape and strength of the superconducting currents vary depending on the geometry and Λ in the SC, whilst the magnetization distribution response will be given by the magnetic constants. To simplify the study we will use the parameters found experimentally in Ref. [334]: $A_{\text{ex}} = 15$ pJ/m, $D_{\text{DM}} = 2.8$ mJ/m^2, $K_{\text{an}} = 70$ KJ/m^3, $M_s = 0.65$ MA/m. For the SC we have used the London penetration depth $\lambda_L = 16$ nm of aluminum.[335]

To study the system presented in Fig. 4.1(a), we first will evaluate a quasiadiabatic hysteresis loop of applied field, with a fixed distance between plates, d, and a ZFC SC. Then, a study of the response to the distance between plates will be done, without applied field ($h_{\text{a}} = 0$) and a ZFC SC. Note that in both of these studies the SC considered is ZFC. Therefore, when the SC is cooled down and transitions to the superconducting state, no magnetic flux gets trapped [$\boldsymbol{\mathcal{A}}_\Phi = 0$ in Eq. (4.2a)].

Once this is done, the previous studies will be repeated with a FC SC. Some studies hint that in FSH systems, some pinning phenomena may appear between the skyrmionic structures in the FM and the SC.[137, 139] The London currents will be modified since now $\boldsymbol{\mathcal{A}}_\Phi \neq 0$ in Eq. (4.2a) as flux has been trapped when transitioning to the superconducting state. The flux penetrates in the form of PVs,[324, 325] which carry an integer multiple, N_f, of flux quantum, Φ_0. If only a single vortex penetrates, it will be found at the center of the SC disk. Note that the flux is a conserved quantity given by Eq. (4.5).

In each of these studies, the procedure will be the same. First, the stable magnetization distributions in the FM for a given distance between plates d and uniform applied field h_{a} will be found. To find the different possible stable states Alg. 1 will be initialized with different ansatzes close to the target magnetization distributions [sketched in Fig. 4.1(b)]. To see the effect of the SC on the FM, the system without any SC in the vicinity is also simulated and compared.

4.3.1 On the response to a uniform applied field

In this section, we will focus our attention on the magnetic field response of the FSH. Due to the large number of possible parameters, we study a specific case in which a set of interesting results appear when the elements are relatively close to each other. In particular, we consider the following non-normalized values: $t_f = 1$ nm, $R_f = 70$ nm, $t_s \simeq 21$ nm, $R_s = 3R_f = 210$ nm, $\Lambda = 24$ nm, and the distance between elements $d = 20$ nm (see Fig. 4.1 for a sketch). This distance is set so that experimentally one could fit a sufficiently thick insulator (4-5 nm) between the FM multilayer and the SC disk such that the proximity effects are avoided. The FM and the SC will be discretized with a fixed $\Delta\rho = R_s/200l_{\text{ex}} \simeq 0.14$ from now on, unless otherwise stated.

Possible magnetic states for a given applied field

The possible states found for both the single FM and the FSH system are shown in Fig. 4.2. The magnetization state of the FM is characterized by the averaged z-component of the magnetization when a linear[c] ZFC SC is present [Fig. 4.2(a)] or not [Fig. 4.2(d)]. Depending on the applied field, up to three different stable states are found. The red, green, and blue lines correspond to the uniform, skyrmion, and 2π state, respectively. These structures are sketched beside their corresponding curve. Note that these are *all* the stable states found in this system and not all of them may be accessible during, for example, a hysteresis loop.

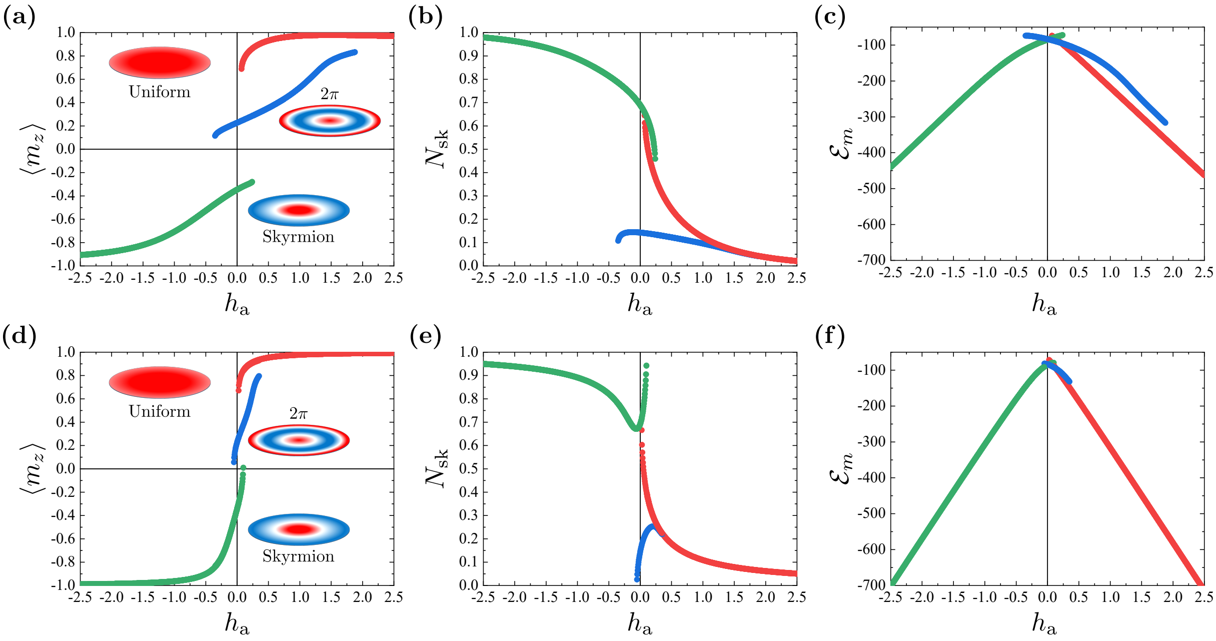

Figure 4.2: (Left) Normalized averaged z-component of the normalized magnetization, (center) skyrmion number, and (right) normalized ferromagnetic energy, of all the stable magnetic states for different applied fields, in the presence [(a-c)] or absence [(d-f)] of a SC. The stable states found are the uniform (red), skyrmion (green), and 2π (blue) states. A sketch of the magnetization distribution is shown in the magnetization (left) panels.

When the SC is present, it can be seen that for large positive applied magnetic fields ($h_\mathrm{a} \gtrsim 2.5$), the ferromagnetic sample saturates to the uniform state [sketched in Fig. 4.1(b)] where the whole magnetization distribution mostly points in the $\hat{\mathbf{z}}$ direction except near the edges, as should be expected. On the opposite side of the field range, for large negative applied fields ($h_\mathrm{a} \lesssim 1.5$) the skyrmion state is found to be stable with $\langle m_z \rangle \simeq -1$. This is an artifact of the model. As the central magnetic moment of the FM is forced to point in the $+\hat{\mathbf{z}}$ direction, it cannot be flipped and therefore the sample is not allowed to saturate completely into the uniform state pointing in $-\hat{\mathbf{z}}$. For intermediate fields, there is a range of fields where several structures are found to be stable. When there is no SC, it can be seen that the range of fields at which the 2π state is stable is severely diminished. This can be explained by the fact that the SC shields the applied field. As the 2π state winds up the most, it competes the most with the z-component of the applied field. Therefore, if a part of the field is shielded, the structure can be stabilized for a wider range of applied fields. The shape of the field on the FM when a SC is present is sketched in Fig. 4.3(a). The shielding currents in the SC can notably modify the field acting over the FM.

---

[c] Recall that the SC is linear within the London model.

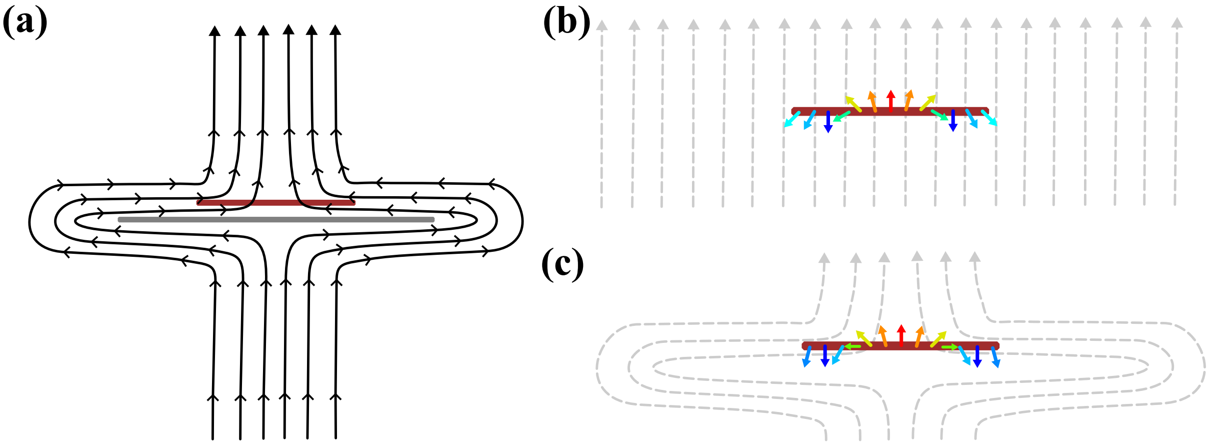

Figure 4.3: (Left) Sketch of the distorted applied field lines (black) due to the presence of a SC element (dark gray). A FM (brown) is placed on top of the SC as in Fig. 4.1 and will be perturbed due to the external field lines. (Right) Sketch of the magnetization distribution of the FM in the skyrmion state as a function of the applied field when a SC is present or not [(c) and (b) respectively]. As can be seen when a SC is present the outermost moments are tilted inwards as compared to when there is no SC. The colored arrows represent the z-component of the magnetization (red-green-blue from $m_z = 1$ to -1). The field lines are depicted in light gray.

To further characterize the stable structures, we also evaluate the skyrmion number with and without SC [Figs. 4.2(b) and 4.2(e), respectively]. For finite samples, the skyrmion number is neither an integer nor must be conserved. This can be seen in our results [Figs. 4.2(b) and 4.2(e)] where the skyrmion number of the uniform state varies from almost $N_{sk} \simeq 0$ (at large applied fields) to up to $N_{\mathrm{sk}} = 0.7$ (near its destabilizing field). In contrast for the 2π state, when stable, it ranges from $N_{sk} \in (0, 0.15)$. If one compares the behavior of the skyrmion number as a function of the applied field with [Fig. 4.2(b)] and without [Fig. 4.2(e)] SC, it can be seen that it is different, with the largest difference for the skyrmion state. We attribute this behavior to the radial component of the field (which points inwards) generated by the superconducting currents, which bends the magnetization inwards near the edges, where it is largest [see Fig. 4.3(b-c)]. This makes it so that when near the destabilizing point, the magnetization tends to wind up more (tilted inwards) instead of unwinding. This effect is largest when the magnetic state is less stable. Further discussion will be done when studying the quasistatic hysteresis loops.

In order to ensure that the previous model findings are not due to the model forcing the innermost magnetic moment to point to $+\hat{z}$, the calculations with and without the SC will be repeated but allowing the system to flip the central magnetic moment. To do so we use the boundary conditions presented in Eqs. (4.15). A relevant remark is that within the continuum approximation, the energy barriers to flip the core of the magnetization state will depend on the discretization used ($\Delta\rho$). As the continuum model considers that within an l_{ex} the magnetization can be regarded as uniform, we decided to set $\Delta\rho = 0.5$ to simulate the system. A drawback is that this boundary condition is valid as long as $\Delta\rho \to 0$, as was discussed when the boundary condition was presented. As such, the model may predict unstable states by breaking the symmetry due to the discretized nature of the simulated system.

For this second model, the system is allowed to transit to six states. The new states correspond to the previously found stable states but with negative polarity (e.g. a "negative skyrmion"). This is true for both when a SC is [Fig. 4.4(b)] or not [Fig. 4.4(d)] present in the system. If compared to fixing the magnetization value at the core [Figs. 4.4(a) and (c)], the most notable change is that the skyrmion is no longer stable for any applied negative field h_a but it transits to the negative uniform state. When a SC is present this happens at $h_\mathrm{a} \simeq -2.5$ whilst when there is no SC, this transition appears before at $h_\mathrm{a} \simeq -0.32$. Another interesting result appears when comparing the behavior of the 2π state. The field range where the 2π state is stable is reduced significantly. As the core magnetization size is reduced with a positive applied field, the transition to the negative skyrmion state is no longer prohibited.

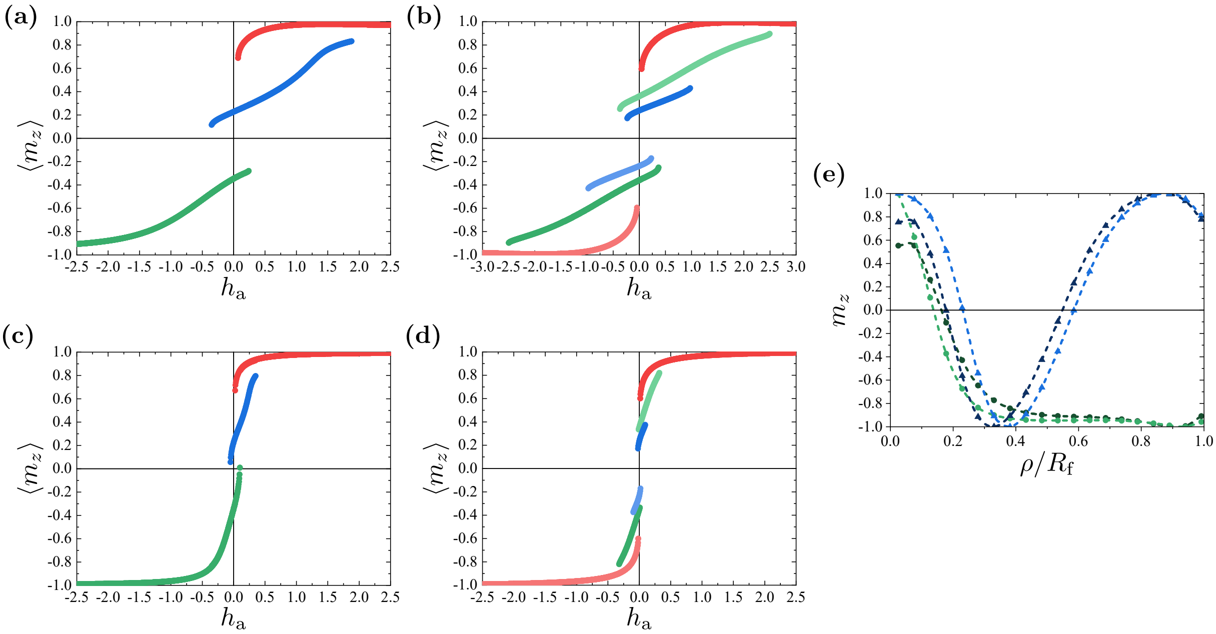

Figure 4.4: Normalized averaged z-component of the normalized magnetization of all the stable magnetic states, for different applied fields, in the presence (a,b) or absence (c,d) of a SC. The stable states are fixing the central magnetic moment $m_z = \hat{\boldsymbol{z}}$ or the central derivative to zero, for the left (a,c) and right (b,d) plots respectively. For the left plots, the stable states found are the uniform (red), skyrmion (green), and 2π (blue) states with both polarities. The negative polarities are denoted with lighter colors. In (e) some magnetization distributions are plotted after fixing the central moment (lighter colors) or fixing the central derivative (darker colors). The skyrmion state (green dots) and the 2π state (blue triangles) are found at $h_\mathrm{a} = -2.5$ and $h_\mathrm{a} = 0.975$, respectively. These fields correspond to the destabilizing field of the structures when fixing the derivative. The dashed lines are plotted for clarity.

This leads to the downside of the model: since $\rho = 0$ is not a part of the discretization, by fixing the derivative as the BC [Eqs. (4.15)] it is possible to find magnetic structures whose innermost magnetic moment ($\rho = \Delta\rho/2$) does not point in $\pm\hat{\boldsymbol{z}}$. To illustrate these phenomena we show in Fig. 4.4(e) some extreme cases found for the skyrmion and the 2π states. We compare them to the findings fixing the inner magnetic moment [same as in Fig. 4.2(a)]. The applied field chosen is the one found to be the last stable applied field for the structures when considering fixing the derivative and the selected cases are when a SC is present. Similar behavior is found when the SC is not present. It is clear that near the destabilizing fields, not fixing the central derivative may break the symmetry of the system, resulting in unphysical results [Fig. 4.4(e)]. That is why we have chosen to study the system by fixing the central magnetic moment as is usually done in the literature. For us, the results of the second model *only* give a range of validity for the findings of the first model and confirm that the findings are not due to the model itself.

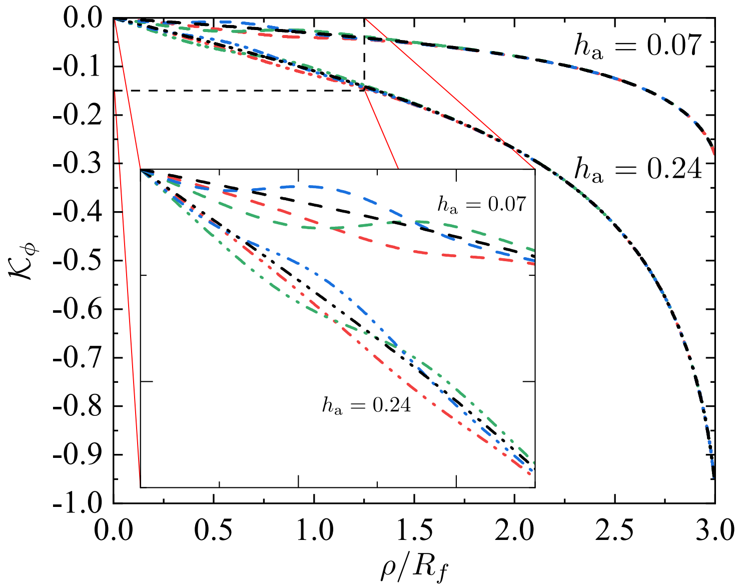

Figure 4.5: Normalized current distribution for two different applied fields when the superconducting currents are not affected by the FM (black) or are affected by a uniform (red), skyrmion (green), or 2π (blue) states. For $\rho \lesssim R_f$ the currents vary significantly. The inset shows a zoom of the marked region of the main plot ($\rho \lesssim 1.25R_f$).

Regarding the SC, the superconducting currents may also be affected by the magnetization distribution. It should be expected that the currents' change due to the magnetization in the FM depends on the intensity of the FM's stray field at the SC. For all the cases studied, the magnetic field generated by the magnetization is smaller, as long as $h_a > 0.05$. Recall that we are quite far away from the field sources as we are dealing with a "realistic" system.The details of the current distribution may be of crucial importance close to the destabilizing fields. To capture this, we show the current distributions for two applied fields (Fig. 4.5). For $\rho \lesssim R_f$, there is a slight variation in the current distribution for all the magnetic states. This variation is on the order of the strength stray field generated by the magnetic structures ($\simeq \pm 0.05$). More interestingly, depending on the magnetization distribution the current distribution also changes in shape accordingly as the stray field is different. This change in the current distribution is more relevant as the interaction between elements is stronger. Thus, it is possible that the effects of the mutual interaction could be critical to accurately characterize the energy landscape and, specially, the stability of such hybrid systems.

Stability analysis of the solutions

Once we have found the possible stable solutions as a function of the applied field, it is desirable to know the dynamics and stability of the magnetization states. As discussed above, our model solves the Brown Eq. (4.2b) for the FM (static limit). Hence, it cannot retrieve the dynamics of the transitions. However if one were to quasiadiabatically follow the curves found in Fig. 4.2 (slow and smooth variation of the applied field) the transitions, for low temperatures, should be expected close to the critical fields that make the structures unstable. To study the possible transitions in the system we will use the GNEB method (Sec. 2.2.7). At this point, we must remark that considering both the magnetization and the currents have too many degrees of freedom. Therefore, the computational time to find the MEP becomes unfeasible, even using the GNEB. Thus, to find an estimate for these transitions we consider the superconducting currents as fixed restricting our study to the magnetization states. The GNEB method is usually done at the atomistic level. We have adapted the GNEB method to work within the micromagnetic model by using the micromagnetic effective fields [Eq. 4.4] instead of the atomistic ones.

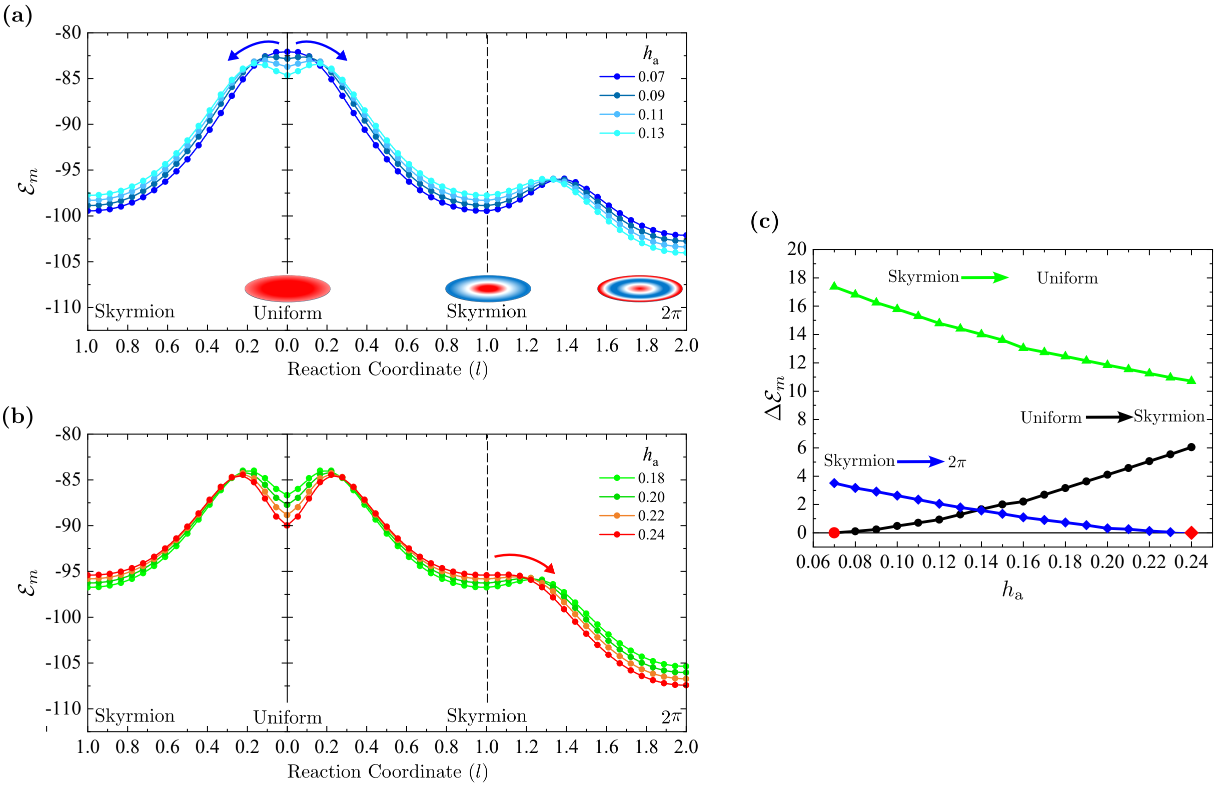

Figure 4.6: MEP calculated using GNEB showing the energy for the transitions occurring near the destabilization field of uniform (a) and skyrmion (b) states, in the presence of a SC. The dots indicate the images computed along the converged path. The arrows indicate the most probable transition found. (c) Normalized energy barrier as a function of the applied field studying the uniform and skyrmion destabilization. The destabilizing fields at which the structures become unstable are highlighted in red.

In Figs. 4.6(a) and 4.6(b) we show the MEP between all stable magnetic states found using the GNEB algorithm near the destabilizing field from the uniform and skyrmion state, respectively, when a SC is present. The destabilizing field found for the uniform state is $h_{\rm a} \simeq 0.07$ and for the skyrmion state is $h_{\rm a} \simeq 0.24$ [see Figs. 4.2(a-c)]. Note that only within this field range, the three magnetic states coexist. Using the GNEB method we compute the MEP and obtain the transition path from each of the stable states to the rest. For simplicity only the MEP is plotted, without the details on the transition mechanism. The horizontal axis is the normalized length of the geodesic path along the reaction coordinate (l) that connects the MEP between those two states. Since the transition from the uniform state to the 2π state was found to go through an intermediate skyrmion state, we arbitrarily normalized the path length such that starting from the uniform state to the skyrmion state is $l = 1$ and to the 2π state is $l = 2$. To remark that there are two different transitions from the uniform state we explicitly plot the uniform to skyrmion transition to the left of the plot and from the uniform or skyrmion state to the 2π state on the right of the plot.

In confined thin-film FMs there are two main transition mechanisms: collapse and escape through the boundary.[156,336] Typically, the energy barrier of the boundary-mediated skyrmion annihilation is lower than that of the destruction by direct collapse.[41,148,337] Our model can only predict the annihilation through the boundaries in the continuum limit.

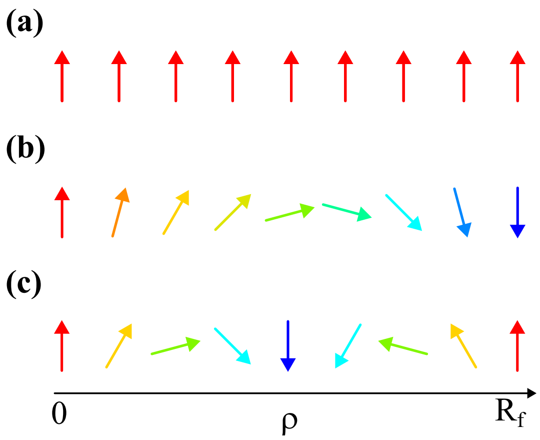

Figure 4.7: Sketch of the different magnetization distributions as a function of ρ for the (a) uniform , (b) skyrmion , and (c) 2π states. The colors represent the z-component of the magnetization.

It is found that, when the field is approaching the destabilizing field ($h_a \simeq 0.07$), the energy minimum corresponding to the uniform state is becoming shallower up to disappearance. This is expected as the structure is not found to be stable for smaller applied fields. At that moment, it is clear from Fig. 4.6(a) that the most probable state, the one with the lowest energy barrier, is the skyrmion state. Actually, in that case, the transition to the 2π state must go through an intermediate skyrmion state due to the symmetry of the system (Fig. 4.7). As we can only transition through the boundaries, when the magnetization is winded up one gets the skyrmion state. To obtain the 2π state one must further wind the magnetization structure. Thus, when the uniform state becomes unstable, the system would evolve to the skyrmion state.

Once in the skyrmion state and increasing the applied field, this state can also be destabilized for $h_a \simeq 0.24$ [see Figs. 4.2(a-c)]. For this case, in Fig. 4.6(b) we show the GNEB results for the MEP for the different possible transitions among all stable magnetic states. In this case, again, when approaching the destabilizing field ($h_a \simeq 0.24$), the minimum corresponding to the skyrmion state tends to disappear and, when this happens, it is clear that the most probable transition is to the 2π state [Fig. 4.6(b)]. In this case, the energy barrier for this transition is smaller than the energy barrier for the skyrmion-to-uniform one. Note that in this model we fixed the central magnetization direction to $\hat{\mathbf{z}}$ and hence the skyrmion remains stable for arbitrarily large negative fields. Nonetheless, the results presented in Fig. 4.4 and the comment below hold for this discussion. Below $h_a \lesssim -2.5$, an additional transition to the uniform state pointing to $-\hat{\mathbf{z}}$ would be found. As such, by restricting ourselves to the field range of Fig. 4.6, we can avoid complicating more the discussion. The findings and energy barriers for the stable solutions with negative polarity are symmetric to the ones obtained for positive polarity.

To more clearly show the energy barriers of all the transitions, we have plotted them in Fig. 4.6(c), for the applied field range $h_a \in [0.07, 0.24]$. It can be seen that, depending on the applied field, the energy barrier is lowest for the uniform to skyrmion transition ($h_a \in [0.06, 0.13]$) or the skyrmion to 2π transition ($h_a \in (0.13, 0.24]$). The most remarkable result is that the transition from the skyrmion to the uniform state is *always* the highest among all of them. Therefore, the probability of this transition will be smaller than the rest. This probability can be estimated from the Arrhenius Law[41, 337] (see Sec. 2.2.7).

For comparison, the same GNEB study was repeated for the case when there is no SC present in the system. In Fig. 4.8(a) the energy along the reaction coordinate of the MEP is shown in the range of applied fields at which the uniform, the skyrmion, and the 2π states were found to be stable [see Figs. 4.2(d-f)]. We found that even though the 2π state might be stable, the transition to that state is less probable than its alternative near the skyrmion annihilation field. The energy barrier to transition to the 2π state is always bigger than the energy barrier of another transition, as is explicitly plotted in Fig. 4.8(b). The uniform-to-skyrmion transition is found to be the most prominent as it has the lowest energy barrier for small applied fields

($h_a \lesssim 0.065$), while for higher applied fields it is the skyrmion-to-uniform transition that will be the most probable. Therefore, without the SC, the 2π state would not be reached. Note that our model does not take into account temperature. The transition to the 2π state might be thermally activated in some cases, but it will always be less probable than in the case where a SC is present [Figs. 4.6(a) and 4.8(a)].

Hence, the addition of a SC element significantly changes the energy landscape and possible transitions of the FM: an additional transition to the 2π state appears.

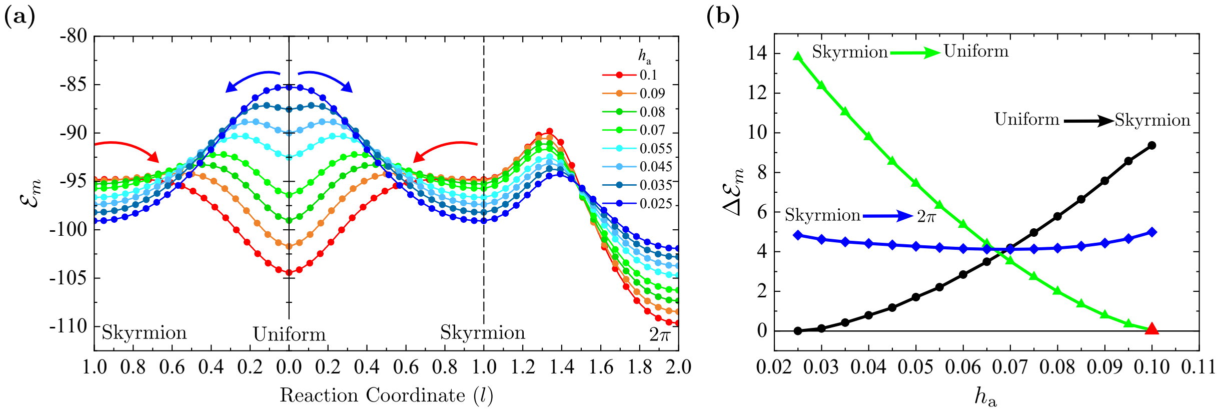

Figure 4.8: (a) MEP calculated using GNEB showing the activation energy for the transitions, when there is no SC present, occurring at applied fields where the three states are stable ($0.025 < h_a < 0.1$). The dots indicate the images computed along the converged path. The arrows indicate the most probable transition found for that applied field. (b) Energy barrier as a function of the applied field studying the uniform and skyrmion destabilization. The destabilizing fields at which the studied structures become unstable are highlighted in red.

There are several considerations at this point. First, due to the symmetry of our system, since there can not be a transition through the angular component of the magnetization, the transition from the uniform to the 2π state the magnetization must occur through an intermediate skyrmion state. Second, the energy barriers found using our implementation of the GNEB algorithm are evaluated within the micromagnetic approach. Hence, the effective field used to optimize the MEP is in the continuum approximation. As such, it does not take into account Bloch point formation. However, in previous works[41,148] it was found that, for finite samples (i. e. racetracks), the transition takes place through the boundaries of the FM and is not mediated by the formation/annihilation of a Bloch point in most cases. This justifies that our calculations give a good estimate of the stability and provides valid information on the most probable transition.

Quasistatic hysteresis loops

Up to this point, we have found the possible stable magnetic states as a function of the applied field (Fig. 4.2). Afterwards, the stability of the different magnetization distributions found to be stable near the transition fields was presented (Figs. 4.6 and 4.8). It is found that the inclusion of a SC element favors the transition from the skyrmion to the 2π state which may not be found without the SC (in the low-temperature limit). As such, it hints at the possibility that a quasiadiabatic hysteresis loop with and without the SC may be different, allowing an additional transition not possible without the SC.

In order to assess this statement, we have done quasiadiabatic hysteresis loops by solving the Brown equation starting from a uniform state and following the loop as a function of the applied field when there is a SC element present in the system. To prepare the system, we prepare each element isolated from each other (i.e. infinite distance between them). The SC is ZFC and the FM is saturated to the uniform state with a large positive field so that the uniform state remains stable even when the SC is close to it. Then, the elements are slowly brought together up to the distance d. After this we decrease the field quasiadiabatically, in steps of $h_\mathrm{a} = 0.005$, and simulate two hysteresis loops:

(a) An outer loop in the range $h_\mathrm{a} = \pm 2.5$. We expect that starting from the uniform state, a transition to the skyrmion state will be found near zero applied field [Fig. 4.6(a)]. This state will be stable for the negative field range and is expected to transition to the 2π state at slightly positive applied fields at the returning part of the loop [Fig. 4.6(b)]. Then we keep increasing the applied field until the FM sample saturated to the uniform state [Fig. 4.2 (a-c)].

(b) An inner loop in the range of $h_\mathrm{a} = \pm 1$. Starting from the uniform state the behavior is expected to be similar to the previous one, except that the field is reversed before the saturation to the uniform state. As such it is expected that the FM stays in the 2π state and transitions to the skyrmion state for negative applied fields [Fig. 4.2(a-c)].

The simulations are presented in Fig. 4.9. For the outer loop [Fig. 4.9(a)], it is found that after reducing the applied field to slightly positive fields ($h_\mathrm{a} \simeq 0.07$), the uniform state destabilizes and a transition to the skyrmion state is found, as predicted with the GNEB algorithm [Fig. 4.6(a)]. Once in the skyrmion state, the model can only compute its destabilization for positive fields as the central magnetic moment is fixed by the model and cannot be flipped. As such when decreasing the field to $h_\mathrm{a} = -2.5$ and increasing it back to $h_\mathrm{a} = 1$, the skyrmion state remains stable and no transition is found. As the field is further increased, a transition is found at $h_\mathrm{a} \simeq 0.24$, where the skyrmion state transits to the 2π state as was previously predicted [Fig. 4.6(b)]. In the 2π state, we continue increasing the field until the FM sample transits again to the uniform state, at $h_\mathrm{a} \simeq 1.88$. For the inner loop [Fig. 4.9(b)] the hysteresis loop is similar except that prior to the transition to the uniform state ($h_\mathrm{a} \simeq 1.88$), we decrease the field while still remaining in the 2π state. The 2π state remains stable as we decrease the field until it destabilizes and transitions to the only remaining stable state, the skyrmion, at $h_\mathrm{a} \simeq -0.35$ [Fig. 4.2(a)]. Therefore two different loops depending on the field range can be found.

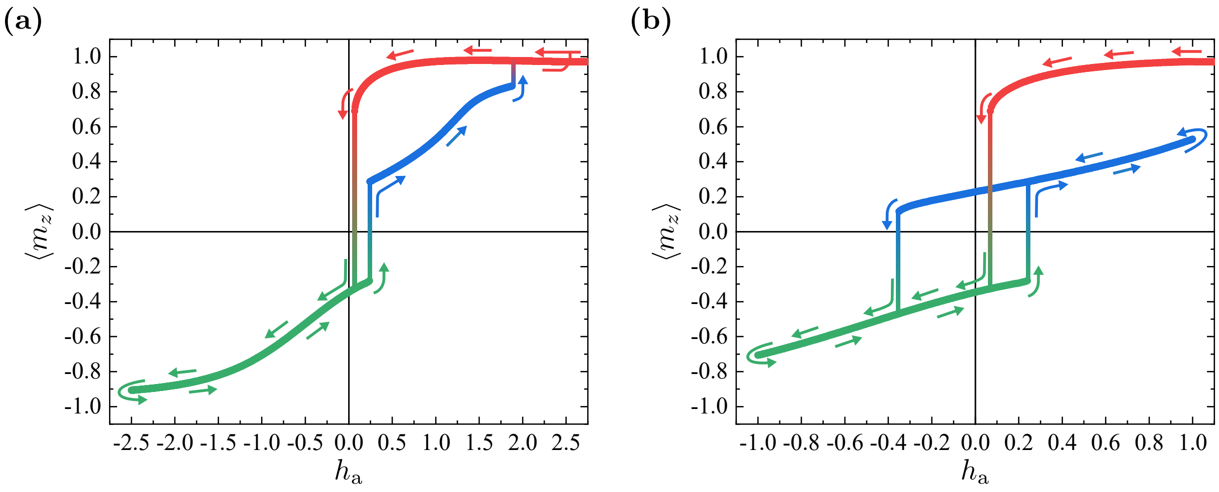

Figure 4.9: Averaged z-component of the normalized magnetization during the hysteresis loop. (a) Outer hysteresis loop with field ranging from ± 2.5. (b) Inner hysteresis loop with field ranging from ± 1. The vertical lines are in gradient colors to indicate transitions between magnetization states: red for the uniform, green for the skyrmion, and blue for the 2π state.

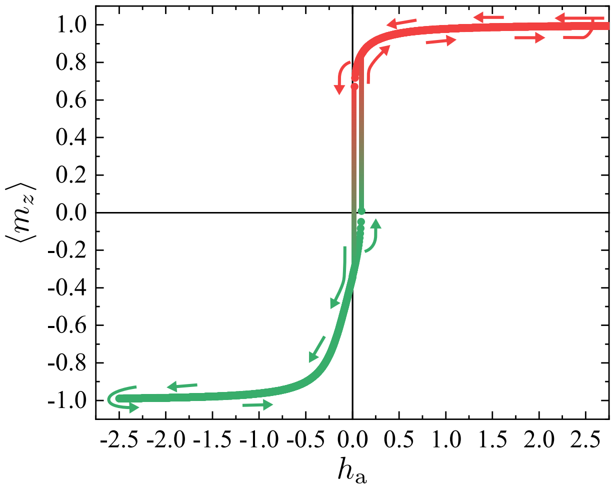

Figure 4.10: Averaged z-component of the normalized magnetization during the hysteresis loop without a SC. Hysteresis loop with field ranging from ± 2.5. The vertical lines are in gradient colors to indicate transitions between magnetization states: red for the uniform and green for the skyrmion.

If there is no SC, the hysteresis loop changes as the transition to the 2π state is not found (Fig. 4.10). In this case, starting from the uniform state we decrease the field until the state becomes unstable and the FM transits to the skyrmion state at $h_\mathrm{a} \simeq 0.02$. There are no further transitions as we keep decreasing the field, similarly to when a SC was present. As the field is increased again, a transition to the uniform state is found at $h_\mathrm{a} \simeq 0.1$. Both transition applied fields match those at which the state became unstable in the static limit [Fig. 4.2(d)].

We attribute the disappearance of the skyrmion-to-2π transition to the fact that the energy barrier near the destabilizing fields to transition from any state to the 2π state is never the smallest one, as predicted with the GNEB algorithm (Fig. 4.8). As such, in the low-temperature limit, the transition to the 2π state is forbidden. But even if one considers temperature, the transition to the 2π state would not be the most favored transition as there is always another transition with a smaller energy barrier [Fig. 4.8(b)]. This clearly contrasts with the case with a SC, where for certain applied fields, the transition to the 2π state is favored over the other possible transitions [Fig. 4.6(c)].

Our explanation for this behavior is that the shielding currents in the SC partially shield the applied field whilst adding a radial field. The radial component of the field tends to tilt the magnetization structure inwards at the edge, favoring the wind-up of the structure [Fig. 4.3(c)]. This is shown in Fig. 4.11(a), where as the applied field increases, the magnetization distribution winds up more. In contrast, when there is no SC present [Fig. 4.11(b)], the magnetization distribution unwinds and the skyrmion transits to the uniform state at $h_\mathrm{a} \simeq 0.01$.

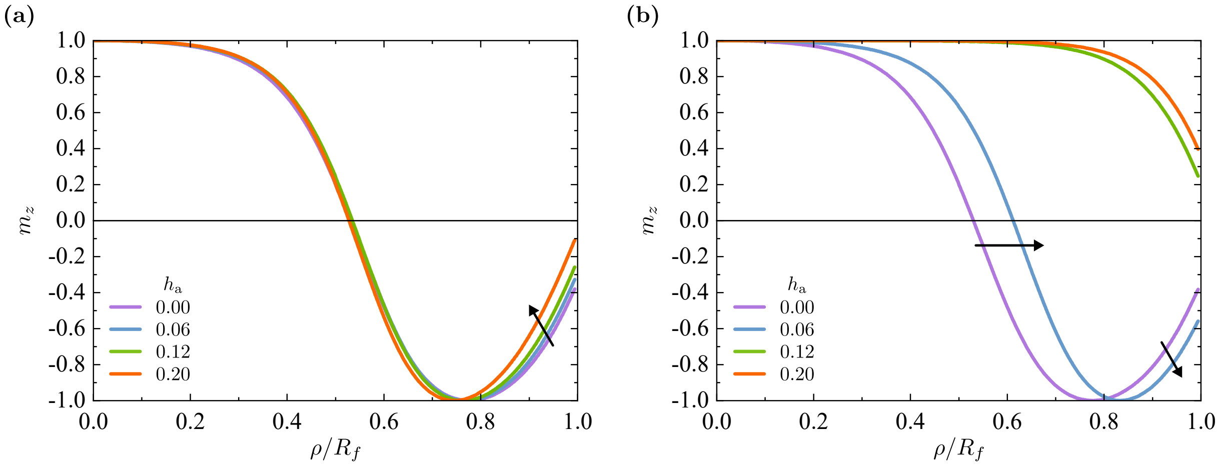

Figure 4.11: Magnetization distributions, starting in the skyrmion state, for different applied fields (a) with a SC present in the system and (b) without it. The applied fields shown are $h_a = 0$ (purple), $h_a = 0.06$ (blue), $h_a = 0.12$ (green), and $h_a = 0.2$ (orange). These were chosen near the skyrmion-to-uniform transition when there is no SC. When a SC is present, the magnetization tends to wind up more. Without a SC, the magnetization unwinds and transitions to the uniform state.

4.3.2 On the response with plates' separation

Once the response of the system to the applied field at a fixed distance is known, it still remains to study its behavior as a function of the separation between the FM and the SC. The magnetic state and the SC will be prepared isolated and then we will get them closer together. It is known that the stray field of the skyrmionic structure is not the same above or below it.[144] Therefore, to fully characterize the interaction we will consider that the FM can be below or on top of the SC. The resulting systems are sketched in Fig. 4.12, where each of these cases is separated by the horizontal dashed line. The coordinate system is considered to be centered at the SC. First, a study with the SC in the Meissner state will be done. Then, we will consider the possibility of having trapped flux inside the SC, in the form of a Pearl vortex (PV).

The magnetic structure in the FM will be characterized as in the previous section (Sec. 4.3.1). As was shown, the transitions are mediated through the boundaries of the sample. To simplify the discussion, the stability analysis will not be presented as a wide range of phenomena is found.

The interaction force can be obtained as follows. The necessary work to approach (or separate) the elements of the system is given by the variation in the total energy of the system, $\mathcal{E}_{\mathrm{tot}}$ [Eq. (4.18)]. It follows then that the interaction force will be given by,

$$\boldsymbol{\mathcal{F}} = -\boldsymbol{\nabla}\mathcal{E}_{\mathrm{tot}}, \tag{4.24}$$

which in our case, as we consider an axisymmetric system, has only z-component. Note that the force in Eq. (4.24) is normalized.

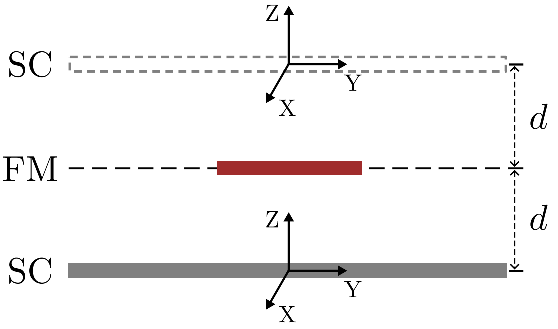

Figure 4.12: Sketch of the FSH. The behavior of the system depends on whether the FM (brown) is on top of the SC (gray) or below it, separated by the black dashed line.

Numerically, the system preparation is done at a distance $d = 100R_f$ and the elements are then brought together. As we want to follow the magnetic history of the FM sample, the distance variation at each step, Δd has to be small. We decided to study the range of distances $d \in [0.15R_f, 3R_f]$. In this region we set $\Delta d = 0.01R_f$, being small enough to characterize the quasiadiabatic limit, and thus enabling to study the FM states as a function of the distance as well as the interaction force between the elements. Furthermore, as the uniform state is not stable at $h_\mathrm{a} = 0$, we will consider a field range of small applied fields $h_\mathrm{a} \in (0, 0.1)$.

First, consider the system without applied field ($h_\mathrm{a} = 0$). It is known that a SC in the Meissner state, responds diamagnetically to magnetic fields. As such, the stray field of the FM will be shielded by the SC, creating an "image" of the magnetic structure. Actually, this is true in the case of an infinite ($R_s \to \infty$) SC with $\Lambda = 0$. Yet, since $R_s - R_f \gg \Lambda$, we may consider this approximation to give us some intuition on the interaction between them. As the FM interacts with something resembling an image of itself, a repulsive interaction is found. The results are shown in Fig. 4.13(a). It can be seen that the response is stronger when the FM is on top of the SC. This is attributed to the asymmetry in the magnetization's stray field, as found in Ref. [144], and the inherent bias induced by the radial component of the SC's stray field (see Fig. 4.14).

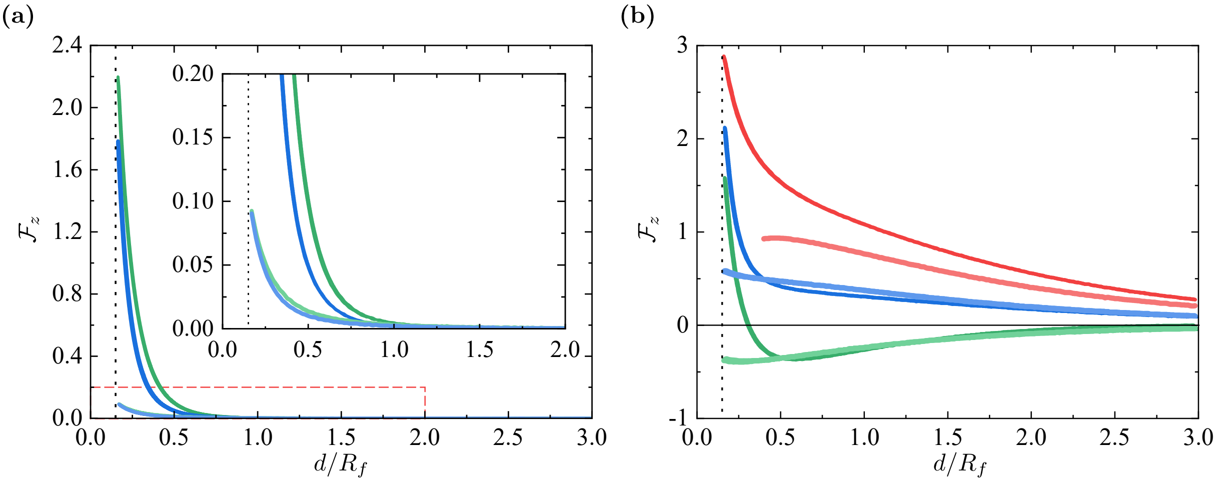

Figure 4.13: Force between the FM and SC elements (a) with no applied field, $h_\mathrm{a} = 0$, and (b) with $h_\mathrm{a} = 0.1$. A positive (negative) force is repulsive (attractive). The magnetization states are the uniform (red), the skyrmion (green), and the 2π (blue). The darker (lighter) colors symbolize that the FM is above (below) the SC [see Fig. 4.12 for a sketch]. The vertical dotted line represents the closest distance between the elements considered. In (a) we show an inset of the red region.

For the studied skyrmion-hosting multilayers, the uniform state is not stable at zero applied field. This was previously found in the hysteresis loops (see Fig. 4.2). Hence, it is interesting to see what happens when a uniform applied field h_a is present. In that case, the FM reacts to the shielding currents induced by the applied field and the stray field of the magnetization distribution. Depending on the applied field, the induced currents due to the magnetization distribution may be negligible.

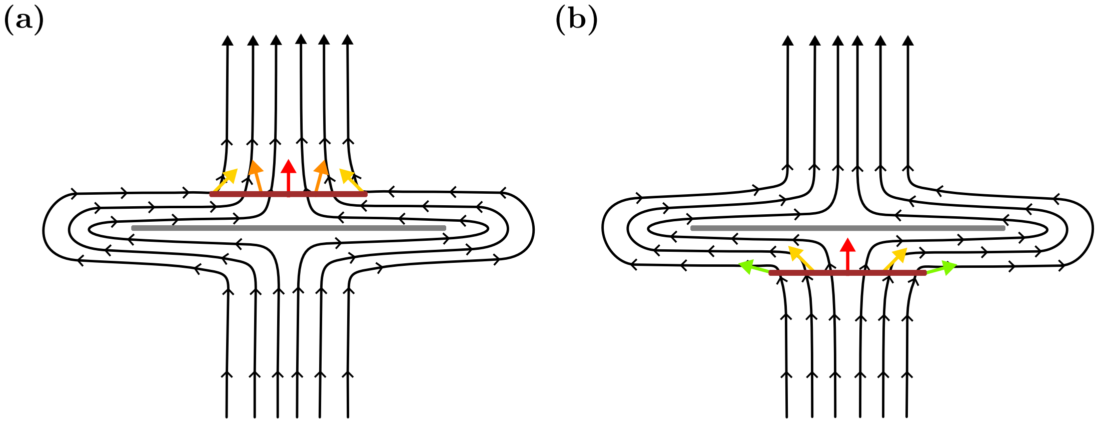

Figure 4.14: Field lines produced by the shielding currents in a SC (light gray) when the FM (brown) is (a) on top or (b) below it. The FM is in the uniform state [see Fig. 4.1(b)]. When the FM is on top of the SC, the edge magnetization is tilted inwards (compared to when there is no SC) due to the fields' radial component, opposing the iDM-imposed chirality. In contrast, when the FM is below the SC, the stray field helps the iDM interaction to tilt the magnetization, favoring the destabilization of the uniform state. The z-component of the magnetization is color coded as in Fig. 4.7.

For a small applied field $h_\mathrm{a} = 0.1$, where the uniform state is stable, we found that the interaction can be either attractive or repulsive. This can be seen in Fig. 4.13(b), where the uniform (red) and 2π (blue) structures have been found to be always repulsive, for the case considered, both if the FM is above or below the SC. If the FM is in the skyrmion state and above the SC (light green line), the interaction is always attractive. To explain this, consider the following. As the applied field is set to be $\mathbf{h}_\mathrm{a} = 0.1\,\hat{\mathbf{z}}^{d}$, the currents generate an opposing magnetic field (see black arrows in Fig. 4.14 for the total magnetic induction field). In a simplified picture, the currents can be seen as a dipole pointing to $-\hat{\mathbf{z}}$ and since the magnetization of the skyrmion state is mostly negative ($\langle m_z \rangle < 0$, as seen in Fig. 4.2), the net force is attractive.

When the FM and SC elements are closer, the "averaged" picture may no longer hold. This may explain the unexpected different behavior when the SC is above (close-range repulsion and long-range attraction) compared to when it is below (always attractive). We attribute this phenomenon to the bias introduced by the radial component of the field, which is reversed above/below the SC, as can be seen in Fig. 4.15. This bias is also shown in the sketch in Fig. 4.14. It is clear from Fig. 4.15 that when the FM is below the SC (dashed lines) a positive radial component of the magnetization is favored, which is dominant in this case. In contrast, when the FM is on top of the SC (solid lines) a negative radial component is preferred. For the cases studied, this yields a repulsive interaction.

---

[d] This field is larger than the stray field produced by the magnetization which is $\simeq 0.05$ for the closest distances. Hence we might neglect it.

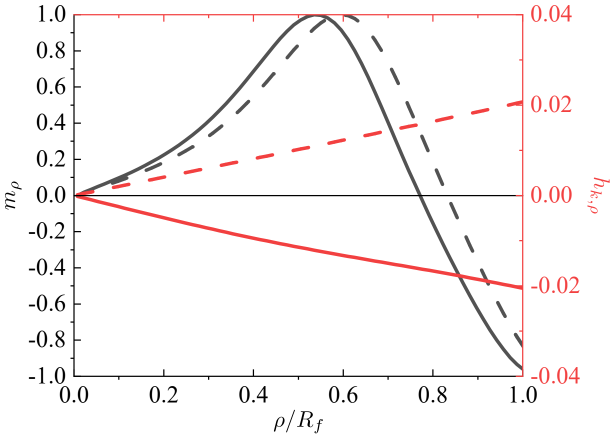

Figure 4.15: Radial component of the skyrmion magnetization (black) and the SC's stray field (red), when $h_\mathrm{a} = 0.1$ and $d = 0.3R_f$. The solid (dashed) lines represent the case of a FM on top (below) of a SC. The radial component of the field induces a bias that not only changes the skyrmion shape, but also can induce repulsion between the FM and SC elements, as seen in Fig. 4.13.

Additionally, it is found that the uniform state destabilizes when approaching the SC from below, a fact that is not found when approaching it from above. It is to be expected that the uniform state will be destabilized since it is not stable, in the system presented, for small applied fields [see Fig. 4.13(a)]. We attribute this last effect to the radial component of the shielding currents. As sketched in Fig. 4.14(a), when the FM is above the SC, the radial component of the field favors the spins to whirl inwards, opposing the chirality imposed by the iDM interaction. In contrast, when the FM is below the SC the radial component of the field favors the iDM interaction, tilting the spins outwards, as sketched in Fig. 4.14(b). This reversal in the behavior, is what allows the uniform state to remain stable in proximity to the SC even though the z-component of the field alone is not enough to stabilize it, as can be seen in Fig. 4.13(a). It is found that the most likely transition, in this case, was to the skyrmion state (green colors in Fig. 4.13). This bias is produced by the stray field of the superconducting currents in the SC, which is also related to the discussion presented together with Fig. 4.7 when we studied the quasiadiabatic hysteresis loop.

Aside from the simplified view presented, the behavior of the system is highly dependent on the magnetization distribution itself. Even in the simplified picture with the dipole moments (Fig. 4.14), the interaction with the skyrmion and 2π states depends on the number of spins in each direction as well as on the distance to the SC. Moreover, since the magnetization distribution depends on the distance, we have a nonlinear interaction that is too intricate to make some general statements about the behavior of the system. In spite of this, we can make qualitative assessments of the physics found as a function of the distance between the FM and SC elements.

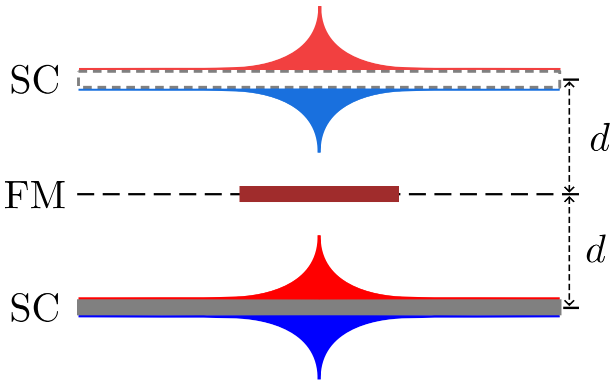

Figure 4.16: Sketch of the SC (light gray) current profile of a +PV (-PV) are shown in red (blue). The symbols and colors are the same as in Fig. 4.12.

Let's consider trapped flux in the SC, a PV. The PV can have positive (+PV) or negative (-PV) polarity. The current profiles are sketched in Fig. 4.16. There are two ways to find such a state: a type-II SC or a FC SC with a tiny hole. The former is described by the Ginzburg-Landau equations,[249] with each vortex entering through the boundaries and going to the center of the sample. In the latter, the hole would act as the suppression of superconductivity at lengths close to the coherence length, ξ_GL. Both of them can be described equally in the London picture (see Sec. 2.3.1).

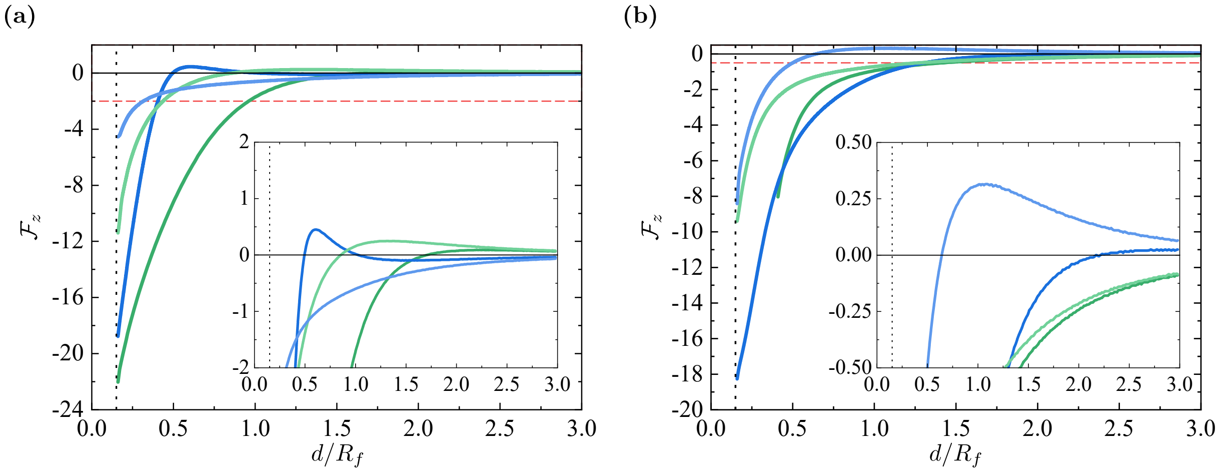

Figure 4.17: Force between the FM and SC elements without applied field when a PV with (a) positive or (b) negative polarity. A positive (negative) force is repulsive (attractive). In (a) and (b) we show an inset of the red region. Note that there is an additional change in the force sign, better seen in the insets. The magnetization states are the skyrmion (green) and the 2π (blue) states. The darker (lighter) colors symbolize that the FM is above (below) the SC. The vertical dotted line represents the closest distance between the elements considered.

In order to simplify the intricate picture presented, the interaction is going to be considered without any applied field. The system is prepared as previously, starting with the FM and SC elements separated from each other and then slowly brought together. Moreover, we focus here on the force between the FM and SC elements and any transition found. Note that at zero applied field, the only stable magnetic structures are the skyrmion and 2π states.

First, let's consider a FM above the SC. For a skyrmion close to a SC with a +PV, it is found that the force is repulsive at long distances, whilst attractive closer [see dark green lines in Fig. 4.17(a)]. In contrast, if a -PV is present, the interaction is found to be always attractive for the distance range studied [see dark green lines in Fig. 4.17(b)]. In the case of the 2π state close to a +PV [darker blue lines in Fig. 4.17(a)], it is found that: at large distances, the interaction is attractive, at medium distances the interaction is repulsive, and at small distances, the interaction is again attractive. In contrast, for a -PV [darker blue lines in Fig. 4.17(b)], at large and medium distances the interaction is repulsive whilst at close distances it is attractive.

These results are similar when the FM is below the SC [lighter colors in Fig. 4.17(a)], except for the distances at which the interaction is attractive/repulsive and their strength. Moreover, it is found that for the 2π state in proximity with a +PV, the force is always attractive. Lastly, when the FM is in the skyrmion state and on top of a SC with a -PV [see dark green line Fig. 4.17(b)], the skyrmion state destabilizes at a distance $d \simeq 0.8R_f$, where it is found that the only possible transition is to the 2π state (the uniform state is not stable).

In Fig. 4.18 we present summarized sketches of these results for the sake of readability. In Fig. 4.18(a) we show the interaction force when the FM is in the skyrmion state and the SC has a PV. Similarly, in Fig. 4.18(b) we show the interaction for the 2π case.

Most of these phenomena can be explained by simplifying the system to its barebones. It is known that in proximity to a PV, the stray field it generates above (below) it can be approximated by a magnetic monopole on the opposite side at a position $d_m = -\Lambda$ ($d_m = \Lambda$).[338] As the SC is quite larger than the FM ($R_s = 3R_f$) to consider this tray field acting on the FM is justifiable. This simplified picture allows us to consider the force between the elements as the force the monopole does over the magnetization distribution. The system considered is depicted in Fig. 4.19(a). To further simplify the system, consider that the DW of the magnetic structure is narrow so that we have domains that can only point in the $\pm\hat{\mathbf{z}}$ direction. This is sketched in Figs. 4.19(b-c) with the dashed lines. This assumption neglects the contribution of the DWs to the overall force.

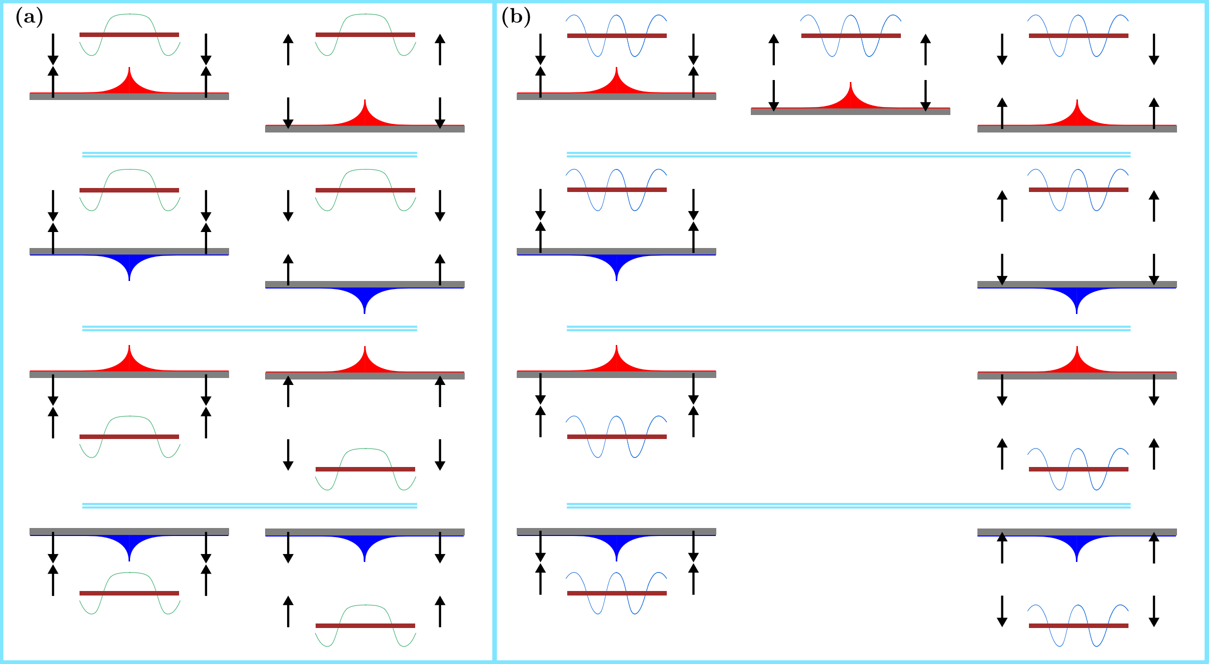

Figure 4.18: Summary sketches of the interaction of (a) a skyrmion and (b) a 2π state with a PV, at zero applied field and different separation distances. The FM (brown) can be on top or below the SC (gray). In (a) the interaction for close (left) and large distances (right) are depicted. In (b), the central column corresponds to medium distances, appearing when there is an intermediate sign change in the force. The black arrows illustrate the resulting interaction force.

Now we can formulate a toy model to explain the origin of the forces. Since the magnetization distribution is simplified to be step functions with only z-component ($\mathbf{m} = m_z\hat{\mathbf{z}}$), only the z-component of the SC-induced stray field is relevant. The stray field of a PV with flux $\mathit{\Phi}_0$ is given by the monopole field,

$$h_{z,\mathrm{PV}}(\rho, z) = \frac{\mathit{\Phi}_0}{2\pi}\frac{z + d_m}{(\rho^2 + (z + d_m)^2)^{3/2}}, \tag{4.25}$$

where the monopole has a charge of $2\mathit{\Phi}_0$. Remember that we defined $\mathit{\Phi}_0 = \Phi_0/(\mu_0 M_s l_{\mathrm{ex}}^2)$. Note that the magnetic field is reversed when considering a -PV. The interaction force over the magnetization distribution is given by,

$$\mathcal{F}_z(z) = -\partial_z \mathcal{E}_{\mathrm{tot}}, \tag{4.26}$$

where the total normalized energy of the system is given by Eq. (4.18). Since in the toy model the magnetization distribution and the currents do not change, only the interaction term $\mathcal{E}_{\text{int}}$ [Eq. (4.21)] is non-zero. Hence the force reads,

$$\mathcal{F}_z(z) = -\partial_z \mathcal{E}_{\text{int}} = -\int_S \frac{\partial h_{z,\text{PV}}(\rho, z)}{\partial z} m_z(\rho) \mathrm{d}S, \tag{4.27}$$

where S is the surface where there is magnetization. Considering the axisymmetry and the step-like function considered in our toy model, the force over each domain is,

$$\mathcal{F}_z(z) = -2\pi \int_{R_{\text{ini}}}^{R_{\text{fin}}} \frac{\partial h_{z,\text{PV}}(\rho, z)}{\partial z} (\pm 1) \rho \,\mathrm{d}\rho = \mp \Phi_0 \left. \frac{\rho^2}{(\rho^2 + (z + d_m)^2)^{3/2}} \right|_{R_{\text{ini}}}^{R_{\text{fin}}}, \tag{4.28}$$

where R_{ini} and R_{fin} delimit the magnetic domain region and the (± 1) is due to the magnetization. The total force is just the sum of the force over each domain. Let's consider first the case of a FM, in the skyrmion state [see Fig. 4.19(b)], on top of a SC with a +PV. We consider a skyrmion with radius R_{sk}. After considering both domains [$m_z = 1$ in $\rho \in (0, R_{\text{sk}})$ and $m_z = -1$ in $\rho \in (R_{\text{sk}}, R_f)$], the force is found to be,

$$\frac{\mathcal{F}_z(z)}{\Phi_0} = \frac{2R_{\text{sk}}^2}{(R_{\text{sk}}^2 + (z + d_m)^2)^{3/2}} - \frac{R_f^2}{(R_f^2 + (z + d_m)^2)^{3/2}}. \tag{4.29}$$

It is helpful to rewrite it as,

$$\frac{\mathcal{F}_z(\tilde{z})}{\Phi_0} = \frac{1}{R_f} \left[\frac{2\tilde{R}_{\text{sk}}^2}{(\tilde{R}_{\text{sk}}^2 + (\tilde{z} + \tilde{d}_m)^2)^{3/2}} - \frac{1}{(1 + (\tilde{z} + \tilde{d}_m)^2)^{3/2}} \right], \tag{4.30}$$

where $\tilde{R}_{\text{sk}} = R_{\text{sk}}/R_f$, $\tilde{z} = z/R_f$, and $\tilde{d}_m = d_m/R_f$. The force now has only one free parameter $\tilde{R}_{\text{sk}}$.

Our toy model allows us to qualitatively predict the overall behavior of the system. Consider, for example, the case of a skyrmion above a +PV. Depending on R_{sk}, the force may be attractive close to the SC and repulsive at larger distances [see Fig. 4.18(a) for a summary]. This is shown in Fig. 4.20(a). Given the skyrmion state [see Fig. 4.19(b)], the tails are usually more relevant than the core. Therefore at larger distances, where the structure can be seen as the average of the magnetization, we have a repulsive force since the skyrmion "dipole" opposes the PV "monopole". At closer distances, the particular magnetization distribution becomes relevant, specially the core due to its proximity to the PV position (center of the elements). As such the force done to the core is larger than the one done to the tails of the magnetization and, thus, the net force is attractive. Note that when $R_{\text{sk}} = 0$ or 1 the uniform state can be found. It can be seen that the uniform with positive (black) and negative (pink) polarities have the opposite response. If the uniform state and the PV "point" in the same direction, the interaction is attractive.

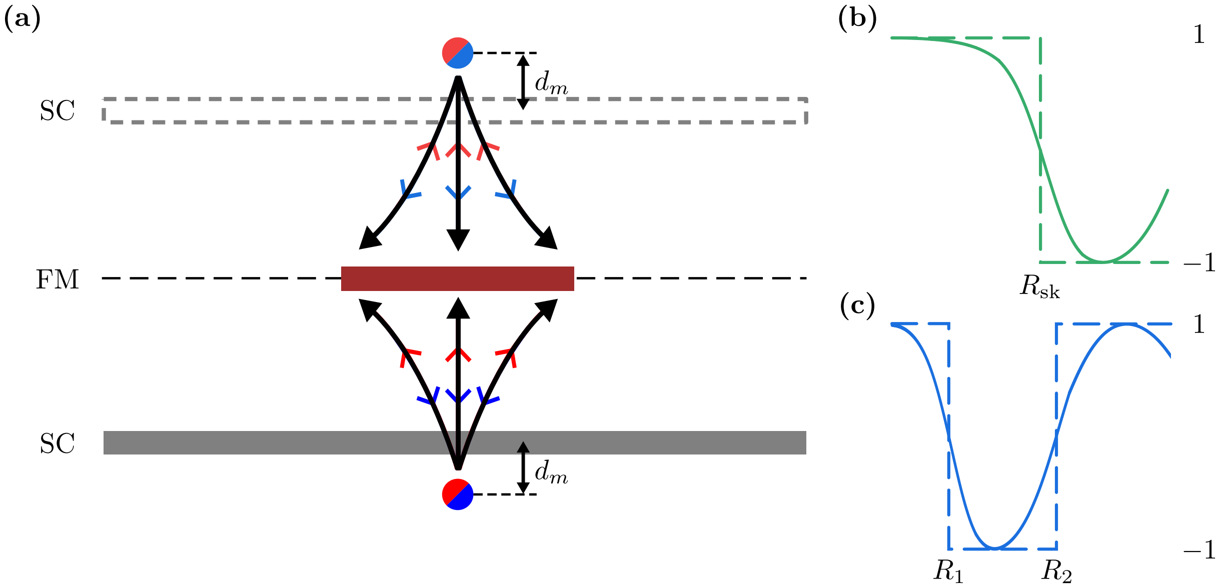

Figure 4.19: (a) Sketch of the toy model when a PV is present in the SC. The stray field of the PV currents can be approximated by that of a magnetic monopole[338] [red (+PV) and blue (-PV) semicircles], depicted with the arrows. The behavior of the system depends on whether the FM is on top of the SC or below it, separated in the sketch by the black dashed line. In the toy model, the magnetization only points in the $\pm\hat{\mathbf{z}}$ direction. The z-component of the magnetization for the (b) skyrmion and (c) 2π states are represented, with the toy model's simplification shown with dashed lines.

This toy model fails to explain the fact that the skyrmion state in the presence of a -PV is attractive at all distances. This is because the model does not consider the magnetization distribution to change during the interaction with the SC. Therefore, the complete calculations are needed to fully characterize the interaction.

Regarding the skyrmion destabilization found when the FM is on top of the SC with a -PV [dark green line in Fig. 4.17(b)], the argument is similar than the one for the uniform destabilization (or lack of it) when the SC is in the Meissner state. Consider a FM on top of a -PV, whose stray field can be approximated by that of a monopole [see Fig. 4.19(a)]. In Fig. 4.20(b), we show an example of a possible skyrmion magnetization distribution. Note that when the skyrmion winds up once ($m_z = -1$), the radial component of the magnetization becomes negative. The z-component of the stray field favors the magnetization in the $-\hat{\mathbf{z}}$ direction, so the core of the skyrmion will tend to be smaller (blue lines). The radial component of the field will also tend to align the magnetic moments in the $-\hat{\boldsymbol{\rho}}$ direction (blue arrows), favoring the wind-up of the structure alongside the z-component of the field. In contrast, when the FM is below the SC, the radial component of the PV's stray field wants the magnetic moments to align in the $\hat{\boldsymbol{\rho}}$ direction (pink arrows), unwinding the structure. This difference introduces a bias on the FM. If the FM is on top of the SC, it is easier to wind up the magnetization and reach the 2π state. In contrast, if the FM is below the SC, the components of the PV's stray field are competing against each other. Explaining the transition found in Fig. 4.17(b).

Now, consider that the FM is in the 2π state, defined by an inner radius R_1 and a second radius R_2 [see Fig. 4.19(c)]. In this case, the same arguments done for the skyrmion case apply, but since there is an additional domain, it is possible to have one more sign change (or none) in the force. Mostly, the same arguments used for the skyrmion case still apply. For more details see Appendix C.2.

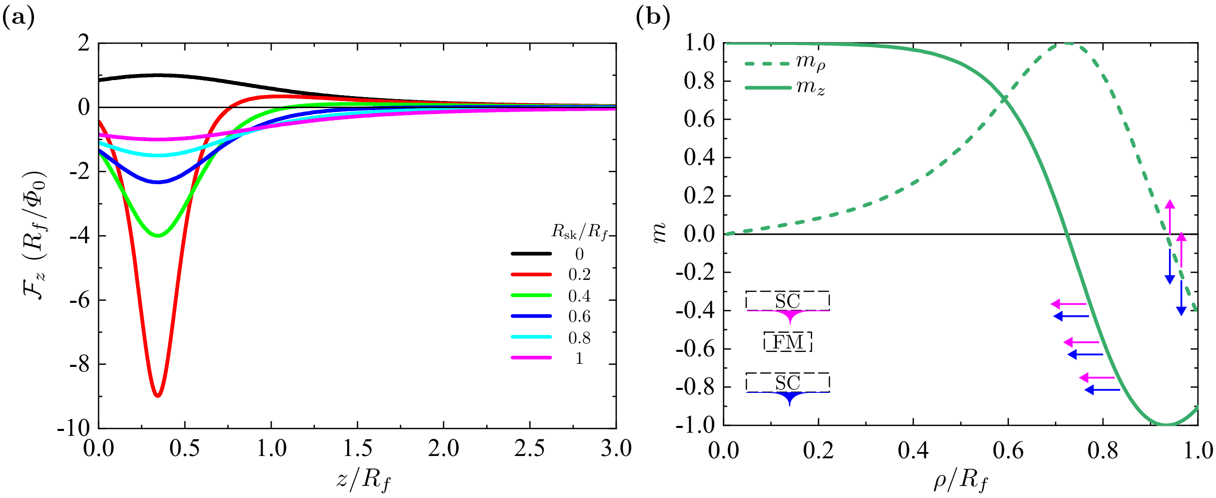

Figure 4.20: (a) Force between the FM, in the skyrmion state, and SC elements without applied field when a +PV is present. A positive (negative) force is repulsive (attractive). Note that for $R_{\text{sk}} = 0, 1$ (black and pink lines) the uniform state ($m_z(\rho) = \pm 1$) is found. (b) Example of a possible magnetization distribution of the FM in the skyrmion state. When close to a -PV, depending on whether the FM is on top (blue) or below (pink), the radial component of the PV's stray field induces a bias over the magnetization. If the FM is below the SC (pink) the radial and z-component of the stray field compete with each other. For a sketch of the PV's stray field see Fig. 4.19(a).

This plethora of phenomena is found without considering the applied field, which further changes the behavior of the system as seen in Fig. 4.13, without considering a PV and applied field simultaneously. In fact, the behavior slightly changes as a function of applied field. This is due to that the interaction among elements strongly depends on the magnetization distribution which is continuously adapting to the SC-induced stray field and the applied field. Even such a simple system has a huge and complex behavior. We limit ourselves to the above understanding of the behavior whilst giving tools for a deeper study if it is deemed necessary. One of the main reasons it is so complex is that there are many interactions competing with each other. In Appendix C.3, the presented and some additional results are shown in different tables.

4.4 Generalizing the model: Ring geometries

The presented model can be generalized straightforwardly to consider ring geometries, such as the one in Fig. 4.21. Consider a FM (SC) ring of radius R_f (R_s) a central axisymmetric hole of radius $R_{f,i}$ ($R_{s,i}$). Despite the difference in the topology, the formulation for the ring system is almost identical to the disk case (Fig. 4.1). In fact, the different topological solutions depending on the geometry will be given by the boundary conditions used to solve the Brown equation [Eq. (4.2b)].

Recall that the BCs for a FM disk were given by [Eq. (4.14)], where the innermost magnetic moment is fixed due to symmetry and the outermost moments have their derivative fixed due to the iDM interaction.[55]

In contrast, in the ring case, we have an additional edged due to the central hole. Therefore, the magnetic moments at the edge of the hole will also have its BC imposed by the iDM interaction. Hence the BCs in this case read,

$$\left.\frac{\mathrm{d}\theta}{\mathrm{d}\rho}\right|_{\rho=R_{f,i},\, R_f} = \frac{\xi}{2}, \tag{4.31}$$

where it can clearly be seen that there is no need to fix the central magnetic moment as it is given by the boundary condition at the inner edge. Here the change in the topology when comparing disks and rings becomes apparent. Now the innermost magnetic moment has no longer to be out-of-plane ($m_z = \pm\hat{\mathbf{z}}$), the energy barrier to flip the magnetization is expected to be smaller. Intuitively, in a disk, we have to flip *all* the surrounding magnetic moments in order to flip the central one, whilst in the ring case, the magnetic moments can be flipped from the inner and outer edges, reducing the energy barrier to change the magnetization state, and thus the stability of the states. Moreover, the so-called topological protection is lost, as a continuous deformation in the field can now flip the magnetization. No singularities in the magnetization occur during the magnetization reversal.

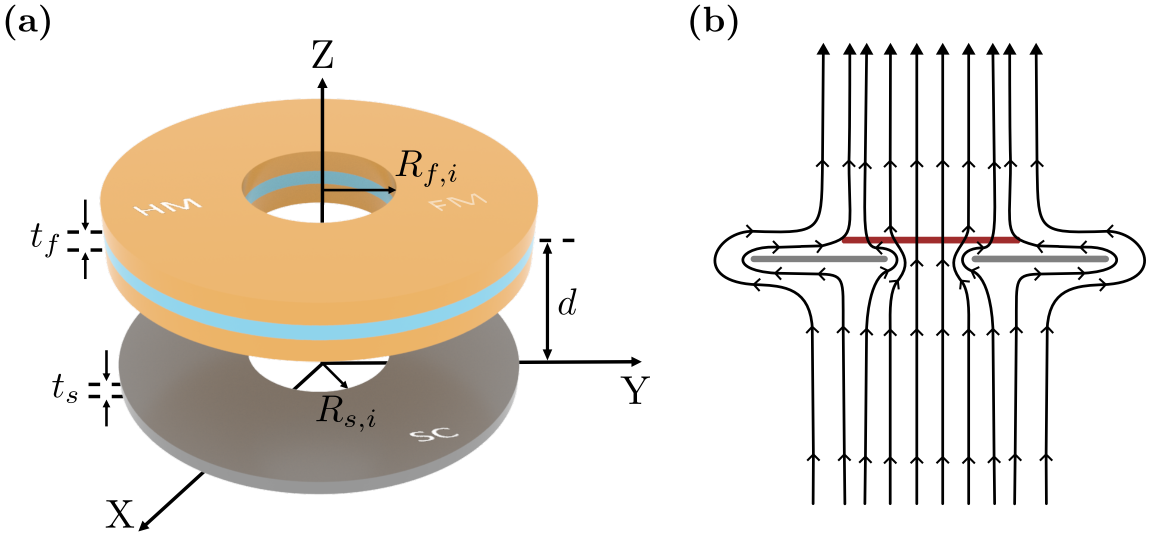

Figure 4.21: (a) Sketch of a hybrid system formed by a FM (brown) and a SC (light gray) rings with inner radius $R_{f,i}$ and $R_{s,i}$, respectively. A superconducting element (gray) is coaxial to a ferromagnetic element (light blue) with iDM interaction due to two different attached heavy metal layers (light orange). The depiction of ring-shaped heavy-metal layers is for illustration purposes. (b) Illustration of the magnetic field lines (in black) in the presence of a ring-shaped SC when an external uniform field is applied.

Regarding the SC ring, it may be interesting for magnetic levitation applications[320] or to have flux focusing in type-I SC. If the hole in the SC is very small (as compared to Λ) and the superconducting transition is made with applied field (FC SC), then the superconducting currents would be similar to the ones produced by a PV. In fact, the initial flux that traverses the SC, when the transition to the superconducting state is made, is trapped in the SC hole. This allows additional control over the magnetic field generated by the SC, as we can somewhat control the shape of the induction field (**B**) that the FM would feel. One could thus control the positions at which the generated field is mostly in the Z-axis (on top of the hole) or has a radial component (on top of the SC). This is sketched in Fig. 4.21(b).

4.5 Chapter summary and conclusions

In this chapter, we have presented a new model to study FM-SC hybrid systems. Our model allows computing the static mutual interaction between both elements, mediated through stray fields, using a two-way coupling. This allows for more realistic simulations as compared to previous models in which a one-way coupling was considered. Moreover, these are, to the best of our knowledge, the first study in which both the SC and FM elements are finite.

To inspect the interaction under confinement in disk geometries, we have performed a two-step study. First, we have studied the system's response to a quasiadiabatic applied field hysteresis loop while considering a ZFC SC at a fixed distance, d, between the FM and SC elements. We have seen that the presence of a SC allows for an additional transition to the 2π state, which is unfavorable without the SC. Using the GNEB method, this possible transition was found to occur across the boundaries of the ferromagnetic system.

Once the response to the applied field is studied, we focus on the interaction as a function of the distance. To do so, we prepared the FM/SC states far from each other (isolated) and then we slowly bring them together, considering a constant applied field. A large plethora of phenomena is found, as many interactions compete with each other. We focus our attention on some specific cases to assess the interaction, considering skyrmionic structures in the FM and the possibility of a PV in the SC. We have studied the force between the FM and SC disks as well as the magnetization states as a function of the elements' separation. Additionally, we provide a toy model that gives some insight into some of the phenomena found.

The presence of three differentiated magnetization states, stable over a large applied field range and accessible at will, could be used for the design of ternary-logic systems. These could allow new computation schemes, as well as increasing the density of stored information, not by increasing the density of dots, but the allowed number of states per dot.

Furthermore, the magnetization states and the possible transitions between states can be tuned by using a SC close to the FM, using the distance and/or applied field to tune the hysteretic behavior of the system. This allows having different magnetic states while controlling the magnetization state and any transition if desired. In this way, the presented FSH could be used as building blocks for novel magnetic metamaterials. It is known that the use of FM's and SC's can be useful to achieve effective permeabilities not possible in nature. The proposed system advantages would be twofold: (i) Considering structure in the FM would give a particular anisotropic and non-linear response to the applied field, which can be further tuned by controlling the transitions and the current state in the FM; (ii) The scale at which the elements are considered (hundreds of nanometers), would potentially enable shaping the magnetic fields at the micrometric scale, allowing applications in which a finer control of the magnetic field is needed.

Chapter 5

Conclusions and future perspectives

The understanding of magnetism and magnetic materials has enabled the development of a wide range of technologies that are present in our daily life; magnetism is nowadays found at the basis of electric generators, credit cards, medical techniques (e.g. magnetic resonance imaging and hyperthermia), and in computers for storage and handling of data, among many other applications. The huge amount of data that can be stored and processed has enabled the so-called information era and global digitalization. Both of them continuously demand faster, denser, non-volatile, and low-power-consuming technologies. In this context, we have found the main topic of this thesis: the theoretical study of a kind of spintronic devices, the skyrmionic devices. In these devices, magnetic skyrmions are used as the building blocks. Their small size (few tens of nanometers), high stability (found at room temperature, with lifetimes up to years), and movement efficiency (smaller current densities needed as compared to DW motion) make them potential candidates for next-generation information storage (and handling) technologies. Hopefully, enabling devices with better performance and smaller energy consumption for a greener future.

The boom in the field of skyrmions is relatively recent since it skyrocketed after the theoretical proposal of the skyrmionic racetrack memory in 2013. In this regard, several advances have been made, but there are still many obstacles to be overcome before they can become a reality. For example, a key aspect in skyrmion racetrack memories is the transport of the information (the skyrmions) along the racetrack. It is known that defects may strongly affect the skyrmion dynamics, both as a perturbation of the magnetic structure, as well as affecting the overall center-of-mass trajectory of the skyrmion. To study the skyrmion-defect interaction, micromagnetism has become a valuable asset, allowing us to study systems of considerable size in reasonable times. Nevertheless, a complete simulation of the dynamics of the magnetization might be impractical for device prototyping. At that point, the rigid model is introduced, where the magnetization is considered to be rigid and its motion is described by its center-of-mass: the Thiele equation.

Due to the ubiquity of defects in real materials and their unavoidable appearance and randomness, it becomes relevant to develop tools to study the skyrmion behavior in their presence. In Ch. 3, we have developed a model (within the rigid approximation) to consider extended defects. Starting from the force expression of an atomic perturbation of a magnetic parameter, we expand it to consider extended defects. The relevance of the model is that it allows, mostly analytically, to determine the different possible motion regimes (pinning or not, guiding along a line defect, etc.) and the conditions under which they are possible as a function of the system's parameters. This effectively allows for faster prototyping, as one can restrict the relevant materials/parameters at which the desired phenomena might occur. These results, from the rigid model, are validated with more detailed micromagnetic simulations, yet more intricate, numerically costly, and non-analytical.

The precise control of skyrmions is of uttermost importance in most skyrmionic devices proposed up to this day. The knowledge of how defects affect the skyrmion trajectories could allow us to tailor them to our needs. In this way, we can envisage a future in which artificially created defects can be beneficial and not only a hindrance for skyrmionic devices. A couple of interesting applications would be the guiding and speeding up of skyrmions along defects or the creation of periodic skyrmion traps for diamagnetic atoms, with potential applications in quantum magnetomechanics.

Nevertheless, skyrmionic applications are not only restricted to skyrmion racetrack memories. Considering materials with opposed magnetic response, in Ch. 4 we present a model that successfully takes into account the mutual interaction of the FM and SC elements, in disk geometries. We simultaneously solve the Brown equation in the FM and the London equation in the SC. This model gives us both magnetization and current distributions. To the best of our knowledge, this is the first time that the interaction of a skyrmion-hosting FM and a SC is studied in confined geometries.

Despite the fast-paced research in the field of magnetic skyrmions, challenging, unexplored physics still lies ahead. For example, the presence of three (or more) different magnetization states, stable over a large range of applied fields and accessible at will could be used to increase the density of stored information or enable ternary (or more) logic. A specially interesting (from my point of view) research direction that could follow from the presented work is in the field of static magnetic metamaterials.

In this context, skyrmionic metamaterials would be formed by a quasirepetition of skyrmion-hosting FMs and SCs. The main idea is to evaluate the properties of a material at a larger scale than that of its constituent elements. At a scale larger than the constituent elements' size, one can find an equivalent magnetization or an effective permeability. It is common to consider the FM and SC as a constant permeability, μ, being $\mu \to \infty$ for the FM and $\mu = 0$ for the SC. But, what would be the effective permeability if one considers structure inside the FM, the SC, or in both of them? The typical sizes of the considered elements would be on the nanometric to micrometric scale, an order of magnitude below regular magnetic metamaterials. Moreover, the non-trivial magnetic structure in the FM would give a non-linear and anisotropic response to the external field that could help to better tune the effective permeability.

The field of skyrmionics is still in its infancy. At this stage, the theory and models are still cornerstones to explain and predict phenomena. This thesis contributes to the skyrmionic field in both ways: explaining interactions as a means of predicting relevant behaviors, thus helping in the development of novel devices.

Appendix A

Thiele equation

In this Appendix, we discuss the derivation of the Thiele equation from the micromagnetic LLG equation. Once obtained, we show that a formulation in the complex plane is helpful to see that, in the rigid approximation, the trajectories of a skyrmion driven by different torques can be obtained by an appropriate rescaling and rotation of the torque itself. This allows studying the dynamics of the skyrmion by considering a single torque, as any other solution can be obtained by a simple rotation and rescaling.

A.1 From LLG to Thiele

Starting from the LLG equation,

$$(1+\alpha^2)\frac{d\mathbf{M}}{dt} = -\gamma\mathbf{M}\times\mathbf{H}_{\text{eff}} - \frac{\gamma\alpha}{M_s}\mathbf{M}\times(\mathbf{M}\times\mathbf{H}_{\text{eff}}) + \mathbf{T}, \tag{A.1}$$

or in written its other form,

$$\frac{d\mathbf{M}}{dt} = -\gamma\mathbf{M}\times\mathbf{H}_{\text{eff}} + \frac{\alpha}{M_s}\mathbf{M}\times\frac{d\mathbf{M}}{dt} + \mathbf{T}, \tag{A.2}$$

where $\gamma = 2.21\cdot 10^5$ m A^{-1} s^{-1}, α is the dimensionless Gilbert damping constant, and $\mathbf{T}$ are all the torques over the magnetization, outside the interactions considered in the effective field $\mathbf{H}_{\text{eff}}$. To go from Eq. (A.2) to the Thiele equation, one assumes the rigid approximation. This can be expressed as, $\mathbf{M}(\mathbf{r}) = \mathbf{M}_0(\mathbf{r}-\mathbf{r}_{\text{sk}})$, which can be rewritten in a more helpful way as,

$$\frac{d\mathbf{M}}{dt} = -(\dot{\mathbf{r}}_{\text{sk}}\cdot\nabla)\mathbf{M} = -\dot{\mathbf{r}}_{\text{sk,j}}\frac{\partial\mathbf{M}_i}{\partial x_j}, \tag{A.3}$$

where the dot is the time derivative and on the rightmost part of the equation we use the Einstein notation (repeated subindices are summed). The derivatives are taken over $x_j = x, y, z$.

To simplify the treatment, we will present the equation when $\mathbf{T} = 0$. Once done, we will present the results obtained for the different driving torques presented in the thesis.

The first step is to do $\mathbf{M}\times$ Eq. (A.2). This reads,

$$\begin{aligned}\mathbf{M}\times\frac{d\mathbf{M}}{dt} &= -\gamma\mathbf{M}\times(\mathbf{M}\times\mathbf{H}_{\text{eff}}) + \frac{\alpha}{M_s}\mathbf{M}\times\left(\mathbf{M}\times\frac{d\mathbf{M}}{dt}\right)\\ &= -\gamma[(\mathbf{M}\cdot\mathbf{H}_{\text{eff}})\cdot\mathbf{M} - M_s^2\mathbf{H}_{\text{eff}}] + \frac{\alpha}{M_s}\left[\left(\mathbf{M}\cdot\frac{d\mathbf{M}}{dt}\right)\mathbf{M} - M_s^2\frac{d\mathbf{M}}{dt}\right].\end{aligned} \tag{A.4}$$

Note that,

$$\mathbf{M} \cdot \frac{d\mathbf{M}}{dt} = \frac{d\mathbf{M}^2}{dt} = \frac{dM_s^2}{dt} = 0,$$

since M_s is assumed to be constant. Therefore, Eq. (A.4) reads,

$$\mathbf{M} \times \frac{d\mathbf{M}}{dt} = -\gamma(\mathbf{M} \cdot \mathbf{H}_{\text{eff}}) \cdot \mathbf{M} + \gamma M_s^2 \mathbf{H}_{\text{eff}} - \alpha M_s \frac{d\mathbf{M}}{dt}. \tag{A.5}$$

Now we multiply it by $\frac{d\mathbf{M}}{dx_i}$,

$$\frac{d\mathbf{M}}{dx_i} \cdot \left(\mathbf{M} \times \frac{d\mathbf{M}}{dt}\right) = -\gamma \frac{d\mathbf{M}}{dx_i} \cdot (\mathbf{M} \cdot \mathbf{H}_{\text{eff}}) \cdot \mathbf{M} + \gamma M_s^2 \frac{d\mathbf{M}}{dx_i} \cdot \mathbf{H}_{\text{eff}} - \alpha M_s \frac{d\mathbf{M}}{dx_i} \cdot \frac{d\mathbf{M}}{dt}, \tag{A.6}$$

and using the rigid property [Eq. (A.3)],

$$\begin{aligned} \frac{d\mathbf{M}}{dx_i} \cdot \left[\mathbf{M} \times \left(-\dot{\mathbf{r}}_{\text{sk,j}} \frac{\partial \mathbf{M}_i}{\partial x_j}\right)\right] &= -\gamma \frac{d\mathbf{M}}{dx_i} \cdot (\mathbf{M} \cdot \mathbf{H}_{\text{eff}}) \cdot \mathbf{M} \\ &\quad + \gamma M_s^2 \frac{d\mathbf{M}}{dx_i} \cdot \mathbf{H}_{\text{eff}} - \alpha M_s \frac{d\mathbf{M}}{dx_i} \cdot \left(-\dot{\mathbf{r}}_{\text{sk,j}} \frac{\partial \mathbf{M}_i}{\partial x_j}\right). \end{aligned} \tag{A.7}$$

The left-hand side can be found to be,

$$-\frac{d\mathbf{M}}{dx_i} \cdot \left[\mathbf{M} \times \left(\dot{\mathbf{r}}_{\text{sk,j}} \frac{\partial \mathbf{M}_i}{\partial x_j}\right)\right] = \dot{\mathbf{r}}_{\text{sk,j}}\, \mathbf{M} \cdot \left(\frac{\partial \mathbf{M}}{\partial x_i} \times \frac{\partial \mathbf{M}}{\partial x_j}\right). \tag{A.8}$$

On the right-hand side, the first term is zero as $\mathbf{M} \cdot \frac{d\mathbf{M}}{dt} = 0$. The last term can also be rewritten as,

$$\alpha M_s \frac{d\mathbf{M}}{dx_i} \cdot \left(\dot{\mathbf{r}}_{\text{sk,j}} \frac{\partial \mathbf{M}_i}{\partial x_j}\right) = \alpha M_s \dot{\mathbf{r}}_{\text{sk,j}} \left(\frac{\partial \mathbf{M}}{\partial x_i} \cdot \frac{\partial \mathbf{M}}{\partial x_j}\right). \tag{A.9}$$

Hence Eq. (A.7) can be rewritten as,

$$\dot{\mathbf{r}}_{\text{sk,j}}\, \mathbf{M} \cdot \left(\frac{\partial \mathbf{M}}{\partial x_i} \times \frac{\partial \mathbf{M}}{\partial x_j}\right) = \gamma M_s^2 \frac{d\mathbf{M}}{dx_i} \cdot \mathbf{H}_{\text{eff}} + \alpha M_s \dot{\mathbf{r}}_{\text{sk,j}} \left(\frac{\partial \mathbf{M}}{\partial x_i} \cdot \frac{\partial \mathbf{M}}{\partial x_j}\right). \tag{A.10}$$

As the last step, one needs to integrate over the sample volume V. For the sake of readability, we will do so term by term. Therefore, the left-hand side of Eq. (A.10) becomes,

$$\dot{\mathbf{r}}_{\text{sk,j}} \int_V \mathbf{M} \cdot \left(\frac{\partial \mathbf{M}}{\partial x_i} \times \frac{\partial \mathbf{M}}{\partial x_j}\right) dV = \dot{\mathbf{r}}_{\text{sk,j}} \mathbb{G}_{ij}, \tag{A.11}$$

obtaining the gyrotropic tensor, $\mathbb{G}$, from Eq. (2.30). The last term in the right-hand side of Eq. (A.10) reads,

$$\alpha M_s \dot{\mathbf{r}}_{\text{sk,j}} \int_V \left(\frac{\partial \mathbf{M}}{\partial x_i} \cdot \frac{\partial \mathbf{M}}{\partial x_j} \right) dV = \alpha M_s \dot{\mathbf{r}}_{\text{sk,j}} \, \mathbb{D}_{ij}, \tag{A.12}$$

obtaining the dissipative tensor, $\mathbb{D}$, from Eq. (2.30). Lastly, the remaining term can be computed to be,

$$\gamma M_s^2 \int_V \frac{d\mathbf{M}}{dx_i} \cdot \mathbf{H}_{\text{eff}} dV = \gamma M_s^2 \int_V \frac{d\mathbf{M}}{dx_i} \cdot \mathbf{H}_{\text{ext, eff}} dV = -\gamma M_s^2 \mathbf{F}_i, \tag{A.13}$$

where only the effective field from external agents, $H_{\text{ext,eff}}$, does not cancel out when doing the integral over the whole sample volume.[59] In this last term, the forces (within the rigid approximation) coming from external agents can be obtained if its $\mathbf{H}_{\text{eff}}$ is known (or modeled in some way). Putting everything together one obtains the Thiele equation,

$$(\mathbb{G} - \alpha M_s \mathbb{D}) \dot{\mathbf{r}}_{\text{sk}} + \gamma M_s^2 \mathbf{F} = 0. \tag{A.14}$$

If one now introduces the torques and follows the same derivation, it can be seen that any torque $\mathbf{T}$ will drive the skyrmion as,

$$\int_V \frac{\partial \mathbf{M}}{\partial x_i} (\mathbf{M} \times \mathbf{T}) dV. \tag{A.15}$$

In the case of an STT driven skyrmion with adiabatic and non-adiabatic torques given by,

$$\mathbf{T}_{\text{ad}} = -\frac{\mu_B P J_{\text{FM}}}{e} \mathbf{m} \times [\mathbf{m} \times (\hat{\boldsymbol{\varphi}} \cdot \nabla) \mathbf{m}] = \frac{\mu_B P J_{\text{FM}}}{e} \mathbf{m} \times (\hat{\boldsymbol{\varphi}} \cdot \nabla) \mathbf{m}, \tag{A.16}$$

$$\mathbf{T}_{\text{non-ad}} = -\beta \frac{\mu_B P J_{\text{FM}}}{e} \mathbf{m} \times (\hat{\boldsymbol{\varphi}} \cdot \nabla) \mathbf{m} = -\beta \mathbf{m} \times \mathbf{T}_{\text{ad}}, \tag{A.17}$$

respectively. This leads to an additional term in the Thiele equation given by,

$$(\mathbb{G} - \beta M_s \mathbb{D}) \mathbf{V}_{\text{FM}}, \tag{A.18}$$

with $\mathbf{V}_{\text{FM}} = -\mu_B P J_{\text{FM}} / (e M_s)$. If the skyrmion instead is driven by the SHE torques,

$$\mathbf{T}_{\text{damp}} = -\frac{\mu_B \theta_{\text{H}} J_{\text{HM}}}{e t_f} \mathbf{m} \times (\mathbf{m} \times \hat{\boldsymbol{\sigma}}), \tag{A.19}$$

$$\mathbf{T}_{\text{field}} = -\nu \frac{\mu_B \theta_{\text{H}} J_{\text{HM}}}{e t_f} \mathbf{m} \times \hat{\boldsymbol{\sigma}} = -\nu \mathbf{m} \times \mathbf{T}_{\text{damp}}, \tag{A.20}$$

being the damping-like and field-like torques, respectively. Here we considered a FM with thickness t_f. In this case, the additional term in the Thiele equation reads,

$$-M_s(\mathbb{N}+\nu M_s\mathbb{Y})\boldsymbol{\sigma}_{\mathrm{HM}}, \tag{A.21}$$

where $\boldsymbol{\sigma}_{\mathrm{HM}} = -\frac{\mu_B\theta_{\mathrm{H}}}{eM_s}\hat{\boldsymbol{z}} \times \mathbf{J}_{\mathrm{HM}} = \hat{\boldsymbol{z}} \times \mathbf{V}_{\mathrm{HM}}$. The tensors $\mathbb{N}$ and $\mathbb{Y}$ are found to be,

$$\mathbb{N}_{ij} = \frac{1}{t_f}\int_V \left(\frac{\partial \mathbf{M}_0}{\partial x_i} \times \mathbf{M}_0\right)_j dV, \tag{A.22}$$

$$\mathbb{Y}_{ij} = \frac{1}{t_f}\int_V \frac{\partial \mathbf{M}_{0,j}}{\partial x_i} dV, \tag{A.23}$$

The complete Thiele equation with all these torques is,

$$(\mathbb{G}-\alpha M_s\mathbb{D})\dot{\mathbf{r}}_{\mathrm{sk}} - (\mathbb{G}-\beta M_s\mathbb{D})\mathbf{V}_{\mathrm{FM}} + M_s(\mathbb{N}+\nu M_s\mathbb{Y})\boldsymbol{\sigma}_{\mathrm{HM}} + \gamma M_s^2\mathbf{F} = 0. \tag{A.24}$$

A.2 Complex Thiele equation

In ultrathin films, the skyrmion motion is restricted to the sample plane. As such, it becomes apparent that a complex formulation is possible. It is convenient to normalize the Thiele equation [Eq. (A.24)] and use non-dimensional variables to describe the system. To do so we will follow the normalization of the LLG equation [Eq. (2.5)], by normalizing the length to the exchange length $l_{\mathrm{ex}} = \sqrt{2A_{\mathrm{ex}}/(\mu_0 M_s^2)}$ and the times to $t_0 = (\gamma M_s)^{-1}$. Regarding the tensors $\mathcal{G}, \mathcal{D}, \mathcal{N}$ and $\mathcal{Y}$ we will use the dimensionless variables $\mathcal{G} = G/(M_s^3 t_f)$, $\mathcal{D} = D/(M_s^2 t_f)$, $\mathcal{N} = D/(M_s^2 l_{\mathrm{ex}})$ and $\mathcal{Y} = D/(M_s^3 l_{\mathrm{ex}})$. As for the force, we can use $f = F/(M_s^2 t_f l_{\mathrm{ex}})$. Furthermore, as the velocities v and the "forces" $\mathbf{f}$ lie on the XY plane, we can redefine them in the complex plane as: $\omega_{(\mathrm{sk,FM,HM})} \equiv v_{(\mathrm{sk,FM,HM}),x} + iv_{(\mathrm{sk,FM,HM}),y}$ and $\xi \equiv \xi_x + i\xi_y$. Therefore Eq. (A.24) is converted to

$$\omega_{\mathrm{sk}} = \frac{1}{\alpha\mathcal{D}+i\mathcal{G}}\xi + \frac{\beta\mathcal{D}+i\mathcal{G}}{\alpha\mathcal{D}+i\mathcal{G}}\omega_{\mathrm{FM}} + \frac{-\mathcal{N}+i\nu\mathcal{Y}}{\alpha\mathcal{D}+i\mathcal{G}}\omega_{\mathrm{HM}}. \tag{A.25}$$

This equation can be interpreted as for each position a skyrmion (a point in the complex plane), $\omega_{\mathrm{FM}}, \omega_{\mathrm{HM}}$ and ξ_{FM} are rescaled and rotated according to their accompanying complex constant. Once rescaled and rotated, the complex skyrmion velocity can be written as,

$$\omega_{\mathrm{sk}} = \omega_{\mathrm{FM}}^{'} + \omega_{\mathrm{HM}}^{'} + \xi^{'}, \tag{A.26}$$

indicating that wherever the origin and directions of the driving current densities, J_{FM} and J_{HM}, all the driving torques can be put in a single term $\omega^{'} = \omega_{\mathrm{FM}}^{'} + \omega_{\mathrm{HM}}^{'}$, which is unambiguously defined. Therefore, one can consider a single driving torque without loss of generality as that skyrmion trajectory could be fulfilled with other driving mechanisms appropriately rescaled and rotated.

Appendix B

Stability of magnetic structures

In this Appendix, we discuss some details on the stability study of the magnetization states. The values for the energy surface example depicted in Fig. 2.11 are given. Then, some alternatives to the GNEB method are introduced, which have been proposed to avoid some of its shortcomings.

B.1 GNEB table

The energy surface depicted in Fig. 2.11 is a sum of Gaussian functions of the Geodesic distance,

$$\varepsilon(\mathbf{m}) = \sum_j a_j e^{\left(-\frac{l_j^2(\mathbf{m})}{2\sigma_j^2}\right)}, \tag{B.1}$$

where $l_j(\mathbf{m})$ is the geodesic distance between the endpoint of vector $\mathbf{m}_j$ and the center of the jth Gaussian, $\mathbf{m}_j$. The geodesic distance can be computed using the haversine formula,[339] given by

$$l_j(\mathbf{m}) = 2\arcsin\sqrt{\frac{1-\mathbf{m}\cdot\mathbf{m}_j}{2}}. \tag{B.2}$$

The values to define the Gaussian centers, $\mathbf{m}_j$ [given in spherical coordinates with the polar (θ) and azimuthal (φ) angles], their amplitude, a_j, and their width σ_j, were chosen so as to form multiple minima, maxima and a single easy-to-spot saddle point on the energy surface. The concrete values for this simulation are presented in Table B.1.

Table B.1: Values of the parameters of the Gaussian function used for the energy landscape [Eq.(B.1)] used to illustrate the GNEB algorithm in Fig. 2.11.

j	a_j	σ_j	θ_i	φ_j
1	-2.5	0.20	0.60	1.2
2	-2	0.15	2.00	5.0
3	1.5	0.40	0.15	5.0
4	1.25	0.20	2.20	1.5
5	2	0.10	2.00	3.2
6	1	0.20	0.00	3.0
7	0.75	0.20	3.00	3.0
8	0.5	0.30	1.57	0.0

B.2 Beyond GNEB

Using the GNEB method to sample the configuration space to obtain the MEP and corresponding saddle point has some drawbacks. Mainly, the fact that one has to create an initial path, either introduces a significant amount of bias or the sampling of the configuration space is too weak. For completeness, we present some recent alternatives even though they have not been used for this thesis. In the recent literature, some alternatives have been proposed to mitigate those drawbacks in magnetic systems such as the Mode Following method.[157]

But both the Mode Following and the GNEB methods make use of HTST to compute the transition rates. One problem one faces is that more than one mechanism may contribute to the switching rate and they might not be independent. As such, it is difficult to assess a priori how one has to compute the transition rates. An alternative method is therefore required. Forward Flux Sampling, a path sampling method that was initially developed to simulate rare switching events[340] has been proposed. In particular, it was used to obtain magnetization switching rates in magnetic microstructures.[341, 342]

The key idea is that one first obtains the MEP using the GNEB or Mode Following method and the pre-exponential factors are calculated using HTST.[155,156,158] Once this is done, one takes the energy landscape of the configuration space and divides it into different regions, e.g. different energy levels (contours) or some order parameter, going from one energy minimum to the other. The interfaces between regions are denoted with λ_i, as depicted in Fig. B.1. Then, an stochastic simulation of the configuration space, usually using the Stochastic-LLG equation [Eq. (2.5) with an additional noise term[343, 344]], starts at a local minimum, λ_A, and many simulations are done until the configuration traverses the closest energy level λ_1 [see Fig. B.1(a)]. Then, starting from the points that reached λ_1 [red crosses in Fig. B.1(a)], the process is repeated until we reach the final minimum configuration state, λ_B. This process of iteratively going from one region λ to the next is depicted in Fig. B.1.

This allows to compute the flux over the diving surface (determined by the saddle point), between reaction λ_A and product λ_B, as the product of the net flux over each of the energy levels that comprise the configuration space. Thus, by following the stochastic motion of the system, one can take into account rare events which may be critical to determine the transition rate and explore the configuration space in an efficient manner. We recommend reading Ref. [159].

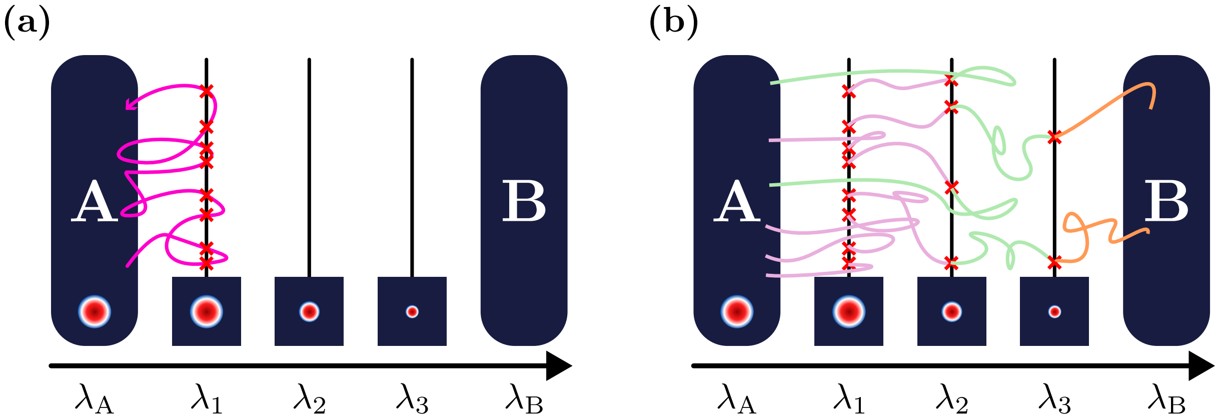

Figure B.1: Illustration of the Forward Flux Sampling method, where the order parameter defining the interfaces λ_i between state A (metastable skyrmion) and state B (FM state). (a) First simulation to compute the rate of crossing the first contour level λ_1. (b) Trial runs at subsequent interfaces. Adapted from Ref. [159].

Appendix C

Interaction with a close SC

In this Appendix, we present a brief discussion and demonstration of the renormalization of the demagnetizing field inside the uniaxial anisotropy effective field. Then, the presented toy model from the text is expanded to explain the 2π interaction force (with a SC) as a function of the distance. Some discussions are also given. Then we give a summary of all the phenomena found for the considered cases in the text in tabular form. An additional figure is provided that is not studied in the text for completeness and to help in the readability of the tables.

C.1 On the renormalization of the demagnetizing field

In Ch. 4 a FSH system composed of a ferromagnetic and superconducting disk was studied. The mutual interaction was considered by coupling the Brown equation (in the FM) and the London equation (in the SC) [Eqs. (4.2b) and (4.2a)]. For the FM, we renormalized the demagnetizing field, $\mathbf{h}_\mathrm{d}$, of the ferromagnetic sample in the anisotropy, arguing that in the infinite case it acts as a shape anisotropy and can be justified.

Even though it has been somewhat discussed in a previous work,[179] it is not clear when this approximation is valid in finite systems. As such, we reproduced the study done in Sec. 4.3.1 without renormalizing the demagnetizing field. For our renormalization to be a reasonable approximation, it is needed that the z component of the demagnetizing field is similar to the z component of the magnetization with its signed change, i.e. $h_{\mathrm{d},z}(\rho) \simeq -m_z(\rho)$. The phenomena found and the transition field are close to the ones found in Sec. 4.3.1, with some deviations due to the nature of the approximation.

In Fig. C.1, we show different snapshots of all the stable states found in the system as a function of the applied field. The magnetization is shown by the triangle symbols, whilst the demagnetizing field is depicted by the solid lines. When a SC is present (darker colors), depending on the field range, different states may be stable. For example, the uniform (red), skyrmion (green) and 2π (blue) states are stable for the shown fields: $h_\mathrm{a} = -0.25$ [Fig. C.1(a)], $h_\mathrm{a} = 0$ [Fig. C.1(b)], $h_\mathrm{a} = 0.25$ [Fig. C.1(c)], and $h_\mathrm{a} = 0.75$ [Fig. C.1(d)]. As can be seen, the renormalization is reasonable, having the largest deviation at the edges of the material for the uniform state at $h_\mathrm{a} = 0.75$ [Fig. C.1(d)]. The fact that the deviation is largest at the edge of the ferromagnetic sample explains the fact that the destabilizing fields for each state might slightly vary. Nevertheless, it is justifiable and avoids the computationally intensive demagnetizing field calculation.

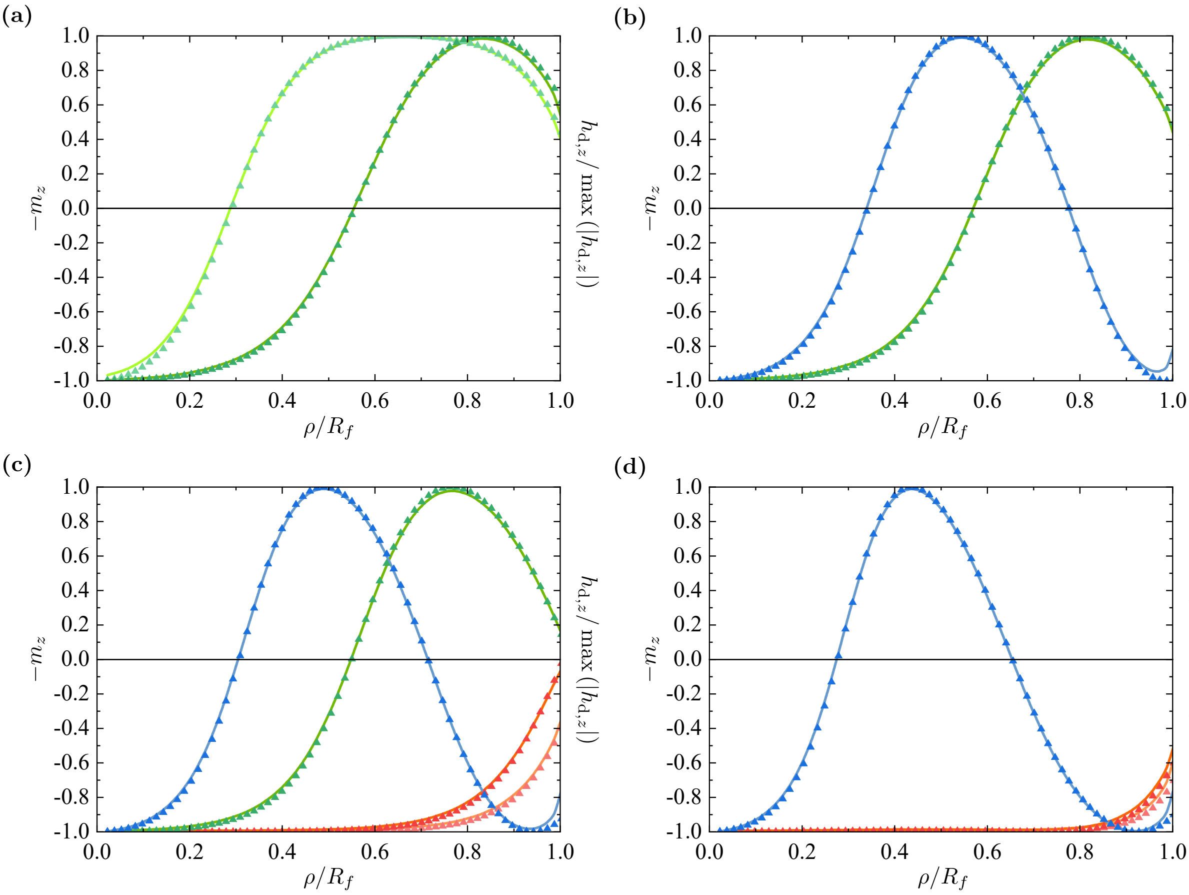

Figure C.1: Simulations considering the demagnetizing field of the FM sample for different applied fields: (a) $h_a = -0.25$, (b) $h_a = 0$, (c) $h_a = 0.25$, and (d) $h_a = 0.75$. The darker (lighter) colors were computed with (without) SC. We find the uniform (red), skyrmion (green), and 2π (blue) states to be stable. The demagnetizing field (solid lines) matches the magnetization distribution (triangles) closely, with the largest discrepancy at the edge of the sample. The hysteresis loops closely match the ones simulated with the results presented in Fig. 4.2.

C.2 On the toy model with the 2π state

In the main text, we have considered the case of a skyrmion state considering a simplified magnetization distribution given by step functions, as depicted in Fig. 4.19(c). In this case, the toy model presented considering a 2π state given by,

$$\begin{cases} m_z(\rho) = 1, & \text{for } \rho \in [0, R_1), \\ m_z(\rho) = -1, & \text{for } \rho \in (R_1, R_2), \\ m_z(\rho) = 1, & \text{for } \rho \in (R_2, R_f]. \end{cases} \tag{C.1}$$

The force can be obtained by using Eq. (4.28). It reads,

$$\frac{\mathcal{F}_z(z)}{\Phi_0} = \frac{1}{R_f}\left[\frac{2\tilde{R}_1^2}{[\tilde{R}_1^2 + (\tilde{z} + \tilde{d}_m)^2]^{3/2}} - \frac{2\tilde{R}_2^2}{[\tilde{R}_2^2 + (\tilde{z} + \tilde{d}_m)^2]^{3/2}} + \frac{1}{[1 + (\tilde{z} + \tilde{d}_m)^2]^{3/2}}\right], \qquad \text{(C.2)}$$

where the tilde symbolizes the variables divided by R_f. The force in this case has two free parameters: $\tilde{R}_1$ and $\tilde{R}_2$. Due to the additional domain, as compared to the skyrmion case [Fig. 4.20(a)], it may be possible to have from no sign changes in the force to up to two sign changes. This is depicted in Figs. 4.20(b-c), where $R_1 = 0.1R_f, 0.2R_f$, respectively. It was found that if $R_2 \leq 0.6$, the force is: attractive close to the SC, repulsive at intermediate distances, and attractive at larger distances. To explain this behavior, recall the arguments for the skyrmion case. When far away, one sees the averaged magnetization. Due to the core and tails of the 2π state pointing in the same direction, it is found that $\langle m_z \rangle > 0$. As such, the equivalent dipole is parallel to the PV and the overall interaction is attractive. As we get closer, it may happen that at intermediate ranges (close enough to see the distribution, but not enough to only care about the core) the domain pointing opposite to the PV dominates and the resulting interaction is repulsive. Lastly, close to the SC, the most relevant interaction is with the core and, as happened with the skyrmion, the interaction is attractive. Note that the case with 2π state is more finicky, as it may also happen that it behaves similarly to the skyrmion if $\langle m_z \rangle < 0$ (when R_2 is larger) or, if the negative domain span is small, that the interaction is always attractive. These two facts explain that the interaction between a PV and a FM in the 2π state found in Fig. 4.20 present from no changes in the force [light blue line in Fig. 4.17(a)] to two changes [dark blue line in Fig. 4.17(a)].

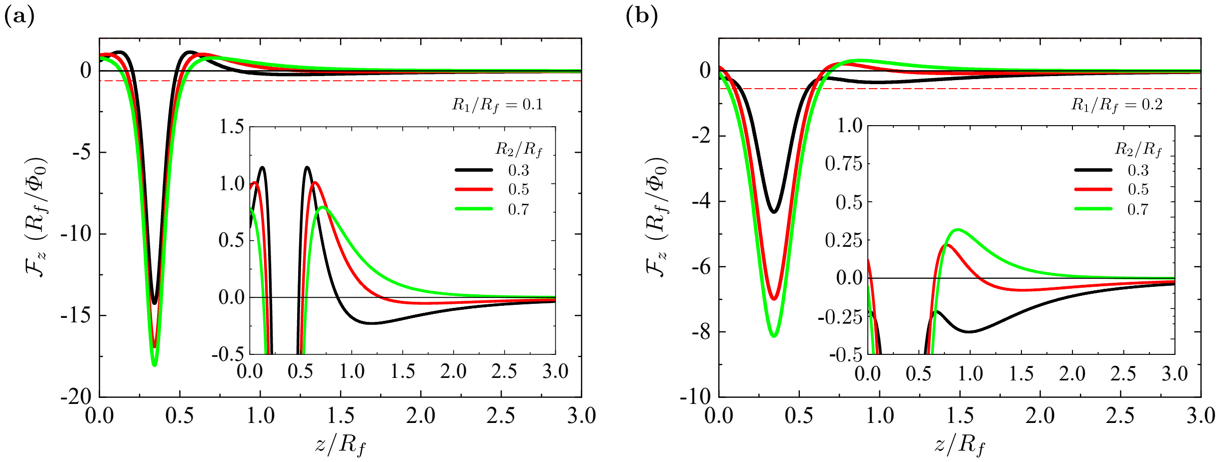

Figure C.2: Force between the FM, in the 2π state, and SC elements without applied field when a +PV is present. A positive (negative) force is repulsive (attractive). We show the force when the inner magnetization disk R_1 is (a) $R_1 = 0.1R_f$ or (b) $R_1 = 0.2R_f$. The insets show the region marked in red were force sign changes are found.

C.3 Summary of FM-SC hybrids response to plate separation

In this section, we give some of the possible results found for a small number of possible configurations. The large plethora of results found is attributed to the several counteracting interactions that, depending on the system configuration (h_a, flux trapping in SC, magnetic structure in the FM, and distance between the FM and SC plates), change the net behavior of the system.

The results presented in the main text, are presented in table format in Tables C.1- C.4. In the tables, we prepare the system with an initial state with a magnetization state [uniform (U), skyrmion (S), and 2π states] and current distribution [no vortex ($\emptyset$), or a Pearl vortex (±PV)]. In some cases, transitions have been found. We show them and give the distance at which they have been found. Finally, the sign of the interaction force [attractive (-) or repulsive (+)] is given. These match the values shown in Figs. 4.13 and 4.17 in the main text.

For completeness, here we also show the results when both an applied field, $h_{\mathrm{a}} = 0.1$ and a ±PV are present in the system in Fig. C.3. Here, some difference can be seen in the overall interaction between the FM and SC elements as compared to when there was no applied field or PVs.

Table C.1: Summary behavior for different combinations of initial magnetization state [Uniform (U), Skyrmion (S), and 2π] and currents in the SC [no trapped flux ($\emptyset$), PV or -PV] when the FM and SC are approximated to each other. Here the FM is on top of the SC and $h_{\mathrm{a}} = 0.1$. The separation distance considered is in the range $d \in [0.15R_f, 2R_f]$.

Initial state	Initial current	Transitions (d/R_f)	Interaction Force
U	$\emptyset$		U (+)
	+PV	U→ S (0.2)	U(-); S(-)
	-PV	U→ 2π (0.32)	U(+); 2π(-, + far)
S	$\emptyset$		S (+, - far)
	+PV		S (-)
	-PV	S→ 2π (0.79)	S(-); 2π(-, + far)
2π	$\emptyset$		2π(+)
	+PV		2π(-, + far)
	-PV		2π(-, + far)

Table C.2: Summary behavior for different combinations of initial magnetization state [Uniform (U), Skyrmion (S), and 2π] and currents in the SC [no trapped flux ($\emptyset$), PV or -PV] when the FM and SC are approximated to each other. Here the FM is on top of the SC and $h_{\mathrm{a}} = 0.0$. The separation distance considered is in the range $d \in [0.15R_f, 2R_f]$.

Initial state	Initial current	Transitions (d/R_f)	Interaction Force
S	$\emptyset$		S(+);
	+PV		S (-, + far)
	-PV	S→ 2π (0.4)	S(-); 2π
2π	$\emptyset$		2π(+)
	+PV		2π(- close, +, - far)
	-PV	2π →-S (0.28)	2π(-)

Table C.3: Summary behavior for different combinations of initial magnetization state [Uniform (U), Skyrmion (S), and 2π] and currents in the SC [no trapped flux ($\emptyset$), PV or -PV] when the FM and SC are approximated to each other. Here the FM is below the SC and $h_\mathrm{a} = 0.1$. The separation distance considered is in the range $d \in [0.15R_f, 2R_f]$.

Initial state	Initial current	Transitions (d/R_f)	Interaction Force
U	$\emptyset$	U→S (-0.37)	U (+); S(-)
	+PV		U(-)
	-PV	U→S (1.14)	U(+); S(-)
S	$\emptyset$		S(-)
	+PV		S(-, + far)
	-PV		S(-)
2π	$\emptyset$		2π(+)
	+PV		2π(-)
	-PV		2π(-, + far)

Table C.4: Summary behavior for different combinations of initial magnetization state [Uniform (U), Skyrmion (S), and 2π] and currents in the SC [no trapped flux ($\emptyset$), PV or -PV] when the FM and SC are approximated to each other. Here the FM is below the SC and $h_\mathrm{a} = 0.0$. The separation distance considered is in the range $d \in [0.15R_f, 2R_f]$.

Initial state	Initial current	Transitions (d/R_f)	Interaction Force
S	$\emptyset$		S(+);
	+PV		S (-, + far)
	-PV		S(-)
2π	$\emptyset$		2π(+)
	+PV		2π(-)
	-PV		2π(-, + far)

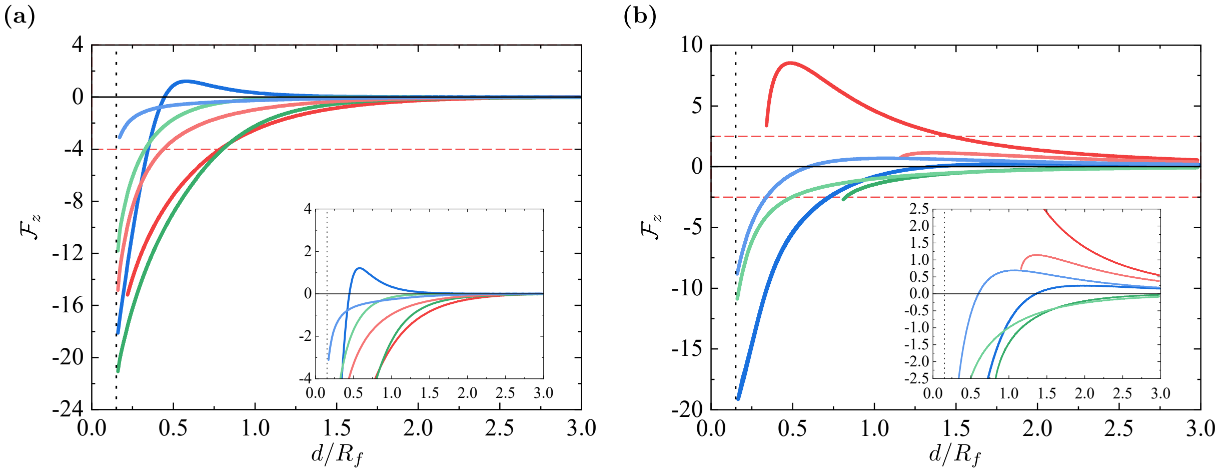

Figure C.3: Force between the FM and SC elements with the applied field, $h_\mathrm{a} = 0.1$, when a PV with (a) positive or (b) negative polarity is present. A positive (negative) force is repulsive (attractive). In (a) and (b) we show an inset of the red region. The magnetization states are the skyrmion (green) and the 2π (blue) states. The darker (lighter) colors symbolize that the FM is above (below) the SC. The vertical dotted line represents the closest distance between the elements considered.

List of Figures

1.1 (a) Scheme of the simplest MRAM design. Its design is based on the dependence of the system's magnetoresistance as a function of the relative orientation of the magnetization of the free layer (light blue) with respect to the reference layer (dark blue). (b) Sketch of a magnetic racetrack memory, based on a magnetic skyrmion. The presence or not of a skyrmion would be a 1 or a 0. The skyrmion is moved with spin currents. Figure (b) is adapted from Woo et al.[12] 2

1.2 (a) Magnetic force microscopy images acquired with a Co thickness of 0.2 nm, finding isolated skyrmions at room temperature. Red and blue contrasts represent the out-of-plane magnetization. (b) Lorentz transmission electron microscopy images of magnetic skyrmions at 250 K. The hexagonal skyrmion lattices are marked with the dotted hexagon. Figure (a) adapted from Brandao et al.[21] Figure (b) is adapted from Chakrabartty et al.[22] 3

1.3 Top-view of (a) Néel-type and (b) Bloch-type skyrmions with the magnetization rotating from the up direction (red) at the skyrmion's center to the down direction (blue) of the external uniform magnetization at the skyrmion's edge. The radial magnetization distribution of (c) a Néel-type and (d) a Bloch-type skyrmion is sketched. The colors represent the z component of the magnetization. In (d) the magnetization arrows are smaller as they rotate out-of-plane. 5

2.1 Magnetic moment $\mathbf{S}$ precessing around the magnetic induction field $\mathbf{B}$ due to a torque $\mathbf{T}$. 8

2.2 Magnetization $\mathbf{m}$ precessing around the magnetic field $\mathbf{H}_{\text{eff}}$ and dampened due to the material. At a later time, the magnetization will have precessed (golden arrow) and aligned a bit (green arrow) with the effective field. 10

2.3 Sketch of the geometry of the considered FM in this thesis. An ultrathin FM (light blue) is placed on top of a HM (orange) substrate. The ultrathin film is in the XY plane. 11

2.4 Sketch of the iDM interaction in a crystal. The interaction is produced at the interface between a ferromagnetic metal (light blue) and a HM substrate (orange) with a strong spin-orbit coupling, as described by the 3-site mechanism proposed by Fert and Levy.[27] 14

2.5 Illustrations of some possible Bloch point configurations with revolution axis vertical to the FM: (a) hedgehog and (b) spiraling Bloch points. (a) is reminiscent of a Néel skyrmion and (b) to a Néel antiskyrmion.[195] This Figure is adapted from Thiavile et al.[193] 16

2.6 (a) A spin-polarized current enters a FM (blue region). The interaction between the spin-polarized current, $\mathbf{J}_{\mathrm{FM}}$, and the magnetization, $\mathbf{m}$, causes a change in the spin direction of the outgoing electron compared with the incident electron (orange arrow). The difference in spin polarization causes adiabatic and non-adiabatic torques on the FM. The blue vertical arrow is the magnetization of the ferromagnetic layer. (b) Magnetization $\mathbf{m}$ precessing around the magnetic field $\mathbf{h}_{\mathrm{eff}}$, dampened due to the material and influenced by the adiabatic and non-adiabatic torques. Figure (a) is adapted from Braatas et al.[198] 18

2.7 Schematics of the SHE and the torques it produces. An electron current, $\mathbf{J}_{\mathrm{HM}}$, is fed into the HM and is converted into a transverse spin current by spin-orbit scattering. The spin current $\mathbf{J}_{\mathrm{S}}$ leads to a spin accumulation at the HM/FM interface that diffuses across the interface into the FM and exerts torques. The spin current then interacts with the magnetic moment in the FM, producing two torques over it. These torques are analogous to the ones in the STT case shown in Fig. 2.6(b). 20

2.8 (a) Illustration of the vectors $\mathbf{r}_{\mathrm{sk}}$, $\mathbf{V}_{\mathrm{sk}}$, and $\mathbf{F}$. The skyrmion is propelled at an angle θ_{sk} with respect to the incident force $\mathbf{F}$. The colors represent the z-component of the magnetization which in the skyrmion goes from pointing in $\hat{\mathbf{z}}$ (red), to the ferromagnetic background pointing in $-\hat{\mathbf{z}}$ (blue), going through zero out-of-plane magnetization (white). The skyrmion experiments a force $\mathbf{F}$ that drives it at a velocity $\mathbf{V}_{\mathrm{sk}}$ with an angle θ_{sk} with respect to it. (b) Illustration of an axisymmetric Néel skyrmion as could be found in (a). The arrows represent the local magnetization along the radius. 21

2.9 Sketch of a possible configuration for the currents. $\mathbf{J}_{\mathrm{FM}}$ and $\mathbf{J}_{\mathrm{HM}}$ are the current densities flowing through the FM (light blue region) and the HM (orange region), respectively. These current densities are associated with a spin current that interacts with the skyrmion (red-white-blue circular structure) stabilized in the FM. 25

2.10 (a) Sketch of an atomic magnetic moment embedded in a unit sphere. $\mathbf{s}$ can be described by the polar and azimuthal angles, θ and φ respectively. (b) Three neighboring atomic moments can be taken into account as the direct product of the unit spheres. 26

2.11 An illustration of a GNEB calculation of an MEP for a single spin system. The positions of the images are shown with filled circles. The initial path was chosen to lie along the short geodesic path (linear path in the θ-φ phase-space) between the energy minima (indicated in blue). It turned out to lie near a maximum (indicated in red). The converged path is shown in pink. One intermediate configuration of the path is also shown in light pink. The saddle point is marked with a dark blue cross. Eight images were used in the illustration (dots along the path). The Hamiltonian of the spin system is given in Appendix B.1. 29

2.12 Sketch of a superconducting vortex that has penetrated a SC sample (green region) under an applied magnetic induction field, **B**. The Cooper pair density, n_s, decays over distances on the order of ξ_{GL}, defining the vortex core (red cylinder). The vortex core allows magnetic flux (**H**) to penetrate the sample over a distance λ_L. Around the vortex one finds circulating currents denoted by the gray region. . . 30

2.13 Sketch of a semi-infinite slab in the Meissner state under an applied field $\mathbf{H}_{\mathrm{a}}$. (a) The magnetic induction field (blue lines) exponentially decays, penetrating the SC a depth on the order of λ_{L}. (b) The superconducting currents (red lines) shield the applied field. 32

2.14 The current (a) and field (b) profiles of a thin superconducting strip of width $2W$, with $\Lambda/W = 0, 0.05, 0.2$ and 0.8 under a perpendicular applied field H_{a}. As $\Lambda \to 0$, the currents are more abrupt near the edge whilst the field penetrates less inside the sample. The vertical dashed lines indicate the edges of the material. Figure adapted from Chen et al.[256] 34

3.1 Sketch of the studied system. $\mathbf{J}_{\mathrm{HM}}$ represents the current density flowing into the HM (light orange region). The skyrmion (red-white-blue structure) moves with a velocity $\mathbf{V}_{\mathrm{sk}}$ in a FM background (light blue region). 38

3.2 Forces over a skyrmion as derived in Ref. [89], considering $\delta = 2$ and $\kappa = 2$. A negative force points towards the defect. A local modification of the exchange interaction results in zero net force. 39

3.3 Illustration of the local defect system. The red dot represents the center-of-mass of the incoming skyrmion and ρ is the distance to the defect (green dot). The blue arrows are the driving velocity ($\mathbf{v}_{\mathrm{HM}}$) and the drift velocity of the skyrmion ($\mathbf{v}_{\mathrm{sk}}$). 40

3.4 Vector field corresponding to (a) the attractive local defect force [Eq. (3.6)], (b) the velocity it produces over the skyrmion, and (c) the addition of driving current. The skyrmion tends to circle around the defect in a counter-clockwise motion or spirals into the defect. Phase portrait of Thiele's equation considering $f_{0,\mathrm{DM}} = 0.0015$ and driving velocities v_{HM} (d) below and (e) above the threshold value [Eq. (3.10)]. The background color indicates the speed of the skyrmion. The green dot corresponds to the defect position. The red dot (cross) indicates the attractor (saddle) point. The red arrows indicate the direction of (left) the driving current density $\mathbf{v}_{\mathrm{HM}}$ and (right) the direction of the skyrmion velocity in the absence of defects. In this particular example the driving velocity angle is $\varphi_{\mathrm{HM}} = 0$ and its modulus is (c,d) $v_{\mathrm{HM}} = 0.75 v_{\mathrm{th,\ pt}}$ and (e) $v_{\mathrm{HM}} = 1.5 v_{\mathrm{th,\ pt}}$, for (c,d) and (e) respectively. 42

3.5 Sketch of the system with a segment defect of width Δ and length l_{d}. The red dot represents the center-of-mass of the incoming skyrmion and the green segment the defect. The blue arrows are the driving velocity ($\mathbf{v}_{\mathrm{HM}}$) and the drift velocity of the skyrmion ($\mathbf{v}_{\mathrm{sk}}$). 43

3.6 Vector field corresponding to (a) the force made by an attractive finite defect segment and (b) the velocity it produces over the skyrmion. The defect length is $l_{\mathrm{d}} = 6$. The skyrmion can be pinned by a defect with a counter-clockwise spiraling motion. Phase portrait of Thiele's equation for the finite defect segment considering $v_{\mathrm{HM}} = 0.0049$ for different values of the driving current angle (c) $\varphi_{\mathrm{HM}} = 0$, (d) $\varphi_{\mathrm{HM}} = \pi/4$, and (e) $\varphi_{\mathrm{HM}} = \pi/2$. For these plots $f_{0,\mathrm{DM}}\Delta = 0.38$ and $v_{\mathrm{HM}} = 0.0049$. The rest of the parameters are the same as in Fig. 3.4. The solid purple lines correspond to trajectories of a skyrmion's center obtained by solving the LLG equation with $v_{\mathrm{HM}} = 0.0049$ and $\delta = 1.5$, for several initial positions. The rest of the parameters in the LLG equation are indicated in the text. The meaning of symbols, bars, colors, and arrows is the same as in Fig. 3.4. 45

3.7 (a) Position of the spiral sink (red dots) and the saddle points (red crosses) for different driving current angles φ_{HM}. The defect segment is indicated by the horizontal green line. (b) Threshold velocity as a function of the defect size l_{d} [Eq. (3.17)] for $\varphi_{\mathrm{HM}} = \pi/4$ (blue squares) and $\varphi_{\mathrm{HM}} = 3\pi/8$ (black triangles). The vertical line indicates the defect length shown in (a). The colored arrows in (a) correspond to the angles shown in (b). The parameters used are the same as in Fig. 3.6. 46

3.8 Phase portrait of Thiele's equation for an infinite attractive (a-c) or repulsive (d-f) defect line considering $v_{\mathrm{HM}} = 0.0025$ for different driving current angles (a, d) $\varphi_{\mathrm{HM}} = \pi/4$, (b,e) $\varphi_{\mathrm{HM}} = \pi/2$. For currents $v_{\mathrm{HM}} = 0.0225 \simeq 6.6 v_{\mathrm{th,line}}$ and $\varphi_{\mathrm{HM}} = \pi/2$, the skyrmion goes through the defect line for both attractive (c) and repulsive (f) line defects. The red solid (dashed) line is the guiding (saddle) nullcline. The meaning of symbols, bars, lines, colors, and arrows is the same as in Fig. 3.4. For these plots, the parameters are the same as in Fig. 3.6. 49

3.9 Vector field corresponding to (a) the force made by an attractive L-shaped defect and (b) the velocity it produces over the skyrmion. The horizontal segment length is $l_{\mathrm{d}} = 3$. (c,d) Phase portrait of Thiele's equation for an attractive L-shaped defect considering $v_{\mathrm{HM}} = 0.025$ for different driving current angles (c) $\varphi_{\mathrm{HM}} = \pi/4$ and (d) $\varphi_{\mathrm{HM}} = \pi/2$. The meaning of the symbols, bars, colors, and arrows is the same as in Fig. 3.4. For these plots, the parameters are the same as in Fig. 3.6. 50

3.10 Vector field corresponding to (a) the force made by an attractive cross defect and (b) the drift velocity it produces to the skyrmion. Phase portrait of Thiele's equation for an attractive (c,d) or repulsive (e,f) defect cross, considering $v_{\mathrm{HM}} = 0.0025$ with different driving current angles (c,e) $\varphi_{\mathrm{HM}} = 0$ and (d,f) $\varphi_{\mathrm{HM}} = \pi/4$. The meaning of symbols, bars, colors, and arrows is the same as in Fig. 3.9. For these plots, the parameters are the same as in Fig. 3.6. 51

3.11 Illustration of the grid defect system. The defect lines that form the periodic grid are shown in green. The defect lines are separated a distance δ_x (δ_y) in the X (Y) axis. The blue arrow is the driving velocity ($\mathbf{v}_{\mathrm{HM}}$) applied at an angle φ_{HM}. . . . 52

3.12 Comparison of the proposed Gaussian defect (solid black line) with the force arising from an atomistic variation of the DM parameter[89] (dashed red line) for (a) a local defect and (b) a line defect. The parameters used are $\lambda_0 = 1/\sqrt{5}$ and $\delta = 2$. A negative force points towards the defect. In (a) the forces are scaled so their maximum is 1. The same scaling is kept in (b). 53

3.13 Vector fields of (a) the force $\mathbf{f}^g_{\rm grid}$ [Eq. (3.31)] produced by a grid defect and (b) the drift velocity it produces. Phase portrait of Thiele's equation for an attractive (c-e) or repulsive (f-h) defect lines considering a driving current $v_{\rm HM} = 0.0049 < v_{\rm th,grid}$ with different incident angles: (c, f) $\varphi_{\rm HM} = 0$ and (d,g) $\varphi_{\rm HM} = \pi/4$. For currents $v_{\rm HM} = 0.0098 > v_{\rm th,grid}$, the skyrmion goes through the defect line for both attractive (e) and repulsive (h) defects. The solid purple lines in (c) and (e) correspond to trajectories of a skyrmion center obtained by solving the LLG equation for several initial positions. For simplicity, these are shown in two cases, (c) and (e), as a similar agreement is also found for the rest. The meaning of symbols, bars, colors, and arrows is the same as in Fig. 3.4 (for simplicity we have only plotted the critical points in one cell as the system is periodic). For these particular examples $f^g_0/\Delta = 0.05$, $\lambda_0 = 1$, $\delta_x = \delta_y = 2.8$, and the micromagnetic simulated defects correspond to $\delta = 1.2$ (purple lines). The rest of the parameters are the same as in Fig. 3.6. 56

4.1 (a) Sketch of the studied hybrid systems: A superconducting element (gray) coaxial to a ferromagnetic element (light blue) with iDM interaction due to two different attached heavy metal layers (light orange). Ferromagnetic and superconducting elements are separated by a distance d. Both plates are considered ultrathin. (b) Sketch of some possible stable skyrmionic structures in a ferromagnetic disk.[55] The colors represent the z-component of the magnetization and the arrows the local magnetization along the radius. 63

4.2 (Left) Normalized averaged z-component of the normalized magnetization, (center) skyrmion number, and (right) normalized ferromagnetic energy, of all the stable magnetic states for different applied fields, in the presence [(a-c)] or absence [(d-f)] of a SC. The stable states found are the uniform (red), skyrmion (green), and 2π (blue) states. A sketch of the magnetization distribution is shown in the magnetization (left) panels. 73

4.3 (Left) Sketch of the distorted applied field lines (black) due to the presence of a SC element (dark gray). A FM (brown) is placed on top of the SC as in Fig. 4.1 and will be perturbed due to the external field lines. (Right) Sketch of the magnetization distribution of the FM in the skyrmion state as a function of the applied field when a SC is present or not [(c) and (b) respectively]. As can be seen when a SC is present the outermost moments are tilted inwards as compared to when there is no SC. The colored arrows represent the z-component of the magnetization (red-green-blue from $m_z = 1$ to -1). The field lines are depicted in light gray. 74

4.4 Normalized averaged z-component of the normalized magnetization of all the stable magnetic states, for different applied fields, in the presence (a,b) or absence (c,d) of a SC. The stable states are fixing the central magnetic moment $m_z = \hat{\boldsymbol{z}}$ or the central derivative to zero, for the left (a,c) and right (b,d) plots respectively. For the left plots, the stable states found are the uniform (red), skyrmion (green), and 2π (blue) states with both polarities. The negative polarities are denoted with lighter colors. In (e) some magnetization distributions are plotted after fixing the central moment (lighter colors) or fixing the central derivative (darker colors). The skyrmion state (green dots) and the 2π state (blue triangles) are found at $h_\mathrm{a} = -2.5$ and $h_\mathrm{a} = 0.975$, respectively. These fields correspond to the destabilizing field of the structures when fixing the derivative. The dashed lines are plotted for clarity. 75

4.5 Normalized current distribution for two different applied fields when the superconducting currents are not affected by the FM (black) or are affected by a uniform (red), skyrmion (green), or 2π (blue) states. For $\rho \lesssim R_f$ the currents vary significantly. The inset shows a zoom of the marked region of the main plot ($\rho \lesssim 1.25R_f$). 76

4.6 MEP calculated using GNEB showing the energy for the transitions occurring near the destabilization field of uniform (a) and skyrmion (b) states, in the presence of a SC. The dots indicate the images computed along the converged path. The arrows indicate the most probable transition found. (c) Normalized energy barrier as a function of the applied field studying the uniform and skyrmion destabilization. The destabilizing fields at which the structures become unstable are highlighted in red. 77

4.7 Sketch of the different magnetization distributions as a function of ρ for the (a) uniform , (b) skyrmion , and (c) 2π states. The colors represent the z-component of the magnetization. 78

4.8 (a) MEP calculated using GNEB showing the activation energy for the transitions, when there is no SC present, occurring at applied fields where the three states are stable ($0.025 < h_\mathrm{a} < 0.1$). The dots indicate the images computed along the converged path. The arrows indicate the most probable transition found for that applied field. (b) Energy barrier as a function of the applied field studying the uniform and skyrmion destabilization. The destabilizing fields at which the studied structures become unstable are highlighted in red. 79

4.9 Averaged z-component of the normalized magnetization during the hysteresis loop. (a) Outer hysteresis loop with field ranging from ±2.5. (b) Inner hysteresis loop with field ranging from ±1. The vertical lines are in gradient colors to indicate transitions between magnetization states: red for the uniform, green for the skyrmion, and blue for the 2π state. 81

4.10 Averaged z-component of the normalized magnetization during the hysteresis loop without a SC. Hysteresis loop with field ranging from ±2.5. The vertical lines are in gradient colors to indicate transitions between magnetization states: red for the uniform and green for the skyrmion. 81

4.11 Magnetization distributions, starting in the skyrmion state, for different applied fields (a) with a SC present in the system and (b) without it. The applied fields shown are $h_\mathrm{a} = 0$ (purple), $h_\mathrm{a} = 0.06$ (blue), $h_\mathrm{a} = 0.12$ (green), and $h_\mathrm{a} = 0.2$ (orange). These were chosen near the skyrmion-to-uniform transition when there is no SC. When a SC is present, the magnetization tends to wind up more. Without a SC, the magnetization unwinds and transitions to the uniform state. 82

4.12 Sketch of the FSH. The behavior of the system depends on whether the FM (brown) is on top of the SC (gray) or below it, separated by the black dashed line. 83

4.13 Force between the FM and SC elements (a) with no applied field, $h_\mathrm{a} = 0$, and (b) with $h_\mathrm{a} = 0.1$. A positive (negative) force is repulsive (attractive). The magnetization states are the uniform (red), the skyrmion (green), and the 2π (blue). The darker (lighter) colors symbolize that the FM is above (below) the SC [see Fig. 4.12 for a sketch]. The vertical dotted line represents the closest distance between the elements considered. In (a) we show an inset of the red region. . . . 83

4.14 Field lines produced by the shielding currents in a SC (light gray) when the FM (brown) is (a) on top or (b) below it. The FM is in the uniform state [see Fig. 4.1(b)]. When the FM is on top of the SC, the edge magnetization is tilted inwards (compared to when there is no SC) due to the fields' radial component, opposing the iDM-imposed chirality. In contrast, when the FM is below the SC, the stray field helps the iDM interaction to tilt the magnetization, favoring the destabilization of the uniform state. The z-component of the magnetization is color coded as in Fig. 4.7. 84

4.15 Radial component of the skyrmion magnetization (black) and the SC's stray field (red), when $h_\mathrm{a} = 0.1$ and $d = 0.3R_f$. The solid (dashed) lines represent the case of a FM on top (below) of a SC. The radial component of the field induces a bias that not only changes the skyrmion shape, but also can induce repulsion between the FM and SC elements, as seen in Fig. 4.13. 85

4.16 Sketch of the SC (light gray) current profile of a +PV (-PV) are shown in red (blue). The symbols and colors are the same as in Fig. 4.12. 85

4.17 Force between the FM and SC elements without applied field when a PV with (a) positive or (b) negative polarity. A positive (negative) force is repulsive (attractive). In (a) and (b) we show an inset of the red region. Note that there is an additional change in the force sign, better seen in the insets. The magnetization states are the skyrmion (green) and the 2π (blue) states. The darker (lighter) colors symbolize that the FM is above (below) the SC. The vertical dotted line represents the closest distance between the elements considered. 86

4.18 Summary sketches of the interaction of (a) a skyrmion and (b) a 2π state with a PV, at zero applied field and different separation distances. The FM (brown) can be on top or below the SC (gray). In (a) the interaction for close (left) and large distances (right) are depicted. In (b), the central column corresponds to medium distances, appearing when there is an intermediate sign change in the force. The black arrows illustrate the resulting interaction force. 87

4.19 (a) Sketch of the toy model when a PV is present in the SC. The stray field of the PV currents can be approximated by that of a magnetic monopole^{338} [red (+PV) and blue (-PV) semicircles], depicted with the arrows. The behavior of the system depends on whether the FM is on top of the SC or below it, separated in the sketch by the black dashed line. In the toy model, the magnetization only points in the $\pm\hat{\mathbf{z}}$ direction. The z-component of the magnetization for the (b) skyrmion and (c) 2π states are represented, with the toy model's simplification shown with dashed lines. 89

4.20 (a) Force between the FM, in the skyrmion state, and SC elements without applied field when a +PV is present. A positive (negative) force is repulsive (attractive). Note that for $R_{\text{sk}} = 0, 1$ (black and pink lines) the uniform state ($m_z(\rho) = \pm 1$) is found. (b) Example of a possible magnetization distribution of the FM in the skyrmion state. When close to a -PV, depending on whether the FM is on top (blue) or below (pink), the radial component of the PV's stray field induces a bias over the magnetization. If the FM is below the SC (pink) the radial and z-component of the stray field compete with each other. For a sketch of the PV's stray field see Fig. 4.19(a). 90

4.21 (a) Sketch of a hybrid system formed by a FM (brown) and a SC (light gray) rings with inner radius $R_{f,i}$ and $R_{s,i}$, respectively. A superconducting element (gray) is coaxial to a ferromagnetic element (light blue) with iDM interaction due to two different attached heavy metal layers (light orange). The depiction of ring-shaped heavy-metal layers is for illustration purposes. (b) Illustration of the magnetic field lines (in black) in the presence of a ring-shaped SC when an external uniform field is applied. 91

B.1 Illustration of the Forward Flux Sampling method, where the order parameter defining the interfaces λ_i between state A (metastable skyrmion) and state B (FM state). (a) First simulation to compute the rate of crossing the first contour level λ_1. (b) Trial runs at subsequent interfaces. Adapted from Ref. [159]. 100

C.1 Simulations considering the demagnetizing field of the FM sample for different applied fields: (a) $h_\text{a} = -0.25$, (b) $h_\text{a} = 0$, (c) $h_\text{a} = 0.25$, and (d) $h_\text{a} = 0.75$. The darker (lighter) colors were computed with (without) SC. We find the uniform (red), skyrmion (green), and 2π (blue) states to be stable. The demagnetizing field (solid lines) matches the magnetization distribution (triangles) closely, with the largest discrepancy at the edge of the sample. The hysteresis loops closely match the ones simulated with the results presented in Fig. 4.2. 102

C.2 Force between the FM, in the 2π state, and SC elements without applied field when a +PV is present. A positive (negative) force is repulsive (attractive). We show the force when the inner magnetization disk R_1 is (a) $R_1 = 0.1R_f$ or (b) $R_1 = 0.2R_f$. The insets show the region marked in red were force sign changes are found. 103

C.3 Force between the FM and SC elements with the applied field, $h_\mathrm{a} = 0.1$, when a PV with (a) positive or (b) negative polarity is present. A positive (negative) force is repulsive (attractive). In (a) and (b) we show an inset of the red region. The magnetization states are the skyrmion (green) and the 2π (blue) states. The darker (lighter) colors symbolize that the FM is above (below) the SC. The vertical dotted line represents the closest distance between the elements considered. . . . 105

Bibliography

[1] H. J. Richter. Recent advances in the recording physics of thin-film media. *J. Phys. D: Appl. Phys.*, 32(21):R147, Nov 1999. 10.1088/0022-3727/32/21/201.

[2] H. J. Richter. The transition from longitudinal to perpendicular recording. *J. Phys. D: Appl. Phys.*, 40(9):R149, Apr 2007. 10.1088/0022-3727/40/9/R01.

[3] Y. Shiroishi, K. Fukuda, et al. Future options for hdd storage. *IEEE Trans. Magn.*, 45(10):3816–3822, 2009. 10.1109/TMAG.2009.2024879.

[4] R. L. Stamps, S. Breitkreutz, et al. The 2014 magnetism roadmap. *J. Phys. D: Appl. Phys.*, 47(33):333001, Jul 2014. 10.1088/0022-3727/47/33/333001.

[5] W.-H. Hsu and R. H. Victora. Heat-assisted magnetic recording — micromagnetic modeling of recording media and areal density: A review. *J. Magn. Magn. Mater.*, 563:169973, Dec 2022.

[6] N. Jones. How to stop data centres from gobbling up the world's electricity. *Nature*, 561:163–166, 9 2018. 10.1038/D41586-018-06610-Y.

[7] S. Bhatti, R. Sbiaa, et al. Spintronics based random access memory: a review. *Mater. Today*, 20:530–548, 11 2017. 10.1016/J.MATTOD.2017.07.007.

[8] I. Žutić, J. Fabian, and S. D. Sarma. Spintronics: Fundamentals and applications. *Rev. Mod. Phys.*, 76:323, 4 2004. 10.1103/RevModPhys.76.323.

[9] M. N. Baibich, J. M. Broto, et al. Giant magnetoresistance of (001)fe/(001)cr magnetic superlattices. *Phys. Rev. Lett.*, 61:2472–2475, Nov 1988. 10.1103/PhysRevLett.61.2472.

[10] G. Binasch, P. Grünberg, et al. Enhanced magnetoresistance in layered magnetic structures with antiferromagnetic interlayer exchange. *Phys. Rev. B*, 39:4828–4830, Mar 1989. 10.1103/PhysRevB.39.4828.

[11] S. S. Parkin, M. Hayashi, and L. Thomas. Magnetic domain-wall racetrack memory. *Science*, 320:190–194, 4 2008. 10.1126/science.1145799.

[12] S. Woo, K. Litzius, et al. Observation of room-temperature magnetic skyrmions and their current-driven dynamics in ultrathin metallic ferromagnets. *Nat. Mater.*, 15(5):501–506, feb 2016. 10.1038/nmat4593.

[13] N. Nagaosa and Y. Tokura. Topological properties and dynamics of magnetic skyrmions. *Nat. Nanotechnol.*, 8(12):899–911, dec 2013. 10.1038/nnano.2013.243.

[14] R. Wiesendanger. Nanoscale magnetic skyrmions in metallic films and multilayers: a new twist for spintronics. *Nat. Rev. Mater.*, 1(7):16044, jul 2016. 10.1038/natrevmats.2016.44.

[15] A. Fert, N. Reyren, and V. Cros. Magnetic skyrmions: Adv. Phys. and potential applications. *Nat. Rev. Mater.*, 2(7):17031, jun 2017. 10.1038/natrevmats.2017.31.

[16] T. H. R. Skyrme and B. F. J. Schonland. A non-linear field theory. *Proc. R. Soc. A: Math. Phys. Eng. Sci.*, 260(1300):127–138, 1961. 10.1098/rspa.1961.0018.

[17] D. C. Wright and N. D. Mermin. Crystalline liquids: the blue phases. *Rev. Mod. Phys.*, 61:385–432, Apr 1989. 10.1103/RevModPhys.61.385.

[18] T.-L. Ho. Spinor bose condensates in optical traps. *Phys. Rev. Lett.*, 81:742–745, Jul 1998. 10.1103/PhysRevLett.81.742.

[19] S. L. Sondhi, A. Karlhede, et al. Skyrmions and the crossover from the integer to fractional quantum hall effect at small zeeman energies. *Phys. Rev. B*, 47:16419–16426, Jun 1993. 10.1103/PhysRevB.47.16419.

[20] M. Abolfath, J. J. Palacios, et al. Critical comparison of classical field theory and microscopic wave functions for skyrmions in quantum hall ferromagnets. *Phys. Rev. B*, 56:6795–6804, Sep 1997. 10.1103/PhysRevB.56.6795.

[21] J. Brandão, D. A. Dugato, et al. Observation of magnetic skyrmions in unpatterned symmetric multilayers at room temperature and zero magnetic field. *Sci. Rep.*, 9, 3 2019. 10.1038/s41598-019-40705-4.

[22] D. Chakrabartty, S. Jamaluddin, et al. Tunable room temperature magnetic skyrmions in centrosymmetric kagome magnet Mn4Ga2Sn. *Commun. Phys.*, 5, 7 2022. 10.1038/s42005-022-00971-7.

[23] Y. Tokura and N. Kanazawa. Magnetic Skyrmion Materials. *Chem. Rev.*, 121, Mar 2021. 10.1021/acs.chemrev.0c00297.

[24] A. N. Bogdanov and D. Yablonskii. Thermodynamically stable “vortices” in magnetically ordered crystals. the mixed state of magnets. *Zh. Eksp. Teor. Fiz*, 95(1):178, 1989.

[25] S. Mühlbauer, B. Binz, et al. Skyrmion lattice in a chiral magnet. *Science*, 323(5916):915–9, feb 2009. 10.1126/science.1166767.

[26] X. Z. Yu, Y. Onose, et al. Real-space observation of a two-dimensional skyrmion crystal. *Nature*, 465(7300):901–4, jun 2010. 10.1038/nature09124.

[27] A. Fert, V. Cros, and J. Sampaio. Skyrmions on the track. *Nat. Nanotechnol.*, 8(3):152–6, mar 2013. 10.1038/nnano.2013.29.

[28] K. Everschor-Sitte, J. Masell, et al. Perspective: Magnetic skyrmions—Overview of recent progress in an active research field. *J. Appl. Phys.*, 124(24):240901, 2018. 10.1063/1.5048972.

[29] Y. Zhou. Magnetic skyrmions: intriguing physics and new spintronic device concepts. *Natl. Sci.*, 6(2):210–212, 10 2018. 10.1093/nsr/nwy109.

[30] B. Göbel, A. Mook, et al. Overcoming the speed limit in skyrmion racetrack devices by suppressing the skyrmion Hall effect. *Phys. Rev. B*, 99(2):020405, jan 2019. 10.1103/PhysRevB.99.020405.

[31] T. Dohi, R. M. Reeve, and M. Kläui. Thin film skyrmionics. *Annual Review of Condensed Matter Physics*, 13(1):73–95, 2022. 10.1146/annurev-conmatphys-031620-110344.

[32] X. Zhang, M. Ezawa, and Y. Zhou. Magnetic skyrmion logic gates: conversion, duplication and merging of skyrmions. *Sci. Rep.*, 5:9400, jan 2015. 10.1038/srep09400.

[33] X. Zhang, Y. Zhou, et al. Magnetic skyrmion transistor: skyrmion motion in a voltage-gated nanotrack. *Sci. Rep.*, 5:11369, jan 2015. 10.1038/srep11369.

[34] S. Zhang, J. Wang, et al. Current-induced magnetic skyrmions oscillator. *New J. Phys.*, 17(2):023061, feb 2015. 10.1088/1367-2630/17/2/023061.

[35] G. Bourianoff, D. Pinna, et al. Potential implementation of reservoir computing models based on magnetic skyrmions. *AIP Adv.*, 8(5):055602, may 2018. 10.1063/1.5006918.

[36] D. Pinna, F. Abreu Araujo, et al. Skyrmion gas manipulation for probabilistic computing. *Phys. Rev. Applied*, 9:064018, Jun 2018. 10.1103/PhysRevApplied.9.064018.

[37] J. Zázvorka, F. Jakobs, et al. Thermal skyrmion diffusion used in a reshuffler device. *Nat. Nanotechnol.*, 14(7):658–661, apr 2019. 10.1038/s41565-019-0436-8.

[38] N. Romming, A. Kubetzka, et al. Field-dependent size and shape of single magnetic Skyrmions. *Phys. Rev. Lett.*, 114(17):177203, may 2015. 10.1103/PhysRevLett.114.177203.

[39] R. Tomasello, A. Giordano, et al. Micromagnetic understanding of the skyrmion Hall angle current dependence in perpendicularly magnetized ferromagnets. *Phys. Rev. B*, 98(22):224418, dec 2018. 10.1103/PhysRevB.98.224418.

[40] O. Boulle, J. Vogel, et al. Room-temperature chiral magnetic skyrmions in ultrathin magnetic nanostructures. *Nat. Nanotechnol.*, 11(5):449–454, jan 2016. 10.1038/nnano.2015.315.

[41] D. Cortés-Ortuño, W. Wang, et al. Thermal stability and topological protection of skyrmions in nanotracks. *Sci. Rep.*, 7:4060, 2017. 10.1038/s41598-017-03391-8.

[42] A. S. Varentcova, S. von Malottki, et al. Toward room-temperature nanoscale skyrmions in ultrathin films. *npj Computational Materials*, 6:1–11, 12 2020. 10.1038/s41524-020-00453-w.

[43] M. Hervé, B. Dupé, et al. Stabilizing spin spirals and isolated skyrmions at low magnetic field exploiting vanishing magnetic anisotropy. *Nat. Commun.*, 9(1):1015, dec 2018. 10.1038/s41467-018-03240-w.

[44] S. Heinze, K. von Bergmann, et al. Spontaneous atomic-scale magnetic skyrmion lattice in two dimensions. *Nature Physics*, 7(9):713–718, sep 2011. 10.1038/nphys2045.

[45] A. Sonntag, J. Hermenau, et al. Thermal Stability of an Interface-Stabilized Skyrmion Lattice. *Phys. Rev. Lett.*, 113(7):077202, aug 2014. 10.1103/PhysRevLett.113.077202.

[46] C. Moreau-Luchaire, C. Moutafis, et al. Additive interfacial chiral interaction in multilayers for stabilization of small individual skyrmions at room temperature. *Nat. Nanotechnol.*, 11:444–448, jan 2016. 10.1038/nnano.2015.313.

[47] V. P. Kravchuk, D. D. Sheka, et al. Multiplet of skyrmion states on a curvilinear defect: Reconfigurable skyrmion lattices. *Phys.*

Rev. Lett., 120:067201, Feb 2018. 10.1103/PhysRevLett.120.067201.

[48] V. L. Carvalho-Santos, M. A. Castro, et al. Skyrmion propagation along curved racetracks. *Appl. Phys. Lett.*, 118(17):172407, 2021. 10.1063/5.0045969.

[49] Y. Gaididei, V. P. Kravchuk, and D. D. Sheka. Curvature effects in thin magnetic shells. *Phys. Rev. Lett.*, 112:257203, Jun 2014. 10.1103/PhysRevLett.112.257203.

[50] R. Streubel, P. Fischer, et al. Magnetism in curved geometries. *J. Phys. D: Appl. Phys.*, 49(36):363001, aug 2016. 10.1088/0022-3727/49/36/363001.

[51] V. P. Kravchuk, U. K. Rößler, et al. Topologically stable magnetization states on a spherical shell: Curvature-stabilized skyrmions. *Phys. Rev. B*, 94:144402, Oct 2016. 10.1103/PhysRevB.94.144402.

[52] D. D. Sheka, O. V. Pylypovskyi, et al. Nonlocal chiral symmetry breaking in curvilinear magnetic shells. *Commun. Phys.*, 3(1), jul 2020. 10.1038/s42005-020-0387-2.

[53] J. Yang, C. Abert, et al. Intrinsic DMI-free skyrmion formation and robust dynamic behaviors in magnetic hemispherical shells. *Sci. Rep.*, 11(1), feb 2021. 10.1038/s41598-021-81624-7.

[54] E. Berganza, J. A. Fernandez-Roldan, et al. 3d quasi-skyrmions in thick cylindrical and dome-shape soft nanodots. *Sci. Rep.*, 12:1–9, 3 2022. 10.1038/s41598-022-07407-w.

[55] S. Rohart and A. Thiaville. Skyrmion confinement in ultrathin film nanostructures in the presence of Dzyaloshinskii-Moriya interaction. *Phys. Rev. B*, 88(18):184422, nov 2013. 10.1103/PhysRevB.88.184422.

[56] C. Back, V. Cros, et al. The 2020 skyrmionics roadmap. *J. Phys. D: Appl. Phys.*, 53(36):363001, sep 2020. 10.1088/1361-6463/ab8418.

[57] A. Aharoni. *Introduction to the theory of ferromagnetism.* Oxford University Press, 2000.

[58] W. F. Brown. *Micromagnetics.* New York: Wiley, 1963.

[59] A. Thiele. Steady-State Motion of Magnetic Domains. *Phys. Rev. Lett.*, 30(6):230–233, feb 1973. 10.1103/PhysRevLett.30.230.

[60] J. Sampaio, V. Cros, et al. Nucleation, stability and current-induced motion of isolated magnetic skyrmions in nanostructures. *Nat. Nanotechnol.*, 8(3):839–844, oct 2013. 10.1038/nnano.2013.210.

[61] S. Finizio, K. Zeissler, et al. Deterministic Field-Free Skyrmion Nucleation at a Nanoengineered Injector Device. *Nano Lett.*, 19:7246–7255, 10 2019. 10.1021/acs.nanolett.9b02840.

[62] G. Finocchio, F. Büttner, et al. Magnetic skyrmions: from fundamental to applications. *J. Phys. D: Appl. Phys.*, 49:423001, 9 2016. 10.1088/0022-3727/49/42/423001.

[63] F. Büttner, I. Lemesh, et al. Field-free deterministic ultrafast creation of magnetic skyrmions by spin-orbit torques. *Nat. Nanotechnol.*, 12, 2017. 10.1038/nnano.2017.178.

[64] R. Juge, K. Bairagi, et al. Helium ions put magnetic skyrmions on the track. *Nano Lett.*, 21:2989–2996, 4 2021. 10.1021/acs.nanolett.1c00136.

[65] Y. Zhou, E. Iacocca, et al. Dynamically stabilized magnetic skyrmions. *Nat. Commun.*, 6:1–10, 9 2015. 10.1038/ncomms9193.

[66] F. Tejo, D. Toneto, et al. Stabilization of magnetic skyrmions on arrays of self-assembled hexagonal nanodomes for magnetic recording applications. *ACS Appl. Mater. Interfaces*, 12:53454–53461, 11 2020. 10.1021/acs.nanolett.1c00136.

[67] S. G. Je, D. Thian, et al. Targeted writing and deleting of magnetic skyrmions in two-terminal nanowire devices. *Nano Lett.*, 21:1253–1259, 2 2021. 10.1021/acs.nanolett.0c03686.

[68] A. Casiraghi, H. Corte-León, et al. Individual skyrmion manipulation by local magnetic field gradients. *Commun. Phys.*, 2:1–9, 11 2019. 10.1038/s42005-019-0242-5.

[69] N. Del-Valle, S. Agramunt-Puig, et al. Imprinting skyrmions in thin films by ferromagnetic and superconducting templates. *Appl. Phys. Lett.*, 107(13), 2015. 10.1063/1.4932090.

[70] S. Woo, K. M. Song, et al. Current-driven dynamics and inhibition of the skyrmion hall effect of ferrimagnetic skyrmions in GdFeCo films. *Nat. Commun.*, 9:1–8, 3 2018. 10.1038/s41467-018-03378-7.

[71] N. S. Kiselev, A. N. Bogdanov, et al. Chiral skyrmions in thin magnetic films: new objects for magnetic storage technologies? *J. Phys. D: Appl. Phys.*, 44:392001, 9 2011. 10.1088/0022-3727/44/39/392001.

[72] B. Zhang, W. Wang, et al. Microwave-induced dynamic switching of magnetic skyrmion cores in nanodots. *Appl. Phys. Lett.*, 106(10):102401, mar 2015. 10.1063/1.4914496.

[73] I. Purnama, W. L. Gan, et al. Guided current-induced skyrmion motion in 1D potential well. *Sci. Rep.*, 5(1):10620, sep 2015. 10.1038/srep10620.

[74] S. Woo, K. M. Song, et al. Spin-orbit torque-driven skyrmion dynamics revealed by time-resolved X-ray microscopy. *Nat. Commun.*, 8:1–8, 5 2017. 10.1038/ncomms15573.

[75] C. Navau, N. Del-Valle, and A. Sanchez. Analytical trajectories of skyrmions in confined geometries: Skyrmionic racetracks and nano-oscillators. *Phys. Rev. B*, 94(18):184104, nov 2016. 10.1103/PhysRevB.94.184104.

[76] V. L. Carvalho-Santos, M. A. Castro, et al. Skyrmion propagation along curved racetracks. *Appl. Phys. Lett.*, 118:172407, 4 2021. 10.1063/5.0045969.

[77] R. Tomasello, E. Martinez, et al. A strategy for the design of skyrmion racetrack memories. *Sci. Rep.*, 4:6784, jan 2014. 10.1038/srep06784.

[78] J. Iwasaki, M. Mochizuki, and N. Nagaosa. Universal current-velocity relation of skyrmion motion in chiral magnets. *Nat. Commun.*, 4:1463, jan 2013. 10.1038/ncomms2442.

[79] C. Jin, C. Song, et al. Dynamics of antiferromagnetic skyrmion driven by the spin Hall effect. *Appl. Phys. Lett.*, 109(18):182404, oct 2016. 10.1063/1.4967006.

[80] S. K. Kim, K. J. Lee, and Y. Tserkovnyak. Self-focusing skyrmion racetracks in ferrimagnets. *Phys. Rev. B*, 95(14):140404, apr 2017. 10.1103/PhysRevB.95.140404.

[81] X. Zhang, M. Ezawa, et al. All-magnetic control of skyrmions in nanowires by a spin wave. *Nanotechnology*, 26(22):225701, jun 2015. 10.1088/0957-4484/26/22/225701.

[82] Y. Zhang, S. Luo, et al. Magnetic skyrmions without the skyrmion Hall effect in a magnetic nanotrack with perpendicular anisotropy. *Nanoscale*, 9(29):10212–10218, jul 2017. 10.1039/c7nr01980g.

[83] P. Upadhyaya, G. Yu, et al. Electric-field guiding of magnetic skyrmions. *Phys. Rev. B*, 92(13):134411, oct 2015. 10.1103/PhysRevB.92.134411.

[84] D. Suess, C. Vogler, et al. A repulsive skyrmion chain as a guiding track for a racetrack memory. *AIP Adv.*, 8:115301, 11 2018. 10.1063/1.4993957.

[85] S. Li, J. Xia, et al. Dynamics of a magnetic skyrmionium driven by spin waves. *Appl. Phys. Lett.*, 112(14):142404, apr 2018. 10.1063/1.5026632.

[86] J. Müller. Magnetic skyrmions on a two-lane racetrack. *New J. Phys.*, 19(2):025002, feb 2017. 10.1088/1367-2630/aa5b55.

[87] N. Del-Valle, J. Castell-Queralt, et al. Defect modeling in skyrmionic ferromagnetic systems. *APL Mater.*, 10(1):010702, 2022. 10.1063/5.0072709.

[88] C. Cheng, Z. Yan, et al. Elliptical skyrmion moving along a track without transverse speed. *Phys. Rev. B*, 104:174409, 11 2021. 10.1103/PhysRevB.104.174409.

[89] C. Navau, N. Del-Valle, and A. Sanchez. Interaction of isolated skyrmions with point and linear defects. *J. Magn. Magn. Mater.*, 465:709–715, nov 2018. 10.1016/j.jmmm.2018.06.044.

[90] H. C. Choi, S.-Z. Lin, and J.-X. Zhu. Density functional theory study of skyrmion pinning by atomic defects in MnSi. *Phys. Rev. B*, 93(11):115112, mar 2016. 10.1103/PhysRevB.93.115112.

[91] C. Hanneken, A. Kubetzka, et al. Pinning and movement of individual nanoscale magnetic skyrmions via defects. *New J. Phys.*, 18(5):055009, may 2016. 10.1088/1367-2630/18/5/055009.

[92] I. Lima Fernandes, J. Bouaziz, et al. Universality of defect-skyrmion interaction profiles. *Nat. Commun.*, 9(1):4395, dec 2018. 10.1038/s41467-018-06827-5.

[93] D. Toscano, S. Leonel, et al. Building traps for skyrmions by the incorporation of magnetic defects into nanomagnets: Pinning and scattering traps by magnetic properties engineering. *J. Magn. Magn. Mater.*, 480:171–185, 2019. 10.1016/j.jmmm.2019.02.075.

[94] X. Chen, W. Kang, et al. Skyrmion dynamics in width-varying nanotracks and implications for skyrmionic applications. *Appl. Phys. Lett.*, 111(20):202406, 2017. 10.1063/1.5005953.

[95] X. Zhang, J. Xia, et al. Magnetic Skyrmion Transport in a Nanotrack With Spatially Varying Damping and Non-adiabatic

Torque. *IEEE Trans. Magn.*, pages 1–1, 2016. 10.1109/tmag.2016.2641384.

[96] I. G. Arjana, I. Lima Fernandes, et al. Subnanoscale atom-by-atom crafting of skyrmion-defect interaction profiles. *Sci. Rep.*, 10:014655, Sep 2020. 10.1038/s41598-020-71232-2.

[97] D. Stosic, T. B. Ludermir, and M. V. Milošević. Pinning of magnetic skyrmions in a monolayer Co film on Pt(111): Theoretical characterization and exemplified utilization. *Phys. Rev. B*, 96:214403, Dec 2017. 10.1103/PhysRevB.96.214403.

[98] J. Ding, X. Yang, and T. Zhu. Manipulating current induced motion of magnetic skyrmions in the magnetic nanotrack. *J. Phys. D: Appl. Phys.*, 48:115004, 2 2015. 10.1088/0022-3727/48/11/115004.

[99] J. Mulkers, B. Van Waeyenberge, and M. V. Milošević. Effects of spatially engineered Dzyaloshinskii-Moriya interaction in ferromagnetic films. *Phys. Rev. B*, 95(14):144401, apr 2017. 10.1103/PhysRevB.95.144401.

[100] A. Hrabec, N. A. Porter, et al. Measuring and tailoring the Dzyaloshinskii-Moriya interaction in perpendicularly magnetized thin films. *Phys. Rev. B*, 90(2):020402, jul 2014. 10.1103/PhysRevB.90.020402.

[101] J. C. Martinez and M. B. A. Jalil. Topological dynamics and current-induced motion in a skyrmion lattice. *New J. Phys.*, 18(3):033008, mar 2016. 10.1088/1367-2630/18/3/033008.

[102] I. Gross, W. Akhtar, et al. Skyrmion morphology in ultrathin magnetic films. *Phys. Rev. Materials*, 2:024406, Feb 2018. 10.1103/PhysRevMaterials.2.024406.

[103] A. Salimath, A. Abbout, et al. Current-driven skyrmion depinning in magnetic granular films. *Phys. Rev. B*, 99(10):104416, mar 2019. 10.1103/PhysRevB.99.104416.

[104] J.-V. Kim and M.-W. Yoo. Current-driven skyrmion dynamics in disordered films. *Appl. Phys. Lett.*, 110(13):132404, mar 2017. 10.1063/1.4979316.

[105] X. Gong, H. Y. Yuan, and X. R. Wang. Current-driven skyrmion motion in granular films. *Phys. Rev. B*, 101:064421, Feb 2020. 10.1103/PhysRevB.101.064421.

[106] C. Reichhardt and C. J. Reichhardt. Nonlinear transport, dynamic ordering, and clustering for driven skyrmions on random pinning. *Phys. Rev. B*, 99:104418, 3 2019. 10.1103/PhysRevB.99.104418.

[107] V. Raposo, R. F. Luis Martinez, and E. Martinez. Current-driven skyrmion motion along disordered magnetic tracks. *AIP Adv.*, 7(5):056017, may 2017. 10.1063/1.4975658.

[108] W. Koshibae and N. Nagaosa. Theory of current-driven skyrmions in disordered magnets. *Sci. Rep.*, 8:1–13, 4 2018. 10.1038/s41598-018-24693-5.

[109] C. Reichhardt, D. Ray, and C. J. O. Reichhardt. Collective Transport Properties of Driven Skyrmions with Random Disorder. *Phys. Rev. Lett.*, 114(21):217202, may 2015. 10.1103/PhysRevLett.114.217202.

[110] C. Reichhardt and C. J. Olson Reichhardt. Noise fluctuations and drive dependence of the skyrmion Hall effect in disordered systems. *New J. Phys.*, 18(9):095005, sep 2016. 10.1088/1367-2630/18/9/095005.

[111] B. L. Brown, U. C. Täuber, and M. Pleimling. Skyrmion relaxation dynamics in the presence of quenched disorder. *Phys. Rev. B*, 100:024410, Jul 2019. 10.1103/PhysRevB.100.024410.

[112] S. A. Díaz, C. Reichhardt, et al. Avalanches and criticality in driven magnetic skyrmions. *Phys. Rev. Lett.*, 120:117203, 3 2018. 10.1103/PhysRevLett.120.117203.

[113] X. Wang, W. L. Gan, et al. Efficient skyrmion transport mediated by a voltage controlled magnetic anisotropy gradient. *Nanoscale*, 10(2):733–740, jan 2018. 10.1039/C7NR06482A.

[114] B. W. Walker, C. Cui, et al. Skyrmion logic clocked via voltage-controlled magnetic anisotropy. *Appl. Phys. Lett.*, 118(19):192404, 2021. 10.1063/5.0049024.

[115] X. Chen, W. Kang, et al. Complementary Skyrmion Racetrack Memory Enables Voltage-Controlled Local Data Update Functionality. *IEEE Trans Electron Devices*, 65(10):4667–4673, oct 2018. 10.1109/TED.2018.2866912.

[116] W. Kang, Y. Huang, et al. Voltage Controlled Magnetic Skyrmion Motion for Racetrack Memory. *Sci. Rep.*, 6(1):23164, sep 2016. 10.1038/srep23164.

[117] R. Loreto, X. Zhang, et al. Manipulation of magnetic skyrmions in a locally modified synthetic antiferromagnetic racetrack. *J. Magn. Magn. Mater.*, 482:155–159, jul 2019. 10.1016/j.jmmm.2019.03.030.

[118] C. Song, C. Jin, et al. Skyrmion-based multi-channel racetrack. *Appl. Phys. Lett.*, 111(19):192413, nov 2017. 10.1063/1.4994093.

[119] X. Zhang, G. P. Zhao, et al. Skyrmion-skyrmion and skyrmion-edge repulsions in skyrmion-based racetrack memory. *Sci. Rep.*, 5:7643, jan 2015. 10.1038/srep07643.

[120] M. G. Morshed, H. Vakili, and A. W. Ghosh. Positional stability of skyrmions in a racetrack memory with notched geometry. *Phys. Rev. Appl.*, 17:064019, Jun 2022. 10.1103/PhysRevApplied.17.064019.

[121] D. Suess, C. Vogler, et al. Spin Torque Efficiency and Analytic Error Rate Estimates of Skyrmion Racetrack Memory. *Sci. Rep.*, 9, 2019. 10.1038/s41598-019-41062-y.

[122] J. Iwasaki, M. Mochizuki, and N. Nagaosa. Current-induced skyrmion dynamics in constricted geometries. *Nat. Nanotechnol.*, 8(10):742–7, oct 2013. 10.1038/nnano.2013.176.

[123] S. Luo, M. Song, et al. Reconfigurable skyrmion logic gates. *Nano Lett.*, 18(2):1180–1184, 2018. 10.1021/acs.nanolett.7b04722. PMID: 29350935.

[124] M. Chauwin, X. Hu, et al. Skyrmion logic system for large-scale reversible computation. *Phys. Rev. Applied*, 12:064053, Dec 2019. 10.1103/PhysRevApplied.12.064053.

[125] K.-W. Moon, D.-H. Kim, et al. Skyrmion motion driven by oscillating magnetic field. *Sci. Rep.*, 6, 2 2016. 10.1038/srep20360.

[126] C. Jin, C. Song, et al. Topological trajectories of a magnetic skyrmion with an in-plane microwave magnetic field. *J. Appl. Phys.*, 122(22):223901, dec 2017. 10.1063/1.4998269.

[127] C. Wang, D. Xiao, et al. Manipulating and trapping skyrmions by magnetic field gradients. *New J. Phys.*, 19(8):083008, aug 2017. 10.1088/1367-2630/aa7812.

[128] J. J. Liang, J. H. Yu, et al. Magnetic field gradient driven dynamics of isolated skyrmions and antiskyrmions in frustrated magnets. *New J. Phys.*, 20:053037, 5 2018. 10.1088/1367-2630/aac24c.

[129] S. L. Zhang, W. W. Wang, et al. Manipulation of skyrmion motion by magnetic field gradients. *Nat. Commun.*, 9(1):2115, dec 2018. 10.1038/s41467-018-04563-4.

[130] R. Khoshlahni, A. Qaiumzadeh, et al. Ultrafast generation and dynamics of isolated skyrmions in antiferromagnetic insulators. *Phys. Rev. B*, 99:054423, Feb 2019. 10.1103/PhysRevB.99.054423.

[131] L. Kong and J. Zang. Dynamics of an Insulating Skyrmion under a Temperature Gradient. *Phys. Rev. Lett.*, 111(6):067203, aug 2013. 10.1103/PhysRevLett.111.067203.

[132] K. Everschor, M. Garst, et al. Rotating skyrmion lattices by spin torques and field or temperature gradients. *Phys. Rev. B*, 86(5):054432, aug 2012. 10.1103/PhysRevB.86.054432.

[133] X. Zhang, M. Ezawa, et al. All-magnetic control of skyrmions in nanowires by a spin wave. *Nanotechnology*, 26(22):225701, may 2015. 10.1088/0957-4484/26/22/225701.

[134] L. Song, H. Yang, et al. A spin-wave driven skyrmion diode under transverse magnetic fields. *J. Magn. Magn. Mater.*, 532:167975, 2021. 10.1016/j.jmmm.2021.167975.

[135] J. Baumard, J. Cayssol, et al. Generation of a superconducting vortex via Néel skyrmions. *Phys. Rev. B*, 99:014511, Jan 2019. 10.1103/PhysRevB.99.014511.

[136] S. Rex, I. V. Gornyi, and A. D. Mirlin. Majorana bound states in magnetic skyrmions imposed onto a superconductor. *Phys. Rev. B*, 100:064504, Aug 2019. 10.1103/PhysRevB.100.064504.

[137] K. M. Hals, M. Schecter, and M. S. Rudner. Composite Topological Excitations in Ferromagnet-Superconductor Heterostructures. *Phys. Rev. Lett.*, 117(1):017001, jun 2016. 10.1103/PhysRevLett.117.017001.

[138] S. M. Dahir, A. F. Volkov, and I. M. Eremin. Interaction of Skyrmions and Pearl Vortices in Superconductor-Chiral Ferromagnet Heterostructures. *Phys. Rev. Lett.*, 122(9):097001, mar 2019. 10.1103/PhysRevLett.122.097001.

[139] R. M. Menezes, J. F. Neto, et al. Manipulation of magnetic skyrmions by superconducting vortices in ferromagnet-superconductor heterostructures. *Phys. Rev. B*, 100(1):014431, jul 2019. 10.1103/PhysRevB.100.014431.

[140] X. Palermo, N. Reyren, et al. Tailored flux pinning in superconductor-ferromagnet multilayers with engineered magnetic domain morphology from stripes to skyrmions. *Phys. Rev. Appl.*, 13:014043, Jan 2020. 10.1103/PhysRevApplied.13.014043.

[141] V. L. Vadimov, M. V. Sapozhnikov, and A. S. Mel'nikov. Magnetic skyrmions in ferromagnet-superconductor (F/S) heterostructures. *Appl. Phys. Lett.*, 113(3):032402, jul 2018. 10.1063/1.5037934.

[142] A. Sander, G. Orfila, et al. Superconducting imprint of magnetic textures in ferromagnets with perpendicular magnetic anisotropy. *Sci. Rep.*, 11(1), 2021. 10.1038/s41598-021-99963-w.

[143] E. S. Andriyakhina and I. S. Burmistrov. Interaction of a Néel-type skyrmion with a superconducting vortex. *Phys. Rev. B*, 103:174519, May 2021. 10.1103/PhysRevB.103.174519.

[144] S. M. Dahir, A. F. Volkov, and I. M. Eremin. Meissner currents induced by topological magnetic textures in hybrid superconductor/ferromagnet structures. *Phys. Rev. B*, 102(1):014503, jul 2020. 10.1103/PhysRevB.102.014503.

[145] A. P. Petrović, M. Raju, et al. Skyrmion-(Anti)Vortex Coupling in a Chiral Magnet-Superconductor Heterostructure. *Phys. Rev. Lett.*, 126:117205, Mar 2021. 10.1103/PhysRevLett.126.117205.

[146] M. Song, M. G. Park, et al. Logic Device Based on Skyrmion Annihilation. *IEEE Trans Electron. Devices*, 68(4):1939–1943, 2021. 10.1109/ted.2021.3055157.

[147] X. Zhang, M. Ezawa, and Y. Zhou. Thermally stable magnetic skyrmions in multilayer synthetic antiferromagnetic racetracks. *Phys. Rev. B*, 94(6):064406, aug 2016. 10.1103/PhysRevB.94.064406.

[148] P. F. Bessarab, G. P. Müller, et al. Lifetime of racetrack skyrmions. *Sci. Rep.*, 8(1):3433, dec 2018. 10.1038/s41598-018-21623-3.

[149] J. Miltat, S. Rohart, and A. Thiaville. Brownian motion of magnetic domain walls and skyrmions, and their diffusion constants. *Phys. Rev. B*, 97(21):214426, jun 2018. 10.1103/PhysRevB.97.214426.

[150] C. T. Ma, Y. Xie, et al. Robust formation of ultrasmall room-temperature neél skyrmions in amorphous ferrimagnets from atomistic simulations. *Sci. Rep.*, 9:1–10, 7 2019. 10.1038/s41598-019-46458-4.

[151] A. Derras-Chouk, E. M. Chudnovsky, and D. A. Garanin. Thermal collapse of a skyrmion. *J. Appl. Phys.*, 126(8):083901, aug 2019. 10.1063/1.5109728.

[152] I. Medlej, A. Hamadeh, and F. E. H. Hassan. Skyrmion based random bit generator. *Physica B Condens. Matter*, 579:411900, feb 2020. 10.1016/J.PHYSB.2019.411900.

[153] L. Zhao, Z. Wang, et al. Topology-dependent brownian gyromotion of a single skyrmion. *Phys. Rev. Lett.*, 125:027206, Jul 2020. 10.1103/PhysRevLett.125.027206.

[154] W. F. Brown. Thermal fluctuations of a single-domain particle. *Phys. Rev.*, 130:1677–1686, Jun 1963. 10.1103/PhysRev.130.1677.

[155] P. F. Bessarab, V. M. Uzdin, and H. Jónsson. Harmonic transition-state theory of thermal spin transitions. *Phys. Rev. B*, 85:184409, May 2012. 10.1103/PhysRevB.85.184409.

[156] P. F. Bessarab, V. M. Uzdin, and H. Jónsson. Method for finding mechanism and activation energy of magnetic transitions, applied to skyrmion and antivortex annihilation. *Comput. Phys. Commun.*, 196:335–347, 2015. 10.1016/j.cpc.2015.07.001.

[157] G. P. Müller, P. F. Bessarab, et al. Duplication, collapse, and escape of magnetic skyrmions revealed using a systematic saddle point search method. *Phys. Rev. Lett.*, 121:197202, Nov 2018. 10.1103/PhysRevLett.121.197202.

[158] L. Desplat, D. Suess, et al. Thermal stability of metastable magnetic skyrmions: Entropic narrowing and significance of internal eigenmodes. *Phys. Rev. B*, 98:134407, Oct 2018. 10.1103/PhysRevB.98.134407.

[159] L. Desplat, C. Vogler, et al. Path sampling for lifetimes of metastable magnetic skyrmions and direct comparison with kramers' method. *Phys. Rev. B*, 101:060403, Feb 2020. 10.1103/PhysRevB.101.060403.

[160] Z. Wang, M. Guo, et al. Thermal generation, manipulation and thermoelectric detection of skyrmions. *Nat. Electron.*, 3:672–679, 2020. 10.1038/s41928-020-00489-2.

[161] H. Zhang, D. Zhu, et al. Stochastic Computing Implemented by Skyrmionic Logic Devices. *Phys. Rev. Applied*, 13:054049, May 2020. 10.1103/PhysRevApplied.13.054049.

[162] S. Li, W. Kang, et al. Magnetic skyrmion-based artificial neuron device. *Nanotechnology*, 28(31):31LT01, jul 2017. 10.1088/1361-6528/aa7af5.

[163] X. Chen, W. Kang, et al. A compact skyrmionic leaky–integrate–fire spiking neuron device. *Nanoscale*, 10:6139–6146, 2018. 10.1039/c7nr09722k.

[164] K. M. Song, J. S. Jeong, et al. Skyrmion-based artificial synapses for neuromorphic computing. *Nat. Electron.*, 3:148–155, mar 2020. 10.1038/s41928-020-0385-0.

[165] S. Li, W. Kang, et al. Magnetic skyrmions for unconventional computing. *Mater. Horiz.*, 8:854–868, 2021. 10.1039/D0MH01603A.

[166] C. Navau and J. Sort. Exploiting random phenomena in magnetic materials for data security, logics, and neuromorphic computing: Challenges and prospects. *APL Mater.*, 9(7):070903, jul 2021. 10.1063/5.0055400.

[167] P. G. De Gennes. *Superconductivity Of Metals And Alloys.* CRC Press, 1 edition, March 1999.

[168] C. Poole, H. Farach, and R. Creswick. *Superconductivity.* Elsevier Science, 2013.

[169] J. D. Jackson. *Classical electrodynamics.* Wiley, New York, NY, 3rd ed. edition, 1999.

[170] L. Exl, D. Suess, and T. Schrefl. Micromagnetism. In M. Coey and S. Parkin, editors, *Handbook of Magnetism and Magnetic Materials*, pages 1–44. Springer International Publishing, Cham, 2020. 10.1007/978-3-030-63101-7_7-1.

[171] L. D. Landau and E. Lifshitz. On the theory of the dispersion of magnetic permeability in ferromagnetic bodies. *Phys. Z. Sowjet.*, 8:153, 1935.

[172] T. Gilbert. A phenomenological theory of damping in ferromagnetic materials. *IEEE Trans. Magn.*, 40(6):3443–3449, 2004. 10.1109/tmag.2004.836740.

[173] M. Lakshmanan. The fascinating world of the landau-lifshitz-gilbert equation: an overview. *Philos. Trans. Royal Soc. A*, 369(1939):1280–1300, 2011. 10.1098/rsta.2010.0319.

[174] H. Kronmuller and M. Fahnle. *Micromagnetism and the microstructure of ferromagnetic solids.* Cambridge University Press, 2003.

[175] C. W. Abert. *Discrete Mathematical Concepts in Micromagnetic Computations.* PhD thesis, Staats-und Universitätsbibliothek Hamburg Carl von Ossietzky, 2013.

[176] J. M. D. Coey. *Magnetism and magnetic materials.* Cambridge University Press, 2010.

[177] K. J. Harte. Theory of magnetization ripple in ferromagnetic films. *J. Appl. Phys.*, 39(3):1503–1524, 1968. 10.1063/1.1656388.

[178] S. Rohart, V. Repain, et al. Limits of the macrospin model in cobalt nanodots with enhanced edge magnetic anisotropy. *Phys. Rev. B*, 76:104401, Sep 2007. 10.1103/PhysRevB.76.104401.

[179] L. Ranno and M. A. Moro. Design Rules for DMI-Stabilised Skyrmions, 2021. 10.48550/arxiv.2107.00767. `https://arxiv.org/abs/2107.00767`.

[180] W. Heisenberg. Mehrkörperproblem und Resonanz in der Quantenmechanik. *Z. Physik*, 38(6):411–426, Jun 1926. 10.1007/BF01397160.

[181] P. A. M. Dirac and R. H. Fowler. On the theory of quantum mechanics. *Proc. R. Soc. Lond. A*, 112(762):661–677, 1926. 10.1098/rspa.1926.0133.

[182] C. Kittel. Symposium on exchange—introduction. *Rev. Mod. Phys.*, 25:191–191, Jan 1953. 10.1103/RevModPhys.25.191.

[183] C. Kittel. Indirect exchange interactions in metals. In F. Seitz, D. Turnbull, and H. Ehrenreich, editors, *Solid State Physics*, volume 22, pages 1–26. Academic Press, 1969. 10.1016/S0081-1947(08)60030-2.

[184] M. van Schilfgaarde and V. P. Antropov. First-principles exchange interactions in fe, ni, and co. *J. Appl. Phys.*, 85(8):4827–4829, 1999. 10.1063/1.370495.

[185] A. R. Biedermann. Magnetic anisotropy in single crystals: A review. *Geosciences 2018, Vol. 8, Page 302*, 8:302, 8 2018. 10.3390/GEOSCIENCES8080302.

[186] A. Soumyanarayanan, N. Reyren, et al. Emergent phenomena induced by spin–orbit coupling at surfaces and interfaces. *Nature*, 539(7630):509–517, nov 2016. 10.1038/nature19820.

[187] I. Dzyaloshinsky. A thermodynamic theory of “weak” ferromagnetism of antiferromagnetics. *Journal of Physics and Chemistry of Solids*, 4(4):241–255, jan 1958. 10.1016/0022-3697(58)90076-3.

[188] T. Moriya. Anisotropic Superexchange Interaction and Weak Ferromagnetism. *Physical Review*, 120(1):91–98, oct 1960. 10.1103/PhysRev.120.91.

[189] P. Bak and M. H. Jensen. Theory of helical magnetic structures and phase transitions in mnsi and fege. *Journal of Physics C: Solid State Physics*, 13, nov 1980. 10.1088/0022-3719/13/31/002.

[190] A. Bogdanov and A. Hubert. Thermodynamically stable magnetic vortex states in magnetic crystals. *J. Magn. Magn. Mater.*, 138(3):255–269, 1994.

[191] B. Krüger. *Current-driven magnetization dynamics: analytical modeling and numerical simulation.* PhD thesis, Staats-und Universitätsbibliothek Hamburg Carl von Ossietzky, 2011.

[192] N. Chowdhury, S. Bedanta, and G. Babu. Study of magnetization reversal processes in a thin co film. *J. Magn. Magn. Mater.*, 336:20–25, 2013. 10.1016/j.jmmm.2013.02.009.

[193] A. Thiaville, J. M. García, et al. Micromagnetic study of bloch-point-mediated vortex core reversal. *Phys. Rev. B*, 67:094410, Mar 2003. 10.1103/PhysRevB.67.094410.

[194] H. Niedoba and M. Labrune. Magnetization reversal via bloch points nucleation in nanowires and dots: a micromagnetic study. *Eur. Phys. J. B*, 47, Oct 2005. 10.1140/epjb/e2005-00353-6.

[195] M. Hoffmann, B. Zimmermann, et al. Antiskyrmions stabilized at interfaces by anisotropic Dzyaloshinskii-Moriya interactions. *Nat. Commun.*, 8, Aug 2017. 10.1038/s41467-017-00313-0.

[196] J. Castell-Queralt, L. González-Gómez, et al. Accelerating, guiding, and compressing skyrmions by defect rails. *Nanoscale*, 11(26):12589–12594, jul 2019. 10.1039/C9NR02171J.

[197] J. Slonczewski. Current-driven excitation of magnetic multilayers. *J. Magn. Magn. Mater.*, 159(1-2):L1–L7, jun 1996. 10.1016/0304-8853(96)00062-5.

[198] A. Brataas, A. D. Kent, and H. Ohno. Current-induced torques in magnetic materials. *Nature Materials*, 11(5):372–381, may 2012. 10.1038/nmat3311.

[199] I. Lisenkov, R. Khymyn, et al. Subterahertz ferrimagnetic spin-transfer torque oscillator. *Phys. Rev. B*, 100:100409, Sep 2019. 10.1103/PhysRevB.100.100409.

[200] R. Cheng, J. Xiao, et al. Spin pumping and spin-transfer torques in antiferromagnets. *Phys. Rev. Lett.*, 113:057601, Jul 2014. 10.1103/PhysRevLett.113.057601.

[201] J. Železný, P. Wadley, et al. Spin transport and spin torque in antiferromagnetic devices. *Nat. Phys.*, 14(3):220–228, Mar 2018. 10.1038/s41567-018-0062-7.

[202] J. Wang, C. Jin, et al. Rapid creation and reversal of skyrmion in spin-valve nanopillars. *J. Magn. Magn. Mater.*, 474, mar 2019. 10.1016/J.JMMM.2018.11.036.

[203] L. Shen, J. Xia, et al. Spin torque nano-oscillators based on antiferromagnetic skyrmions. *Appl. Phys. Lett.*, 114(4):042402, jan 2019. 10.1063/1.5080302.

[204] Z. Li and S. Zhang. Domain-Wall Dynamics and Spin-Wave Excitations with Spin-Transfer Torques. *Phys. Rev. Lett.*, 92(20):207203, may 2004. 10.1103/PhysRevLett.92.207203.

[205] Y. B. Bazaliy, B. A. Jones, and S.-C. Zhang. Modification of the Landau-Lifshitz equation in the presence of a spin-polarized current in colossal- and giant-magnetoresistive materials. *Phys. Rev. B*, 57(6):R3213–R3216, feb 1998. 10.1103/PhysRevB.57.R3213.

[206] S. Zhang and Z. Li. Roles of Nonequilibrium Conduction Electrons on the Magnetization Dynamics of Ferromagnets. *Phys. Rev. Lett.*, 93(12):127204, sep 2004. 10.1103/PhysRevLett.93.127204.

[207] S. Emori, U. Bauer, et al. Current-driven dynamics of chiral ferromagnetic domain walls. *Nat. Mater.*, 12(7):611–616, jul 2013. 10.1038/nmat3675.

[208] L. Liu, O. J. Lee, et al. Current-Induced Switching of Perpendicularly Magnetized Magnetic Layers Using Spin Torque from the Spin Hall Effect. *Phys. Rev. Lett.*, 109(9):096602, aug 2012. 10.1103/PhysRevLett.109.096602.

[209] M. Dyakonov and V. Perel. Current-induced spin orientation of electrons in semiconductors. *Physics Letters A*, 35(6):459–460, 1971. 0375-9601(71)90196-4.

[210] M. I. DYakonov and V. I. Perel. Possibility of Orienting Electron Spins with Current. *Soviet Journal of Experimental and Theoretical Physics Letters*, 13:467, June 1971.

[211] K. Litzius, J. Leliaert, et al. The role of temperature and drive current in skyrmion dynamics. *Nature Electronics*, 3, 1 2020. 10.1038/s41928-019-0359-2.

[212] S. Lepadatu. Effect of inter-layer spin diffusion on skyrmion motion in magnetic multilayers. *Sci. Rep.*, 9, Jul 2019. 10.1038/s41598-019-46091-1.

[213] C. R. MacKinnon, S. Lepadatu, et al. Role of an additional interfacial spin-transfer torque for current-driven skyrmion dynamics in chiral magnetic layers. *Phys. Rev. B*, 102:214408, Dec 2020. 10.1103/PhysRevB.102.214408.

[214] C. R. MacKinnon, K. Zeissler, et al. Collective skyrmion motion under the influence of an additional interfacial spin-transfer torque. *Sci. Rep.*, 12:10786, Jun 2022. 10.1038/s41598-022-14969-2.

[215] X. Zhao, S. Wang, et al. Thermal effects on current-related skyrmion formation in a nanobelt. *Appl. Phys. Lett.*, 112(21):212403, may 2018. 10.1063/1.5031474.

[216] R. Juge, S. G. Je, et al. Magnetic skyrmions in confined geometries: Effect of the magnetic field and the disorder. *J. Magn. Magn. Mater.*, 455:3–8, jun 2018. 10.1016/j.jmmm.2017.10.030.

[217] W. Akhtar, A. Hrabec, et al. Current-Induced Nucleation and Dynamics of Skyrmions in a Co-based Heusler Alloy. *Phys. Rev. Appl.*, 11(3):034066, mar 2019. 10.1103/PhysRevApplied.11.034066.

[218] W. Legrand, D. Maccariello, et al. Room-temperature stabilization of antiferromagnetic skyrmions in synthetic antiferromagnets. *Nat. Mater.*, sep 2019. 10.1038/s41563-019-0468-3.

[219] W. Legrand, D. Maccariello, et al. Room-Temperature Current-Induced Generation and Motion of sub-100 nm Skyrmions. *Nano Lett.*, 17(4):2703–2712, apr 2017. 10.1021/acs.nanolett.7b00649.

[220] G. Yu, P. Upadhyaya, et al. Room-Temperature Creation and Spin–Orbit Torque Manipulation of Skyrmions in Thin Films with Engineered Asymmetry. *Nano Lett.*, 16(3):1981–1988, mar 2016. 10.1021/acs.nanolett.5b05257.

[221] G. Yu, P. Upadhyaya, et al. Room-Temperature Skyrmion Shift Device for Memory Application. *Nano Lett.*, 17:21, 2017. 10.1021/acs.nanolett.6b04010.

[222] S. Zhang, J. Zhang, et al. Direct writing of room temperature and zero field skyrmion lattices by a scanning local magnetic field. *Appl. Phys. Lett.*, 112(13):132405, mar 2018. 10.1063/1.5021172.

[223] T. Matsumoto, Y.-G. So, et al. Stable Magnetic Skyrmion States at Room Temperature Confined to Corrals of Artificial Surface Pits Fabricated by a Focused Electron Beam. *Nano Letters*, 2018. 10.1021/acs.nanolett.7b03967.

[224] C. Reichhardt, D. Ray, and C. J. O. Reichhardt. Quantized transport for a skyrmion moving on a two-dimensional periodic substrate. *Phys. Rev. B*, 91(10):104426, mar 2015. 10.1103/PhysRevB.91.104426.

[225] C. Reichhardt and C. J. O. Reichhardt. Nonlinear transport, dynamic ordering, and clustering for driven skyrmions on random pinning. *Phys. Rev. B*, 99:104418, Mar 2019. 10.1103/PhysRevB.99.104418.

[226] J. Müller and A. Rosch. Capturing of a magnetic skyrmion with a hole. *Phys. Rev. B*, 91(5):054410, feb 2015. 10.1103/PhysRevB.91.054410.

[227] S. L. Zhang, W. W. Wang, et al. Manipulation of skyrmion motion by magnetic field gradients. *Nat. Commun.*, 9(1), May 2018. 10.1038/s41467-018-04563-4.

[228] I. Makhfudz, B. Krüger, and O. Tchernyshyov. Inertia and chiral edge modes of a skyrmion magnetic bubble. *Phys. Rev. Lett.*, 109:217201, Nov 2012. 10.1103/PhysRevLett.109.217201.

[229] C. Schütte, J. Iwasaki, et al. Inertia, diffusion, and dynamics of a driven skyrmion. *Phys. Rev. B*, 90:174434, Nov 2014. 10.1103/PhysRevB.90.174434.

[230] F. Büttner, C. Moutafis, et al. Dynamics and inertia of skyrmionic spin structures. *Nat. Phys.*, 11:225–228, Mar 2015. 10.1038/nphys3234.

[231] T. Shiino, K.-J. Kim, et al. Inertia-driven resonant excitation of a magnetic skyrmion. *Sci. Rep.*, 7(1):13993, dec 2017. 10.1038/s41598-017-13241-2.

[232] J. Martinez and M. Jalil. Mass of a skyrmion under a driving current. *J. Magn. Magn. Mater.*, 424:291–297, 2017. 10.1016/j.jmmm.2016.10.026.

[233] J. Zang, M. Mostovoy, et al. Dynamics of skyrmion crystals in metallic thin films. *Phys. Rev. Lett.*, 107:136804, Sep 2011. 10.1103/PhysRevLett.107.136804.

[234] W. Jiang, G. Chen, et al. Skyrmions in magnetic multilayers. *Phys. Rep.*, 704, 2017. 10.1016/j.physrep.2017.08.001.

[235] T. Schulz, R. Ritz, et al. Emergent electrodynamics of skyrmions in a chiral magnet. *Nat. Phys.*, 8(4):301–304, apr 2012. 10.1038/nphys2231.

[236] K. Litzius, I. Lemesh, et al. Skyrmion Hall effect revealed by direct time-resolved X-ray microscopy. *Nat. Phys.*, 13(2):170–175, dec 2016. 10.1038/nphys4000.

[237] H. Jónsson, G. Mills, and K. W. Jacobsen. Nudged elastic band method for finding minimum energy paths of transitions. In Berne, Bruce J and Ciccotti, Giovanni and Coker, David F, editor, *Classical and Quantum Dynamics in Condensed Phase Simulations*, chapter 16, pages 385–404. World Scientific, Jun 1998. 10.1142/9789812839664_0016.

[238] G. Henkelman, B. P. Uberuaga, and H. Jónsson. A climbing image nudged elastic band method for finding saddle points and minimum energy paths. *The Journal of Chemical Physics*, 113(22), 2000. 10.1063/1.1329672.

[239] W. Ee, W. Ren, and E. Vanden-Eijnden. String method for the study of rare events. *Phys. Rev. B*, 66:052301, Aug 2002. 10.1103/PhysRevB.66.052301.

[240] J. Langer. Statistical theory of the decay of metastable states. *Annals of Physics*, 54(2), 1969. 10.1016/0003-4916(69)90153-5.

[241] S. von Malottki, B. Dupé, et al. Enhanced skyrmion stability due to exchange frustration. *Sci. Rep.*, 7(1):12299, 2017. 10.1038/s41598-017-12525-x.

[242] S. Haldar, S. von Malottki, et al. First-principles prediction of sub-10-nm skyrmions in pd/fe bilayers on rh(111). *Phys. Rev. B*, 98:060413, Aug 2018. 10.1103/PhysRevB.98.060413.

[243] F. Muckel, S. von Malottki, et al. Experimental identification of two distinct skyrmion collapse mechanisms. *Nat. Phys.*, 17:395–402, 2021. 10.1038/s41567-020-01101-2.

[244] W. Meissner and R. Ochsenfeld. Ein neuer Effekt bei Eintritt der Supraleitfähigkeit. *Naturwissenschaften*, 21(44):787–788, November 1933. 10.1007/BF01504252.

[245] J. G. Bednorz and K. A. Müller. Possible hightc superconductivity in the balacuo system. *Z. Phys B Cond. Matt.*, 64(2):189–193, Jun 1986. 10.1007/BF01303701.

[246] M. K. Wu, J. R. Ashburn, et al. Superconductivity at 93 K in a new mixed-phase Y-Ba-Cu-O compound system at ambient pressure. *Phys. Rev. Lett.*, 58:908–910, Mar 1987. 10.1103/PhysRevLett.58.908.

[247] H. Maeda, Y. Tanaka, et al. A New High-T_c Oxide Superconductor without a Rare Earth Element. *Jpn. J. Appl. Phys.*, 27(Part 2, No. 2):209–210, feb 1988. 10.1143/jjap.27.l209.

[248] J. Bardeen, L. N. Cooper, and J. R. Schrieffer. Microscopic theory of superconductivity. *Phys. Rev.*, 106:162–164, Apr 1957. 10.1103/PhysRev.106.162.

[249] . 73 - On the theory of Superconductivity. In D. T. Haar, editor, *Collected Papers of L.D. Landau*, pages 546–568. Pergamon, 1965. 10.1016/B978-0-08-010586-4.50078-X.

[250] A. A. Abrikosov. On the Magnetic properties of superconductors of the second group. *Sov. Phys. JETP*, 5:1174–1182, 1957.

[251] L. F. and L. H. The electromagnetic equations of the supraconductor. *Proc. R. Soc. Lond.*, 149, Mar 1935. 10.1098/rspa.1935.0048.

[252] G. Blatter, M. V. Feigel'man, et al. Vortices in high-temperature superconductors. *Rev. Mod. Phys.*, 66(4):1125–1388, oct 1994. 10.1103/RevModPhys.66.1125.

[253] H. T. Coffey. Modified london model for type-ii superconductors. *Phys. Rev.*, 166:447–456, Feb 1968. 10.1103/PhysRev.166.447.

[254] J. Pearl. CURRENT DISTRIBUTION IN SUPERCONDUCTING FILMS CARRYING QUANTIZED FLUXOIDS. *Appl. Phys. Lett.*, 5(4):65, nov 1964. 10.1063/1.1754056.

[255] E. H. Brandt and J. R. Clem. Superconducting thin rings with finite penetration depth. *Phys. Rev. B*, 69(18):184509, may 2004. 10.1103/PhysRevB.69.184509.

[256] D.-X. Chen, C. Navau, et al. Effective penetration depths of a thin type-II superconducting strip. *Supercond. Sci. Technol.*, 21(10):105010, jul 2008. 10.1088/0953-2048/21/10/105010.

[257] S. Parkin and S.-H. Yang. Memory on the racetrack. *Nat. Nanotechnol.*, 10(3):195–198, mar 2015. 10.1038/nnano.2015.41.

[258] C. Reichhardt, C. J. O. Reichhardt, and M. V. Milošević. Statics and dynamics of skyrmions interacting with disorder and nanostructures. *Rev. Mod. Phys.*, 94:035005, Sep 2022. 10.1103/RevModPhys.94.035005.

[259] M. Potkina, I. Lobanov, and V. Uzdin. Nonmagnetic impurities in skyrmion racetrack memory. *Nanosystems: Phys. Chem. Math.*, 11, 2020. 10.17586/2220-8054-2020-11-6-628-635.

[260] L. Gnoli, F. Riente, et al. Skyrmion logic-in-memory architecture for maximum/minimum search. *Electronics*, 10(2), 2021. 10.3390/electronics10020155.

[261] X. Liang, J. Xia, et al. Antiferromagnetic skyrmion-based logic gates controlled by electric currents and fields. *Appl. Phys. Lett.*, 119(6):062403, 2021. 10.1063/5.0056259.

[262] Y.-H. Liu and Y.-Q. Li. A mechanism to pin skyrmions in chiral magnets. *J. Phys.: Condens. Matter*, 25(7):076005, feb 2013. 10.1088/0953-8984/25/7/076005.

[263] S.-Z. Lin, C. Reichhardt, et al. Particle model for skyrmions in metallic chiral magnets: Dynamics, pinning, and creep. *Phys. Rev. B*, 87(21):214419, jun 2013. 10.1103/PhysRevB.87.214419.

[264] K. Everschor-Sitte, M. Sitte, et al. Skyrmion production on demand by homogeneous DC currents. *New J. Phys.*, 19(9):092001, sep 2017. 10.1088/1367-2630/aa8569.

[265] F. Garcia-Sanchez, J. Sampaio, et al. A skyrmion-based spin-torque nano-oscillator. *New J. Phys.*, 18(7):075011, jul 2016. 10.1088/1367-2630/18/7/075011.

[266] S. Saha, M. Zelent, et al. Formation of néel-type skyrmions in an antidot lattice with perpendicular magnetic anisotropy. *Phys. Rev. B*, 100:144435, Oct 2019. 10.1103/PhysRevB.100.144435.

[267] N. P. Vizarim, C. J. O. Reichhardt, et al. Skyrmion dynamics and transverse mobility: skyrmion Hall angle reversal on 2D periodic substrates with dc and biharmonic ac drives. *Eur. Phys. J. B*, 93(6), Jun 2020. 10.1140/epjb/e2020-10135-1.

[268] N. P. Vizarim, C. Reichhardt, et al. Skyrmion dynamics and topological sorting on periodic obstacle arrays. *New J. Phys.*, 22(5):053025, may 2020. 10.1088/1367-2630/ab8045.

[269] N. P. Vizarim, C. J. O. Reichhardt, et al. Skyrmion pinball and directed motion on obstacle arrays. *J. Phys. Commun.*, 4(8):085001, Aug 2020. 10.1088/2399-6528/aba9fb.

[270] N. P. Vizarim, C. Reichhardt, et al. Guided skyrmion motion along pinning array interfaces. *J. Magn. Magn. Mater.*, 528:167710, Jun 2021.

[271] S. H. Guan, Y. Yang, et al. Unidirectional localization and track-selection of antiferromagnetic skyrmions through tuning magnetocrystalline anisotropy barriers. *J. Magn. Magn. Mater.*, 546:168852, Mar 2022.

[272] S.-Z. Lin, C. Reichhardt, and A. Saxena. Manipulation of skyrmions in nanodisks with a current pulse and skyrmion rectifier. *Appl. Phys. Lett.*, 102(22):222405, jun 2013. 10.1063/1.4809751.

[273] J. Iwasaki, W. Koshibae, and N. Nagaosa. Colossal Spin Transfer Torque Effect on Skyrmion along the Edge. *Nano Lett.*, 14(8):4432–4437, aug 2014. 10.1021/nl501379k.

[274] C. Reichhardt and C. J. O. Reichhardt. Magnus-induced dynamics of driven skyrmions on a quasi-one-dimensional periodic substrate. *Phys. Rev. B*, 94:094413, Sep 2016. 10.1103/PhysRevB.94.094413.

[275] Y. Hirata, D.-H. Kim, et al. Vanishing skyrmion hall effect at the angular momentum compensation temperature of a ferrimagnet. *Nat. Nanotechnol.*, 14(3):232–236, Mar 2019. 10.1038/s41565-018-0345-2.

[276] L.-M. Kern, B. Pfau, et al. Deterministic Generation and Guided Motion of Magnetic Skyrmions by Focused He+-Ion Irradiation. *Nano Lett.*, 22(10):4028–4035, 2022. 10.1021/acs.nanolett.2c00670.

[277] L. González-Gómez, J. Castell-Queralt, et al. Analytical modeling of the interaction between skyrmions and extended defects. *Phys. Rev. B*, 100:054440, Aug 2019. 10.1103/PhysRevB.100.054440.

[278] M. Abramowitz and I. A. Stegun. *Handbook of Mathematical Functions*, chapter 16. Dover Publications Inc., 9 edition, 1965.

[279] C. Reichhardt, D. Ray, and C. J. O. Reichhardt. Magnus-induced ratchet effects for skyrmions interacting with asymmetric substrates. *New J. Phys.*, 17(7):073034, jul 2015. 10.1088/1367-2630/17/7/073034.

[280] C. Reichhardt and C. J. O. Reichhardt. Commensuration effects on skyrmion hall angle and drag for manipulation of skyrmions on two-dimensional periodic substrates. *Phys. Rev. B*, 105:214437, Jun 2022. 10.1103/PhysRevB.105.214437.

[281] C. J. O. Reichhardt and C. Reichhardt. Active rheology and anticommensuration effects for driven probe particles on two-dimensional periodic pinning substrates. *Phys. Rev. Res*, 4:013190, Mar 2022. 10.1103/PhysRevResearch.4.013190.

[282] O. Romero-Isart, C. Navau, et al. Superconducting Vortex Lattices for Ultracold Atoms. *Phys. Rev. Lett.*, 111, Oct 2013. 10.1103/PhysRevLett.111.145304.

[283] R. Qin and Y. Wang. Control of ultracold atoms with a chiral ferromagnetic film. *Phys. Rev. A*, 99:013401, Jan 2019. 10.1103/PhysRevA.99.013401.

[284] R. Qin and Y. Wang. Skyrmion-based magnetic traps for ultracold atoms. *Phys. Rev. A*, 101:053428, May 2020. 10.1103/PhysRevA.101.053428.

[285] X. Zhang, J. Xia, et al. Configurable pixelated skyrmions on nanoscale magnetic grids. *Commun. Phys.*, 4(1), Dec 2021. 10.1038/s42005-021-00761-7.

[286] C. Back, V. Cros, et al. The 2020 skyrmionics roadmap. *J. Phys. D: Appl. Phys.*, 53(36):363001, jun 2020. 10.1088/1361-6463/ab8418.

[287] I. F. Lyuksyutov and V. L. Pokrovsky. Ferromagnet-Superconductor Hybrids. *Adv. Phys.*, 54(1):67–136, sep 2004. 10.1080/00018730500057536.

[288] A. Y. Aladyshkin, A. V. Silhanek, et al. Nucleation of superconductivity and vortex matter in superconductor-ferromagnet hybrids. *Supercond. Sci. Technol.*, 22(5):053001, mar 2009. 10.1088/0953-2048/22/5/053001.

[289] M. Vélez, J. Martín, et al. Superconducting vortex pinning with artificial magnetic nanostructures. *J. Magn. Magn. Mater.*, 320(21):2547–2562, 2008. 10.1016/j.jmmm.2008.06.013.

[290] S. Wang, J. Wang, et al. The man-loading high-temperature superconducting Maglev test vehicle. *IEEE Trans. Appl. Supercond.*, 13(2):2134–2137, 2003. 10.1109/TASC.2003.813017.

[291] I. F. Lyuksyutov and V. L. Pokrovsky. Ferromagnet–superconductor hybrids. *Adv. Phys.*, 54(1):67–136, 2005. 10.1080/00018730500057536.

[292] T. Yokoyama and J. Linder. Josephson effect through magnetic skyrmions. *Phys. Rev. B*, 92:060503, Aug 2015. 10.1103/PhysRevB.92.060503.

[293] P. B. Pal. Dirac, Majorana, and Weyl fermions. *Am. J. Phys.*, 79(5):485–498, 2011. 10.1119/1.3549729.

[294] M. Garnier, A. Mesaros, and P. Simon. Topological superconductivity with deformable magnetic skyrmions. *Commun. Phys.*, 2(126), 2019. 10.1038/s42005-019-0226-5.

[295] E. Mascot, J. Bedow, et al. Topological superconductivity in skyrmion lattices. *npj Quantum Mater.*, 6(6), 2021. 10.1038/s41535-020-00299-x.

[296] J. Linder and J. W. A. Robinson. Superconducting spintronics. *Nat. Phys.*, 11:307, Apr 2015. 10.1038/nphys3242.

[297] J. Prat-Camps, C. Teo, et al. Ultrasensitive inertial and force sensors with diamagnetically levitated magnets. *Phys. Rev. Appl.*, 8:034002, Sep 2017. 10.1103/PhysRevApplied.8.034002.

[298] C. P. Bean. Magnetization of hard superconductors. *Phys. Rev. Lett.*, 8:250–253, Mar 1962. 10.1103/PhysRevLett.8.250.

[299] J. Prat-Camps, C. Navau, and A. Sanchez. A Magnetic Wormhole. *Sci. Rep.*, 5, Aug 2015. 10.1038/srep12488.

[300] L. A. I. and Y. N. Ovchinnikov. Nonuniform state of superconductors. *Sov. Phys.*, 20:762–770, March 1965.

[301] P. Fulde and R. A. Ferrell. Superconductivity in a strong spin-exchange field. *Phys. Rev.*, 135:A550–A563, Aug 1964. 10.1103/PhysRev.135.A550.

[302] M. Leijnse and K. Flensberg. Introduction to topological superconductivity and Majorana fermions. *Semicond. Sci. Technol.*, 27(12):124003, nov 2012. 10.1088/0268-1242/27/12/124003.

[303] A. L. R. Manesco, G. Weber, and D. Rodrigues. One-Dimensional *p*-Wave Superconductor Toy-Model for Majorana Fermions in Multiband Semiconductor Nanowires. *IEEE Trans. Appl. Supercond.*, 28(4):1–5, 2018. 10.1109/TASC.2018.2807361.

[304] G. Yang, C. Ciccarelli, and J. W. A. Robinson. Boosting spintronics with superconductivity. *APL Mater.*, 9(5):050703, 2021. 10.1063/5.0048904.

[305] V. Rouco, R. Córdoba, et al. Competition between Superconductor – Ferromagnetic stray magnetic fields in YBa2Cu3O7x films pierced with Co nano-rods. *Sci. Rep.*, 7(2):5663, 2017. 10.1038/s41598-017-05909-6.

[306] N. Del-Valle, C. Navau, et al. Transport critical-current density of superconducting films with hysteretic ferromagnetic dots. *AIP Adv.*, 2(2):022166, 2012. 10.1063/1.4732314.

[307] J. Pendry, A. Holden, et al. Magnetism from conductors and enhanced nonlinear phenomena. *IIEEE Trans. Microw Theory Tech.*, 47(11):2075–2084, 1999. 10.1109/22.798002.

[308] R. Kshetrimayum. A brief intro to metamaterials. *IEEE Potentials*, 23(5):44–46, 2005. 10.1109/MP.2005.1368916.

[309] J. Zhu, W. Jiang, et al. Three-dimensional magnetic cloak working from d.c. to 250 khz. *Nat. Commun.*, 6, Nov 2015. 10.1038/ncomms9931.

[310] I. A. Golovchanskiy, N. N. Abramov, et al. Ferromagnet/superconductor hybrid magnonic metamaterials. *Adv. Sci.*, 6(16):1900435, 2019. 10.1002/advs.201900435.

[311] R. Mach-Batlle, M. G. Bason, et al. Tailoring magnetic fields in inaccessible regions. *Phys. Rev. Lett.*, 125:177204, Oct 2020. 10.1103/PhysRevLett.125.177204.

[312] S. M. Anlage. The physics and applications of superconducting metamaterials. *J. Opt.*, 13(2):024001, nov 2010. 10.1088/2040-8978/13/2/024001.

[313] J. Prat-Camps, A. Sanchez, and C. Navau. Superconductor-ferromagnetic metamaterials for magnetic cloaking and concentration. *Supercond. Sci. Technol.*, 26(7):074001, may 2013. 10.1088/0953-2048/26/7/074001.

[314] S. Earnshaw. On the Nature of the Molecular Forces which Regulate the Constitution of the Luminiferous Ether. *Trans. Cambdrige Philos. Soc.*, 7(96), 1842.

[315] F. C. Moon. *Superconducting levitation.* Wiley, 1 edition, 1994.

[316] M. V. Berry and A. K. Geim. Of flying frogs and levitrons. *Eur. J. Phys.*, 18(4):307–313, jul 1997. 10.1088/0143-0807/18/4/012.

[317] N. Del-Valle, S. Agramunt-Puig, et al. Shaping magnetic fields with soft ferromagnets: Application to levitation of superconductors. *J. Appl. Phys.*, 111(1):013921, 2012. 10.1063/1.3676578.

[318] S. Agramunt-Puig, N. Del-Valle, et al. Optimization of a superconducting linear levitation system using a soft ferromagnet. *Physica C Supercond.*, 487:11–15, 2013. 10.1016/j.physc.2013.01.013.

[319] O. Romero-Isart, L. Clemente, et al. Quantum Magnetomechanics with Levitating Superconducting Microspheres. *Phys. Rev. Lett.*, 109, Oct 2012. 10.1103/PhysRevLett.109.147205.

[320] C. Navau, S. Minniberger, et al. Levitation of superconducting microrings for quantum magnetomechanics. *Phys. Rev. B*, 103:174436, May 2021. 10.1103/PhysRevB.103.174436.

[321] M. V. Milošević and F. M. Peeters. Interaction between a superconducting vortex and an out-of-plane magnetized ferromagnetic disk: Influence of the magnet geometry. *Phys. Rev. B*, 68:094510, Sep 2003. 10.1103/PhysRevB.68.094510.

[322] S. Erdin, I. F. Lyuksyutov, et al. Topological Textures in a Ferromagnet-Superconductor Bilayer. *Phys. Rev. Lett.*, 88:017001, Dec 2001. 10.1103/PhysRevLett.88.017001.

[323] R. Laiho, E. Lähderanta, et al. Penetration of vortices into the ferromagnet/type-II superconductor bilayer. *Phys. Rev. B*, 67:144522, Apr 2003. 10.1103/PhysRevB.67.144522.

[324] J. Pearl. Structure of Superconductive Vortices near a Metal-Air Interface. *J. Appl. Phys.*, 37:4139, 1966. 10.1063/1.1707989.

[325] J. R. Kirtley, C. C. Tsuei, et al. Fluxoid dynamics in superconducting thin film rings. *Phys. Rev. B*, 68:214505, Dec 2003. 10.1103/PhysRevB.68.214505.

[326] J. Castell-Queralt, L. González-Gómez, et al. Exploiting symmetries in skyrmionic micromagnetic simulations: Cylindrical and radial meshes. *J. Magn. Magn. Mater.*, 549:168972, 2022. 10.1016/j.jmmm.2021.168972.

[327] L. Mougel, P. M. Buhl, et al. Instability of skyrmions in magnetic fields. *Appl. Phys. Lett.*, 116(26):262406, 2020. 10.1063/5.0013488.

[328] H.-B. Braun. Topological effects in nanomagnetism: from superparamagnetism to chiral quantum solitons. *Adv. Phys.*, 61(1):1–116, 2012. 10.1080/00018732.2012.663070.

[329] M. Tinkham. *Introduction to Superconductivity.* Dover Publications, 2 edition, June 2004.

[330] W. H. Press, S. A. Teukolsky, et al. *Numerical recipes in C : the art of scientific computing.* Cambridge University Press, 2 edition, 1992.

[331] N.-H. Kim, D.-S. Han, et al. Improvement of the interfacial Dzyaloshinskii-Moriya interaction by introducing a Ta buffer layer. *Appl. Phys. Lett.*, 107(14):142408, oct 2015. 10.1063/1.4932550.

[332] R. Soucaille, M. Belmeguenai, et al. Probing the Dzyaloshinskii-Moriya interaction in CoFeB ultrathin films using domain wall creep and Brillouin light spectroscopy. *Phys. Rev. B*, 94(10):104431, sep 2016. 10.1103/PhysRevB.94.104431.

[333] S. Jaiswal, K. Litzius, et al. Investigation of the Dzyaloshinskii-Moriya interaction and room temperature skyrmions in W/CoFeB/MgO thin films and microwires. *Appl. Phys. Lett.*, 111(2):022409, jul 2017. 10.1063/1.4991360.

[334] A. Cao, R. Chen, et al. Enhanced interfacial Dzyaloshinskii - Moriya interactions in annealed Pt/Co/MgO structures. *Nanotechnology*, 31(15):155705, jan 2020. 10.1088/1361-6528/ab62cd.

[335] C. Kittel. *Introduction to Solid State Physics*, chapter 12, pages 352–354. John Wiley & Sons, 1996.

[336] I. S. Lobanov, H. Jónsson, and V. M. Uzdin. Mechanism and activation energy of magnetic skyrmion annihilation obtained from minimum energy path calculations. *Phys. Rev. B*, 94:174418, Nov 2016. 10.1103/PhysRevB.94.174418.

[337] D. Stosic, J. Mulkers, et al. Paths to collapse for isolated skyrmions in few-monolayer ferromagnetic films. *Phys. Rev. B*, 95:214418, Jun 2017. 10.1103/PhysRevB.95.214418.

[338] G. Carneiro and E. H. Brandt. Vortex lines in films: Fields and interactions. *Phys. Rev. B*, 61:6370–6376, Mar 2000. 10.1103/PhysRevB.61.6370.

[339] R. W. Sinnott. Virtues of the Haversine. *Sky Telescope*, 68(2):158, December 1984.

[340] R. J. Allen, C. Valeriani, and P. R. ten Wolde. Forward flux sampling for rare event simulations. *J. Phys.: Condens. Matter*, 21(46):463102, oct 2009. 10.1088/0953-8984/21/46/463102.

[341] C. Vogler, F. Bruckner, et al. Simulating rare switching events of magnetic nanostructures with forward flux sampling. *Phys. Rev. B*, 88:134409, Oct 2013. 10.1103/PhysRevB.88.134409.

[342] C. Vogler, F. Bruckner, et al. Calculating thermal stability and attempt frequency of advanced recording structures without free parameters. *J. Appl. Phys.*, 117(16):163907, 2015. 10.1063/1.4918902.

[343] B. Lubomir, B. Zdzislaw, et al. *Stochastic Ferromagnetism: Analysis and Numerics*, chapter 2, pages 103–195. De Gruyter, Berlin, Boston, 2013. 10.1515/9783110307108.103.

[344] J. Leliaert, J. Mulkers, et al. Adaptively time stepping the stochastic landau-lifshitz-gilbert equation at nonzero temperature: Implementation and validation in mumax3. *AIP Advances*, 7(12):125010, 2017. 10.1063/1.5003957.

List of publications

orcid.org/0000-0002-4214-4374

J. Castell-Queralt, L. González-Gómez, N. Del-Valle, A. Sanchez, C. Navau. Accelerating, guiding, and compressing skyrmions by defect rails. *Nanoscale*, 11 (26):12589-12594, 2019. 10.1039/C9NR02171J

L. González-Gómez, J. Castell-Queralt, N. Del-Valle, A. Sanchez, C. Navau. Analytical modeling of the interaction between skyrmions and extended defects. *Phys. Rev. B*, 100 (5):054440, 2019. 10.1103/PhysRevB.100.054440

J. Castell-Queralt, L. González-Gómez, N. Del-Valle, C. Navau. Deterministic approach to skyrmionic dynamics at nonzero temperatures: Pinning sites and racetracks. *Phys. Rev. B*, 101 (14):140404, 2020. 10.1103/PhysRevB.101.140404

N. Del-Valle, J. Castell-Queralt, L. González-Gómez, C. Navau. Defect modeling in skyrmionic ferromagnetic systems. *APL materials* 10 (1): 010702, 2022. 10.1063/5.0072709

J. Castell-Queralt, L. González-Gómez, N. Del-Valle, C. Navau. Exploiting symmetries in skyrmionic micromagnetic simulations: Cylindrical and radial meshes. J. Magn. Magn. Mater 549: 168972, 2022. 10.1016/j.jmmm.2021.168972

L. González-Gómez, J. Castell-Queralt, N. Del-Valle, C. Navau. Mutual Interaction between Superconductors and Ferromagnetic Skyrmionic Structures in Confined Geometries. Phys. Rev. Appl. 17 (3): 034069, 2022. 10.1103/PhysRevApplied.17.034069

J. Castell-Queralt, L. González-Gómez, N. Del-Valle, C. Navau. Survival of skyrmions along granular racetracks at room temperature. (Under Review)